Photophysical Approaches to Sensing Melanoma

PhD Thesis

Alastair Douglas Davy

Photophysics - Biomolecular and Chemical Physics

Department of Physics

University of Strathclyde, Glasgow

August 9, 2019

Signed:

Date:

Abstract

The spectroscopic/structure relationship of melanin is poorly understood which impedes the development of new biomaterials and skin cancer sensing techniques. Current methods for detecting melanoma ether lack the diagnostic capabilities or require high expense and training to use. There is a need for a melanoma diagnostic device that is both simple to use and cost-effective. The intrinsic response of eumelanin and pheomelanin with spectrophotometry, spectrofluorometry and time-correlated single photon counting were measured in order to investigate the photophysics of melanin and find a potential new technique for diagnosing melanoma that could be developed into a point-of-care device.

The optical and radiosensitising properties of gold nanorods make them attractive for biosensing applications. The toxicity of different gold nanorods, with alternative coatings, were investigated in order to establish their viability for development of a melanoma-specific biosensor. The results from the clonogenic toxicity assay and flow cytometry suggest that the gold nanorods induces long term damaging effects to the cells which hinder their viability as a biosensor.

The spectroscopic response of the sheet sensing fluorescent probe thioflavin T was measured during the formation of pheomelanin as the evidence for sheet formation in the red/yellow pigment is not as well established as the brown/black pigment, eumelanin. The increase of the dye molecule's fluorescence intensity provides strong evidence for the presence of sheet structures within pheomelanin and open up the potential use of extrinsic fluorophores as melanoma sensing probes. Successful implementation of extrinsic fluorophores could lead to investigating melanin's structure via super-resolution techniques.

Contents

Acknowledgements

Though the journey was difficult and many challenges were faced, I was not alone. During my time I have met many wonderful people who have helped me during my PhD studies. I have benefited immensely from my supervisor, Prof. David Birch's experience and I am grateful for his supervision and mentorship. I would like to thank Jens for introducing me to the melanin field and whose company and advice I have always appreciated. Also, my thanks to Dr Olaf Rolinski, Dr Yu Chen and Dr Sebastian van de Linde for their assistance and I hope for their continued success as the Photophysics group grows.

I thank Dr Ben Russell and Dr Philip Yip for their friendship and help with not only fixing fluorimeters but with getting through the PhD.

To Ben, Chloe, Hazel, Gillian, Rhona, Hajar, Lucas, Milan, Natakorn and Daniel I thank you for putting up with me, for it can't have been easy. It has been great getting to know you all as we all work towards our Doctorates and I thank you for all the Friday lunches we shared.

As one of the first OPTIMA PhD students, I have seen the CDT grow year upon year and become better during that time. I am grateful to have been a part of it and wish success for everyone else as they work towards their own PhDs. I have had some wonderful times, as part of the OPTIMA CDT and I am immensely grateful to Jean, Sam and Kirsty who work tirelessly to ensure OPTIMA is the best it can be. To Rachael and Evita, thank you for looking after me during these challenging times and for being there throughout all the business courses and presentations.

I would like to thank Dr Marie Boyd for allowing me the opportunity to investigate nanoparticle toxicity within her labs. Your enthusiasm and passion was always infectious and helped spur me on. Both David Scott and Dr Annette Sorensen deserve thanks for training me in cell culture practices and helping me collect data. I would also like to thank Peter, Ross and Graham for their friendship during the time I was working within SIPBS. My thanks to Prof. Liz Patton for her help in exploring the possibilities of extending the research toward *in vivo* studies with zebrafish.

I appreciate the help and use of equipment offered by Dr Graham Hungerford (as part of Horiba IBH, Glasgow) for the measurement of melanin's near-infrared lifetime response. Thanks also go towards Dr Steven Oldenburg and the rest of NanoComposix for allowing me the chance to work within an industry environment and also experience life in California. To Madison, Bret and Mick I thank you for showing me the best side of America. To John and his family, I thank you for opening your home to me during my time in the States and wish you the best.

I would like to thank the National Physical Laboratory for including me within the Post-Graduate Institute. I gained a great deal from my interactions with the other students on the program. My appreciation extends to Dr Alex Knight and Dr Max Ryadnov for their contributions.

To my family, thank you. Thank you for sticking by me and encouraging me to continue. To my brother-in-law, who conducted initial proofreading of this work, sorry. Finally, to my niece Amelia, who is about a month old at the time of writing. I thank you for bringing our family joy, and I hope you meet as many wonderful people, who will help you in life, as fortunately have I.

Publications and Conference Proceedings

A. D. Davy and D.J. S. Birch, "Evidence for pheomelanin sheet structure", *Appl Phys Lett*, vol. 113, no. 26, p. 263701, 2018.

A. D. Davy and D. J. S. Birch, "Probing pheomelanin synthesis using thioflavin T fluorescence", *Proc. SPIE 10893, Reporters, Markers, Dyes, Nanoparticles, and Molecular Probes for Biomedical Applications XI*, 108930L, 2019.

A. D. Davy, E. Patton, A. Knight, D. J. S. Birch, "Development of gold nanorods for use as *in vivo* biosensor", Poster Presentation, *MAF 14*, Würzburg, 2015.

A. D. Davy, E. Patton, A. Knight, D. J. S. Birch, "Development of gold nanorods biosensor: toxicity *in vitro*", Poster Presentation, *Emerging Analytical Professional Conference*, Fareham, 2016.

A. D. Davy, E. Patton, D. J. S. Birch, "Development of gold nanorods biosensor: toxicity *in vitro*", Poster Presentation, *FluoroFest*, Glasgow, 2017.

A. D. Davy, "Spectroscopy: back to basics", Oral presentation, *Emerging Analytical Professional Conference*, Kettering, 2017.

A. D. Davy, "Evidence for sheet structure in pheomelanin", Oral presentation, *PostGraduate Institute fo measurement science conference*, Glasgow, 2018.

Abbreviations

A.A. - Ascorbic Acid

AFM - Atomic Force Microscopy

AHP - Aminohydroxyphenylalanine

Aβ - Amyloid-β

bGNR - Big Gold Nanorod

cON - Complimentary Oligonucleotide

CTAB - Hexadecyltrimethylammonium Bromide

$CuSO_4$ - Copper Sulfate

Cyst - Cysteine

DAS - Data Analysis Software

DHI - Dihydroxyindole

DHICA - dihydroxyindole Carboxylic Acid

DNA - Deoxyribonucleic Acid

EEM - Excitation Emission Matrix

ESPT - Excited State Proton Transfer

ESIPT - Excited State Intermolecular Proton Transfer

Eu - Eumelanin

FACS - Fluorescence Assisted Cell Sorting

FLIM - Fluorescence Lifetime Imaging Microscopy

FRET - Förster Resonance Energy Transfer

fs - Femtosecond

FWHM - Full Width Half Maximum

GNR - Gold Nanorod

GNR-Cit - Gold Nanorods with sodium Citrate coating

GNR-CTAB - Gold Nanorods with Hexadecyltrimethylammonium Bromide coating

$HAuCl_4$ - Chloroauric acid (Gold (III) chloride)

HOMO - Highest Occupied Molecular Level

HPLC - High Performance Liquid Chromatography

ICP-MS - Inductively Coupled Plasma Mass Spectrometry

IRF - Instrumental Response Function

KH_2PO_4 - Potassium Phosphate

$KMnO_4$ - Potassium Permanganate

L-DOPA (DOPA) - Dihydroxy-L-phenylalanine

LSPR - Longitudinal Surface Plasmon Resonance

LUMO - Lowest Unoccupied Molecular Level

MEM - Maximum Entropy Method

MEM - Minimum Essential Medium

MHA - Mercaptohexanoic Acid

mRNA - Messenger Ribonucleic Acid

μAmps - Micro Amperes

NaN - Not-A-Number

NaOH - Sodium Hydroxide

Na-PAA - Sodium Polyacrylate Acid

NH_3 - Ammonia

NIR - Near Infrared

ns - Nanosecond

OD - Optical Density

OPE - One-Photon Excitation

PAH - Polyallylamine Hydrochloride

PARAFAC - Parallel Factor

PCA - Principle Component Analysis

Pheo - Pheomelanin

PMT - Photomultiplier Tube

POC - Point-Of-Care

PPD - Picosecond Photon Detection

ps - Picosecond

PSS - Poly(styrenesulfonate)

PTCA - Pyrrole Tricarboxylic Acid

R6G - Rhodamine 6G

RNA - Ribonucleic Acid

ROS - Radical Oxygen Species

SD - Standard Deviation

SEM - Scanning Electron Microscopy

SET - Surface Energy Transfer

sGNR - Small Gold Nanorod

S/N - Signal to Noise

SPAD - Single Photon Avalanche Diode

SPR - Surface Plasmon Resonance

TCSPC - Time-Correlated Single Photon Counting

ThT - Thioflavin T

TICT - Twisted Intermolecular Charge Transfer

TPE - Two-Photon Excitation

TRES - Time-Resolved Emission Spectrum

TRP - Tyrosinase Related Proteins

TSPR - Transverse Surface Plasmon Resonance

TYR - Tyrosinase

UV - Ultraviolet

UVW - Human Glioblastoma Cell Line

List of Figures

List of Tables

Chapter 1

General Introduction

1.1 Melanin

1.1.1 The photo protector

Melanin is a biological macromolecule whose primary role is as a photoprotector against ultraviolet (UV) radiation. [1] Within the body, melanin is produced by specialised cells called melanocytes. These cells occur irregularity but are evenly distributed throughout the basal layer of the skin and in hair follicles. [1] These cells produce organelles called melanosomes ($\sim$ 500 nm) [2], which are small lipid bilayer packages where the actual biosynthesis of melanin takes place.

The melanocyte's primary function is to distribute these melanosomes throughout the surrounding keratinocytes, the main cell type of the skin. The melanocyte has a dendritic form, as can be seen in figure 1.1, which allows the cell to pass its melanin producing packages to the neighbouring keratinocytes. The melanosomes can then protect the keratinocytes from UV radiation. Serving between 30 to 50 keratinocytes each, the melanocytes can respond to the level of UV exposure by producing more melanosomes. The result of which is a darkening of the skin which is commonly referred to as tanning. [1] People living in sunnier climates will have greater exposure to UV radiation. In response to this, the melanocytes produce a higher number of larger melanosomes. As a result, the tone of their skin is darker than people who live at higher latitudes. [1]

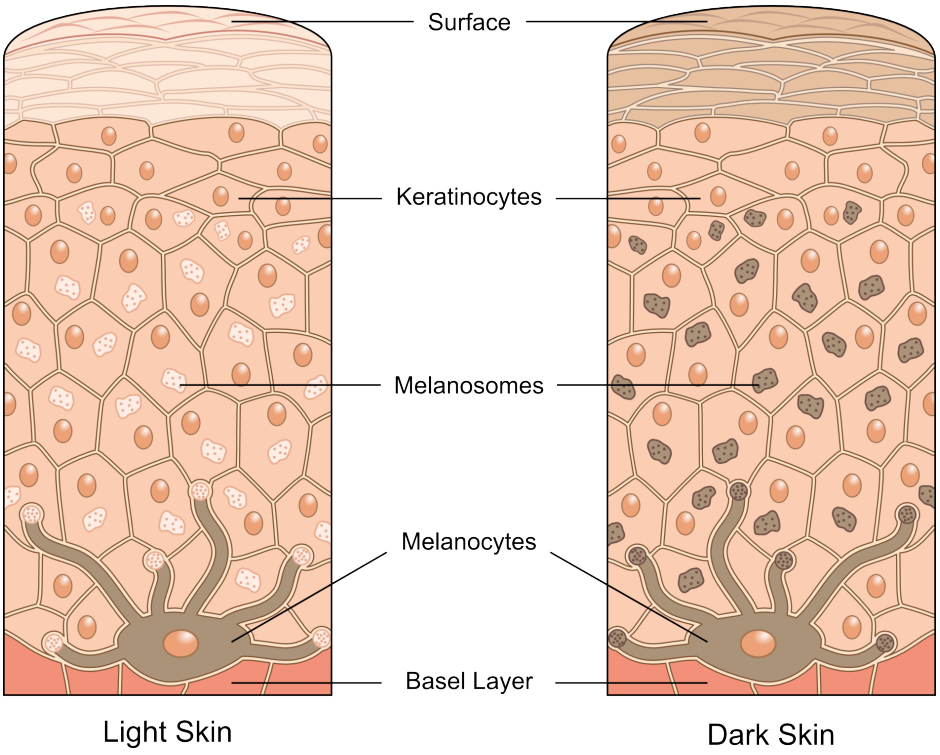

Figure 1.1: Drawing of skin cross section showing the keratinocytes, melanocytes and melanosomes.

1.1.2 Different kinds

Melanin is found in the skin, eyes, hair and the brain. The two main types are the brown/black eumelanin and the red form, pheomelanin. Pheomelanin, being the pigment responsible for red hair, remains at a constant level in other hair colours while the level of eumelanin changes. Individuals with black hair have the highest level of eumelanin and progressing through dark brown, brown, light brown and blonde the level of eumelanin decreases. [3]

Melanin can be found in the iris and while its role is only partly understood it does act as an absorber. The melanin, in the iris, can prevent the retina from excess levels of light and absorb interference as light reflects off the Bruch's membrane. Similar to skin melanoma, there is evidence which suggests that uveal melanoma and age-related macular degeneration are related to the pigmentation of the eye. [3] Melanin that is found within the brain is defined as neuromelanin, which consists of a pheomelanin core that is wrapped by a eumelanin-like dopamine shell. [4]

The most common commercial sources of eumelanin are from the reaction of tyrosine with hydrogen peroxide and natural eumelanin, extracted from the ink sacks of cutlet fish (*Sepia Officialise*). Currently, there are no commercial sources for pheomelanin, but there exists a multitude of methods for generating both types of melanins, including extraction from the feathers of chickens [5, 6].

Starting with dihydroxy-L-phenylalanine (L-DOPA), the formation of eumelanin can be achieved by enzymatically reacting the compound with tyrosinase from mushrooms. In the melanosome, the tyrosinase-related proteins (TRP1 and TRP2) act as regulators and help catalyse the subsequent reaction. While an important part of melanogenesis, melanin can successfully be synthesised with only DOPA and tyrosinase as the synthesis follows an auto-oxidative process. [7, 8] While there are differences between the synthetic and natural forms of melanin it is generally accepted that the synthetic forms act as adequate melanin forms for experimentation.

To synthesise, the red pigment, pheomelanin, the amino acid L-Cysteine (Cyst) is added to the initial mixture of DOPA and tyrosinase. The cysteine is needed to change the DOPA into cysteinyldopa and consequently, the benzothiazine and benzothiazole intermediates. It is interesting to note that while DOPA will auto-oxidise into eumelanin, the enzyme is needed to generate pheomelanin as just mixing DOPA and L-Cysteine fails to produce pheomelanin. [8] Indeed, it has been uncovered that the activation energy of the cysteinyldopa reaction means that the tyrosinase is required to catalyse the reaction.

Studies into the quantity of eu and pheomelanin within different cells showed a change to the ratio of the two pigments when the cell became malignant. [9] Researchers have taken advantage of this property to develop a two-photon excitation method for detecting melanoma. [10] However, the technique is difficult, expensive and would require extensive training to use. [11] There exists the possibility of replicating this measurement with conventional spectroscopic techniques which would greatly decrease the cost and complexity of the measurement.

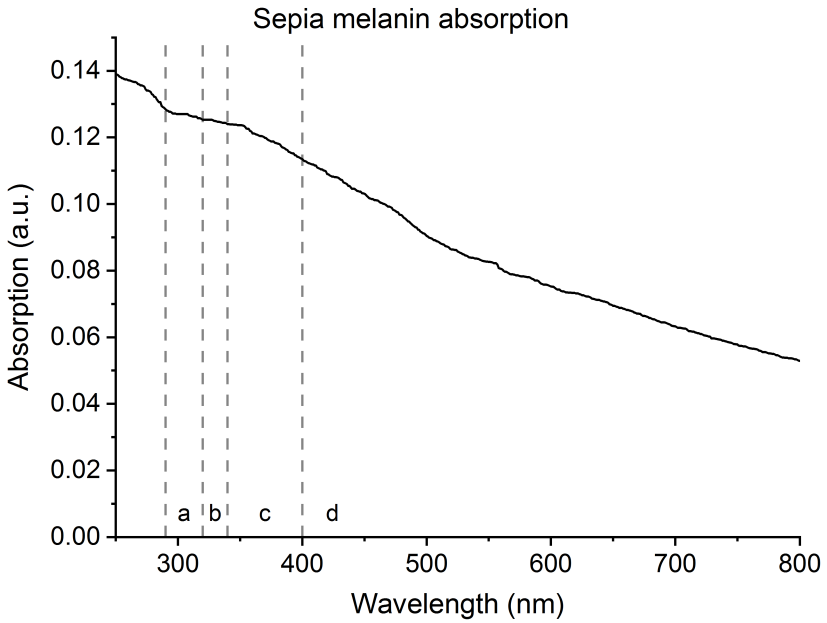

Figure 1.2: A UV/Vis plot showing the absorption of melanin from the UV to the near IR. The labelled potions of the spectrum refer to the different bands of UV radiation. The (a) region is the UVB while (b) and (c) are the UVA1 and UVA2 regions respectfully. The (d) region is the visible part of the spectrum.

1.1.3 Properties

At the heart of the melanin debate is the question of its structure. Despite over 50 years of research into melanin, we are still unable to identify a fundamental unit of melanin, and while certain parts of the structure narrative are known, their connection to the physical properties are still unclear. This can be illustrated by looking at melanin's absorption spectrum; the broad, featureless, profile that decreases in intensity from the UV to the infrared.

The typical absorption spectrum shown in figure 1.2 contains no peaks and covers the whole range of the UV and visible spectrum. Typically, biomolecules exhibit distinct peaks that represent the electronic states of the molecule. [12] This can help determine the structure of the molecule since only specific structural models will replicate the peaks seen in the absorption spectrum. For melanin, this task proves more challenging since the model needs to produce a particle capable of absorbing light across the whole UV and visible spectrum.

Another deviation from conventional organic fluorophores is the shape of the absorption profile. When plotted against wavelength the absorption can be fitted to an exponential decay model. [12] This has led to several structural models being proposed which aim to explain the features seen in the absorption spectrum. The first model describes melanin as an amorphous semiconductor since the absorption profile resembles an inorganic material rather than an organic one. When a crystalline structure becomes amorphous, there is a loss in the long-term order of the lattice. [13] This broadens the energy band structure of the material to create a continuum of possible states.

Similar in mechanism, the heterogeneous polymer model identifies possible polymer chains of melanin's starting molecules. [14] This would increase the amount of delocalisation of the electrons and would broaden the absorption spectrum. Alternatively, there is the chemical disorder model which does away with structure at all. [15] The theory here is that melanin consists of a mixture of small oligomer units and their various redox forms and when grouped they produce the typical broad absorption spectrum. Calculating the absorption values (using density-functional theory) of the initial molecular units of melanin do show a large redshift when the molecules are converted into their quinone forms. Using density-functional theory the highest occupied molecular orbital (HOMO) and lowest unoccupied molecular orbital (LUMO) bandgap energies were calculated for different oxidative states of dihydroxyindole. In the hydroquinone state, the HOMO-LUMO gap energy was equivalent to 344 nm with the indolequinone and semiquinone states having gap energies equivalent to 615 nm and 1110 nm respectfully. [16]

An alternative model links the absorption spectrum to the scattering properties of melanin particles. Rayleigh scattering has a λ^{-4} dependence on the absorption, which is similar to the melanin absorption profile. Investigating the scattering contributions reveal that they are linked to the degree of aggregation and how soluble the sample is. [12] For well-dissolved samples of melanin, scattering only contributed $\sim 6\%$ while more poorly solubilised solutions had closer to 13% scattering contributions. [17]

Despite the discussion surrounding which model best describes melanin, the one thing that most researchers can agree on is that melanin's broad absorption spectrum is the reason it can offer such good protection against UV radiation.

Given that one of melanin's main roles is to absorb light, it should come as no surprise that melanin is not a strong fluorophore. The quantum yield, the ratio of emitted photons to absorbed photons, for melanin is small with values in the UV measuring $< 7x10^{-4}$. [12] A strong emitter like rhodamine 6G, measured at its fluorescence peak (550 nm) has a quantum yield value around 0.94. [18] With over 99.9% of the incidence light being absorbed, melanin has proven challenging when trying to understand its fluorescence properties. [19]

Investigations have been hampered because of inner-filtering effects, the interference when the emitted fluorescence photon is reabsorbed by neighbouring molecules. Signs that inner-filtering effects were occurring came from fluorescence steady-state measurements where the spectra were changing as the concentration was increased. A simple solution to this problem is to reduce the concentration to an absorption value below 0.1 OD (optical density), where the solution can be defined as dilute. [20] The drawback of this approach is the increased signal-to-noise (S/N) ratio that results from having a low number of fluorescent units. This can lead to extended measurement times as the standard way to combat high S/N ratio is to increase the time the instrument records each data point for. [12]

Regardless, of the studies into melanin's steady-state fluorescence there is agreement that, like the absorption, the spectrum is broad and generally featureless. Given the range of wavelengths, melanin can absorb at; it is necessary to measure emission across a range of excitation values and generate a 3-dimensional excitation, emission matrix if the full steady-state response is to be observed.

Interestingly, measurements of the excitation spectra, where the emission wavelength is fixed, and spectra are scanned through a range of excitation wavelengths, do not correlate with the absorption spectra implying that the mirror rule (the fluorescence spectrum curve being the mirror image of the absorption curve) does not apply. This coupled with an excitation energy dependent emission spectrum were clear indicators that melanin's photophysics were not the response of a single melanin chromophore. [12]

Lifetime Component (ns)	0.06	0.52	2.5	6.9
Percentage Contribution (%)	52	22	19	0.08

Table 1.1: Taken from Forest et al. [21] The lifetime values for the four exponential model fitted to eumelanin's fluorescence lifetime decay.

Evidence supporting multiple fluorescent species of melanin can be found via time-resolved fluorescence spectroscopy. The fluorescence lifetime decay for melanins are complicated and require multi-exponential models to fit. Measurements consistently require three or four exponentials model to fit the lifetime data and result in lifetime values from the sub-nanosecond to the nanosecond range (Table 1.1). [21]

It is worth keeping in mind that the fluorescence photons being measured are only a small fraction of the energy that was absorbed. Investigations into where this energy transfers to revealed that the majority of the absorbed energy is dissipated via non-radiative pathways around a nanosecond after excitation. The time delay before dissipation was increased when excitation wavelengths were below 300 nm. The generation of long-lived excited states implies that under UV radiation, there may be excited state photochemistry taking place. [12]

Investigating the fluorescence kinetics of excited building blocks of melanins has revealed the occurrence of excited state proton transfer (ESPT) to the solvent and excited state intermolecular proton transfer (ESIPT) which add yet more complexity to the fluorescence kinetics of melanin. This is already on top of the particle size effects and the rapid depolarisation (80 ps) which is consistent with the chemical and structural disorder models. [12, 22, 23]

The photochemical properties discussed are only a part of melanin's electronic properties. Along with photoconductivity, melanin exhibits electrical conductivity plus threshold and memory switching. Much of the studies into melanin's electrical properties follow semiconductor models and the case made that these studies furthered the interpretation that melanin is an amorphous semiconductor. [12]

In 1974, McGinness et al. [24] were able to get dried pellets of natural and synthetic eumelanin to act as reversible switches, similar to a semiconductor transistor. Researchers were able to calculate the activation, or band gap, of the melanin switches. Their calculation place the band gap between 0.49 eV and 0.76 eV. The range of energies is due to the different levels of hydration as water facilitated better conductivity.

The effects redox states have on the electrical properties is unclear, but they do impact melanins ability to reduce and oxidise other molecules. The electron transfer properties of melanin are largely due to the redox properties of its monomer units. Therefore, studies have focused on understanding these smaller molecular units. However, there will be differences between melanins redox properties and the chemical properties of its monomer units. Certain quinone forms are highly unstable and will react with molecules readily. When combined into sub-units of melanin, the reactivity is reduced implying more intermolecular interactions. [12]

With the formation of quinone forms, melanin can produce free radicals which have been identified using electron spin resonance measurements. The free radicals are responsible for melanin's paramagnetic properties, the induced magnetic field generated by a material via an external magnetic field. [12] Altering the concentration of free radicals, and therefore the degree of paramagnetism can be done with pH, temperature, irradiation with light and reducing agents. A difference between eumelanin and pheomelanin is in the form of the free radicals that are dominant. For eumelanin, researchers find semiquinone radicals while pheomelanin contains semiquinoimine radicals. [5] Binding to paramagnetic metal ions like Cu(II), Mn(II) or Fe(III) reduced melanin's paramagnetic intensity and was shown to be independent of any chemical reaction. [25]

Melanin can bind to more than just paramagnetic metals ion. However, the functional group to which they bind varies. The monomer units of melanin have three distinct chemical groups which the metal ion can bind to. Ions like Cu(II) can bind to all three, the hydroxyl group, the carboxylic group and the amine group. The same is true for Fe(III), Zn(II) and Ni(II). Whereas Li(I), Rb(I) and Ti(I) only bind to the carboxylic group and generally it is the biologically relevant ions that exhibit binding to multiple groups. [26]

1.1.4 Melanogenesis

As mentioned before, the synthesis of melanin starts with the formation of DOPA from the reaction of tyrosine with tyrosinase. From there the DOPA compound converts into dopachrome and then into dihydroxyindole (DHI) and dihydroxyindole carboxylic acid (DHICA). Both DHI and DHICA are the fundamental molecular units that makeup eumelanin (Figure 1.3). [8]

For pheomelanin, the initial reactants are joined by L-Cysteine which reacts with DOPA to produce cysteinyldopa. After some restructuring, the benzothiazine/zole intermediates are formed as are the fundamental units of pheomelanin (Figure 1.3). [8]

Once the base sub-units are synthesised, the hierarchical build-up model (Figure 1.3) [27] has the sub-units form sheet structures. This follows the same kind of π-bonding seen in graphite where the molecules are oriented such that the sheets are parallel to the plane of the phenol ring of the molecules. From measurements it is proposed that the sheets π-stack into roughly ten sheet units which define the protoparticle of melanin. [27]

The next stage of the hierarchical build-up model involves the bending of the protoparticles as they come together to form spherical particles known as type-A particles. The type-A particle has a diameter of 20 nm, and while the exact formation mechanism is still under debate, it is believed that the inherent curvature of the sheets may lead to a polar distribution which could generate the forces need to attract and bend adjacent sheets. [27]

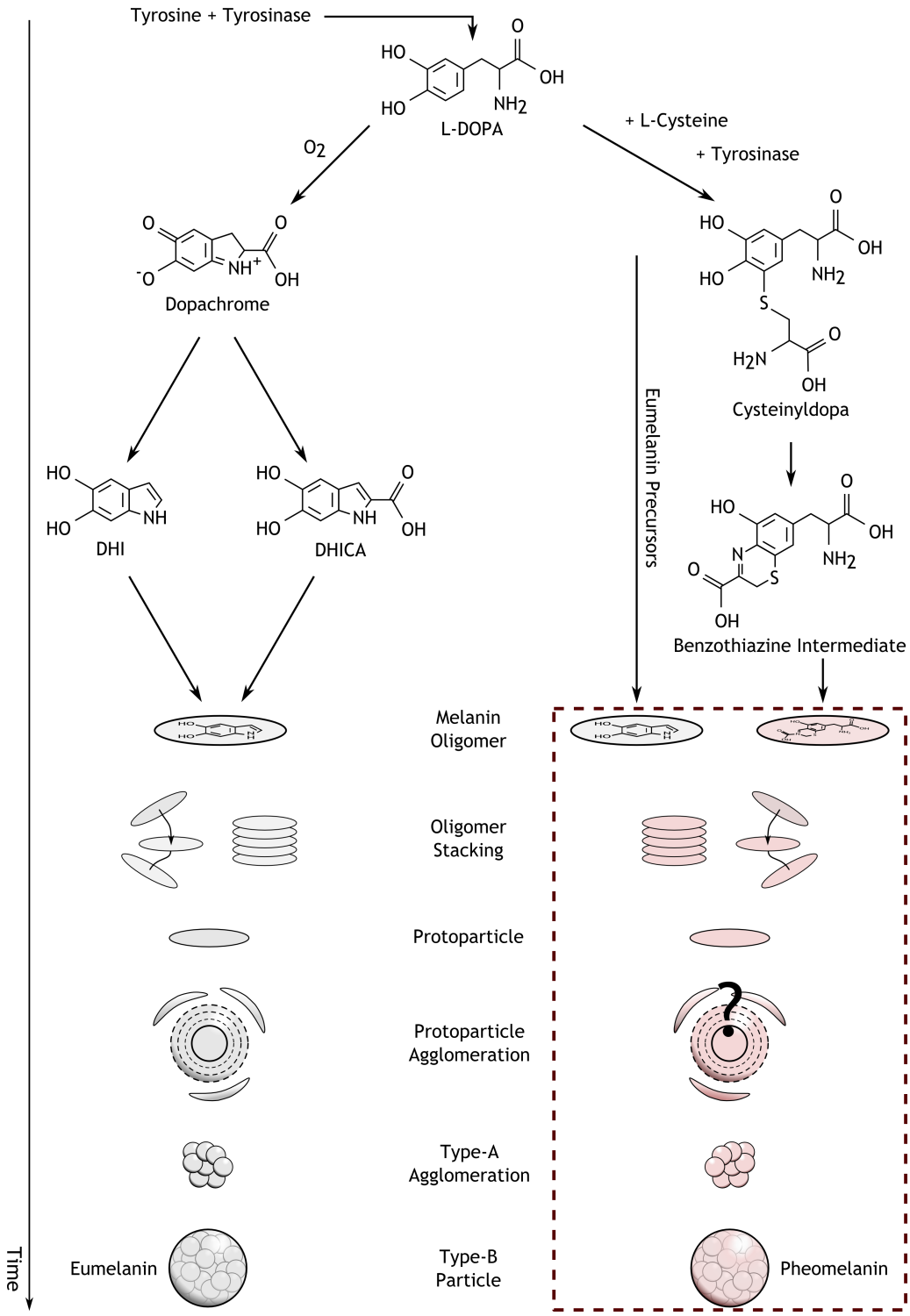

Figure 1.3: Melanogenesis diagram showing the initial molecular units and the four stages of structural agglomeration. However, questions remain unanswered regarding pheomelanin's structure and whether it follows the same structural model (boxed area) as eumelanin.

Once the type-A particles are formed, they aggregate together to form larger spherical structures called type-B particles (Figure 1.3). These particles average 200 nm in diameter and are the subunits of micron-sized melanosomes seen with electron and atomic force microscopy [28, 29]

The melanogenesis of eumelanin and pheomelanin are considered to follow a similar structural pathway with the main difference stemming from the initial compounds used. The formation of melanin is complex and involves multiple stages which make investigations challenging. While great strides have been made in understanding the process of melanogenesis, researchers are still grappling with the structure of melanin. With the assumption that pheomelanin follows the same processes, the majority of research has focused on eumelanin. This means that much of the pheomelanogenesis process is left unanswered. A fundamental question concerns whether pheomelanin also forms sheet structures in a similar manor as eumelanin.

Several theories have been tested with the formation of phenol rings being an early solution that has gained traction. This proposes a structure of four molecular units which produce a phenol ring in the centre. Computational studies on this structure have shown optical properties which fall within the wavelength range of melanin fluorescence (peaks near 350 nm and 480 nm). [30, 31]

Other attempts construct conjugates of DHI and DHICA to from dimer structures up to octamer structures, then generates stacks from three of the initial structures. From these simulations, it can be seen that these stacked structures are not perfectly flat and follow an almost sinusoidal curve. [32] This inherent curvature may facilitate the protoparticle agglomeration that forms the type-A particles.

1.2 Melanoma

1.2.1 Cancer introduction & statistics

For melanoma, the 20th most common cause of cancer-related death, around 2,400 deaths are related to this cancer each year in the UK. Globally, around 55,000 deaths are caused by melanoma. In the UK, the mortality rate has increased by 14% in the last decade, but predictions expect a decrease in the melanoma mortality rate of 15% in the coming decades. The continued developments in diagnostic technologies and the greater awareness of the general public are likely the source for the projected mortality rates. [33]

Melanoma is not the only type of skin cancer, with basal cell carcinoma and squamous cell carcinoma accounting for 75% and 20% of skin cancers respectfully. While the incidence rate for non-melanoma skin cancers is higher, with around 136,000 new cases being diagnosed each year in the UK, the total deaths per year (950) is less than the deaths caused by melanoma. [33]

The statistical data of cancer incidence rates show that the highest incidence values are for older demographics of the population. [33] This is due to cancer being the result of a build-up of genetic mutations within the cell (Figure 1.4). [34] These mutations can be caused when the cell is damaged by radiation (both atomic and high energy electromagnetic) or by carcinogens like tobacco smoke. [34]

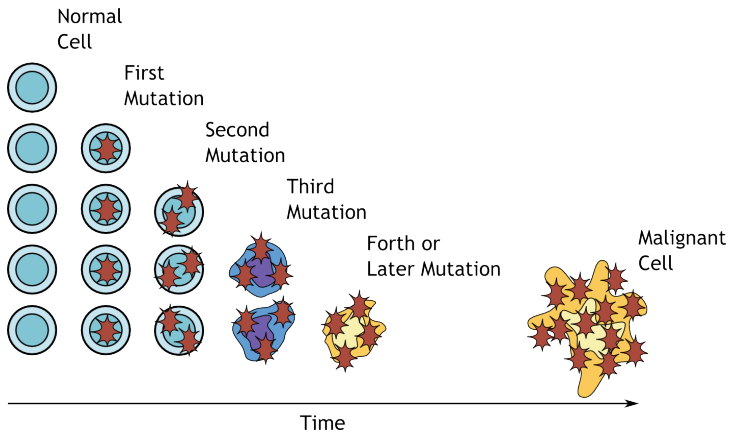

Figure 1.4: Image showing the occurrence of a malignant cell from the continued addition of genetic mutations.

Regarding melanoma, it is the exposure to high levels of ultraviolet radiation that are the main cause of this cancer. UV radiation plays both a beneficial and detrimental role to our health. To produce vitamin D, we need exposure to UV radiation. However, since UV radiation contains around 4 eV of energy, it can break down covalent bonds. This can damage the DNA directly or indirectly by the formation of free radicals. With UV radiation, it becomes a matter of balancing our exposure, so we can generate the vitamins our body need but prevent prolonged exposure that increases the chance of inducing damage. [34]

There are two ways we are protected (with the exception of sunscreens), the first being the ozone layer which absorbs most of the UV radiation that reaches the Earth, from the Sun. Next is the specialised pigment cells, the melanocytes, which produce the melanin pigment that absorbs harmful UV radiation. Damage to these cells will lead to melanoma while damage to the basal and squamous cells lead to basal cell carcinoma and squamous cell carcinoma respectfully. [34]

1.2.2 Current clinical methods

Early diagnosis is important since surgery can deal with most cases. However, the challenge for general practitioners is differentiating benign lesions from malignant lesions. [35, 36] In 1991, the 7-point checklist was published in order to aid healthcare professionals and the general public with identifying melanomas. Utilising dermoscopy greatly increases the accuracy of naked eye examinations and remains the gold standard. [36]

Dermoscopy is suitable for initial examination and screening. Biopsy and genetic testing are the current standards for confirmation and genetic grouping of melanomas. Preparation of samples for confirmation requires collecting samples from the patient, processing and assessment from experienced dermatologist. This process requires multiple weeks to complete and depends on the experience of the clinician making the assessment. [36] These drawbacks have been identified, and several methods are being developed to improve the identification and diagnostics of melanomas. [11, 35] Many of them aim to provide an assessment/diagnosis non-invasively.

1.2.3 New methods of detection

Technologies and techniques being developed for melanoma sensing applications can be divided into four categories. The first category is suitable for large scale screening on account of their simplicity and quick measurement time. This includes dermoscopy and sequential digital dermoscopy [11] along with total body photography [11, 37]. These techniques are based on photographing the lesions to aid visual inspection with multiple images being acquired over time to help identify whether the lesions is changing.

The second category is not suitable for whole body screening, due to factors like low specificity and lengthy measurement/analysis times (up to 20 mins). However, these techniques introduce computational algorithms that aim to assess the malignancy of the lesion. Computer-aided multispectral digital analysis and Raman spectroscopy are included within this category and measure the spectral response of the tissue after illumination with visible and near-infrared light. [11] Electrical impedance spectroscopy measures the difference between how an alternating electrical signal propagates through normal tissue and the lesion. Despite the more analytical approach these techniques are only capable of providing a predictive score that is useful for specifying whether the patient should be referred for further examination. [11]

With category III and IV devices, we move to techniques and equipment that need extensive training in order to interpret the microscope images. The use of high-end equipment like confocal microscopes results in these devices having a high capital cost and the techniques used require substantial training to uses effectively. However, these categories of devices offer both high sensitivity and specificity, making these techniques suitable for diagnostics applications as opposed to initial assessment of selected lesions.

Category III techniques include reflectance confocal microscopy and multiphoton tomography. [11, 38, 39] Reflectance confocal microscopy uses the reflected light signal to look for structural changes that occur when the tissue becomes malignant. Multiphoton tomography uses a near infrared emitting, femtosecond pulsed laser source to excite the tissue and both two-photon excitation spectroscopy and second harmonic generation are used to identify malignant lesions. [9, 11] These techniques can achieve sensitivities and specificities above 85%.

Category IV devices like stepwise two-photon laser spectroscopy and quantitative dynamic infrared imaging are still in the experimental stage while the other categories devices are within the commercial development stage. [11] Stepwise two-photon laser spectroscopy takes advantage of melanins step-wise two-photon excitation spectral response, which in conjunction with the different responses between eumelanin and pheomelanin allow for the diagnosis of melanoma. [9, 40] Quantitative dynamic infrared imaging measures the thermal recovery of normal and malignant tissue which can diagnose melanoma since the blood supply is different which also changes the heat generation of the tumour. [11, 41]

1.3 Luminescence

1.3.1 The physical phenomenon

Early observations of this phenomenon were made by Nicolas Monardes [42] in the 16th century by noting the slight blue tinge of the water contained within cups of "*Vlignum nephriticum*". [42, 43] This was followed later by the work of Robert Boyle in the 17th century and is counted as one of the first to describe phosphorescence, thermoluminescence, electroluminescence and triboluminescence. [44]

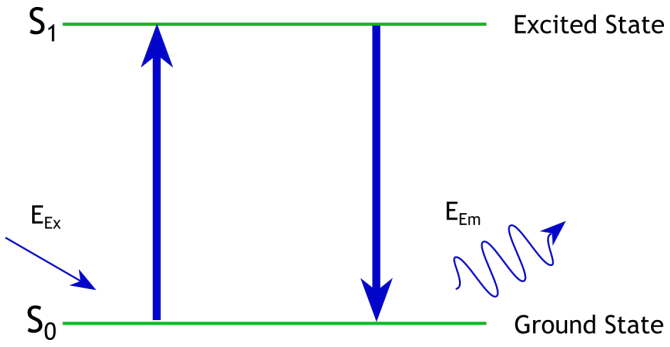

Figure 1.5: Simple energy level diagram to cover the principle of luminescence. The energy that excites the electron from the ground state (S_0) is show as E_{Ex}. The emission of electromagnetic radiation is from the excited state (S_1) and is labelled as E_{Em}. For molecules, the electronic states (S_0 & S_1) form bands of energy, due to the Pauli exclusion principle. Photoluminescence typically occurs with aromatic molecules since the energy band gap of the delocalised π orbitals is lower than dissociation energies.

Phenomenon	**Energy Source**	**Types**
Photoluminescence	Electromagnetic radiation	Fluorescence Phosphorescence
Radioluminescence	Ionised radiation	
Electroluminescence	Electric field	Cathodoluminescence
Chemiluminescecne	Chemical reaction	Bioluminescence Electrochemiluminescence
Thermoluminesecnce	Ionising radiation and heat	
Mechanoluminescence	Mechanical energy	Triboluminescence Fractoluminescence Pizoluminescence Sonoluminescence
Crystalloluminescence	Crystallisation	

Table 1.2: Classification of luminescence and its subtypes. Included are the types of energy that excite the samples to produce the emitted light. [45]

Not to be confused with black body radiation, called incandescence, luminescence does not involve the vibrations of the atoms which are associated with temperature. [45] Luminescence relates to the transitions of electrons from different energy states within the atom or molecule. [20] The energy needed to transition to the excited state is larger than the thermal energy of the electrons, at room temperature. This means it is possible to investigate photoluminescence without interference from incandescence effects. [20]

Atoms and molecules have quantised energy levels (Figure 1.5) which the electrons transition to and from. Starting at the lowest energy level, known as the ground state, the electron absorbs energy and jumps to a higher energy level. [45] After some time in the excited state, the electron transitions back down to the ground state and the loss in energy is transferred into electromagnetic radiation. [20]

The process of luminescence involves the exchange of energy into the emission of light. This can involve the reaction of chemicals, mechanical or radiative energy being converted, by the sample, into light. The different types of luminescence are listed in Table 1.2 along with the initial source of energy.

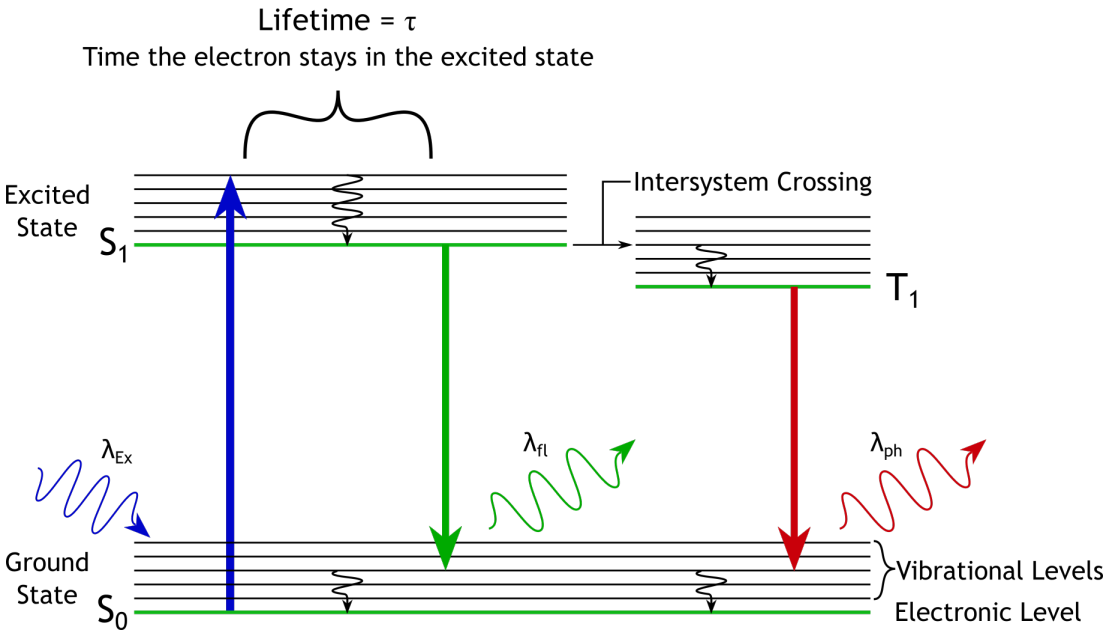

Figure 1.6: Jablonski diagram showing the process of photoluminescence. The lifetime has been indicated as the time the electron spends in the excited state. The singlet ground and excited states are labelled S_0 & S_1 respectfully. The first triplet state is labelled T_1 and can be populated via intersystem crossing from the singlet state.

1.3.2 Jablonski diagram

To better understand the underlying physics, we use the Jablonski diagram. This simple representation of the energy levels of a molecular species helps break down the processes that constitute photoluminescence and explains the difference between fluorescence and phosphorescence.

In Figure 1.6 the ground (S_0) and first (S_1) electronic singlet states are shown, with each state being comprised of some vibrational states. Incident photons can excite the election from the ground state to either of the vibrational levels, within the excited state, if the energy of the photon is equivalent to the difference between the excited and ground state. From there, the electron will pass through the vibrational levels to reach the lowest vibration level. This energy is lost in a non-radiative process whereby the energy is transferred into the vibrational modes of the molecule (thermal energy).

After a period the electron will transition to a level within the ground state (S_0) with the loss of energy being converted into an emission of a photon. This photon is the photoluminescent light that is detected, and its energy is equivalent to the energy difference between the excited state and ground state the electron transitioned between. If the electron de-excited to one of the vibrational levels of the ground state then, through more non-radiative processes, the electron will return to the lowest vibrational level of the ground state, ready to start the process again.

Individual transitions from different energy levels occur at different times with energy state transitions happening within the femtosecond (fs) range and internal conversion, from different thermal energy levels taking place within the picosecond (ps) time range. [20, 46] Since photoluminescence lifetimes are typically within the nanosecond (ns) to second time-range, the emitted photoluminescence photons are generally from electrons transitioning from the lowest vibration state. That is to say; the photoluminescence emission is from the lowest level of S_1. [20]

1.3.3 Absorption

Since electronic transitions occur within the femtosecond range, there is not enough time to alter the position of the nucleus. This is referred to as the Frank-Condon principle. [20, 46] Within a molecular system, the total energy will be made up by the contributions from each part of the molecular system. When a photon is absorbed by a molecule, the energy will be transferred to the electronic, the vibrational and the rotational parts of the molecules total energy. [46]

For an atomic system, the absorption spectrum would consist of narrow lines as the atom has discrete, quantised electronic levels. When atoms come together to form molecules, the electrons cannot occupy the same electronic level which results in the electrons having slightly altered energies. This results in a distribution of energies about the electronic energy level, which forms an energy band. Since molecules have these energy bands, that make up the electronic state, the incidence of photons can excite the ground state electron to any of the excited state vibrational levels. This has the effect of broadening the absorption spectrum and since vibrational levels are a consequence of thermal energy, changing the temperature will also change the absorption spectrum. [46]

Given the short time for intersystem transitions ($\sim$ ps) the ground state electron is most likely to be in the lowest vibrational level of the ground state when the incidence photon arrives. Additionally, since the lowest vibrational level of the excited state requires the least amount of energy to excite, there is a higher probability that the electron will excite to this level. As a result, the absorption maximum is from the lowest ground state level to the lowest excited state level. This means the other absorption peaks are from transitions to other vibrational levels. [46]

1.3.4 Beer-Lambert law

An absorbing material contains molecules with a cross-sectional area of 'σ' which the incident light (I(0)) is attenuated by such that the light that makes it through the sample has an intensity value of I(t), where t is for time. The molecules are contained within a volume of length l and contain N number of molecules.

Focusing on a thin slab of solution of thickness (dl) the number of molecules within this volume (V) will be:

$$N = n \times V = n \times A_{TS} \times dl \tag{1.1}$$

Where A_{TS} is the area of the thin slab of solution and n is the number density of the molecules within the volume.

Within a given plane, perpendicular to the incident light beam, the fraction of the area A_{TS} where the light can be absorbed is given by the fractional cross-sectional area:

$$\sigma_F = \frac{N\sigma}{A_{TS}} \tag{1.2}$$

This is proportional to the fraction of light that is absorbed. Substituting equation 1.1 into 1.2 gives:

$$\sigma_F = n\sigma dl \tag{1.3}$$

Now, focusing on the light that passes through the area A_{TS}, the fraction of light that is absorbed relative to the total incidence light (I_i) equals.

$$I_{Abs} = -\frac{dI}{I_i} \tag{1.4}$$

Where dI is the intensity of light that is absorbed by the sample. The negative sign is there to signify a loss in intensity. Equations 1.3 and 1.4 both give the fractional absorbance which gives:

$$-\frac{dI}{I_i} = n\sigma dl \tag{1.5}$$

Equation 1.5 can now be integrated.

$$-\int_{I_0}^{I} \frac{1}{I_i} dI = n\sigma \int_0^l dl \tag{1.6}$$

$$-\left[\ln\left(I_i\right)\right]_{I_0}^{I} = n\sigma \left[C\right]_0^l \tag{1.7}$$

$$\ln\left(I_0\right) - \ln\left(I\right) = \ln\left(\frac{I_0}{I}\right) = n\sigma l \tag{1.8}$$

At this point, it is prudent to take advantage of the conversion rule ($In(x) = log_e(x)$) and the change of base rule such that:

$$log_b(a) = \frac{log_c(a)}{log_c(b)} \tag{1.9}$$

Substituting $\frac{I_0}{I}$ for a, making b the exponential constant (e) and $c = 10$ results in equation 1.8 becoming:

$$2.303 log_{10} \frac{I_0}{I} = n\sigma l \tag{1.10}$$

Finally, the variables are converted into more convenient ones since concentration is:

$$c = \frac{n}{N_A} \tag{1.11}$$

Where N_A is Avogadro's constant. Lastly, the remaining constants are defined as the extinction coefficient, 'ε_i':

$$\ln\left(\frac{I_0}{I}\right) = 2.303 log_{10}\left(\frac{I_0}{I}\right) = \sigma N_A c l \tag{1.12}$$

$$A = log_{10}\left(\frac{I_0}{I}\right) = \left(\frac{\sigma N_A}{2.303}\right) c l = \varepsilon_i c l \tag{1.13}$$

The absorption is the logarithmic ratio of intensities. Therefore units of absorption are dimensionless. Concentration has units of molar (M) or 'mol/l'. Optical path length has units of meters (m) and extinction coefficient has units of 'M/cm'. [46]

Factors that can alter the electronic/vibrational levels of a molecule include: temperature, type of solvent and interactions with other molecules. For example, the absorption peaks will decrease to lower wavelength values if the solvent is highly polar since the induced dipole-dipole interactions will require more energy to form. For the case when a molecule binds to a protein, the binding site is generally more hydrophobic than the solution. This results in a redshift in the absorption peak since the hydrophobic binding site will be a less polar environment. [46]

1.3.5 Photoluminescence

Fluorescence

The fluorescence photon that is emitted comes from the transition of the electron from the excited state to the ground state. The electronic transition to and from the ground state do not significantly alter the nuclear geometry which means the spacing of the vibrational levels of the excited state share a similarity to those in the ground state. Additionally, the transition probability (Frank-Condon factor) that is most likely for absorption levels will also be the most probable transitional levels for the fluorescence transition. [20]

Named after the Irish Physicist, Sir George Gabriel Stokes, the Stokes shift describes the change in wavelength between the absorption and fluorescence spectrums. [20] Given the fast process of internal conversion (ps), the fluorescence photon is likely to be from the lowest excited state vibrational level. [45] This loss in energy through thermal relaxation leads to the red-shift of the fluorescence peak when compared to the absorption peak. [46]

The Frank-Condon principle dictates that electronic transitions do not affect the nucleus position which maintains the symmetry of the vibrational layer between the ground and excited states. As a result, the energy of an incident photon will not affect the excited state vibrational levels as long as a photon can excite the electron into the excited state, then the emission spectrum will be the same. This allows for the complete fluorescence spectrum to be measured by exciting the sample with higher energy (lower wavelength) photons, without distorting the emission spectrum in the process. [20, 46]

There are some ways that the excited electron can transfer its energy into the surrounding environment, without emitting a photon. This process is called quenching and results in a reduction or loss of emission intensity. [20] The main form of quenching is when the fluorophore is in contact with another molecule. Referred to as collisional quenching, the process involves the fluorophore and quencher encountering each other via diffusive processes. [46] Other forms of quenching do not rely on diffusive processes and involve the fluorophore forming a non-fluorescent complex with the quencher. [45]

Since there are non-radiative pathways which the excited electron can dissipate energy through, the fluorescence process is not 100% efficient. The measure of how efficient a molecule is at emitting fluorescence photons is called its quantum yield. [20, 46] Defined as the ratio of the number of photons emitted to the number of photons absorbed. [46] Since the number of photons emitted is related to the emissive rate (Γ_{Em}) and the number of photons absorbed is equivalent to the sum of fluorescence photons plus the number of non-radiative electron transitions, the quantum yield can be written as:

$$QY = \frac{\Gamma_{Em}}{\Gamma_{Em} + k_{nr}} \tag{1.14}$$

Where k_{nr} is the non-radiative decay rate.

Phosphorescence

Phosphorescence lifetimes are longer than fluorescence (ms to sec range). This increase in lifetime is a result of intersystem crossing which places the excited electron into an excited triplet state (T_1) which prohibits its transition to the singlet ground state since it is a forbidden transition.

The term singlet and triplet states derive their names from the number of possible spin configuration obtainable from paired electrons. For a pair of electrons with opposite spins, there is only one possible configuration. For a pair of electrons with the same spin direction, there are three possible configurations. Both electron spins can be up, down or they can have opposite spin directions. [46]

When the excited singlet electron transitions to the excited triplet state, via intersystem crossing, the electron changes spin. Since the Pauli exclusion principle prohibits electrons from occupying the same state when they have the same spin value, the excited triplet state electron is forbidden from transitioning to the ground singlet state.

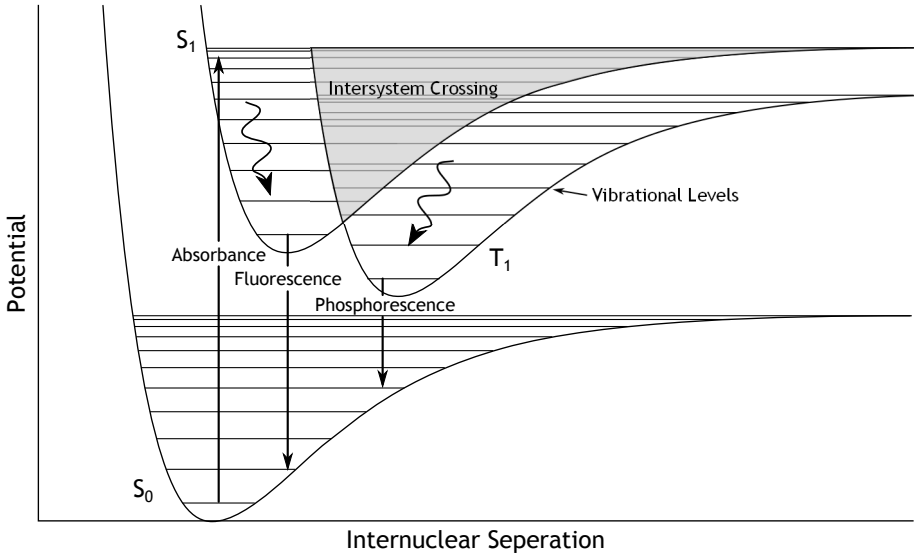

Figure 1.7: Potential energy of a molecule verses internuclear separation showing the ground and excited singlet states along with the excited triplet state. The overlap of potential energies between the two excited states can allow for intersystem crossing which will see an excited election transitioning to the triplet state.

The phosphorescence process starts the same as fluorescence since the electron is excited to the excited electronic state by absorbing a photon. The electron will transition through the vibrational levels as with fluorescence, but occasionally the electron will undergo intersystem crossing (Figure 1.7) and enter the triplet state. Upon reaching the lowest vibrational level of this excited triplet electronic level, the electron is restricted from transitioning to the ground state since triplet-singlet transitions are forbidden. While the probability of this transition is low, it can occur if there is a change in the excited electrons spin quantum number. As a result of the low probability of the triplet-singlet transition, the lifetimes measured extend beyond the nanosecond range and are typically within the millisecond to the second range. [20, 45, 46]

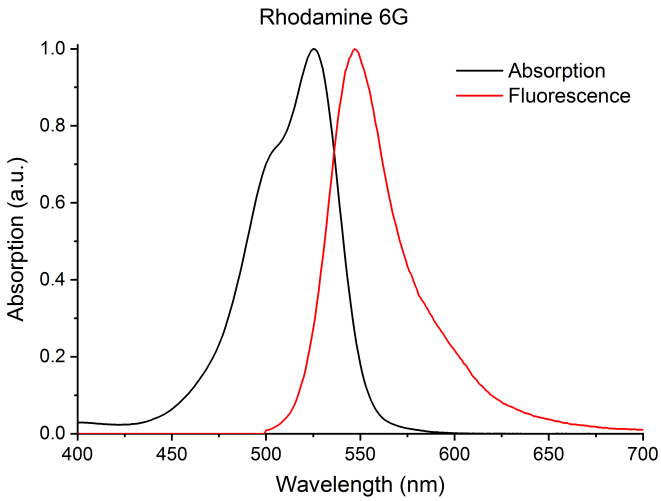

Figure 1.8: The absorption and emission spectra for the fluorescent dye molecule, Rhodamine 6G.

1.3.6 Fluorescence lifetime

When the electron is excited to the excited state, it does not deactivate immediately. The excited electron will stay in the excited state for a period of time; this is due to the electron going through the non-radiative process or, in the case of phosphorescence, there is a forbidden transition to the ground state. The average time the electron spends in the singlet excited state is referred to as the fluorescence lifetime. [20, 46]

The formation of energy bands when atoms form molecules results in their absorption and emission spectrum deviating from the discrete lines seen in the atomic spectrum. The electrons occupy levels that have slightly different energy than the other electrons, and as has been discussed, the electronic transitions can move to any of these vibrational, as well as rotational, levels. This is seen in the broadening of the absorption and emission spectra (Figure 1.8).

When dealing with more complex systems, these broad spectra will overlap and make distinguishing between individual fluorophores more challenging. While the energy difference between the electronic state can be similar, the deactivation of the excited electron is likely to be different. By measuring the fluorescence lifetime, it would be possible to distinguish each fluorophore in Table 1.3 and as will be discussed in the next section, determine the relative contributions of each.

Dye	Ex (nm)	Em (nm)	Lifetime (ns)
DAPI	341	496	0.16
Fluorescein	495	517	4.0
GFP	498	516	3.2
Rhodamine 6G	525	555	4.0
Rhodamine B	562	583	1.68

Table 1.3: Spectra of typical dyes and table of their spectral peaks and lifetimes.

Consider N(t) number of excited electrons deactivating to the ground state with a total rate constant k. The total rate constant will be comprised of the superposition of the rate constants form each deactivation pathway available to the electron. Where the radiative rate constant is k_r and for the sake of simplicity, the combined non-radiative rate constant is defined as k_{nr}. The rate at which excited electrons deactivate is defined by the differential equation:

$$-\frac{dN(t)}{dt} = (k_r + k_{nr})N(t) \tag{1.15}$$

A negative sign is used since the population of excited electrons will be decreasing. Rearranging and integrating both side results in equation 1.19.

$$\int_{N_0}^{N} \frac{1}{N(t)} dN(t) = -(k_r + k_{nr}) \int_0^t dt \tag{1.16}$$

We define the limits from the initial excited electron population N_0 to a value equal to N, within a time frame from 0 ($N(t=0) = N_0$) to time t.

$$[\ln(N(t))]_{N_0}^{N} = -(k_r + k_{nr})[t]_0^t \tag{1.17}$$

$$[\ln(n) - \ln(N_0)] = -(k_r + k_{nr})[t - 0] \tag{1.18}$$

$$\ln\left(\frac{N}{N_0}\right) = (k_r + k_{nr})t \tag{1.19}$$

Using the properties of logarithms and multiplying by an exponential results in:

$$\frac{N}{N_0} = \exp\left[-(k_r + k_{nr})t\right] \tag{1.20}$$

Rearranging for N give equation 1.21 and the fluorescence lifetime is given by t.

$$N = N_0 \exp\left[-(k_r + k_{nr})t\right] \tag{1.21}$$

From equation 1.21 it is clear that the lifetime is affected by both the radiative and non-radiative rate constants. The rate which an excited electron will deactivate is subject to multiple factors in a similar way to the absorption and fluorescence spectra are. The radiative rate will be determined by the molecular structure and electronic state energies. The non-radiative rate constants will be affected by the molecular structure as well as factors like the type of solvent used; the presence of quenchers, internal conversions; temperature and neighbouring molecules. [20, 46]

The vast majority of fluorescent dyes have a monoexponential fluorescence lifetime decay. This is an attractive feature for a fluorescent probe as monoexponential decays are easier to analyse and identify in a mixture of fluorophores. In general, the presence of multiple fluorescence lifetime components means there are multiple fluorophores present. However, this is not always the case. For instance, the fluorescent amino acid phenylalanine, tyrosine, and tryptophan have two-lifetime components that arise from different rotamers. A molecule that can adopt different conformational states as a result of rotation about a bond has different rotational isomers, called rotamers. [20, 45, 46]

Chapter 2

Spectroscopic Equipment Overview

The research documented within this work is based within the spectroscopy field, with spectrophotometry, spectrofluorimetry and time-resolved spectrofluorometry being employed throughout. This chapter aims to cover the operation of the instruments and techniques used in order to aid the reader in interpreting the data within Chapters 3-5. Specific settings and operational conditions are detailed within the relevant chapter.

2.1 Spectrophotometry

2.1.1 Instrument set-up

When presented with a new sample, the first spectroscopic measurement to be performed will aim to acquire the absorption spectrum. A spectrophotometer measures the amount of light that passes through the sample in order to quantify how much light has been absorbed. Figure 2.1 is the layout for the Lambda 25 (Perkin Elmer) spectrophotometer and shows the path the light takes through the instrument.

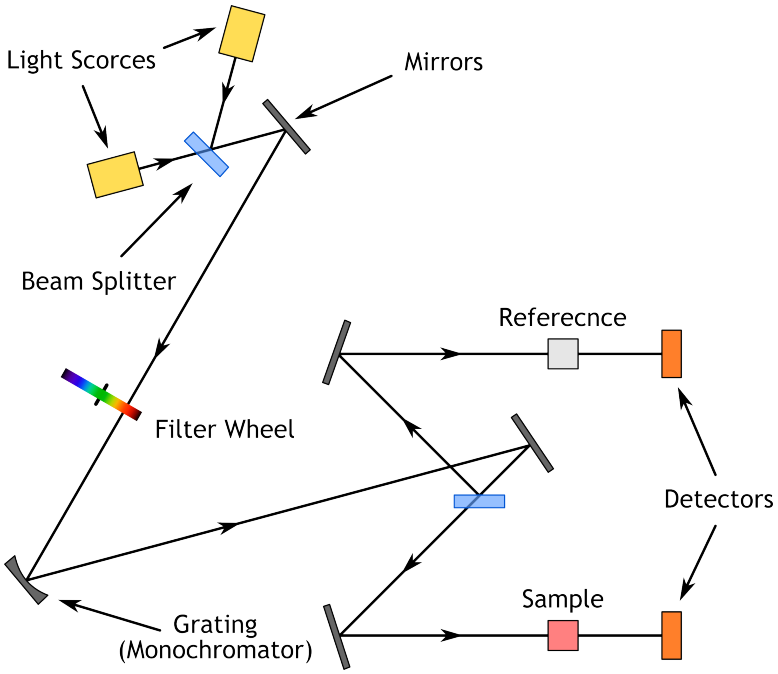

Figure 2.1: Layout of the Lambda 25 spectrophotometer showing the path the light takes through the instrument.

The instrument has two light sources, one covering lower UV wavelengths (a 25 W deuterium lamp, 190 nm – 330 nm) and another covering the visible/NIR region (a 20 W halogen lamp, 330 nm – 1100 nm). There is a motorised blocker that switches between the two lamps during measurement. The lamplight passes through a filter wheel before reaching the grating monochromator. The filter wheel helps improve the selection of wavelengths by blocking out most other wavelengths. Specific wavelengths are then selected with the monochromator, which then passes through a beam splitter. This separates the beam into two, one that passes through the sample and the other passes through the reference sample.

2.1.2 Measurement protocol

There are two photodiode detectors to measure the intensity of light that passes through the solutions, and the ratio of values is used to calculate the absorption value according to Equation 2.1.

$$A(\lambda) = A_s(\lambda) - A_r(\lambda) = log\frac{I_s(\lambda)}{I_0(\lambda)} - log\frac{I_r(\lambda)}{I_0(\lambda)} = log\frac{I_s(\lambda)}{I_r(\lambda)} \tag{2.1}$$

Where A_s and I_s are the sample absorption and intensity values while the reference values have the 'r' subscript. The incident light value is denoted by I_0 and by subtracting the absorption values it is possible to measure the absorption without needing to measure I_0 (Equation 2.1). The absorption is also called the optical density (OD), and since the measured absorption results from the ratio of intensity values, it is dimensionless. [46] Measurements involve two steps with the aim of correcting the spectrum from the absorption of the cuvettes and the solvent used. [47] The first is called the baseline measurement and uses solvent filled cuvettes in both the sample and reference paths. This corrects for the variation in the cuvettes since no two cuvettes are perfectly equal. The second measurement replaces the solvent in the sample cuvette with the actual sample dilution. Utilising a two-arm geometry and baseline correction, the true absorption of the sample can be measured. [47]

The spectrophotometers were controlled with the UV WinLab software and settings include wavelength range, speed and measurement increment. With both the deuterium and halogen lamps, the full measurement range of the spectrophotometer is 190 nm – 1100 nm. Specific wavelength ranges used are specified within the relevant chapter methodology sections. The speed is in nanometers per minute (nm/min) and describes the number of nm wavelengths measured in 60 seconds. Throughout this thesis, the speed was set to 960 nm/min, and the instrument was set to measure in 1 nm increments.

The concentration of the sample can impact the accuracy of the measurement since the linearity of the Beer-Lambert law breaks down at high concentration values. [20] A dilute sample typically falls within the nM to μM regime where the OD value is ≤ 0.1. [20, 48]

2.2 Spectrofluorimetry

2.2.1 Instrument set-up

For fluorescence intensity measurements the detector is placed at right angles to the direction of the excitation path in order to minimise the detection of excitation light (Figure 2.2). This is referred to as the L-configuration while the T-configuration has a second detector positioned opposite to the first. [20] For excitation, a xenon lamp (450 W for the Fluorolog 3 (Horiba Scientific) and 150 W for the FluoroMax 2 (Horiba Scientific)) is used which allows for excitation between 240 nm to 600 nm.

The fluorimeter uses a Hamamatsu R928 photomultiplier tube (PMT) as a detector with a detection range from 290 nm to 800 nm. Monochromators use the Czerny-Turner geometry (Figure 2.2) where the first mirror collimates the light onto the grating. A second mirror refocuses the diffracted light out of the monochromator. Different from a spectrophotometer, a spectrofluorimeter can use two monochromators with one selecting the excitation wavelengths and the other selecting the emission wavelengths.

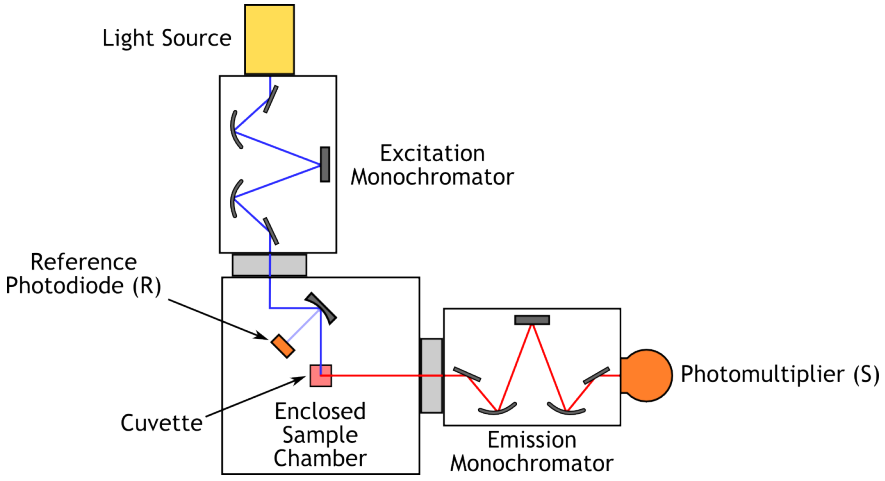

Figure 2.2: Layout for a spectrofluorimeter. A xenon lamp is used as the light source, and a photomultiplier tube is used as the detector. The sample's fluorescence is detected at right angles to the direction of excitation. The instrument has two Czerny-Turner geometry monochromators that allow for the selection of excitation and emission light. During the measurement, $\sim 8\%$ of the excitation light is reflected onto a photodiode which records the lamp profile that can be used to correct the fluorescence signal.

2.2.2 Correcting fluorescence spectra

The measurement of fluorescence intensity is quantitative while the measurement of absorption is a relative one. As a result, any fluctuation or wavelength dependency in the xenon lamps output will impact the measurement. The effect of the lamp output can be corrected for, which is why spectrofluorimeters have a reference photodiode (Figure 2.2) that is illuminated with around 8% of the excitation light. [20,48] This photodiode measures the response of the xenon lamp, during the fluorescence measurement, in microampere (μAmps). Dividing the measured fluorescence signal (S) by the lamp reference signal (R) corrects the fluorescence spectrum from the wavelength-dependent output of the xenon lamp as well as source and temporal fluctuations.

The lamp output is not the only correction factor needed as there is a non-linear wavelength response from the system itself. Each spectrofluorimeter has its own response which means that a correction file for each instrument needs to be measured. This measurement is performed with the use of a calibrated photodiode and is measured by the manufactures before each unit is shipped. The correction is applied during measurement for both the reference signal (R_C) and the measured fluorescence signal (S_C). For fluorescence measurements, the S_C/R_C signal is used as this accounts for the wavelength dependences of both the xenon lamp and the instrument.

2.2.3 Software

Software used was the FluorEssence (Horiba Scientific) package and allows for excitation, emission, kinetic and excitation-emission matrix measurements to be performed. The software merges data-acquisition directly into the data processing program, Origin® (OriginLab®). Variables that can be adjusted include the excitation and emission wavelength range, bandpass, measurement increment and the integration time. The speed of measurement is primarily controlled by adjusting the integration time which determines how long the instrument spends sampling a data point. This can help reduce the S/N ratio as the instrument can sample more photons in determining an intensity value.

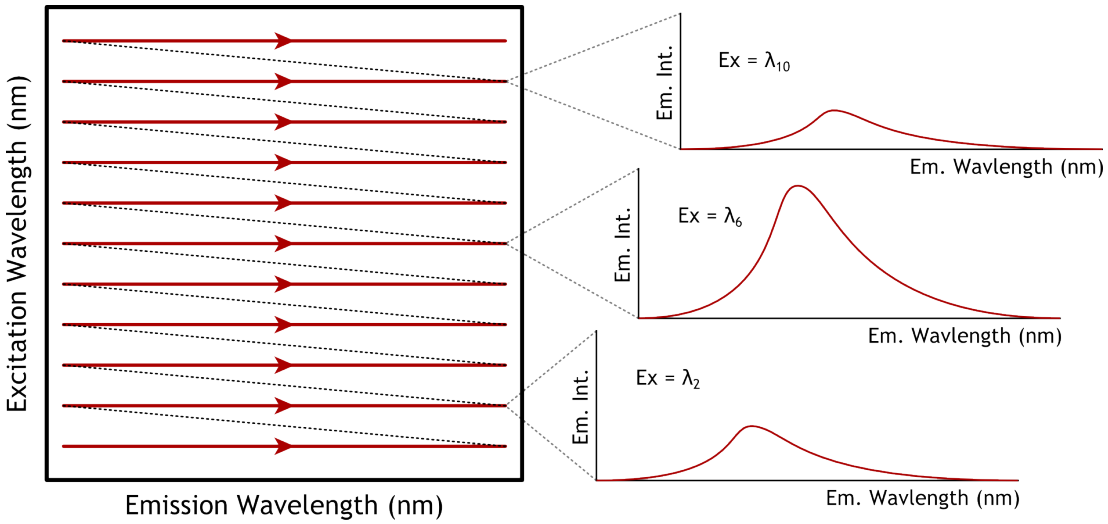

Figure 2.3: Illustration showing the sequential acquisition of an EEM dataset by measuring fluorescence spectra across an excitation wavelength range.

2.2.4 Excitation-emission matrix

A spectrofluorimeter with dual monochromators is capable of performing an excitation-emission matrix (EEM) measurement. The EEM measurement aims to produce a three-dimensional data cube with fluorescence intensity information across both the excitation and emission axis. Collecting the EEM data is done via the sequential acquisition of fluorescence spectra across an excitation wavelength range, as illustrated in Figure 2.3.

The data from an EEM measurement is plotted on a false colour contour plot where the intensity values are translated into a colour scale, with warm colours indicating high-intensity values and cool colours indicating lower intensity values. From the EEM dataset of water Figure 2.4 the first and second Rayleigh and Raman scatter lines are visible. The FluorEssence package allows for the masking of these scatter lines which only needs the user to input the bandpass values used. However, the scatter lines can provide information on the degree of aggregation of particles. The colour intensity scales are plotted in a log scale in order to make clearer the weaker fluorescence responses at longer wavelengths.

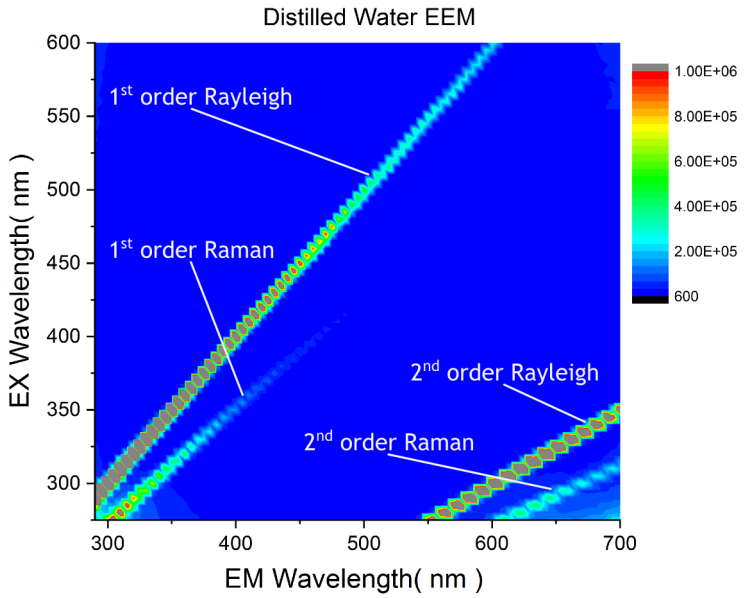

Figure 2.4: EEM contour plot for a sample of distilled water showing the first and second Rayleigh and Raman scatter lines. The colour code on the right indicates the intensity value with warm colours representing higher intensity values and cool colours representing lower intensity values. Grey and black regions indicate that the intensity values are outwith the range of selected intensity values. For clarity this EEM has a linear colour scale while the rest of the EEMs reported have a log colour scale.

2.3 Time-Resolved Fluorescence Spectroscopy

2.3.1 Time-correlated single photon counting

Of the two methods for measuring the time-resolved fluorescence, frequency-domain and time-domain, the time-domain method of time-correlated single photon counting (TCSPC) was used. TCSPC is a single photon counting method that uses pulsed light sources to measure the time-of-flight of photons through the spectrofluorometer (Figure 2.5). Since the path length is the same for each photon, the only disruption to the photon's time-of-flight is the time it takes to be converted into a fluorescence photon. Repeated time-of-flight measurements build up a histogram of photon counts versus time which can be fitted using reconvolution analysis in order to determine the fluorescence lifetime of the sample.

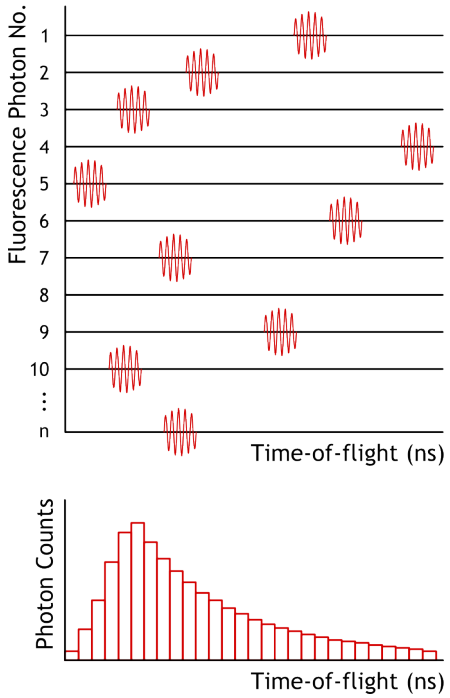

Figure 2.5: Principle of time-correlated single photon counting where the time-of-flight of a photon, through the spectrofluorometer, is measured repeatedly in order to generate a histogram of photon counts versus time. The acquired histogram is then analysed via reconvolution analysis.

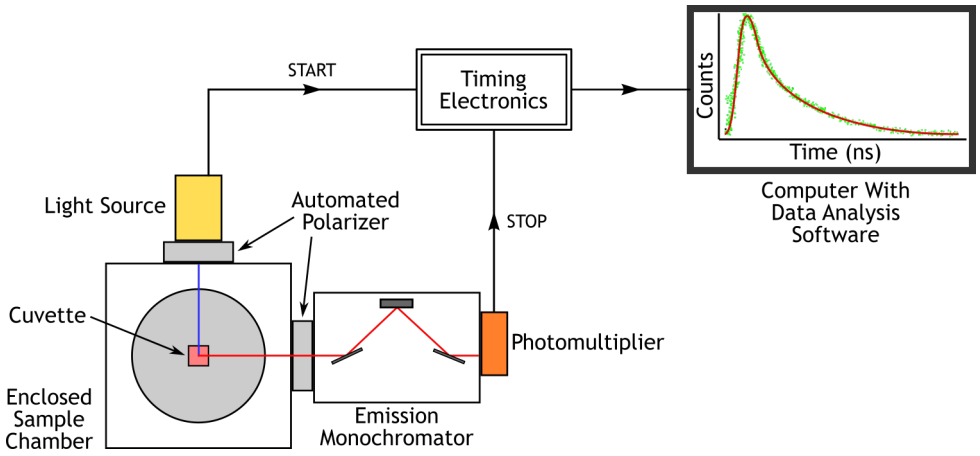

Figure 2.6: Geometry for the spectrofluorometer with the excitation path in blue and the emission path in red. This illustrates the forward mode operation where the light source sends the START signal to the timing electronics while the detector (a photomultiplier) sends the STOP signal when a fluorescence photon is detected.

An individual time-of-flight measurement begins with the laser diode emitting a pulse of monochromatic light. At the same time, the laser diode sends an electronic signal to the timing electronics unit (Figure 2.6) which starts the timing electronics. The excitation pulse travels to the sample where it can be absorbed and converted into fluorescence photons. The emitted fluorescence photons travels through to the detector, and when the first photon is detected, the detector sends an electronic signal to stop the timing electronics unit. The time interval between the START and STOP signals constitutes the time-of-flight of the photon and can be sent to the measurement system where it is added to the histogram. The system then repeats this time-of-flight measurement until a set time limit is reached (seconds to minutes) or a set peak photon count value is reached (Typically 10,000).

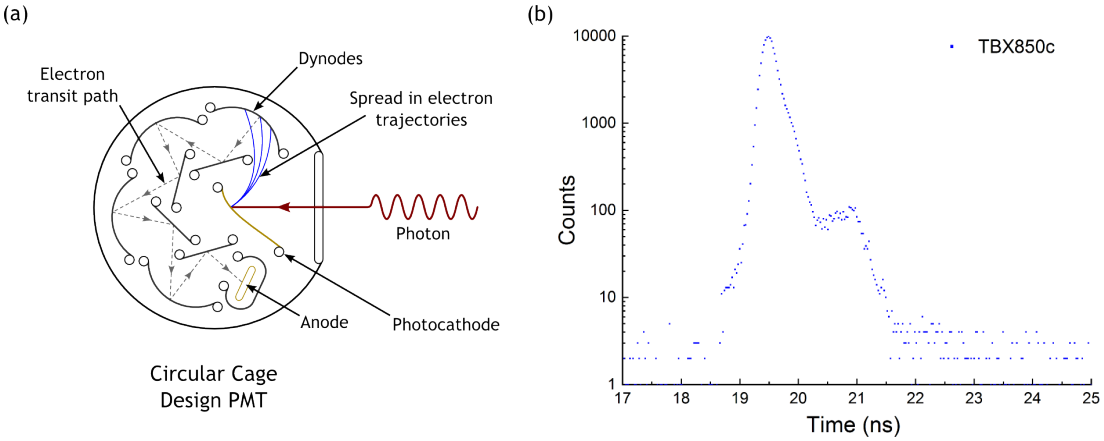

Figure 2.7: (a) In order to illustrate the time response of a PMT the design of a circular cage PMT is shown with the release of electrons when the photon reaches the photocathode. The electrons have slightly different trajectories which result in a variation of transit times through the rest of the PMT. The dashed line shows the path the electrons take through the PMT, with each dynode interaction producing more elections before arriving at the anode. (b) The instrumental response decay profile for the TBX850c PMT produced by measuring the Rayleigh scatter of a LUDOX sample with a DeltaDiode (peak 503 nm) excitation source. The after peak, from the transit time spread, is visible at 21 ns.

2.3.2 Pulsed excitation sources & photomultipliers

The sample is excited by either a NanoLED or DeltaDiode (Horiba Scientific) pulsed laser diode as part of the DeltaFlex TCSPC system (Horiba Scientific). These sources typically operate at a repetition rate of 1 MHz for the NanoLED and 8 MHz for the DeltaDiode. The pulse width of the NanoLED laser diode is $<$ 200 ps while the DeltaDiode has a pulse width from 45 ps to 110 ps, depending on the model. The laser diodes operate at a discrete wavelength ($\pm \sim$ 10 nm of peak wavelength), so the spectrofluorometer has only one monochromator for selecting the fluorescence wavelength (Figure 2.6) and uses the Seya-Namioka geometry.

The laser diodes used for lifetime measurements are vertically polarised which means that only those fluorophores whose dipoles are aligned will be excited. [20] In order to account for this polarisation effect two polarisers are used with the excitation polariser vertically oriented and the emission polariser set to the magic angle (54.7^{o}). [47]

The detector used was the TBX850c PMT (Horiba Scientific) which has a detection range from 250 nm up to 850 nm. The PMT contains a photocathode that converts the detected photon into an electron via the photoelectric effect. The electrical signal is amplified by multiplying the number of electrons produced through repeated interactions down the dynode chain (Figure 2.7(a)). This multiplication process ensures that the current at the anode end is sufficient to trigger the rest of the electronics.

The PMT has three distinct time responses that affect the profile of the measured decay profile. The transit time is the time it takes electrons to travel down the dynode chain and the rise time is the time taken for the anode signal to rise from 10% to 90% of its final value. [20] The transit time spread results from the difference in transit times as the electrons can eject from the dynodes with slightly different trajectories Figure 2.7(a). The time responses of PMTs impacts the measured decay profile along with the pulse profile of the laser diode.

Figure 2.7(b) shows the instrumental response decay profile for the TBX850c detector measuring the Rayleigh scatter of dilute LUDOX with a 503 nm emitting DeltaDiode. The full width half maximum (FWHM) of instrumental responses can range from $\sim$ 180 ps to 250 ps [49] for detectors like the TBX850c. The appearance of an after pulse is due to the non-linear transit time spread of the PMT. [49]

2.3.3 Repetition rate, time range & delay

An important aspect to TCSPC measurements involves the selection of a laser diode repetition rate and measurement time range (i.e. the time range on the x-axis of the histogram). Time-of-flight measurements are synchronised with the repetition rate of the laser diode which influences the time window available to measure a lifetime decay. With a repetition rate of 8 MHz (8 laser diode pulses every second) the time between pulses equals 125 ns, so in order not to record a second laser pulse and disrupt analysis, the measurement time range needs to be less than 125 ns. If the sample has a lifetime decay that exceeds the 125 ns time range (Figure 2.8(a)), then a lower repetition rate and longer time range are needed. This is the case when measuring phosphorescence where the lifetime values exceed the nanosecond range.

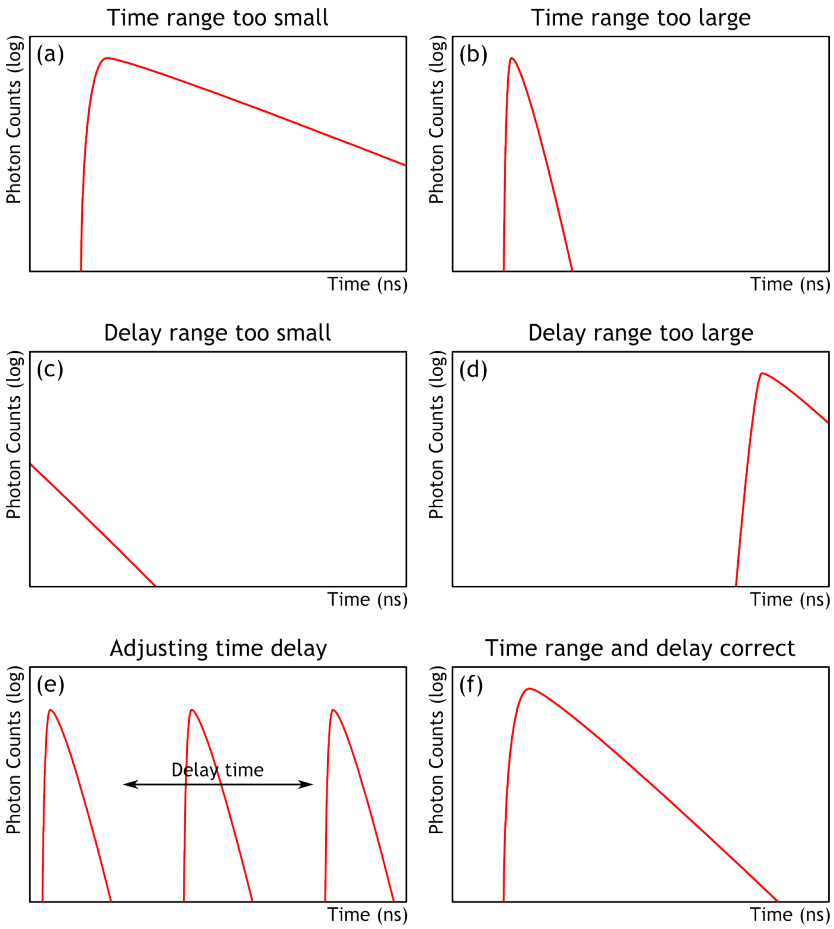

Figure 2.8: Illustrations demonstrating the change in measured lifetime decay when the time range and delay are adjusted. When the time range is incorrect (a & b) the full decay is not captured, or the full decay covers too few time channels to allow for effective analysis. When the delay is incorrect (c & d) only parts of the decay is measured. Adjusting the delay (e) alters the position of the decay within the time range. The correct settings for the time range and delay (f) capture the full decay while maximising the number of time channels the decay occupies.

The generation of the lifetime decay histogram involves dividing the time range into bin values. For the lifetime systems use here the time range was divided into 4000 bins. This value remains constant regardless of the time range used which results in different time calibration values (i.e. the time range of each bin). Setting the time range to 100 ns results in 4000-time channels with a time calibration value of 0.0259 ns/channel. Increasing the time range to 400 ns still has 4000-time channels but has a time calibration of 0.104 ns.

In order to obtain the best results, it is important that the lifetime decay covers a large range of time channels. This ensures that the decay information is covered by a wide range of time channels which effectively increase the resolution of the data.

Several sources induce a delay in the time-of-flight measurement. A photoelectron can take up to 20 ns to exit a PMT. [20] The length of cables that transfer the start and stop signals delay the recording of these signals by the timing electronics unit with large coils of coaxial cable being used to deliberately introduce a delay in either the start or stop signal (useful for phosphorescence measurements). The reset time of the timing electronics also contributes to the delay time as well as the instrument geometry and optics. In order to compensate for these delay sources, the measurement software (DataStation, Horiba Scientific) allows the user to adjust an electronic delay value in order to centre the lifetime decay profile within the measurement window. Figure 2.8(c & d) shows the effect of having the delay set incorrectly while Figure 2.8(e) shows the change in decay position when the delay value is changed.

2.3.4 Forward & reverse configuration

The instrumental set-up shown in Figure 2.6 is in the forward configuration, where the start signal comes from the light source and the stop signal comes from the detector. In this configuration, a start signal is initiated for every pulse of the laser diode while a stop signal is sent when the first fluorescence photon is detected. Since the quantum yield of fluorophores is less than one, there will be times when no fluorescence photon is detected. The stop-start ratio is usually kept below 2% to ensure that the system is detecting single fluorescence photons. When the stop-start ratio is increased, there will be an increased chance that there will be more than one fluorescence photon available for detection. Since the system measures the first fluorescence photon to be detected, an increase in stop-start ratio can result in a lower lifetime value being measured than the genuine lifetime value.

The low quantum yield of melanin means the stop-start ratio can be significantly less than 2%. In order to speed up acquisition times, the lifetime system was operated in the reverse configuration. The reverse configuration has the start signal coming from the detector while the stop signal comes from the pulse of the laser diode. Instead of measuring the time-of-flight of the photon from the light source to the detector, a reverse mode system measures the time interval from the detection of a fluorescence photon to the start of the next pulse of light from the laser diode. This can reduce the time needed to measure a fluorescence lifetime decay since the electronics are only reset after a photon is detected instead of after every laser diode pulse.

2.3.5 Scatter, background & more complex decay profiles

The fluorescence lifetime decay can also be affected by the presence of scatter and a high background level (Figure 2.9). A sample that contains particles that scatter strongly can be identified from the narrow peak that forms at the start of the decay as shown in Figure 2.9(b). The profile of the scatter peak will follow the instrumental response closely and will produce a very short time component. It should be noted that the instrument has a lower limit of time component values which can be resolved. The presence of a scatter peak may be from time components that are below the limit of detection of the instrument.

When working in the red or near-infrared (NIR) part of the spectrum, there will be a greater influence from thermal photons. This source of background photons can increase the background level of the fluorescence decay as illustrated in Figure 2.9(b). Additionally, if stray light is allowed into the system, then the background level will also increase. Naturally, the level of the background is related to the acquisition time since the longer the measurement runs the more background photons are detected.

For more complex samples, like a solution of two fluorescent molecules, the measured decay profile will be made up of the two individual fluorescence decay as seen in Figure 2.9(c). Should the individual lifetime decays be mono-exponential then the measured decay of the mixture will follow a two-exponential function with two time component values. However, other photophysical effects can alter the fluorescence decay such as rotors, solvent relaxation, oligomerisation and quenching. [20]

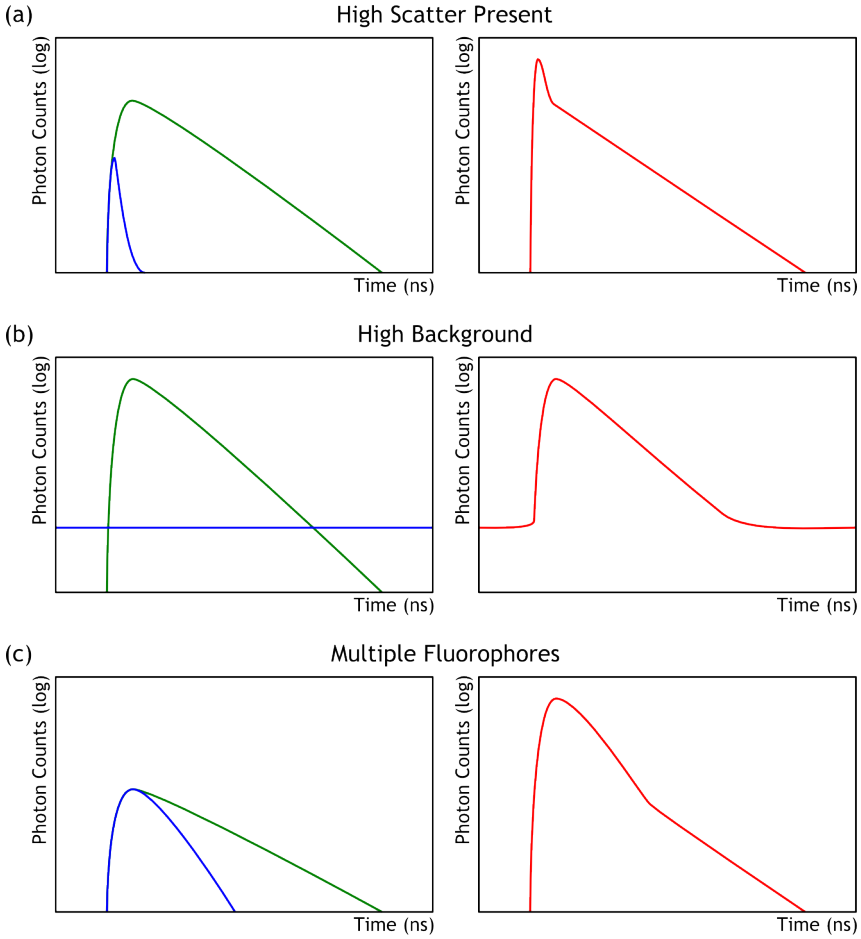

Figure 2.9: Illustration showing the effect on the fluorescence decay of (a) scattering, (b) high background and (c) having multiple fluorophores present.

2.3.6 The challenge with analysing decay data

TCSPC is an indirect method for measuring the fluorescence lifetime of a sample by performing time-of-flight measurements of individual photons as they travel from the light source, interact with the sample, and then the fluorescence photons travel to the detector. The lifetime decay follows the formula for exponential decay (assuming a mono-exponential species) but the measured decay profile is different and analysing the decay with a simple exponential function will not produce a good fit. This is the result of the instrument itself as the excitation pulse has its own decay profile.

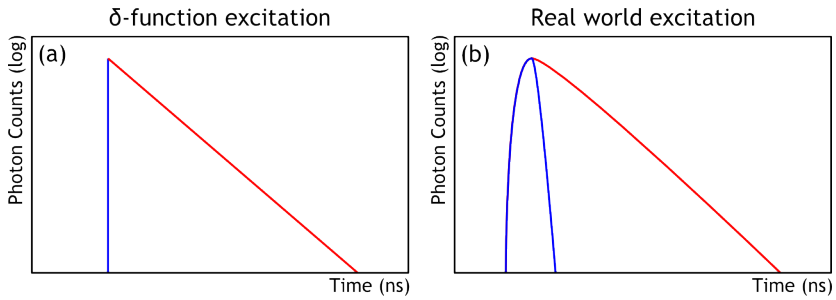

Figure 2.10: (a) The fluorescence decay profile when the excitation pulse is equal to a δ-function. (b) The decay profile for a real-world light source and instrument where the excitation pulse has its own profile.

In an ideal case, the excitation pulse would be a δ-function as seen in Figure 2.10(a), and the decay profile would fit an exponential function. However, real light sources have their own profile, and imperfection from the electronics and optical components can also broaden the excitation pulse. [49, 50] This instrumental response (Figure 2.7(b)) impacts the fluorescence decay as seen in Figure 2.10(b). In order to extract fluorescence lifetime information from the measured decay profile, a different decay function needs to be used. This is why fluorescence decays are analysed using reconvolution analysis.

2.4 Reconvolution Analysis of Lifetime Decays

2.4.1 Construction of test function

The measured fluorescence decay is the result of the convolution of the instrumental response and the actual fluorescence decay of the sample. Consider that the instrumental response is made up of δ-functions as shown in Figure 2.11. Each δ-function produces a fluorescence decay with the maximum being equal to the intensity of the δ-functions. The measured fluorescence decay is then the sum of all the fluorescence decays produced via δ-function excitation.

Mathematically, convolution can be denoted with an asterisk ($*$) symbol, so each δ-function produces a fluorescence decay such that,

$$D_M(t) = P(t) * F(t) = \sum_{t=0}^{t=t_k} \delta(t_k) f(t - t_k) \Delta t \tag{2.2}$$

With f(t) being the decay function following δ-function excitation. The term (t-t_k) is used since the fluorescence decay starts at t_k with no emission from times below t_k. The measured decay (D_M(t)) will be the sum of all the decays produced by δ-functions. For small values of Δt Equation 2.2 can be expressed as an integral. However, since the measurement produces a histogram with defined time bins the summation form of Equation 2.2 is an adequate description. [20]

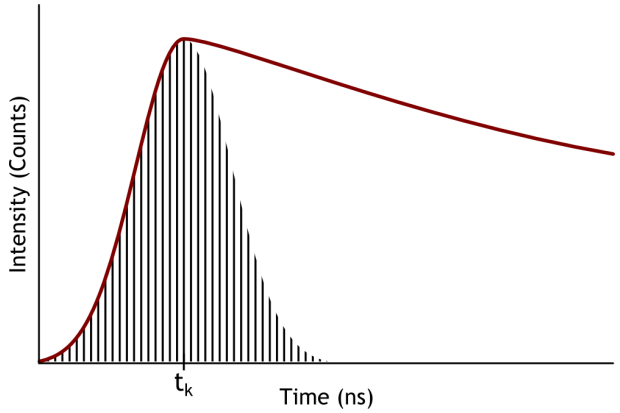

Figure 2.11: The measured lifetime decay with the instrumental response shown as a series of δ-functions. The time at t_k signifies the peak of the excitation pulse.

In order to extract lifetime values from the measured signal, a test function is constructed from the convolution of the theoretical decay model and the instrumental response function (IRF). The IRF (also called the prompt signal) is produced by measuring the TCSPC response of a scattering sample. Typically a dilute sample of LUDOX® silica particles is used, and the instrument is set-up to measure the Rayleigh scatter response. The prompt signal (P(t)) is then convoluted with an appropriate model that describes the fluorescence decay (F(t)) with the simplest being a mono-exponential function (Figure 2.12(a)). The constructed test function is then fitted to the measured fluorescence decay using the least-squares method (Figure 2.12(b)). This method is referred to as reconvolution analysis since the test function has to be constructed from the measured prompt signal and the theoretical decay model.

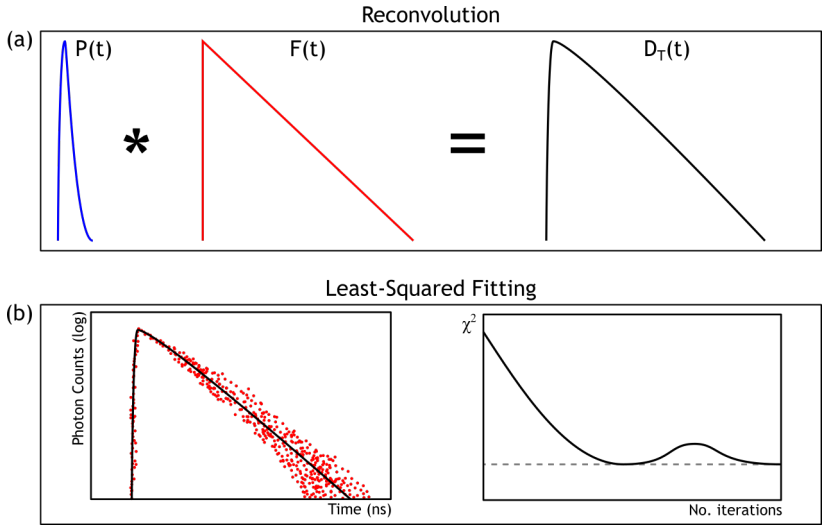

Figure 2.12: Processes for reconvolution analysis. (a) The test function ($D_T(t)$) is generated by the reconvolution of the measured prompt signal and the theoretical decay model function. (b) The test function is fitted to the measured fluorescence decay data using the least-squares method. The goodness-of-fit (χ^2) value is shown opposite and illustrates how the fitting algorithm aims to minimise the χ^2 value.

2.4.2 Least-squares fitting

Least-squares fitting begins by selecting a set of initial parameter values for the test function and testing the goodness-of-fit of the test function to the experimental data. The algorithm will aim to minimise the goodness-of-fit value by iteratively changing the parameter values and reassessing the fit statistics. The χ^2 test is used to assess the goodness-of-fit and is described as:

$$\chi^2 = \sum_{k=1}^{n} \frac{[D_M(t_k) - D_T(t_k)]^2}{\sigma^2} \tag{2.3}$$

$D_M(t)$ is the measured decay data while the reconvoluted decay model is labelled $D_T(t)$. For TCSPC the standard deviation (σ) is taken from Poisson statistics and is known to be equivalent to the square root of the number of measured photons $\sqrt{(D_M(t_k)}$. [20] The standard χ^2 values will be dependent on the number of data points (n) so in order to facilitate comparison between different fits, the reduced χ^2 value is used:

$$\chi^2_R = \frac{\chi^2}{n-p} \tag{2.4}$$

Where p equals the number of parameters within the fitted function. Since the number of time channels is large (4000 channels) then the number of data points is much larger than the number of fitted parameters. This means that for good fits, the reduced χ^2 value will approach unity. [20]

Along with the reduced χ^2 value the weighted residuals are also used to determine the goodness-of-fit. The weighted residuals (or deviation plots) are calculated for each data point using Equation 2.5. For a good fit, the weighted residuals will be randomly centred about zero and have a squared mean value near unity. [20]

$$W_i = \frac{D_M(t_k) - D_T(t_k)}{\sqrt{D_M(t_k)}} \tag{2.5}$$

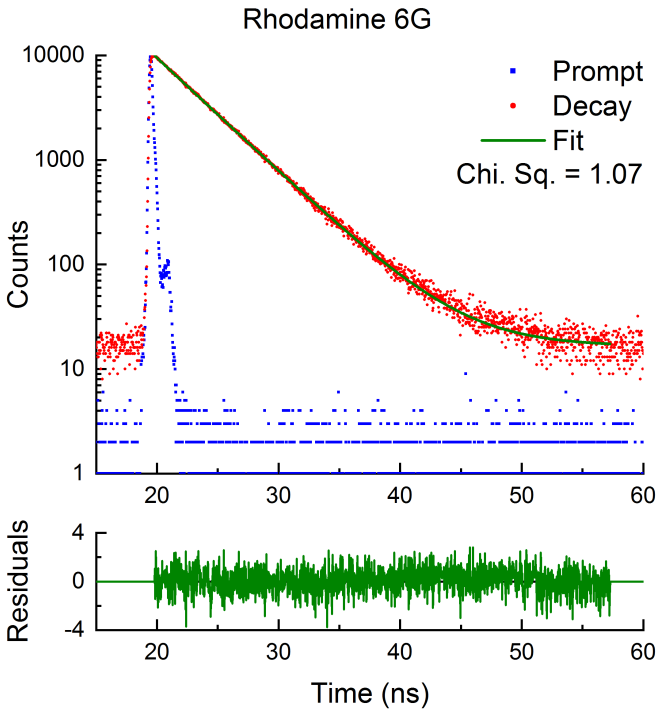

Figure 2.13: Fluorescence decay (red) for a dilute sample of rhodamine 6G, fitted to a one-exponential model (green line). The instrumental response function is shown in blue, and the weighted residuals are shown underneath in green.

2.4.3 Example using a fluorescent dye

Putting this all together, the measured fluorescence decay of the fluorescent dye molecule, rhodamine 6G (R6G), is shown in Figure 2.13. The fluorescence decay is in red, and the instrumental response is in blue while the weighted residuals are underneath in green. The sample was excited with a DeltaDiode laser diode (503 nm) with the emission monochromator set to 550 nm, and the bandpass was set to 32 nm. The repetition rate was 8 MHz while the time range was set to 100 ns. The emission polariser was set to the magic angle, and the instrument measured until a peak count of 10,000 photon counts was reached. A dilute sample of LUDOX® was used to measure the IRF.

Parameters	τ (ns)	B (%)	A	Shift (ns)	χ^2
Fitted Values	3.99	100	16.59	0.01	1.07

Table 2.1: The table shows the fitted parameter values from reconvolution analysis.

Reconvolution analysis was performed with the Data Analysis Software (DAS) (Horiba Scientific). A single exponential decay model (Equation 2.6) was used for the reconvolution process with B being the amplitude value, A being the background value and τ being the time component value (or lifetime value if the model is valid for the system being studied).

$$F(t) = Bexp\left(-\frac{t}{\tau}\right) + A \tag{2.6}$$

Performing reconvolution analysis with a single exponential model (Equation 2.6) has produced a χ^2 value of 1.07 (Table 2.1). This is close to unity and indicates that a single exponential model is appropriate for describing the fluorescence decay of R6G. The residuals are randomly distributed about zero and corroborate that a mono-exponential model is appropriate.

The time component (τ(ns)) recovered from reconvolution analysis is 3.99 ns, and since there is only one exponential being used, the relative amplitude (B(%)) equals 100%. The A-value is the background value and in this case, equals 16.56 photon counts. The shift parameter is included since the peak of the fluorescence decay is different from the prompt which is due to the wavelength dependence of the transit spread time of the photomultiplier. [20, 50] For R6G, the accepted lifetime is $\sim$ 4 ns [18, 51] which agrees with the analysis of Figure 2.13.

Chapter 3

Intrinsic Spectroscopic Methods for Distinguishing Melanins

3.1 Introduction

3.1.1 Melanoma detection via intrinsic spectroscopy

In 1985, Ito and Fujita [52] adapted degradation studies and developed a micro-analytical method to quantify the amounts of eumelanin and pheomelanin. The method degrades the eumelanin polymer into pyrrole-2,3,5-tricarboxylic acid (PTCA) with potassium permanganate ($KMnO_4$) while pheomelanin is degraded into aminohydroxyphenylalanine (AHP) isomers by hydriodic acid. The degraded products are then measured via high-performance liquid chromatography (HPLC), with a precision of tens of ng per mg of sample. [8]

While the indirect HPLC method works, it is an expensive, destructive technique that is not ideal for medical applications. Krasieva et al. [10] utilised step-wise, two-photon excitation spectroscopy of melanin pigments and were able to measure ratios of eumelanin and pheomelanin. Also, it was found that two-photon excitation was able to distinguish between melanoma cells and non-cancerous skin tissue by measuring the relative concentration ratio of eumelanin and pheomelanin. [9]

While two-photon excitation is a viable method for detecting melanoma, with a sensitivity of 93.5% and specificity of 80.1%, [9, 11] the technology and methodology are both expensive and difficult to use for the average clinician. If it were possible to replicate the measurement with conventional, one-photon excitation, spectroscopy then it would be possible to develop a point-of-care (POC) device that could be used by the clinician, general practitioner or even the patent themselves.

In pursuit of this aim, there are several spectroscopic techniques that can be investigated — measurements such as spectrophotometry, one-photon excited spectrofluorimetry and time-resolved spectrofluorometry. Along with different measurement techniques, there are different analysis methods which can be leveraged to quantify the spectral differences between eumelanin and pheomelanin, such as parallel factor (PARAFAC) analysis [53] and maximum entropy method (MEM) [54].

3.1.2 Multivariate analysis (PARAFAC)

Currently, there is no documented case where PARAFAC analysis has been used to investigate the underlying spectral features of melanins. However, principal component analysis (PCA) has been used with spectral data, of skin, to determine a person's age, blood volume and blood oxygenation. [55, 56] PCA is a statistical bi-linear decomposition method which, converts a set of, possibly correlated, observations into a set of linearly uncorrelated variables, called principal components. In doing so, the transformation aims to maximise the variance between each component.

This can be used to identify, or separate, different fundamental features of a dataset. For example, separate highland and island signal-malt whiskies from spectroscopic data as Mignani et al. [57] demonstrated. PARAFAC analysis is within the same family as PCA but extends the analysis from bi-linear data to multi-way data arrays. [53]

PARAFAC is one method for decomposing a multi-way dataset with the biggest competitors being the Tucker3 method and simply unpacking the multi-way data into matrices and performing standard two-way PCA. [53] The ultimate goal of decomposition analysis is to describe the data in a more condensed manner which should allow for better insight into the system being investigated. This is similar to the way solving simultaneous equations allows for the derivation of solutions, to any single equation, to be reduced to a unique solution for each unknown that fits all the equations in parallel. [58]

PARAFAC is considered a more constrained version of Tucker3, which itself is a more constrained version of two-way PCA. This is because PCA has the greatest degrees of freedom, while PARAFAC (despite being a simpler, more general model) has fewer degrees of freedom. That is to say if a PARAFAC model is sufficient, then Tucker3 and PCA will fit the data better as the extra degrees of freedom are used to fit noise. These restrictions may yield worse fits, than PCA, but the results from PARAFAC are more robust and interpretable. [53]

Extending a bi-linear decomposition model to a three-way (data cube) array begins by assuming the three-way array $\underline{X}$ is given by three loading matrices, **A**, **B** and **C**. The elements of these matrices are, a_{if}, b_{jf} and c_{kf}. The PARAFAC model uses least squares fitting to minimise the sum of squares of the residuals, e_{ijk} in Equation 3.1, given a set number of components (factors) F. [53, 59]

$$x_{ijk} = \sum_{f=1}^{F} a_{if} b_{jf} c_{kf} + e_{ijk} \tag{3.1}$$

The main advantage of PARAFAC, over PCA, is the uniqueness of the result. The well-known problem with PCA is its rotational freedom. This is where the scores and loadings of the bi-linear fit can be rotated (change the axis rotation) without impacting the goodness-of-fit. [53,58] As a result, external knowledge is needed to affirm the orientation of the PCA scores and loadings before the outcomes can be interpreted. By extending PCA to a trilinear model, the PARAFAC model cannot be rotated without a loss of fit, thus ensuring that the solution obtained is unique.

The uniqueness of the PARAFAC result has led to an increase in its use, within the analytical and spectroscopic field. Murphy et al. [60] demonstrated the capability of PARAFAC in identifying underlying spectral structures within the EEM of dissolved organic matter. In the work of Bro and Gallagher [61] PARAFAC was able to recover, from the EEM data, the excitation and emission spectra of the three fluorophores that were mixed. PARAFAC also gave the relative abundance of each fluorophore which, when calibrated, gave the concentration of each fluorophore in the samples. [61]

Given melanin's broad and complex emission response, it is likely that decomposition analysis is needed to identify underlying spectral structures and that PARAFAC would offer a better option for analysing the EEMs of melanin. While it is unlikely that PARAFAC will recover the precise spectra of the molecular species responsible, it is possible that the algorithm can distinguish between eumelanin and pheomelanin.

3.1.3 Different lifetime analysis methods

After measuring the fluorescence lifetime decay, it is common practice to use reconvolution analysis and least-squares fitting to fit, to the decay data, a multi-exponential function of the form:

$$I(t) = \sum_{i=1}^{N} B_i exp\left(-\frac{t}{\tau_i}\right) \tag{3.2}$$

Where I(t) is the fluorescence emission intensity and 'i' being equal to the number of exponentials used in the linear combination. The amplitude of components is given by 'B_i' and the lifetime component value is given by 'τ'. [20]

The multi-exponential model is commonly used for systems that contain separate and distinct fluorescence species or a single fluorophore that exists within different environments. Where each lifetime component is attributed to one fluorophore or photophysical mechanism. Since the lifetime is related to the excited state, the presence of multiple excited states would result in multiple lifetime components being measured.

The B value for a single fluorophore, in different environments, would represent the proportion of fluorescence associated with each fluorophore in each environment. Meanwhile, for a mixture of fluorescent species, the amplitude value would relate to the concentration of each fluorophore and would depend on the absorption, quantum yield and the intensities of each fluorophore at the measurement wavelength. [20]

The multi-exponential model, much like the bi-linear PCA mentioned earlier, would likely produce a reasonable fit to the data. However, while it would be possible to confirm that the data are consistent with equation 3.2, the fluorescence decays may not result from distinct fluorescent species. [20] This could be the case where a fluorophore is in a mixture of solvents or where the effects of oligomeric structures, energy-transferences and structural conformations result in a distribution of decay times.

This is likely the case with melanin as it is known that the bio-macromolecule has multiple structural forms [27] and internal and external proton transfer processes [22, 62] which will, inevitably, have their own effect of the lifetime components. Fitting to a distribution of lifetime components will allow for new insights into the photophysics of melanin as the distribution functions are more sensitive to change than a limited number of exponential components. This should improve the chances of quantifying any differences between eumelanin and pheomelanin. Along with the multi-exponential model, the general relaxation function [63] and the maximum entropy method [54] were used to analyse melanin fluorescence lifetime decays.

The general relaxation function (Equation 3.3) came from the observation that the dielectric relaxation phenomena in complex condensed systems deviated from Debye exponential relaxation laws. [64] This deviation from the exponential model implied that the fundamental principles governing relaxation must have a general form. [65]

$$I_{\alpha,\kappa} = exp\left[-\frac{1}{\kappa}\int_0^{\kappa\left(\frac{t}{\tau_0}\right)^{\alpha}}\left(1-exp\left[-\frac{1}{x}\right]\right)dx\right] \tag{3.3}$$

The fluorescence lifetime is given by τ_0 while the parameters κ and α determine the stable distributions of fluorescence transition rates. [63] From this general form, it is possible to recover the standard exponential model, for the case where $\alpha = 1$ and $\kappa = 0$. [63] Alternative, specific, cases include the Kohlraush (stretched exponential) decay function (for $\alpha < 1$, $\kappa = 0$) and the Becquerel function ($\alpha = 1$, $\kappa > 0$). [66, 67] For MEM equation 3.2 is extended such that α is now a function of time.

$$I(t) = \int \alpha(t) exp\left(-\frac{t}{\tau}\right)dt \tag{3.4}$$

Fitting this model requires determining the spectrum of decay constants $(\alpha(\tau))$ which is the inverse Laplace transform of the measured light, deconvoluted from the IRF. The challenge is that inverting the Laplace transform is ill-conditioned and results in large errors in the reconstruction of $(\alpha(\tau))$, from the small errors in the measurement. The solution to this is to define $(\alpha(\tau))$ as the Shannon-Jaynes entropy function (Equation 3.5) since it introduces the least correlations and hence the least spurious structures into the reconstructed distribution of decay times. [54] and maximising the function during the fitting process.

$$S = -\int \alpha(\tau) log\frac{\alpha(\tau)}{m(\tau)}d\tau \tag{3.5}$$

Where $(\alpha(\tau))$ is the number of fluorophores that decay with a time constant τ and $m(\tau)$ is the model that encodes our prior knowledge about the system, with $m_i = \frac{1}{\tau_i}$ being the case when there is no prior knowledge available. [54]

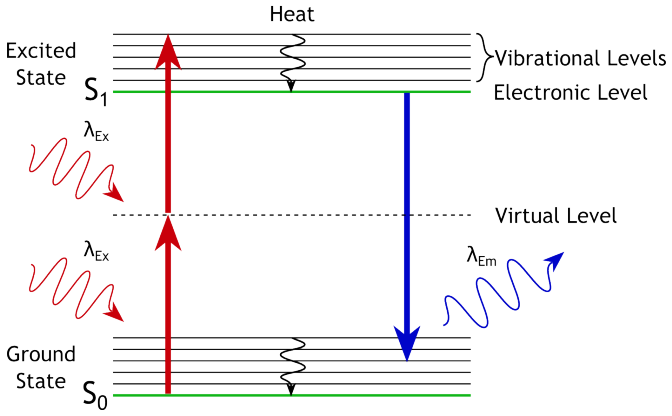

Figure 3.1: Jablonski diagram for simultaneous two-photon excitation. The first low energy photon excites the ground state electron to a virtual level. The second low energy photon then excited the electron from the virtual level to the excited state.

3.1.4 Two-photon excitation

Two-photon excitation (TPE) excites a fluorescent molecule into the excited state by absorbing the energy from two lower energy photons. Typically, TPE follows a simultaneous approach (Figure 3.1) where the two lower energy photons, of the same wavelength, arrive at the molecule within a very short time of each other. [20] As a consequence, the photon flux needs to be higher for TPE than one-photon excitation (OPE) which means that higher laser powers are required. Given this requirement, it is possible to check whether the mode of excitation is genuinely simultaneous TPE by checking the linearity of the plot of luminescence intensity versus the incidence laser power, with a Log-Log axis. [68] This also means the position of excitation is highly localised such that absorption only occurs near the focal point. [20]

When considering centrosymmetric molecules (like the porphyrin ring that Kaxiras et al. [30] proposed for melanins) the energy states of the molecule have ether positive or negative inversion symmetry and are labelled ‘g’ and ‘u’ respectfully. [68] For OPE, of a centrosymmetric molecule, transitions can only occur between states that have different inversion symmetry (i.e. g $\leftrightarrow$ u or u $\leftrightarrow$ g) while TPE can only occur between states that have the same inversion symmetry (i.e. g $\leftrightarrow$ g or u $\leftrightarrow$ u). This selection rule can result in a change in the fluorescence spectrum and along with features like the excitation wavelengths being within the optical window of tissue and the localised excitation volume make TPE attractive in medical imaging. [20, 68]

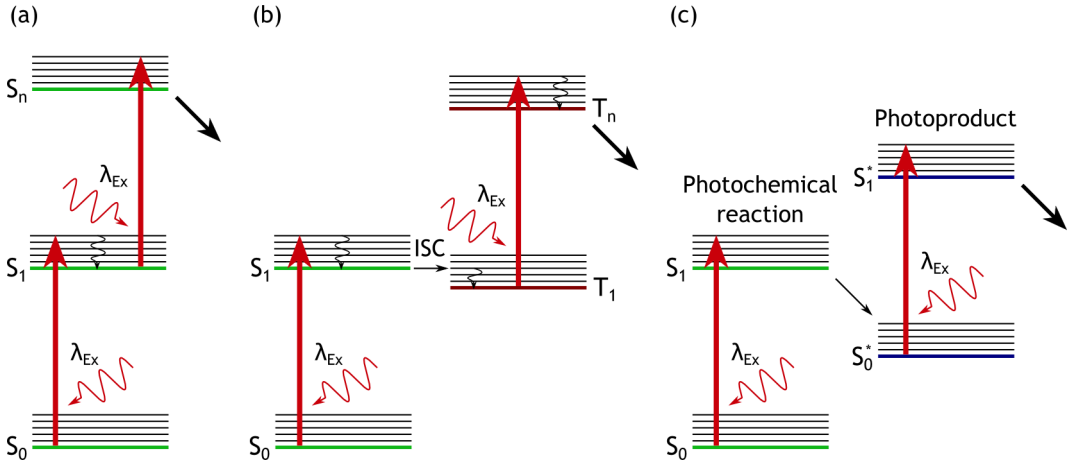

Figure 3.2: Jablonski diagram for stepwise two-photon excitation. (a) After the first photon promotes the electron from the ground singlet state (S_0) to the first excited singlet state (S_1) the second electron excites the electron from S_1 state to a higher singlet state (S_n). (b) The second electron promotes the electron to a higher triplet state (T_n) after the excited singlet electron has transitioned to the triplet state (T_1) via intersystem crossing (ISC). (c) Excitation with the first photon imparts enough energy to induce a photochemical reaction that alters the electronic structure which the second photon can excite via the new photoproduct states $S_0{}^*$ and $S_1{}^*$.

The stepwise TPE process differs from the simultaneous process on account of the excitation involving a real state and not a virtual state. The first variant (Figure 3.2(a)) has the first photon promote the electron to the excited singlet state (S_1), then the second photon excites the electron to a higher singlet state (S_n). The second variant (Figure 3.2(b)) has the excited electron transition to the triplet state (T_1), via intersystem crossing, then the second photon promotes the electron to a high triplet state (T_n). Finally, excitation with the first photon can induce a photochemical reaction (Figure 3.2(c)) which changes the electronic structure. The second excitation photon then excited the new photoproduct ($S_0{}^* \rightarrow S_1{}^*$).

Methodologies have been developed that use TPE to study melanin's two-photon, stepwise, spectroscopy [40, 69] and as a means to detect melanoma. [9–11] This method is based on the different TPE response of eumelanin and pheomelanin and the fact melanoma cells have a higher ratio of pheomelanin to eumelanin than normal cells. [70] Given the TPE process follows a stepwise process, it is likely that the real intermediate state (S_1) has its own electronic structure, including vibrational states. As such it should be possible to use NIR photons to perform OPE spectroscopy on melanin samples.

3.2 Methodology

Chemicals 3,4-dihydroxy-L-phenylalanine (L-DOPA, $> 98\%$). L-Cysteine (Cyst, $> 97\%$). Tyrosinase from Mushroom (TYR, 2687 u/mg). Melanin from *Sepia Officinalis*. Solutions were prepared in distilled water. All chemicals were acquired through Sigma-Aldrich.

3.2.1 Melanin synthesis

Melanin samples were synthesised according to d'Ischia [7] where L-DOPA was oxidised by tyrosinase to create eumelanin and L-Cysteine was added to promote pheomelanin synthesis. Stock solutions of L-DOPA, Cyst and TYR were mixed at concentrations of 3 mM, 3 mM and 1500 units per millilitre (u/ml) respectfully. Eumelanin samples had final concentrations of 1 mM L-DOPA and 500 u/ml TYR. Pheomelanin samples comprised of 1 mM L-DOPA, 1 mM Cyst and 500 u/ml TYR. Sepia melanin stock solutions were made by mixing the Sepia powder with distilled water at a concentration of 1 mg/ml. All preparations were at room temperature, and the water had a pH around 6.4 – 7.0. The pH was measured with a Horiba Scientific pH probe (model D-51). For the Cyst concentration sweep samples, the method of preparation remained the same except that the volume of Cyst was altered such that the final concentrations were 0 mM, 0.01 mM, 0.1 mM, 0.2 mM, 0.4 mM, 0.6 mM, 0.8 mM, 1.0 mM, 1.5 mM and 3.0 mM. With the exception of the absorption time-series measurements, all samples were allowed to react for at least 24 hours, in the dark, at room temperature.

3.2.2 Absorption spectra

Absorption measurements were performed on a Perkin-Elmer Lambda 25 spectrophotometer. The wavelength range was set from 190 nm to 1100 nm with a scan speed of 960 nm/min. Clear walled UV grade plastic cuvettes (Fisher Scientific) were used, and distilled water was used for the solvent correction. Mixed samples of melanin were diluted for measurement such that the majority of OD values were below 1 unless stated otherwise.

3.2.3 Corrected EEMs

The spectroscopic measurement of melanin often requires working at concentrations where the effects of inner-filtering (reabsorption of emitted photons) strongly distort the resulting spectra. [17] This prompted Riesz et al. [17] to develop a procedure to correct for inner-filtering effects. Looking at the excitation path and emission path separately, Beer-Lambert expressions are derived for a small excitation volume, within the cuvette. When expanded to include the background response the final expression takes the form

$$F_{corrected} = kF_{measured} - F_{background} \tag{3.6}$$

Where $F_{corrected}$ is the corrected fluorescence signal, and $F_{measured}$ is the raw data from the instrument. $F_{background}$ is the fluorescence response from the solvent and k is the corrective term and takes the form.

$$k(\lambda_{Ex}, \lambda_{Em}) = exp(\alpha_{Ex} d_{Ex} + \alpha_{Em} d_{Em}) \tag{3.7}$$

The α term is the absorption coefficient for the excitation and emission wavelengths and was calculated from the absorbance data. The d parameter is the optical path length from the cuvette wall to the centre of the cuvette, for the excitation and emission path. As the measurements were conducted using a right-angle geometry, with square-based cuvettes, the value of d equalled 0.5 cm.

A MATLAB® (R2017b – 9.3.0.713579, MathWorks®) script was written to perform the mathematical operations on the measured data, and the code is contained in Appendix A. The code imported the sample EEM data, the solvent EEM data and the absorption spectrum for the sample that was used in the sample EEM measurement. The absorption values were converted to absorption coefficients ($\alpha_{i,j}$), and a matrix was constructed such that:

$$\alpha_{i,j} = \frac{A_{i,j} \times In(10)}{l} \tag{3.8}$$

Where $A_{i,j}$ is the matrix of absorption values, with i and j being the row and column elements of the matrix. The path length l is for the absorption measurement and equalled 1 cm. With the absorption coefficients calculated the correction matric (Equation 3.7) was generated and the corrected EEM data was calculated according to Equation 3.6.

3.2.4 PARAFAC analysis

Parallel factor analysis was performed in MATLAB® (code available in Appendix A) using the function `parafac()`, which comes with the N-way toolbox (Rasmus Bro). [59] The toolbox provides advanced functions and features for fitting multi-way models including, PARAFAC, Tucker, N-PLS, GRAM and TLD. Performing parallel factor analysis only needed the corrected EEM data to be passed to the `parafac()` function and the number of factors to fit to specified. However, the Rayleigh and water Raman scatter lines interfered with the analysis.

Removing the scatter lines from the EEM data was done one emission spectrum at a time, within a `for` loop. The position of the scatter peaks was determined via the relations: [20]

$$\lambda_{Ray_1} = \lambda_{Ex} \tag{3.9}$$

$$\lambda_{Ray_2} = 2\lambda_{Ex} \tag{3.10}$$

$$\lambda_{Ram_1} = 1x10^7 \left(\frac{1x10^7}{\lambda_{Ex}} - 3400 \right)^{-1} \tag{3.11}$$

$$\lambda_{Ram_2} = 2\lambda_{Ram_1} \tag{3.12}$$

Where λ_{Ray_1} is the wavelength position of the first order Rayleigh scatter peak and λ_{Ray_2} being the second order Rayleigh scatter peak. The first and second order water Raman scatter peaks are labelled λ_{Ram_1} [71] and λ_{Ram_2} respectfully, and the excitation wavelength is λ_{Ex}. Intensity values about these scatter peaks (i.e. $\pm$ n (nm), where n is an integer) were converted to 'not a number' (`NaN`) which equated to their removal from the EEM data. The magnitude of n was altered until the whole scatter peaks had been removed. The missing data were replaced with new values that were determined by interpolation of the full emission spectrum. Interpolation was performed using the built-in function `interp1()` with the `spline` option enabled.

With the EEM data corrected for solvent emission, inner-filter effects and the scatter lines replaced with interpolated values, parallel factor analysis could now be performed with the `parafac()` function. In addition to running parallel factor analysis, `pftest()` was also executed. This test algorithm performs parallel factor analysis for a different number of factors. The function analyses the data in triplicate and outputs the residual sum of squares, core consistency values and the number of iterations needed to achieve the fit. This test function was used to trial different numbers of factors in order to determine which performed the best.

3.2.5 Fluorescence lifetime measurements

UV & visible excitation wavelengths

A DeltaFlex (HORIBA Jobin Yvon IBH, Glasgow) spectrometer was used to record lifetime decays via TCSPC. A 375 nm DeltaDiode (HORIBA Scientific) laser diode, with a 8 MHz repetition rate and $<$ 50 ps pulse width, was used to excite the melanin samples. The detector was a PMT (model – TBX-850c). The emission monochromator was set to 450 nm with a bandpass of 32 nm. The time range was 100 ns, and the measurement was run until a peak count of 10,000 counts was reached. The cysteine concentration sweep samples were run until 40,000 peak counts were reached. This was due to the higher proportion of short lifetime components. Increasing the peak count allows for more counts in the longer components which would improve the fitting. In order to measure the IRF, a dilute sample of LUDOX® was used. The emission polariser was set to the magic angle (55^o) with respect to the excitation polariser. Samples were in 4 ml UV grade clear walled cuvettes (Fisher Scientific).

NIR excitation wavelengths

Lifetime TCSPC measurements of melanin in the NIR were conducted at IBH (Glasgow) using a DeltaFlex spectrometer (HORIBA Scientific, Jobin Yvon, IBH, Glasgow). A 780 nm DeltaDiode (HORIBA Scientific) laser diode, with a max 50 MHz repetition rate and < 50 ps pulse width, was used to excite the melanin samples. The detector was a Picosecond Photon Detection (PPD), fast rise time photomultiplier (model – PPD900). The TBX-850 has an upper detection limit of 850 nm while the PPD900 has an upper detection limit of 900 nm. The emission monochromator was set to 860 nm, and the bandpass was 18 nm. The time range was 20 ns and measurements were run until a few 1000 peak count. This was because the measured signal was very low with the stop rate (the number of fluorescence photons detected) being in the single figure range.

Time-resolved emission spectra (TRES) measurements used the same settings as for single lifetime decay measurements. The emission range was from 810 nm to 900 nm, in 5 nm increments. Each decay was measured for 4 mins before moving to the next emission wavelength.

Along with TRES, the steady-state emission spectrum was measured with the same instrument. In this case, the instrument would count the number of fluorescence photons detected, within a set time, for each emission wavelength. Exciting at 780 nm, the emission monochromator scanned wavelengths from 810 nm to 920 nm in 1 nm increments. The time interval between each measurement was 3 secs.

3.3 Absorption Sensing

The most commonly known feature of melanin is its absorption spectrum which decreases from the UV to the NIR. An early observation of melanin's absorption spectrum was the presence of isosbestic points (a wavelength where the absorption value remains constant during a chemical reaction). Figure 3.3 shows the change in melanin's absorption spectra, over time, as L-DOPA reacts into eumelanin (Figure 3.3(a)) or pheomelanin (Figure 3.3(b)). The isosbestic points can be seen in both plots but are clearer in Figure 3.3(b). The isosbestic points are located at 213 nm, 240 nm, 290 nm, 325 nm and possibly 450 nm as well. These points agree well with the positions reported by Sutter and Birch. [72]

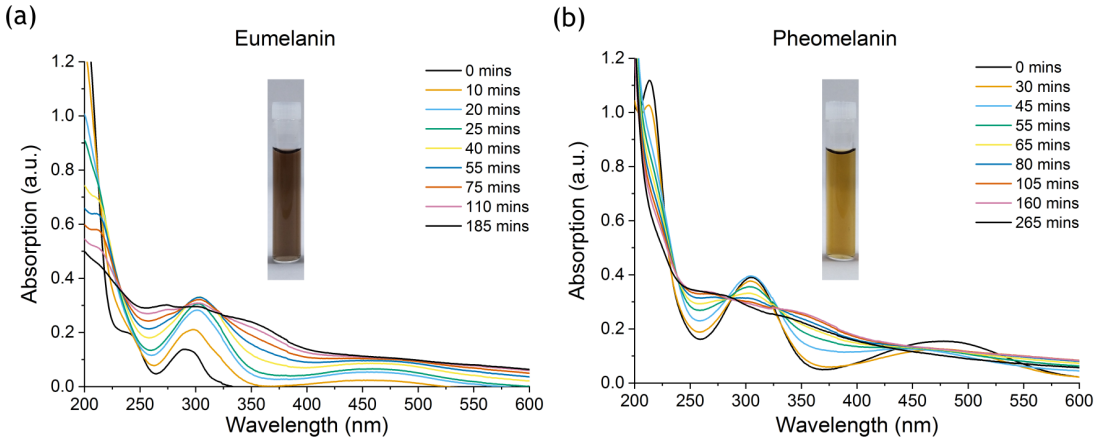

Figure 3.3: Time-series data showing the development of (a) eumelanin and (b) pheomelanin absorption over time. Isosbestic points can be identified at 240 nm, 290 nm, 325 nm and 450 nm which indicate the presence of distinct molecular species. Inserted into the plots are the photographs of the samples of eumelanin and pheomelanin after the measurement was concluded.

While similarly positioned isosbestic points are visible in both sub-plots of Figure 3.3, the kinetics are different for each melanin. The sample of eumelanin was formed from L-DOPA in an alkaline solution of ammonia (pH 10 – 10.5). The copper-containing enzyme tyrosinase was used to react L-DOPA and L-Cysteine into pheomelanin. This is interesting as the evolution of the absorption spectrum bare similarity to the findings of Sutter and Birch [72]. Their eumelanin sample (L-DOPA in pH 10 water) follows the trend of Figure 3.3(a) while their copper containing eumelanin sample (L-DOPA with $CuSO_4$) follows the trend seen in Figure 3.3(b). This may suggest that copper ions are important to the process of pheomelanin generation.

The appearance of isosbestic points suggests n + 1 number of molecular species, where n is the number of isosbestic points. This would imply that melanin has five or six discrete species present which leads to some interesting possibilities regarding the structure/spectroscopic relationship. While evidence linking these isosbestic points to the structure of melanin is sparse, a possible explanation may associate the spectral species to the larger structural forms of melanin described by Büngeler et al. [27] However, 3.3(b) shows the isosbestic points are present throughout the melanogenesis process so it is more likely that the isosbestic points are related to the oligomeric units that are formed during the initial stages of melanogenesis, like

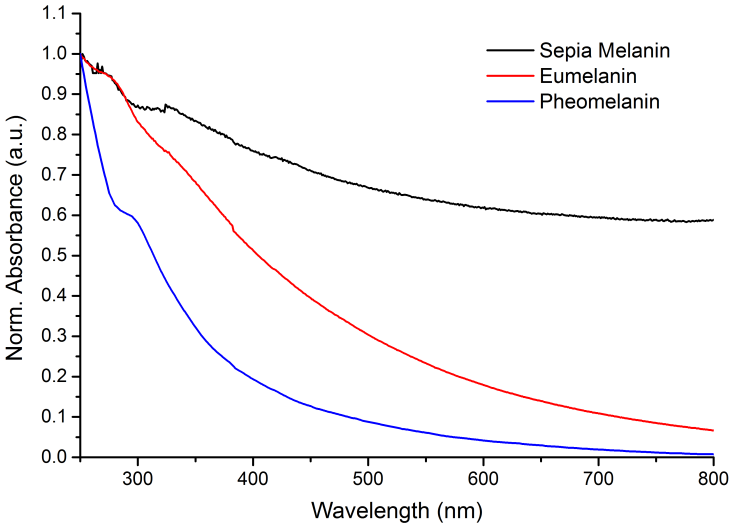

Figure 3.4: Normalised absorption of natural melanin with synthetic melanin which shows the different distribution of absorbers, with Sepia melanin having more red and NIR absorbers than the synthetic varieties.

the tetrameric model proposed by Kaxiras et al. [30] or the stacked oligomeric systems reported by Chen et al. [32]

There is evidence that the indole and benzothiazole structures that make up melanins have multiple absorption peaks and fluorescence lifetime components as a result of rotamers and energy transference processes. [22,62,73,74] This could mean that the main features of melanin's absorption spectrum are due to the photophysics of the smaller indole and benzothiazole/zine structures while the larger structural forms of melanin serve to homogenise the spectrum, so it is most effective at absorbing across a large number of wavelengths.

Looking at the end product absorption spectra Figure 3.4, there are clear differences between the two pigments of melanin. Pheomelanin has a greater response in the UV than the visible and NIR while eumelanin has a higher OD value across the whole spectrum. Comparing the synthetic melanin spectra to natural eumelanin from *Sepia Officinalis* show how the natural pigment has far greater absorption over the spectrum. This is likely due to the better regulation of the melanogenesis process in the natural system since the tyrosinase-related proteins (TRP1 & TRP2) will be better able to control the formation of chemical structures which absorb over the whole spectrum. [8,75]

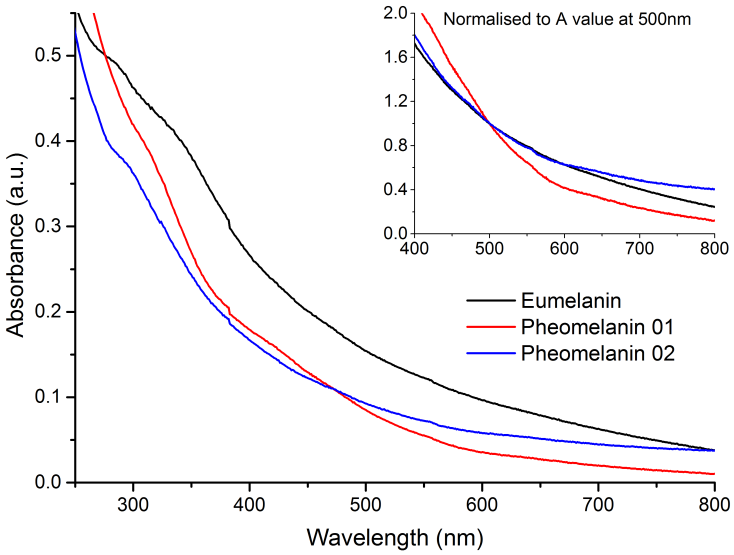

Figure 3.5: Absorption spectra for eumelanin and two samples of pheomelanin, made with the same protocol. Insert, the spectra are normalised to the absorption value at 500 nm wavelength, based on the work by Ozeki et al. [75]

The differences in absorption, between eumelanin and pheomelanin, are clear and easy to measure. This prompted Ozeki et al. [75] to develop a way for distinguishing between the two pigments via simply calculating the ratio of the OD values at 650 nm and 500 nm. Unfortunately, this method for identifying pigments of melanin is not reliable.

Figure 3.5 shows the absorption spectra for one sample of eumelanin and two samples of pheomelanin. The samples of pheomelanin were synthesised at the same time and under the same conditions, yet the final absorption spectra are slightly different. Both pheomelanin absorption spectra have lower absorption values than the eumelanin sample, and the solutions were consistent with the red/yellow colouration that is common for pheomelanin. When normalised to the OD value at 500 nm (insert of Figure 3.5) the absorption value for eumelanin, at 650 nm, is less than that for the second pheomelanin sample. As a result, the ratio of the 650 nm to 500 nm OD values cannot be used to identify eumelanin from pheomelanin since the pheomelanin values can be both higher or lower than eumelanin. While a simple method which takes advantage of melanin's main spectroscopic feature, the variation in the final spectrum obtained renders this simple protocol unsuitable for distinguishing melanins.

3.4 Fluorescence Sensing

3.4.1 Corrected excitation-emission matrices

From the paper of Riesz et al. [76] it is known that the emission data of melanin needs to be corrected based on the absorption coefficient value at that wavelength. Figure 3.6(a) and (b) shows the absorption spectra for eumelanin and pheomelanin along with the absorption coefficient for each pigment, as calculated from Equation 3.8.

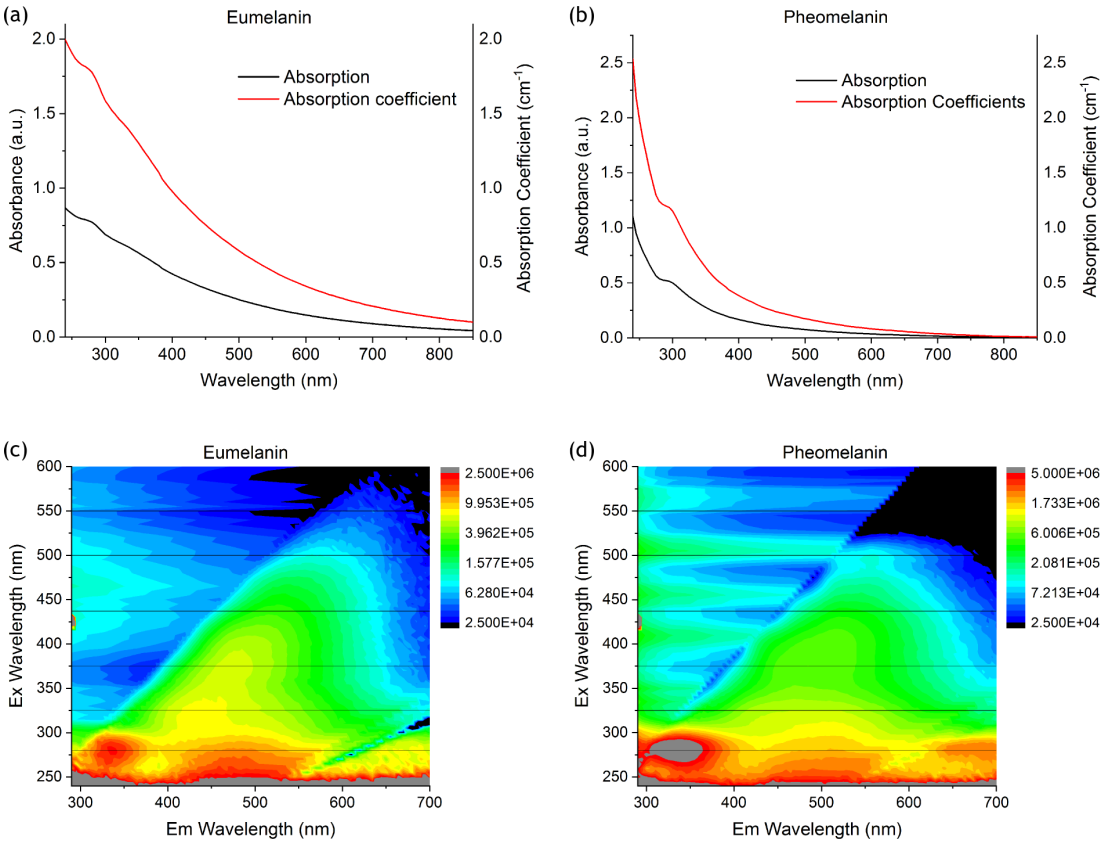

Figure 3.6: Absorption and absorption coefficient spectra of (a) eumelanin and (b) pheomelanin. The absorption coefficient values were used to correct the EEM data. Corrected EEM contour plots for (c) eumelanin and (d) pheomelanin. The horizontal lines show which emission spectra are compared in Figure 3.7.

The EEM data of Figure 3.6(c) and (d) show melanin's broad fluorescence signal which extends over a large range of emission wavelengths and produces a fluorescence signal when excited with wavelengths up to 500 nm, before approaching the level of the background. Both responses are similar but have some slight differences about them.

Mirroring the absorption spectra, the contour plots do not feature discrete emission peaks, with exception to the peak at coordinates 280 nm by 340 nm. Both plots share an intense feature around the coordinate 250 nm by 500 nm which appears to extend out to higher excitation wavelengths. Eumelanin contains additional features around the coordinate 325 nm by 440 nm and the 375 nm by 475 nm region which pheomelanin shows less prominently. Given the small circular nature of these features, it is possible that they are the response of discrete fluorescence species. Eumelanin's response also extends further into the red corner of the contour plot which is due to the greater absorbance of eumelanin at these excitation wavelengths.

In order to quantify whether there are differences within the EEM contour plots, select excitation wavelengths were chosen, and the fluorescence spectra are compared in Figure 3.7. The melanins share a close similarity in the shape and position of their emission peaks, but the spectra are not exact. When exciting at 280 nm, the pheomelanin response at 500 nm is significantly less than eumelanin. Both pigments absorb strongly in the UV which suggests that the quenching dynamics of pheomelanin are more prevalent than eumelanin.

For excitation wavelengths 325 nm, 375 nm and 437 nm the pheomelanin response extends further into the red part of the spectrum, with 437 nm showing the least amount of change. This difference is reversed when excited at 500 nm as eumelanin fluoresces further into the red part of the spectrum. Exciting at 550 nm produces little difference between the two pigments and have a high S/N ratio plus the high thermal noise at 700 nm – 800 nm makes distinguishing the emission peaks more challenging. Utilising simple normalisation techniques will be prone to the variation within the melanin samples. However, there is more information contained within the three-dimensional EEM datasets that may contain more subtle differences which multivariant analysis may reveal.

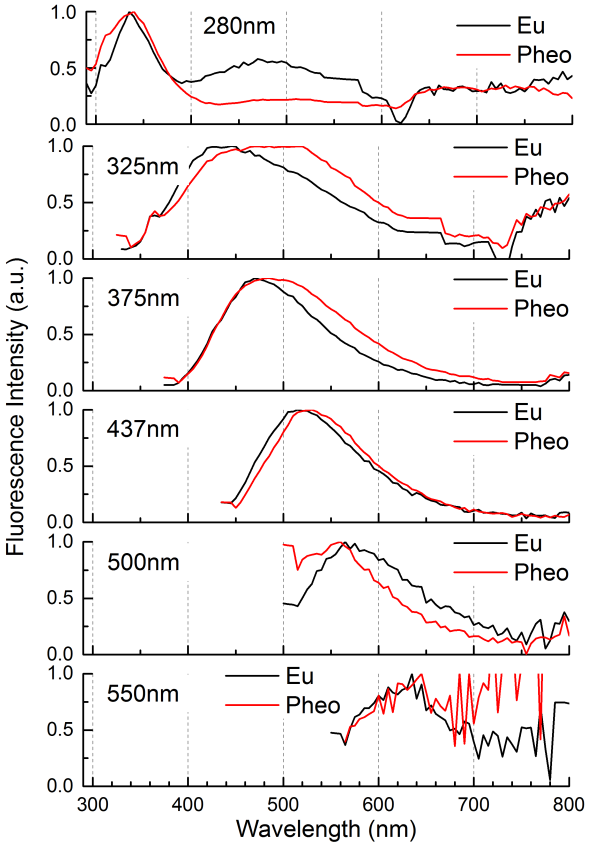

Figure 3.7: Fluorescence slices of EEM contour plots (Figure 3.6) in order to find differences within the broad emission region of melanins. The plots are normalised to the emission peak maximum for better clarity of the spectral differences.

3.4.2 Multivariate analysis of eumelanin & pheomelanin EEM data

The fluorescence emission spectra for melanins is likely to be from the contributions of multiple fluorescent species. The spectral peaks of these fluorophores will be altered by the formation of larger structures and the various energy transfer process like static quenching, ESPT and ESIPT. [22,62,77] From Figures 3.5 & 3.7 it is clear that a more sophisticated analysis method is needed in order to extract underlying spectral differences and accurately measure the ratio of eumelanin and pheomelanin from the EEM data.

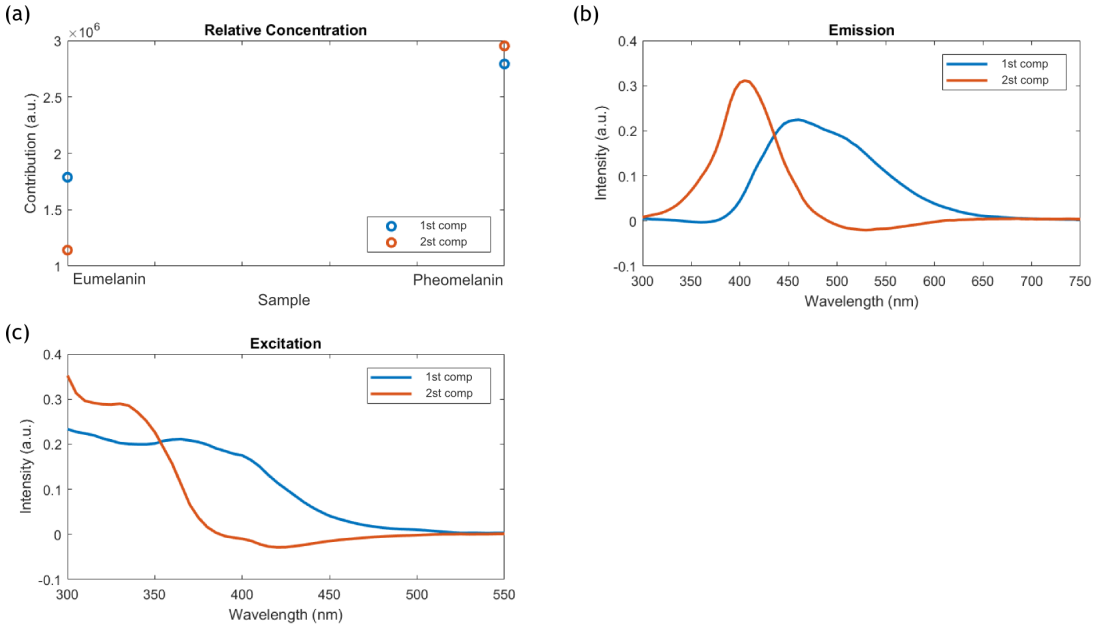

Figure 3.8: Graphical outputs from analysing the EEM datasets of Figure 3.6(c) and (d) with PARAFAC analysis. Two factors were used to fit the data. (a) Shows the relative concentration of each component identified. The (b) emission spectra and the (c) excitation spectra of the identified components.

PARAFAC analysis was used with the EEM data in order to reduce the dimensionality of the data and investigate the underlying spectral features of melanin's fluorescence. Figure 3.8 shows the outputs of the PARAFAC algorithm, when set to identify two factors. Using three factors (Figure 3.9) did not produce rational outcomes with negative relative concentration values. Running the algorithm up to five factors did not improve the outcomes. Figure 3.10 shows how the parameters: residual sum of squares, core consistency and number of iterations change with the number of factors used by the PARAFAC algorithm. An appropriate number of factors yields low residuals, high core consistency and repeatedly low number of iterations.

Two factors produce a higher residual value than three factors. However, two factors are more stable as increasing the number of factors also increases the number of iterations values. For the EEM data used in Figure 3.6, both the realistic outputs and the fitting metrics agree that two factors are sufficient to describe the EEM data.

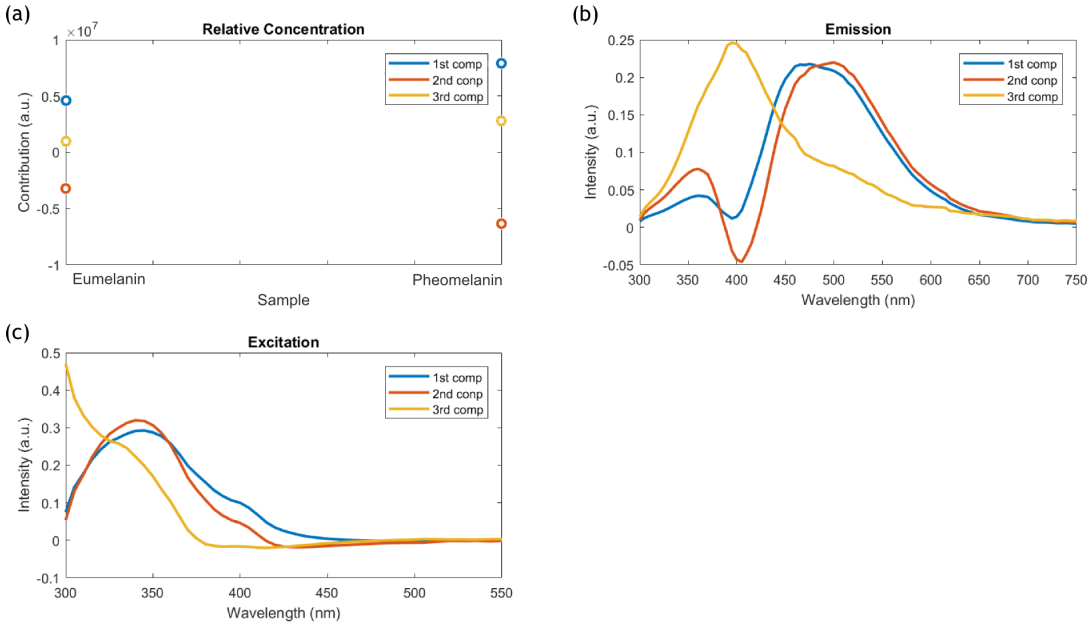

Figure 3.9: The PARAFAC analysis outputs of the same EEM data as was used for Figure 3.8. The number of factors the algorithm fitted to was increased to 3.

When performing PARAFAC analysis on melanin EEM data, it was expected that a high number of components would be needed in order to represent the multiple fluorescence species making up the complex emission profile. However, based on the results of Figure 3.8-3.10 it appears the algorithm has identified two fundamental components of the melanin fluorescence. In this context, the spectra produced in Figure 3.8 are not distinct fluorophores but rather the algorithm identifying the fundamental spectrums which describe the EEM data. Importantly, there is a distinct difference between the relative amplitude values for eumelanin when compared to pheomelanin.

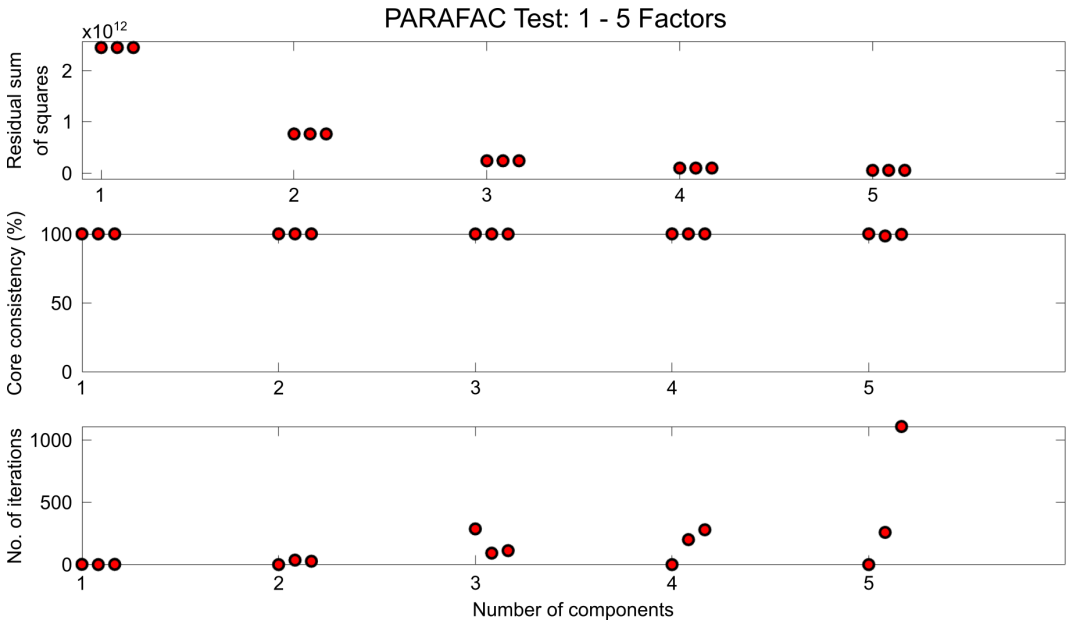

Figure 3.10: Output from PARAFAC test algorithm, which performs the PARAFAC analysis multiple times, with a different number of components, and reports the residual sum of squares, core consistency and number of iterations.

3.4.3 PARAFAC analysis on cysteine concentration sweep EEMs

The differences in relative concentration seen in Figure 3.8(a) prompted further investigation. The study was extended to a range of melanin samples where the concentration of cysteine was altered. Increasing the concentration of cysteine promotes greater pheomelanin production with maximum pheomelanin production being reached with equal concentrations of L-DOPA and L-Cysteine. Figure 3.11(a) shows the absorption spectra for melanin samples made with different concentrations of cysteine. The OD values at 500 nm have been plotted separately in Figure 3.11(b), following the methodology of Ozeki et al. [75] and illustrate the change from eumelanin to pheomelanin production once the concentration of cysteine reaches equilibrium with the concentration of L-DOPA.

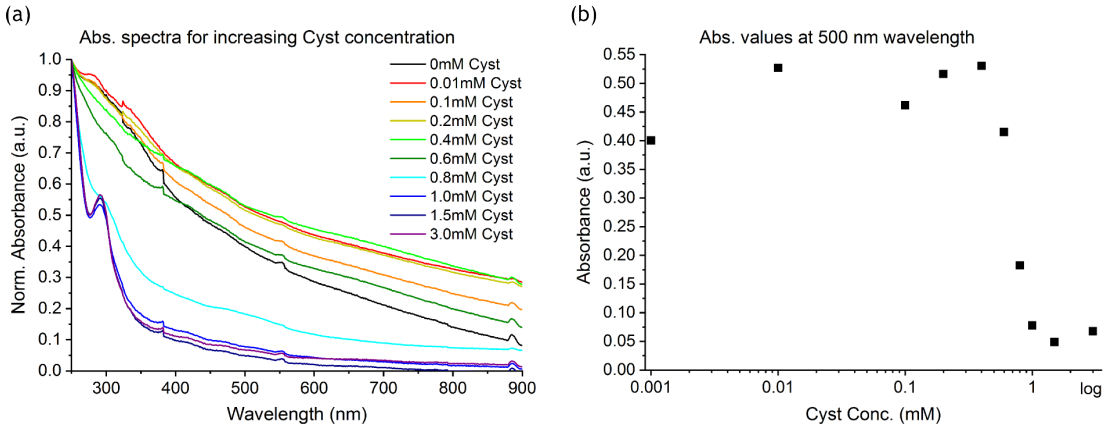

Figure 3.11: (a) Normalised (to the absorption value at 250 nm) absorption plot of melanin samples with different concentrations of cysteine. (b) The absorption values at 500 nm wavelength which shows that pheomelanin production dominates when the cysteine concentration is greater than 0.6 mM. This is in agreement with the work by Ozeki et al. [75]

The melanin samples measured for Figure 3.11 were then measured via fluorescence spectroscopy to produce EEM datasets that could be analysed by PARAFAC analysis. The outcomes of which to be compared with the trend in Figure 3.11(b) to assess whether the PARAFAC results are consistent with a change from eumelanin to pheomelanin. In order to analyse the EEM data with PARAFAC analysis, not only does the EEM data need to be corrected for the absorption profile (as was done in Section 3.4.1) but the Rayleigh and water Raman lines have to be removed as to not interfere in the analysis. Processing the EEM data for analysis was done with the MATLAB code contained in Appendix A, and the outputs are grouped as surface plots in Figure 3.12.

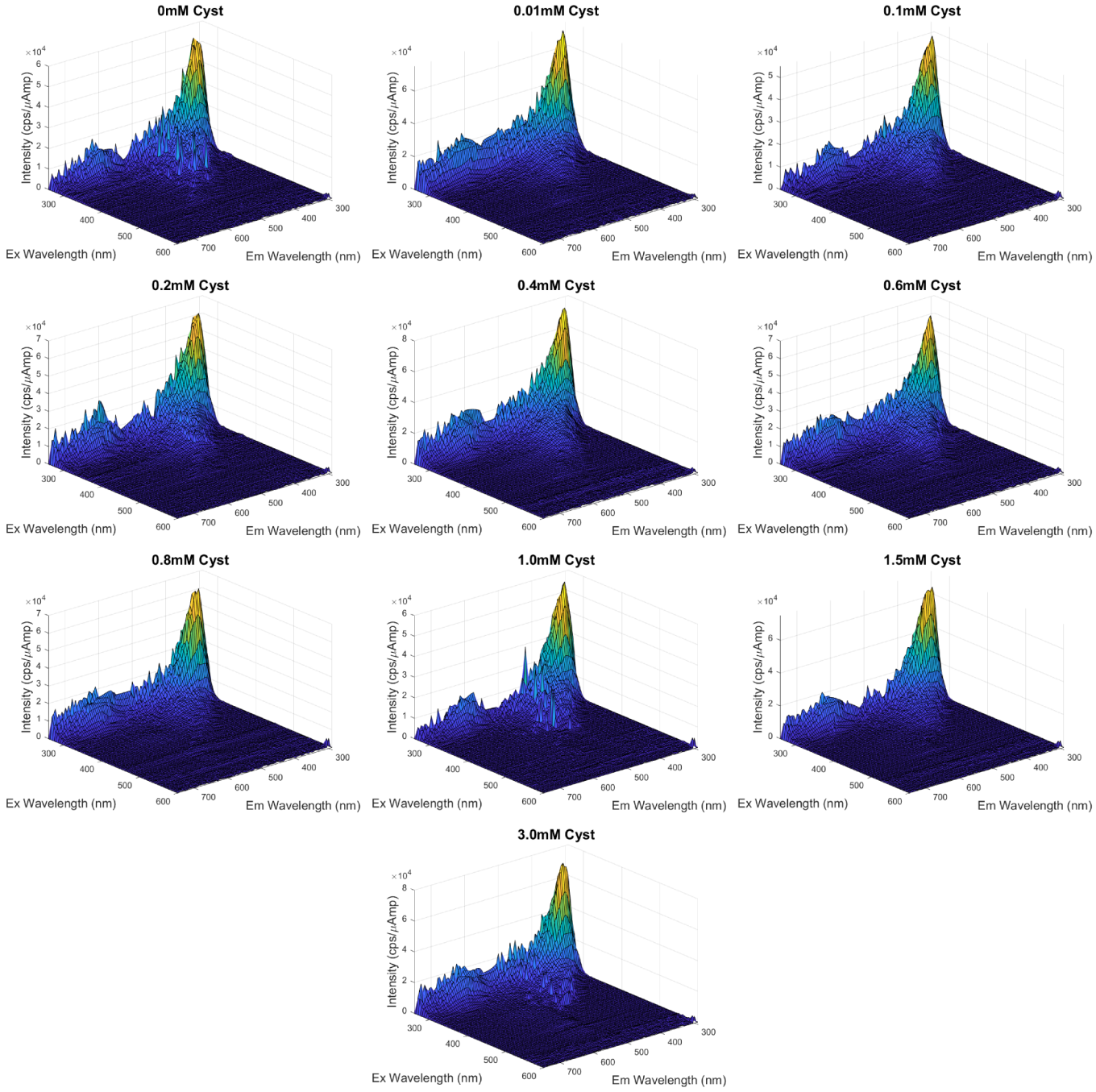

Figure 3.12: Corrected EEM data for melanin samples with a different concentration of cysteine. Rayleigh and Raman lines have been removed. However, some of the EEMs still contain some signal spikes that may have resulted from particulates passing through the excitation beam.

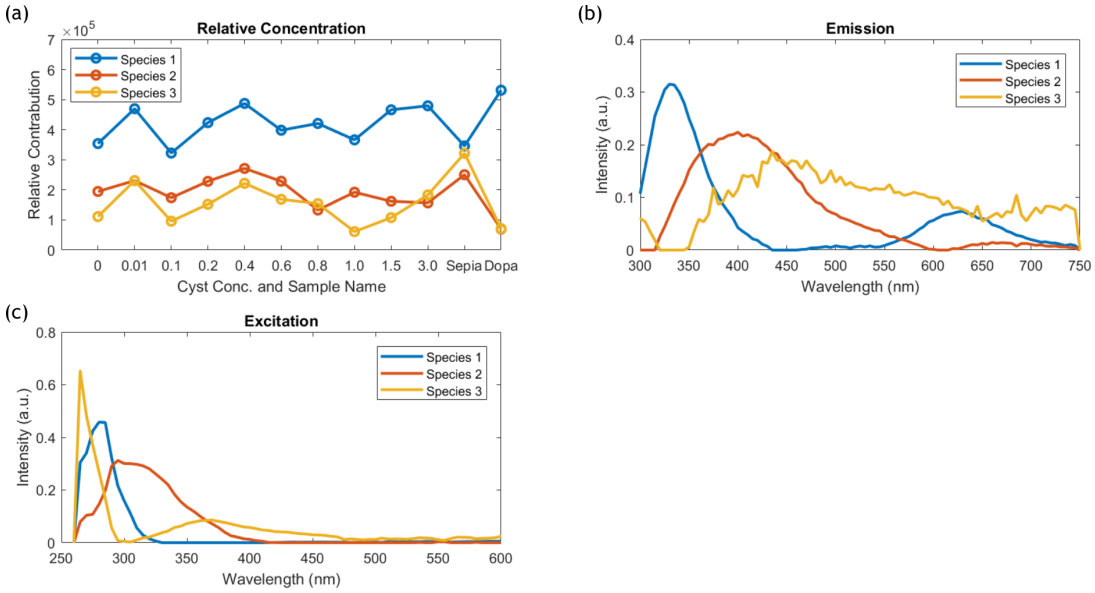

Figure 3.13: Results from PARAFAC analysis of the data of Figure 3.12, with three factors. Included for analysis were the EEM datasets for sepia melanin and DOPA-eumelanin, made without the enzyme. The relative concentration (a) does not significantly change from 0 mM cysteine to 3 mM cysteine while sepia and DOPA eumelanin do change. The component emission (b) and excitation (c) spectra are plotted.

While the removal of the scatter lines was achieved, the EEM data contains a couple of features that may interfere with the PARAFAC analysis. First is the high response along the 250 nm excitation line. The signal here will contain melanin fluorescence, but there will also be a response from the second order fluorescence signal. Secondly, the EEMs for cysteine concentrations 0 mM, 1 mM and 3 mM have noticeable signal spikes present which is suspected to be due to particulates within the solution.

While care is taken to prevent contamination, there is the chance that some will be present during measurement. Given the long acquisition time for each data point (1 sec), it is likely that strongly scattering particulates can pass through the beam path and contribute significantly to the photon counts. By the time the next data point is measured, the scattering particle has passed through the beam. While undesirable, the effect of these signal spikes is negligible and do not appear in the PARAFAC results.

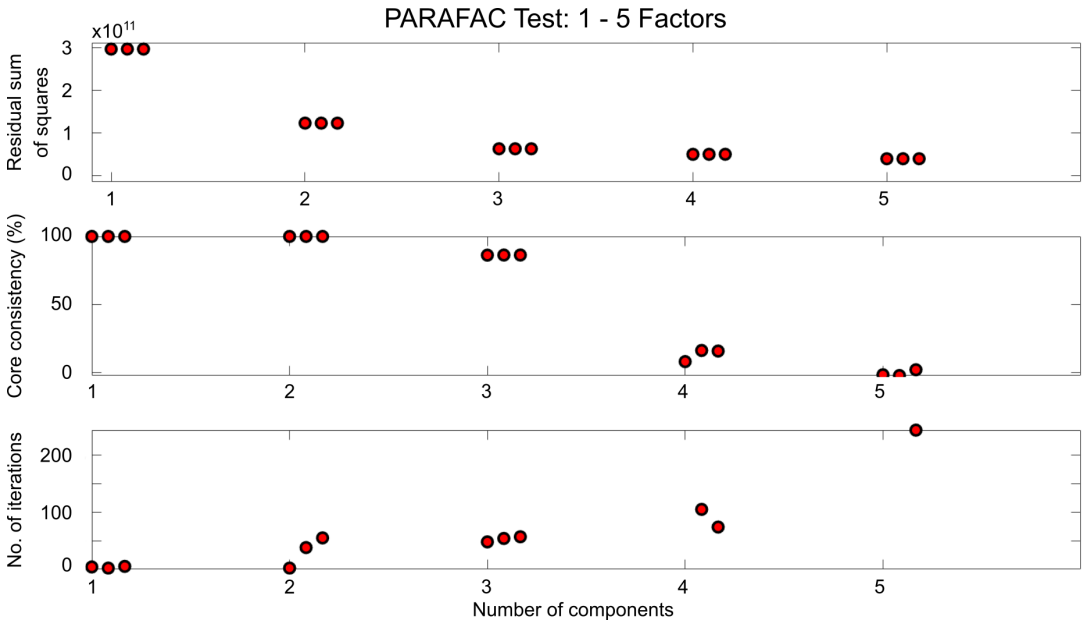

Figure 3.14: A test of the PARAFAC algorithm with 1 to 5 factors. Three factors has the lowest residual sum of squares and number of iterations while having the highest core consistency.

The analysis of the EEM data from Figure 3.12 is contained in Figure 3.13 and was analysed using three factors. The third component is attributed to the response along the 250 nm excitation line, given the short wavelength peak of the excitation spectra and the noisy, broad, spectrum in the emission plot. Species 1 would be a good match for the main emission peak at 280 nm x 325 nm since the second order fluorescence signal is present at 650 nm Figure 3.12(b). The rest of the spectral information seems to be represented by the second component which has an excitation peak at 300 nm and an emission peak at 400 nm.

Looking at the relative contribution plot Figure 3.12(a), there is no significant change as the concentration of cysteine is altered. No systematic change occurs like what was observed in the absorption spectra of Figure 3.11. While the algorithm was able to uncover realistic spectral data from the EEMs of Figure 3.12, the spectral components do not facilitate the measurement of the ratio of eumelanin and pheomelanin.

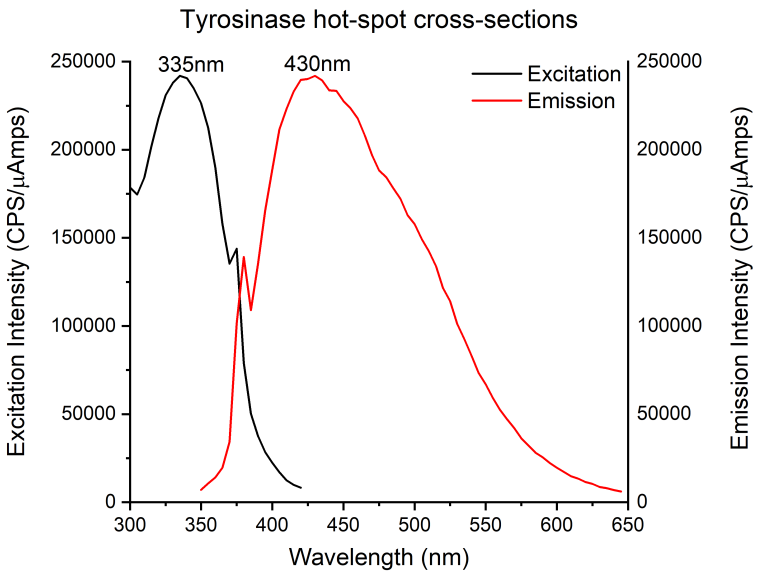

Figure 3.15: The spectral cross-sections from the EEM of dilute tyrosinase. The excitation spectrum was along the peak emission line of 430 nm while the emission spectrum was along the peak excitation line of 335 nm. The spectral peaks and profile of the spectra are similar to species 2 in Figure 3.13(b) and (c).

Included with the analysis are the PARAFAC results from samples of Sepia melanin and DOPA melanin. The DOPA melanin used the same conditions as the 0 mM sample but did not use the tyrosinase enzyme to catalyse the melanogenesis. This has resulted in different relative concentration values for DOPA melanin when compared to the 0 mM sample values. The first component value for DOPA melanin is higher while the second and third component values are lower. This suggests that either the tyrosinase intrinsic fluorescence is significant or that DOPA melanin has a greater distribution of emitters which fluoresce in the same region. In contrast, the relative concentration values for Sepia melanin are more equal to each other than the other samples. This would match with the absorption spectra for Sepia melanin seen in Figure 3.4 since there is a more even distribution of UV, visible and NIR absorbers.

Running the test algorithm, plotted in Figure 3.14, shows that three components are the best model. The residuals are lower than one and two components, and three components have a lower number of iterations than four and five components. The number of iterations is also consistent across the triplicate analysis while four and five components have different values. The core consistency is a bit lower than two components but is much higher than four and five.

As mentioned, PARAFAC analysis aims to determine fundamental features that may help distinguish eumelanin and pheomelanin. It is not expected for the algorithm to uncover the true spectra of the fluorophores within melanin. However, comparing the spectra for species 2 (Figure 3.13) with the spectra of tyrosinase (Figure 3.15) the spectral peaks are a close match, and the emission spectra are similar in profile. This would explain how the relative amplitude values do not show a systematic change with cysteine concentration and only change significantly with the DOPA-eumelanin sample, which does not have any tyrosinase present.

The three-dimensional EEM data of melanin samples was successfully decomposed by the multi-variant method of PARAFAC analysis. The algorithm consistently performed best with two or three factors suggesting that the fluorescence emission properties of melanin can be described by a limited number of discrete spectra. Comparison of eumelanin and pheomelanin with PARAFAC analysis did result in different relative concentration values which opens up possible avenues for utilising PARAFAC analysis for melanoma sensing. However, a deeper investigation involving melanin samples with different concentrations of L-Cysteine did not produce a quantifiable difference when analysed with parallel factor analysis. The interference from the enzyme tyrosinase has been attributed to the lack of significant variation in the relative amplitude values. Future studies should aim to quantify the tyrosinase fluorescence or attempt removal of the enzyme before measurements are taken. It would also be interesting to observe the outcomes of PARAFAC analysis when melanins are exposed to different pH solutions, metal ions, temperatures and the changes observed during the melanogenesis.

3.5 Time-Resolved Fluorescence Sensing

Similar to the absorption spectrum, the emission spectrum of melanins do not show a clear structure. Despite utilising algorithms to pick apart the spectral data, no clear distinction was found between eumelanin and pheomelanin. Fluorescence lifetimes have previously allowed for the identification of spectrally overlapping fluorophores and offered another spectroscopic avenue for investigation.

3.5.1 Cysteine concentration sweep

The challenge with measuring melanin fluorescence lifetimes is deciding which part of the spectrum to focus on. Currently, there is no rapid, multiplexed TCSPC system capable of recording multiple lifetime decays at the same time. Recent developments in single photon avalanche diodes (SPAD) arrays has brought these capabilities closer to realisation [78, 79], and it is expected that this technology will have a great impact on melanin research.

Until such time, conventional systems have been used to investigate the lifetime components of melanin. The low quantum yield of melanin means TCSPC measurements take more time to complete than conventional fluorescence dyes. With no restriction of what wavelengths to choose, it was decided that lifetimes should focus on a central point of the melanin EEM. Additionally, it is preferable to use the DeltaDiode laser light source since it has a high laser power and a fast repetition rate. For these reasons, the 375 nm DeltaDiode was used to excite the melanin samples and the emission would be measured at 450 nm.

Comparing melanin fluorescence decays with 0 mM, and 1.5 mM Cysteine does show a change in the shape of the decay. The eumelanin sample (0 mM cysteine) has a high contribution from a short component that is not as prominent in the pheomelanin (1.5 mM cysteine) sample. The longer time components appear to be greater for eumelanin which is confirmed in the fitted parameters of Table 3.1.

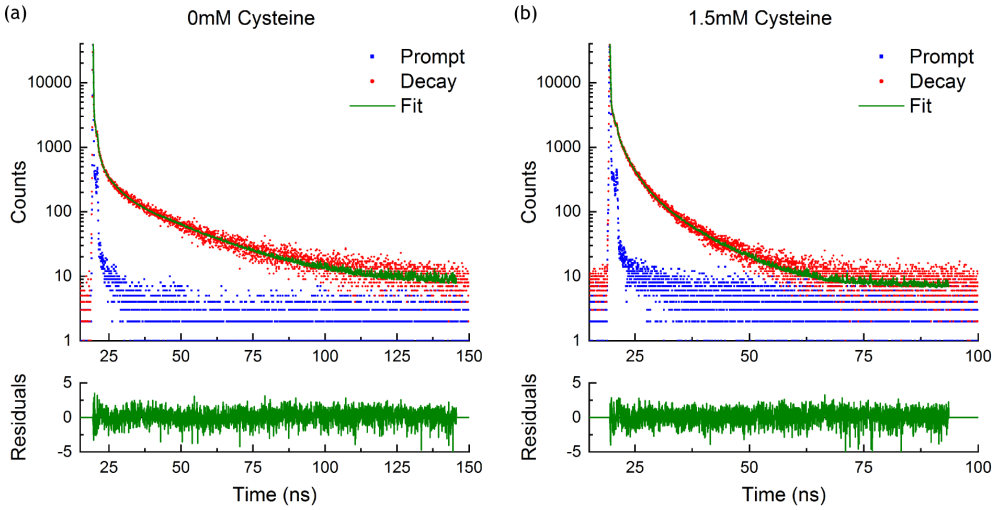

Figure 3.16: Lifetime decays for melanin samples with (a) 0mM L-Cysteine, to form eumelanin and (b) 1.5 mM L-Cysteine, to form pheomelanin. Excitation was at 374 nm, and the emission was measured at 450 nm.

Cyst. Conc.	0	0.005	0.025	0.1	0.4	1.5
τ_1 (ns)	0.03	0.05	0.06	0.05	0.07	0.03
τ_2 (ns)	0.83	0.80	1.00	1.14	1.05	0.60
τ_3 (ns)	4.23	3.78	4.84	6.09	4.76	2.37
τ_4 (ns)	22.21	21.90	26.88	29.48	23.34	8.69
B_1 (%)	72.45	59.34	67.38	69.56	41.14	57.05
B_2 (%)	7.86	10.17	10.33	10.04	24.18	9.13
B_3 (%)	6.50	14.11	12.21	10.75	15.88	20.79
B_4 (%)	13.20	14.37	10.08	9.65	18.80	13.03
χ^2	1.14	1.23	1.35	1.40	1.20	1.18

Table 3.1: Table of fitted values when a four-exponential model was fitted to the fluorescence decays of melanins with different concentrations of L-Cysteine.

Looking at the time components, the short components do not change significantly with τ_1 staying around 50 ps and τ_2 remaining near 0.9 ns. The value of τ_3 rises from 4.23 ns to 6.09 ns as the concentration increases from 0 mM to 0.1 mM. At higher concentrations, τ_3 decreases to 2.37 ns at 1.5 mM. This trend is present for τ_4 with the lifetime values changing from 22.21 ns to 29.48 ns when the concentration is increased from 0 mM to 0.1 mM, before decreasing to 8.69 ns at 1.5 mM cysteine concentration.

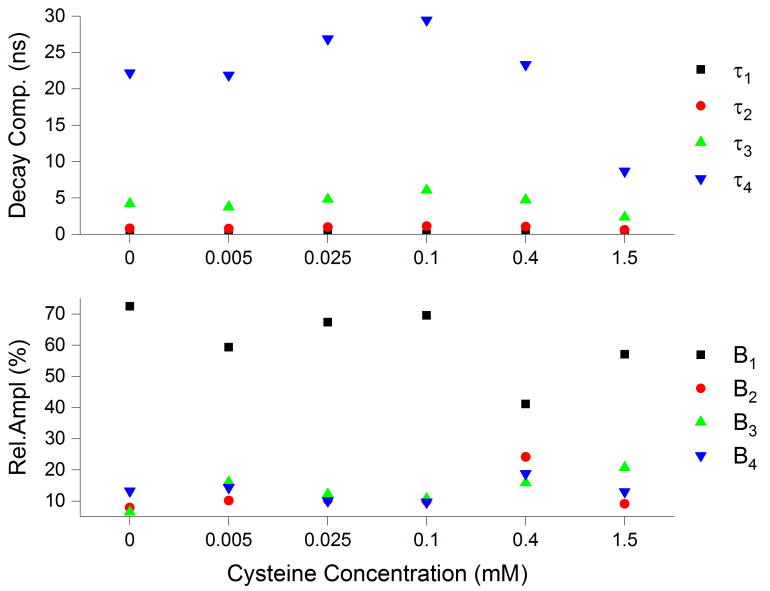

Figure 3.17: Plot of time components values and B values from Table 3.1. The values for τ_4 follow the trend observed for the absorption spectra of Figure 3.11.

With an increase in cysteine concentration, the decay component value for τ_4 increases before decreasing after 0.1 mM of cysteine. Similar to the absorption data of 3.11 the decrease in the time component value only occurs at higher cysteine concentration values. From the data of Figure 3.16, it would seem that time-correlated single photon counting (TCSPC) is capable of distinguishing between eumelanin and pheomelanin, opening opportunities for the development of non-invasive melanoma point of care (POC) devices that would satisfy the design points outlined in Chapter 1. However, further testing would be needed to test the robustness of this technique before proceeding to *in vitro* testing.

While the data of Figure 3.16 is encouraging, there are some points worth raising which reduce the confidence of this result. The decays of Figure 3.16 have a high contribution from a very short time component ($\sim$ 50 ps). This is likely the combination of scattering off larger melanin structures and the reduction in lifetime as larger melanin structures are made. [62] Regardless of their origins, the dominance of these shorter components complicates fitting as they reduce the total number of counts of the longer time components. It is for this reason that these measurements were run to 40,000 peak counts, as opposed to the more conventional 10,000 peak counts.

Fitting to a four-exponential model gave the best χ^2 values, while still producing realistic parameter values. However, the χ^2 values for L-Cysteine concentrations of 0.005 mM, 0.025 mM and 0.1 mM are above 1.2 which indicate that the algorithm is underfitting the data. This may be the result of increased heterogeneity as some of the L-DOPA will have propagated down the pheomelanogenesis pathway. It is also possible that multi-exponential models are not suited to fitting melanin's complex fluorescence decays. For this reason, different methods for analysing fluorescence lifetime decays were investigated including multi-exponentials, the general relaxation function and maximum entropy method.

3.5.2 Applying different fitting algorithms

Fitting to a multi-exponential function does not always lead to a good fit. Both the residuals and the χ^2 value are used to quantify the quality of the fit. The question of which model accurately describes melanin has not been answered as most papers, looking into melanin's fluorescence lifetimes, only use multi-exponential models. Different models for describing fluorescence decays are fitted to decays of eumelanin and pheomelanin in order to assess which model best describes melanin's fluorescence decays. To begin, the multi-exponential model fitted using the DAS 6.2 (Horiba Scientific) software was tried. The decays were measured by exciting the samples at 375 nm and measuring the fluorescence decay at 440 nm.

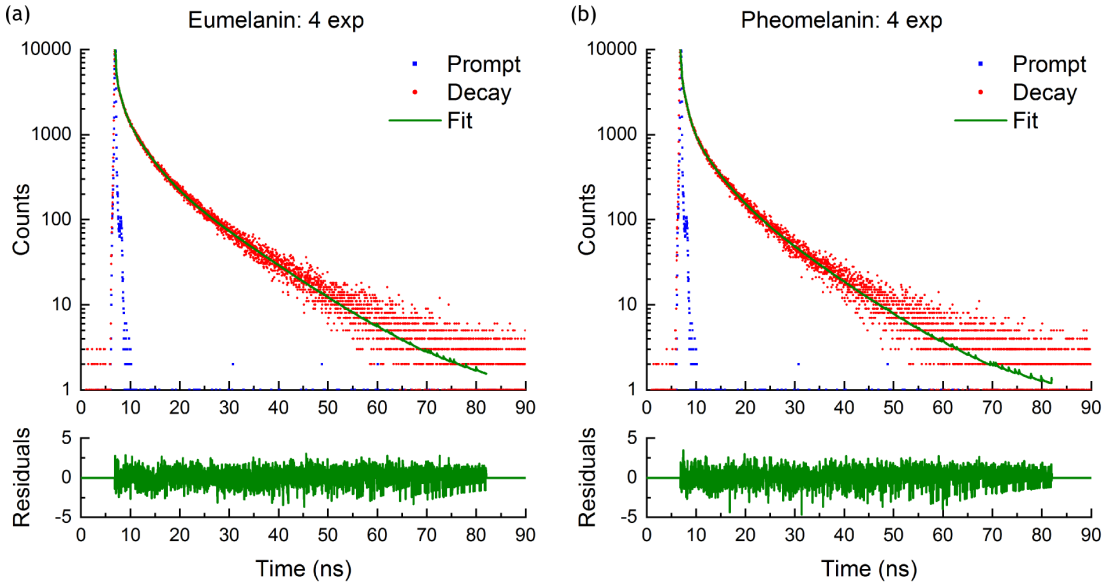

Figure 3.18: Fluorescence decays of (a) eumelanin and (b) pheomelanin fitted to a four-exponential model using the DAS software. The χ^2 values were (a) 1.05 for eumelanin and (b) 1.09 for pheomelanin

Multi-exponentials

Fitting to a four exponential model, the fittings are acceptable as the χ^2 values are near 1 and the residuals are randomly, and evenly, distributed about the zero line. It is interesting to note the difference between the decays of Figure 3.18 and those of Figure 3.16, as the latter has high contributions from a short ($\sim$ 50 ps) time component while the former has a more even contribution from each time component. This may reflect a more fundamental change in the melanin structure. Despite maintaining consistent synthesis conditions, some factors (including ambient temperatures, pH, reactant condition and agitation) could result in the differences observed between Figure 3.16 and 3.18.

Sample	Eu, 3 exp	Pheo, 3 exp	Eu, 4 exp	Pheo, 4 exp
τ_1 (ns)	0.28	0.26	0.13	0.15
τ_2 (ns)	2.55	1.91	0.87	0.92
τ_3 (ns)	9.94	8.78	3.50	3.78
τ_4 (ns)			10.99	10.73
B_1 (%)	37.34	48.41	13.26	17.13
B_2 (%)	32.78	27.26	16.47	26.60
B_3 (%)	29.88	24.33	37.48	30.90
B_4 (%)			32.97	25.37
χ^2	1.22	1.30	1.05	1.09

Table 3.2: Fitted parameters from using multi-exponential decay models on the fluorescence decays of Figure 3.18.

Given the differences that can occur between batches of melanin, the rest of this section uses the same decays of Figure 3.18 as to allow comparison of the fitting algorithms. This is necessary as each algorithm has numerous parameters which can be altered to improve fitting. For the case of DAS 6.2 the alteration made was to the number of exponentials used. While DAS 6.2 has the option to fix each fitted parameter, the parameters were left free floating to facilitate comparison between the different fitting models.

From the χ^2 values in Table 3.2, it is clear that four exponentials are needed to describe the decays due to the χ^2 values being closer to one. With a three-exponential model, the decay components obtained included one short component around 0.27 ns, another around 2 ns and a long component approaching 9 ns – 10 ns. The second and third decay components are different between eu- and pheo- melanin but the relative amplitude values show a greater change with the most significant being the 11% increase of B_1.

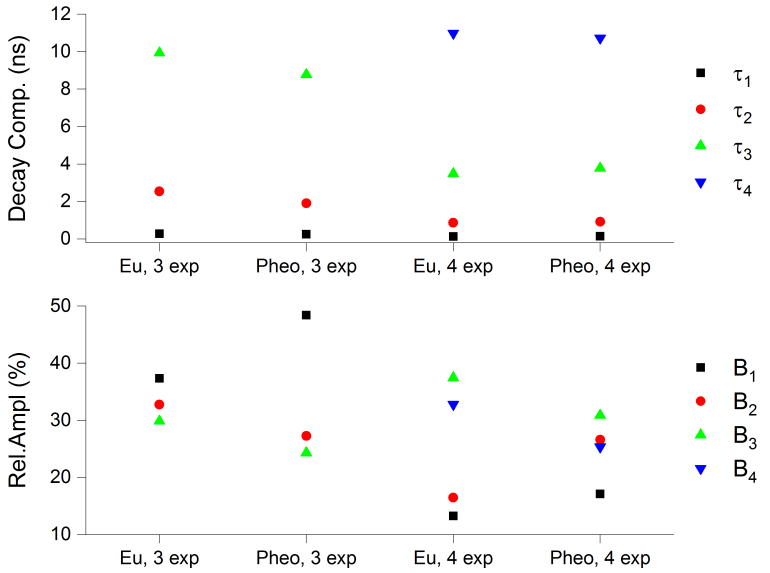

Figure 3.19: The fitted parameters values from fitting multi-exponential models to the decays of Figure 3.18.

Including an additional exponential to the fitting model has had the effect of splitting the $\sim$ 2 ns component (of the three-exponential fit) into a $\sim$ 0.9 ns and $\sim$ 3.5 ns component. With four components, the lifetime values show less variation between eu- and pheo- melanin. The majority of the changes occur with the relative amplitude values. Going from eumelanin to pheomelanin, the first and second components increase by $\sim 4\%$ and $\sim 10\%$ respectfully while the third and fourth components decrease by $\sim 7\%$ each. This implies that the fluorescent species producing the decays have similar lifetimes but exists at different concentration ratios. This is different from the values obtained in Figure 3.17 which showed a greater change in the lifetime values. When considering a fluorescence based technique for detecting melanoma, it could be possible to use the relative amplitude values rather than the decay component values.

General relaxation function

Instead of fitting to the multi-exponential function, the decays can be fitted to a more generalised form of the decay function. The general relaxation function Equation 3.3 was fitted following the approach used by Rolinski et al. [63, 80, 81]. Fitting the general relaxation function is more challenging when using double parameters so as an initial test, the single form was used.

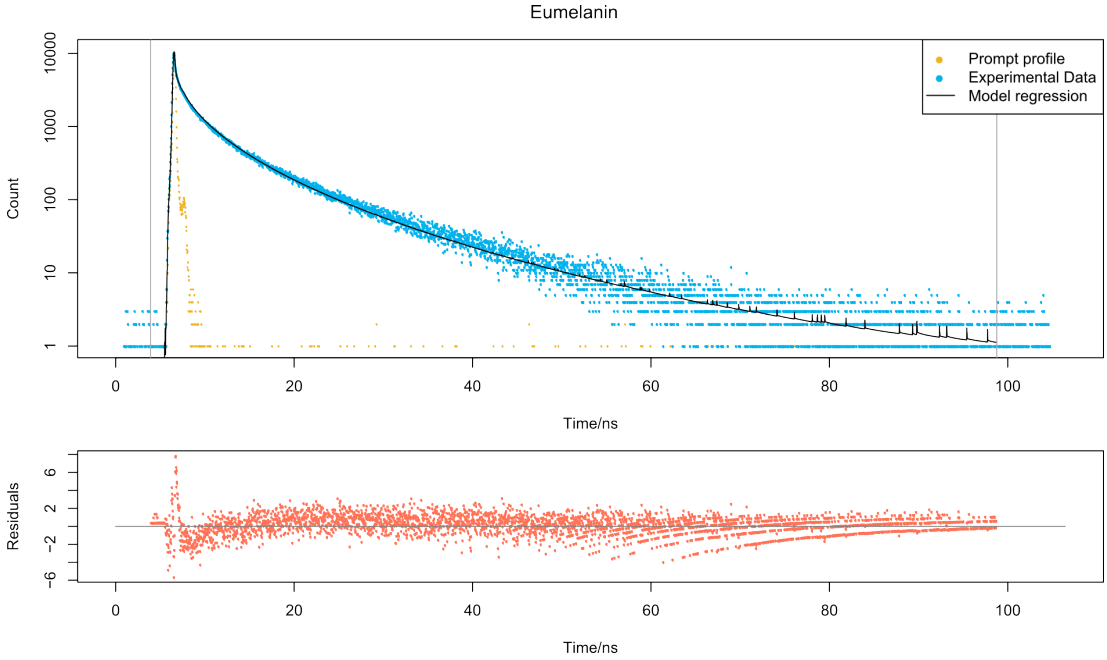

Figure 3.20: The same fluorescence decay for eumelanin as in Figure 3.18(a), fitted to the general relaxation function with the residuals shown underneath.

Fitting to the single parameter form of the general relaxation function has not produced a good fit as the χ^2 value is above 1.2 (Table 3.3) and the residuals show a peak near the time value of the decay peak (Figure 3.20). Given the need for multiple exponentials when using the multi-exponential model, it comes as no surprise that melanin does not fit well to the single parameter form of the general relaxation function. Extending the model to two parameters can be done in three ways. The general relaxation function can be altered to include either two κ, α or τ parameters. Each version has been used with the decays of Figure 3.18, and the fitted parameters are tabulated in Table 3.4.

α	κ	τ_1 (ns)	B_1 (%)	C (%)	Shift (ns)	A	χ^2
0.48	0.0033	0.79	89.66	10.34	0.098	0.56	1.45

Table 3.3: Parameter values from fitting the general relaxation function to the fluorescence decay of Figure 3.18(a).

Double κ			Double α			Double τ		
Sample	Eu	Pheo	Sample	Eu	Pheo	Sample	Eu	Pheo
α	0.42	0.65	α_1	0.42	0.49	α	0.59	0.64
κ_1	0.037	0.15	α_2	0.46	1.45	κ	0.002	0.062
κ_2	0.059	0.00	κ	0.00	0.011	τ_1	2.05	2.70
τ_1	0.51	0.82	τ_1	0.44	0.84	τ_2	0.27	0.39
B_1 (%)	345.05	392.20	B_1 (%)	580.83	78.53	B_1 (%)	75.9	60.51
B_2 (%)	-254.01	-303.41	B_2 (%)	489.95	9.78	B_2 (%)	15.79	29.56
A	0.56	0.49	A	0.56	0.49	A	0.56	0.49
C (%)	8.96	11.22	C (%)	9.12	12.00	C (%)	8.32	9.93
Shift (ns)	0.11	0.18	Shift (ns)	0.21	0.18	Shift (ns)	0.11	0.19
χ^2	1.18	1.13	χ^2	1.27	1.14	χ^2	1.08	1.04

Table 3.4: Fitted parameters from the extended general relaxation function that include two of ether κ, α or τ parameters.

Using two parameters has improved the χ^2 values, and the fittings have converged. However, looking at the table data in more detail reveals that only one form of the double general relaxation function has fitted the data adequately. With double κ's the amplitude values are negative ($<$ -100%) which is a non-realistic outcome and suggests that double κ's are not an appropriate model for melanin.

With double α's the percentage amplitude values are positive with pheomelanin's α values split 78% and 10%. However, eumelanin contains unrealistic percentage values as the values exceed 100%. The unsuitability if this model, for eumelanin, is also shown in the χ^2 value which exceeds 1.2. While using two α parameters has fitted well to pheomelanin, the poor fit to eumelanin suggests that this form of the general relaxation function is not appropriate for modelling the fluorescence decays of melanin.

The final version of the double general relaxation function has two τ values which are equivalent to having two fluorescence decay components like a two-exponential model. In this case, the model has performed well with realistic values, good χ^2 values and adequate residuals (Figure 3.21). Fitting the melanin decay with the double τ version of the general relaxation function performs best, which would imply that the melanin of Figure 3.18 fit best to the Kohlrausch decay function (stretched exponential) since the α values are less than one

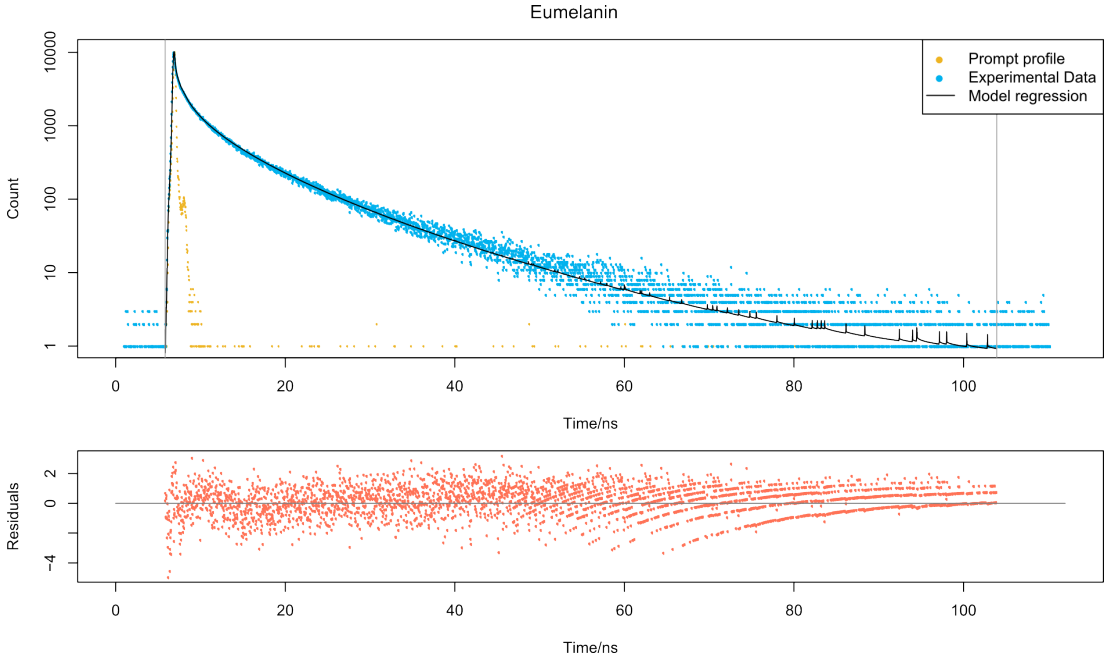

Figure 3.21: Plot of eumelanin fluorescence decay fitted to the general relaxation function with two τ values. The residuals are shown below.

and the κ value is close to zero. [66] The stretched exponential has been shown to apply to excitation energy transport [82] where emission from one excited fluorophore is transferred through multiple neighbouring fluorophores before the energy is released as a fluorescence photon.

A particular mechanism for melanin's excited state energy transfer has already been discussed by Corani et al. [62] and El Nahhas et al. [22]. The energy transference processes in melanin, as a result of ESPT and ESIPT, could explain why the fluorescence decays fit best to a stretched exponential function. Future studies could use the general relaxation function to investigate the photophysics of ESPT and ESIPT by monitoring the change in fitted parameters when melanins are subjected to different solvent environments.

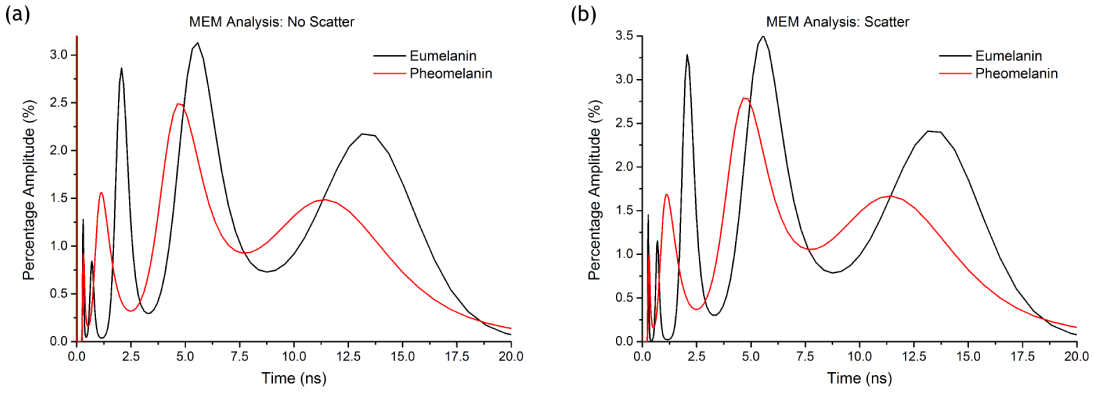

Figure 3.22: Decay component distribution spectra for the same samples of eumelanin and pheomelanin as in figure 3.18. The two plots show the change in distributions when scatter contributions were (a) not accounted for and (b) accounted for.

Lifetime distribution

The general relaxation function and the Kohlrausch (stretched exponential) function describe the lifetime decay as a distribution of rate constants. [81] Extending this idea further, the lifetime decays of Figure 3.18 were fitted to a distribution of lifetime components. The method used to achieve this kind of fit was the maximum entropy method, as part of the Pulse 6 algorithm (Maximum Entropy Ltd).

The distributions show a broad range of lifetimes present within the melanin samples, extending from picoseconds to $\sim$ 20 ns. Both pigments contain around 4-5 peaks which relate well to the multi-exponential fitting of Figure 3.19. The presence of these peaks could indicate that distinct fluorescence species are present, but their exponential decay profile is perturbed by the energy transfer process described in the last section. There may also be a structural component to the distribution of lifetimes in Figure 3.22. As larger melanin structures are formed, there will be changes to the electronic structure of the melanin molecules. The distribution in lifetimes could reflect the inherent heterogeneity of the melanin structures indicating that the peaks at longer times are form a wider range of particle sizes.

Sample	τ (ns)	$\Delta\tau$ (ns)	B (%)	$\Delta\tau$ (%)	FWHM (ns)	Δ (ns)	χ^2
Eu, no scatter	0.03	0.00	8.58	0.23	0.00	0.00	1.07
	0.30	0.07	5.66	4.03	0.03	0.07	
	0.70	0.27	6.32	4.82	0.10	0.23	
	2.14	0.40	23.56	7.04	0.36	0.53	
	5.75	1.04	33.13	0.47	1.18	1.29	
	13.04	1.99	21.43	8.90	2.22	2.52	
Eu, scatter	0.28	0.05	5.68	2.79	0.02	0.07	1.08
	0.70	0.22	7.68	3.90	0.09	0.24	
	2.15	0.39	25.81	7.39	0.34	0.53	
	5.77	1.05	36.37	11.51	1.17	1.31	
	13.08	1.95	23.64	9.84	2.24	2.62	
	198.58	321.14	0.26	3.78	17.78	190.14	
Pheo, no scatter	0.03	0.00	9.92	2.15	0.00	0.00	1.02
	0.34	0.11	8.27	4.78	0.07	0.15	
	1.26	0.30	27.18	7.88	0.41	0.43	
	4.93	0.90	33.43	10.69	1.20	1.05	
	11.76	2.84	19.72	9.21	2.69	3.40	
Pheo, scatter	0.33	0.11	8.35	4.80	0.06	0.15	1.08
	1.25	0.30	30.28	8.75	0.42	0.43	
	4.93	0.90	37.63	12.16	1.20	1.05	
	10.69	5.22	23.26	11.16	5.58	19.08	

Table 3.5: The peaks lifetime values from Figure 3.22 along with the relative amplitude (B), FWHM of the peaks and the χ^2 goodness of fit parameter.

The distribution of lifetimes for eumelanin is different from the distribution for pheomelanin. Both the peak position and the amplitude values are different. Pheomelanin has lower lifetime values and lower amplitude values than eumelanin. Despite the differences, both distributions have a similar overall profile as the peaks at longer times have a larger FWHM and the peak around 5ns has the highest percentage value.

These distributions could be described by the chemical disorder model, [83] where the absorption spectrum is due to the different redox states of the constituent molecules of melanin (i.e. DHI, DHICA for eumelanin and benzothiazole/zine for pheomelanin). Looking at the MEM plots, it can be imagined that the peak lifetimes stem from these redox indole and benzothiazole/zine molecules. The fluorescence lifetimes are altered to form a distribution as the molecules from the different structures detailed by Büngeler et al. [27]

Table 3.5 shows the details of the main characteristics of each distribution peak identified by the MEM algorithm. Without accounting for scattering, there is a short decay component at 30 ps which has a width of zero (a δ function). This short component is at the lower limit the algorithm was set to (based on the time calibration of the instrument). For this reason, it is preferable to have scatter accounted for when analysing the decays. The eumelanin fitting, with scatter accounted for, gave a peak at 196 ns (not included in Figure 3.22) which is at the upper limit of lifetime values the algorithm was restricted to. The 196 ns peak is not taken to represent a real lifetime but rather the algorithm incorporating the background signal as a long time component since the peak only accounts for 0.26% of the whole distribution. This value is similar to the background parameter fitted for the multi-exponential analysis of section 3.5.2.

The position of these peaks are different from those from fitting multi-exponential functions, but the overall breakdown is similar. There is a short component at 30 ps, which is likely scatter, then a 10^{-10} sec component which is followed by nanosecond components around 2.5 ns and 5 ns. Lastly, there is a longer component that is over 10 ns. The occurrence of similar magnitude lifetime components from different fitting algorithms adds weight to the notion that these lifetime components are based on real fluorescent species and that with the right model a system can be developed to identify melanin pigments and measure their relative concentrations, providing a simple method for identifying melanoma.

3.6 NIR Time-Resolved Measurements

Krasieva et al. [10] used two-photon excitation to identify melanin pigments. The excitation followed a step-wise path as opposed to a simultaneous excitation path. The difference between step-wise and simultaneous excitation is the existence of a real state during the first NIR photon excitation (Figure 3.2). This implies that the electron can transition to the ground state from this real state and emit a low energy photon. Should this be the case, it is reasonable to expect that the spectroscopy of this transition can be measured, thus opening up opportunities to replicate the diagnostic capabilities demonstrated by Krasieva et al. [10]

Exciting the melanin samples with 780 nm laser light, and measuring the emission spectrum, has revealed a peak at 860 nm (Figure 3.23). For both eumelanin and pheomelanin, there is an emission peak which is separate from other sources like the water Raman peak seen at 880 nm of the pheomelanin spectra. The change in overall intensity is a result of the emission polariser being changed from the magic angle to 0^{o} when changing to the pheomelanin sample. This was done to increase the number of counts measured, which would help when measuring the lifetime decays.

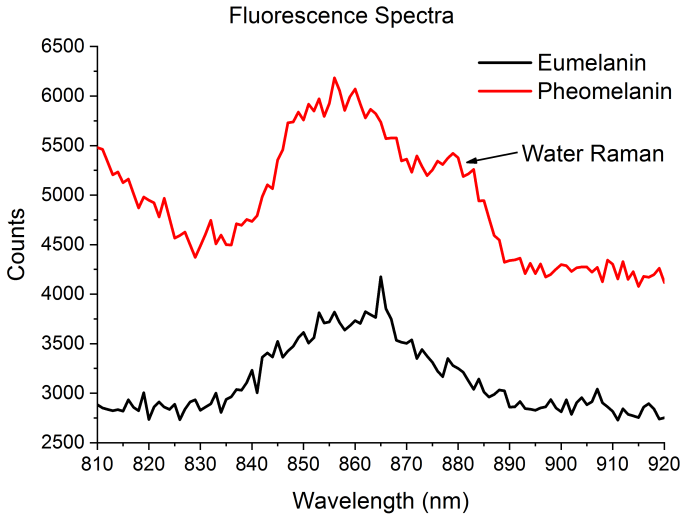

Figure 3.23: Fluorescence emission spectra for a sample of eumelanin and pheomelanin when excited at 780 nm laser light.

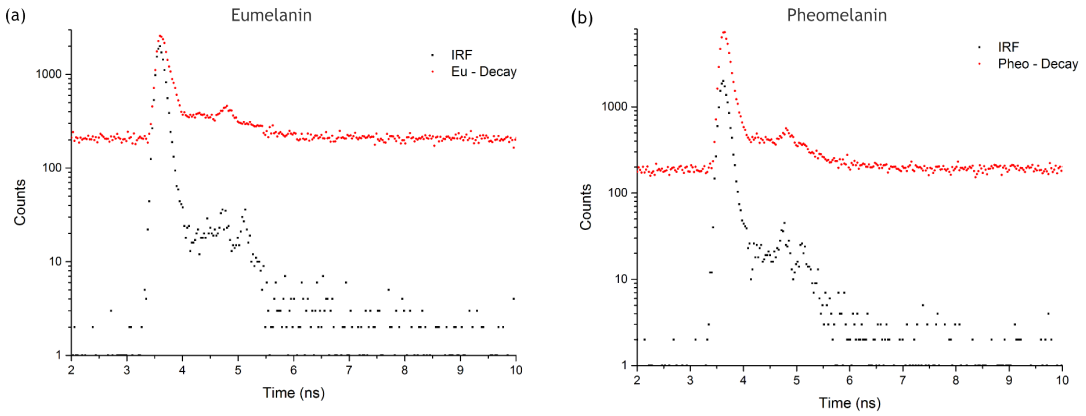

Figure 3.24: Fluorescence decays for (a) eumelanin and (b) pheomelanin, when excited at 780 nm and fluorescence, was measured at 860 nm. The instrumental response is shown in black. The high background signal is due to thermal noise.

From the absorption spectrum (Figure 3.4), the amount of light that is absorbed in the NIR is low. This means that, even though a fluorescence signal is measurable, the emission intensity will be low. From Figure 3.23 the number of photons counted was, at most, 6000 despite using 0^{o} oriented polarisers, 0.1 mM concentration, a more powerful DeltaDiode laser source (than the NanoLED diode sources) and a measurement time of 3 secs for each emission wavelength. While the existence of a NIR emission peak is further evidence for melanin's two-photon excitation process following a step-wise path, the low quantum yield significantly increases the measurement time and results in high S/N ratio. This could impact the usefulness of this technique as a melanoma sensing method since short acquisition times are an important feature of any future medical device. Additionally, the high S/N ratio would further complicate measurements when working with more physiologically relevant samples. Regardless, the observation of a fluorescence peak prompted further investigation.

In Figure 3.24, the fluorescence lifetime decays are shown for eumelanin and pheomelanin, along with the instrumental response. The fluorescence decays show a high background response which is due to high thermal noise. Given the measurement is in the NIR part of the spectrum the detector will pick up a large number of thermal photons. The influence of which could be reduced with increased cooling of the system. However, the long measurement times would hinder any attempt to reduce thermal noise.

Sample	τ_1 (ns)	τ_2 (ns)	B_1 (%)	B_2 (%)	χ^2
Eumelanin	0.013	7.48	65.96	34.04	2.94
Pheomelanin	0.013	1.03	93.95	6.05	3.23

Table 3.6: Parameter values from fitting a two-exponential function to the decays of Figure 3.24. The first decay component was fixed to half the time value of a single channel in order to account for scatter and improve fitting.

The decay from both melanins is short and follows the IRF closely. However, the decay slope does have a different gradient than the IRF which indicates that there is a genuine decay component present. Fitting to a two-exponential function revealed a longer decay component with $\sim$ 7.5 ns for eumelanin and $\sim$ 1.0 ns for pheomelanin (Table 3.6). The first component was fixed to half a channel value ($\sim$ 13 ps) in order to account for scatter and improve the χ^2 values. The fittings show a significant difference in decay components and relative amplitude. However, the high χ^2 values reduce the confidence in this result. It is unclear what the underlying cause is for the larger χ^2 values though possible candidates include the wavelength response of the PM, the lower number of counts or the fitting algorithm including the background into the value of τ_2.

Measuring the fluorescence decays at different emission wavelengths allowed for the spectral and time-resolved information to be combined into the one measurement. This time-resolved emission spectra (TRES) measurement would help identify which emission wavelengths contribute to which lifetime decay components and could allow for better contrast between the two pigments.

The global analysis of the decays was fitted to a three-exponential function where the first decay component was fixed at half a channel value. Unlike the analysis of the individual decays of Figure 3.24 the decay component times are more consistent with each other as both melanins produce a short component around 50 ps – 70 ps and a longer component around 1 ns.

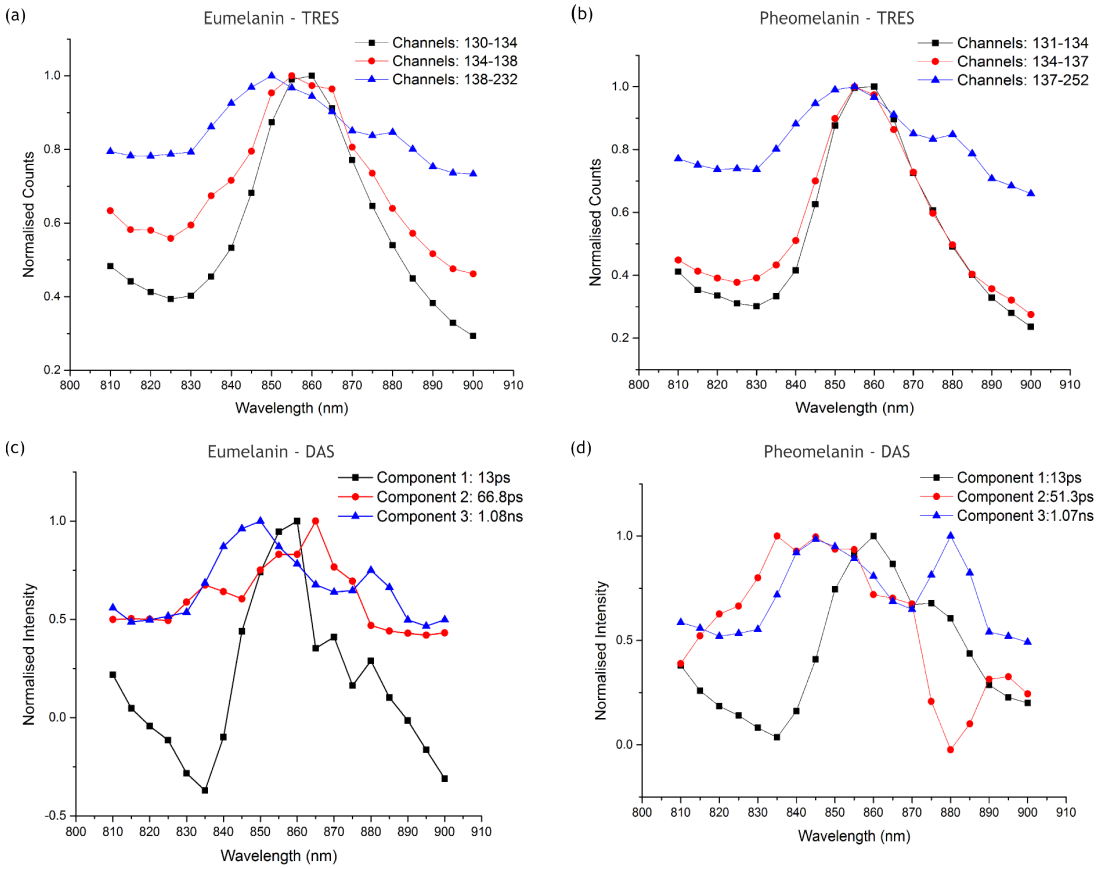

Figure 3.25: Time-resolved emission spectra for (a) eumelanin and (b) pheomelanin when samples were excited at 780 nm. Decay associated spectra for (a) eumelanin and (b) pheomelanin. Decays were fitted to a three-exponential model.

With one main fluorescence peak in Figure 3.23 it is understandable that each time component has a TRES peak near 860 nm. However, the decay associated spectra show the longer components peaking at different emission wavelengths. Notably, the second component for eumelanin peaks at 865 nm while for pheomelanin the peak is at 835 nm – 845 nm. It is this kind of difference that could facilitate a melanoma sensing technique. However, the presence of a Raman peak (peak $\sim$ 880 nm), for pheomelanin, may account for the change in wavelength seen for the second component.

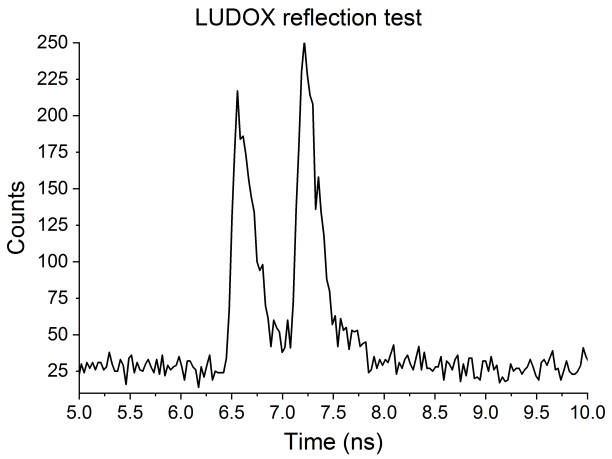

Figure 3.26: Fluorescence decay plot for a sample of dilute LUDOX®. The sample was excited at 780 nm, and the emission was fixed at 780 nm.

Contradicting convention, the Raman response is prominent for later time channels and decay components (most evident in Figure 3.25(d)). It would be expected that scatter responses would occur at the shortest times. This indicates that the instrument was not only detecting the main Raman scatter signal but a reflected Raman signal as well. Evidence for the presence of a scatter reflection can be seen in Figure 3.26 as a second Rayleigh scatter peak is viable when a dilute sample of LUDOX® was excited at 780 nm. While attempts were made to reduce the presence of reflections via altering the orientation of the cuvette and adding black strips around the cuvette to help absorb or alter the path of the reflections, the weak fluorescence signal and long acquisition times meant that the reflected signal remained. The presence of a reflection signal will undoubtedly contribute to the poor χ^2 value obtained.

It is encouraging to identify a NIR fluorescence peak for both eumelanin and pheomelanin, as this is further evidence that exciting melanin with two NIR photons follows a step-wise process. However, melanin's low quantum yield and low absorption in the NIR make conventional (one-photon) spectroscopic measurements time-consuming, with high S/N ratios and is prone to interference from high thermal backgrounds and scatter reflection signals. Using OPE to measure this real state presents great challenges should it be developed for the identification of different pigments as is done for the step-wise TPE process.

3.7 Conclusion

Currently, there is no simple, cost-effective, non-invasive method for detecting melanoma while those that are simple and non-invasive are not suitable for diagnostic purposes. Multiple spectroscopic methods have been investigated in order to find an alternative melanoma sensing technique that follows the design principles discussed in Chapter 1. The main goal was establishing a clear spectroscopic difference between eumelanin and pheomelanin that would allow for the development of a medical device which followed the strategy of Krasieva et al. [10].

Despite following standard protocols for melanin synthesis, both absorption and emission (steady-state and time-resolved) results show variation between different samples. This meant that simple normalisation strategies, like those seen in Figures 3.5 and 3.7 proved ineffective at repeatedly distinguishing eumelanin and pheomelanin. However, the presence of isosbestic points, in the absorption spectra, does indicate that melanin's photophysics stems from a limited number of molecular species.

The fluorescence of melanin covers a wide range of emission wavelengths and can be excited across an equally large number of wavelengths too. Excitation-emission matrix measurements allowed for the full fluorescence emission picture to be captured. However, the three-dimensional data-sets contained a substantial amount of information which made identifying differences difficult. By using parallel factor analysis, the dimensionality of the data was reduced, and fundamental spectral features were identified. While a simple comparison of eumelanin and pheomelanin prove encouraging for identifying differences between the two pigments, further experiments failed to follow the same trend as observed in Figure 3.11(b) and the work of Ozeki et al. [75].

The melanin samples with different concentrations of cysteine were measured via time-correlated single photon counting and the fitted parameter, τ_4, from reconvolution analysis does follow the trend observed in Figure 3.11(b). This was from fitting a four-exponential function to the decay data. However, given the complexity of melanin's photophysics, a different fitting function like the general relaxation function and lifetime distribution fitting like maximum entropy method were also used. Since the fitted parameters from using the general relaxation function conform to the Kohlrausch (stretched exponential) function [66] it is

likely that melanin's fluorescence lifetimes are affected by energy transfer processes with ESPT and ESIPT being possible candidates. [22, 62] The distributions of lifetimes from MEM contained 4-5 distinct peaks which fall within a similar time range as the decay components from multi-exponential fitting and is consistent with the number of isosbestic points from Figure 3.3. This is further evidence that the photophysics of melanin originates from a limited number of molecular species, with mechanisms like oligomerisation and energy transference leading to the alteration of discrete lifetimes into a distribution as observed in Figure 3.22.

Evidence for melanin's two-photon excitation process following a step-wise path was found in the measurement of a fluorescence peak at 860 nm, after excitation with 780 nm light. Measuring the fluorescence lifetime decay and TRES revealed the potential of this technique as a sensing technology. However, the low signal, long aquisition times and presence of scatter reflections hinder this technique's potential and would require further investigation to verify these findings. The advent of new photon-counting technologies like the SPAD array could overcome the challenges of working with a low quantum yield samples by allowing for simultaneous measurements of TRES data, but the lower active area of SPADs as compared to photomultpliers is also a major limitation in spectroscopy.

Chapter 4

Evidence for Sheet Structure Formation During Pheomelanogenesis

4.1 Introduction

4.1.1 Sheet structure formation in melanin

A current model for melanins larger structural forms is the three-step, four-level, hierarchical build-up model. [27] This description of melanin starts with the formation of sheet structures, comprised of tens of monomer units [84–86], which then π-stack on top of one another with an inter-sheet spacing around 0.3 nm - 0.4 nm apart. [28] Like in Figure 1.3, the stacked sheets then come together to form spherical Type-A particles, around 20 nm in diameter, [87] before aggregating together to form spherical Type-B particles, around 200 nm in diameter. [88] This model is based on findings from electron microscopy, Atomic Force Microscopy (AFM), X-ray scattering, X-ray diffraction, and mass spectrometry. [27, 28, 84, 89, 90] Spectroscopically, evidence for sheet structure formation came from studying the change in fluorescence intensity from the sheet-structure sensing probe Thioflavin T (ThT). [91]

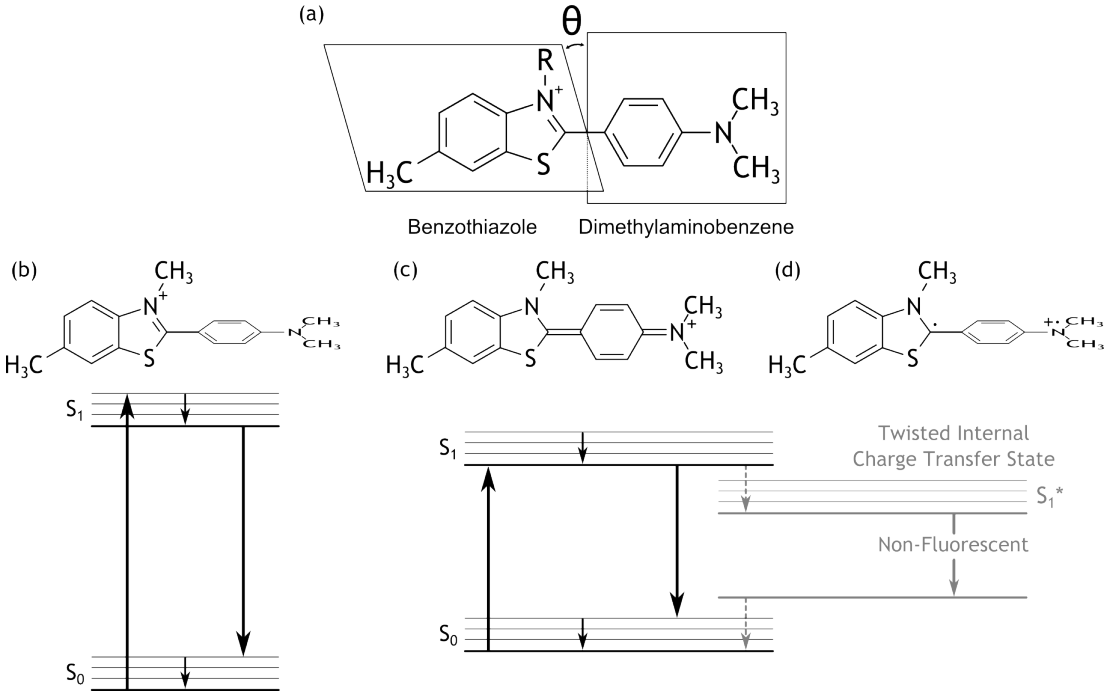

Figure 4.1: (a) ThT structure with benzothiazole and dimethylaminobenzene structures identified. The torsional angle between the two groups has been labelled as 'θ'. (b) When θ = 90^o ThT is in the twisted state with an emission peak near 440 nm (Figure 4.4(b)). (c) The emission peak red-shifts when θ = 0^o and allows for charge transfer to take place between the amino group and the dimethylaminobenzene part of the ThT molecule. (d) Instead of returning to the state in (b), the ThT molecule can enter the non-fluorescent twisted internal charge transfer state. Representative energy level diagrams are shown underneath the different structural states of ThT seen in (b-d).

ThT (or Basic Yellow 1 [92]) is a fluorescence dye molecule (Figure 4.1) that can act as a structure probe. It is a benzothiazole salt that has been used to report on the fibrillation of amyloid proteins, specifically amyloid-β (Aβ). [92–95] Measurements involved exciting the ThT at 450 nm, then observing the increase in fluorescence intensity at 490 nm. [91, 94–96] A change of the photophysics occurs when the ThT molecule becomes restricted in a viscous environment or within sheet structures.

From Figure 4.1(a) the benzothiazole and dimethylaminobenzene groups have been identified, and the torsional angle between the benzothiazole and benzene parts has been labelled 'θ'. When θ equals 90^o (Figure 4.1(b)) the fluorescence maximum is at 440 nm and when the torsional angle equals zero, the fluorescence maximum red-shifts to 490 nm (Figure 4.4(b)). However, rotation of these groups can also result in an intermolecular charge transfer pro-

cesses [97] which leads to a transition from a locally excited state (Figure 4.1(b) & (c)) to a non-fluorescent twisted internal charge transfer (TICT) state (Figure 4.1(d)). [97, 98] Due to the photophysics of ThT being linked to the rotation of this rotor, the fluorescence of ThT is sensitive to the rigidity of the microenvironment. Stsiapura et al. [97] observed a decrease in fluorescence intensity (at 490 nm), for increasing temperatures, of a ThT/glycerol sample demonstrating a direct relationship between viscosity and fluorescence quantum yield of the locally excited state. [97] Studies of Aβ, with ThT, observe an increase in fluorescence intensity and is attributed to the ThT rotor becoming restricted upon intercalation within β-sheets during Aβ fibrillation. [92–95]

Along with investigating Aβ fibrillation, the ThT dye molecule was successfully used to identify and monitor the formation of sheet structures during eumelanin's melanogenesis. [91] Monitoring the fluorescence spectrum, a similar increase in emission intensity was observed. The results confirmed that the ThT rotor had become restricted within the sheet structures of eumelanin, equivalent to studies on Aβ. [91] Fitting the time-series data to the Logistic sigmoidal function (Equation 4.1) [99] it was possible to compare the kinetics of sheet formation at different pH values and confirm that the time of formation decreased with increasing pH.

$$I(t) \sim I(0) + \frac{\alpha}{1 + e^{-k(t-t_0)}} \tag{4.1}$$

Where I(t) is the measured emission intensity, and I(0) is the background intensity value. The α value is the fluorescence maximum above the background value while t_0 is the time value where the intensity reaches the half maximum value. The rate of melanin sheet formation is equated to the parameter k. The Logistic function has been used previously to model two-three stage nucleation-growth such as fibrillation [100, 101] along with population growth, market studies of new products and describing the diffusion of epidemic diseases. [99] For the time-series data of pheomelanin with ThT, the logistic function of Equation 4.1 was fitted in order to quantify the growth in the fluorescence emission intensity. Along with the Logistic function, the Hill function (Equation 4.1) [102] was also fitted to the pheomelanin with ThT time-series data.

$$I(t) \sim I(0) + (\alpha - I(0)) \frac{t^n}{t_0^n + t^n} \tag{4.2}$$

The Hill function, first introduced by Archibald Vivian Hill, was used to describe the relationship between oxygen tension and the saturation of haemoglobin. [102] The background intensity and fluorescence intensity above the background are represented by the I(0) and α parameters respectfully. The time at which the fluorescence intensity has reached the half maximum value is given by t_0 while n refers to the Hill coefficient. [103] The Hill coefficient typically describes the degree of cooperativity of molecular binding but may describe other biochemical properties, depending on the context. Positive cooperative binding ($n > 1$) implies that once a molecule has become bound, there is a greater affinity for other molecules to bind. In contrast, for negative cooperative binding ($n < 1$) there is a decrease in the affinity of the macromolecule to bind another molecule, once one has already been bound. Finally, there is non-cooperative binding ($n = 1$) where the binding of a second molecule is independent of the first. [103]

While this is typically taken to be the case, a later report by Heino Prinz [104] determined that the Hill coefficient may reveal information on the number of interacting sites but could not distinguish between cooperative or non-cooperative mechanisms. Concluding that if the Hill coefficient is different from one, then that is proof for multiple molecular units binding to the biomacromolecule. [104] While the system under study here is not related to ligand binding or the oxygen saturation of proteins the system does involve the formation of a new complex, form two initial entities such that:

$$n \times T + P \Leftrightarrow T_n P \tag{4.3}$$

Where T represents a single ThT molecule and P would represent the pheomelanin sheets that restrict the ThT rotor. The n parameter would equate to the number of intercalated ThT molecules. Should the time-series data for pheomelanin with ThT follow the Hill function, to a reasonable statistical certainty, then it will be possible to comment on the quantity of ThT intercalation. Values of n above one would imply that more than one ThT molecule intercalates within the sheets of melanin. [104]

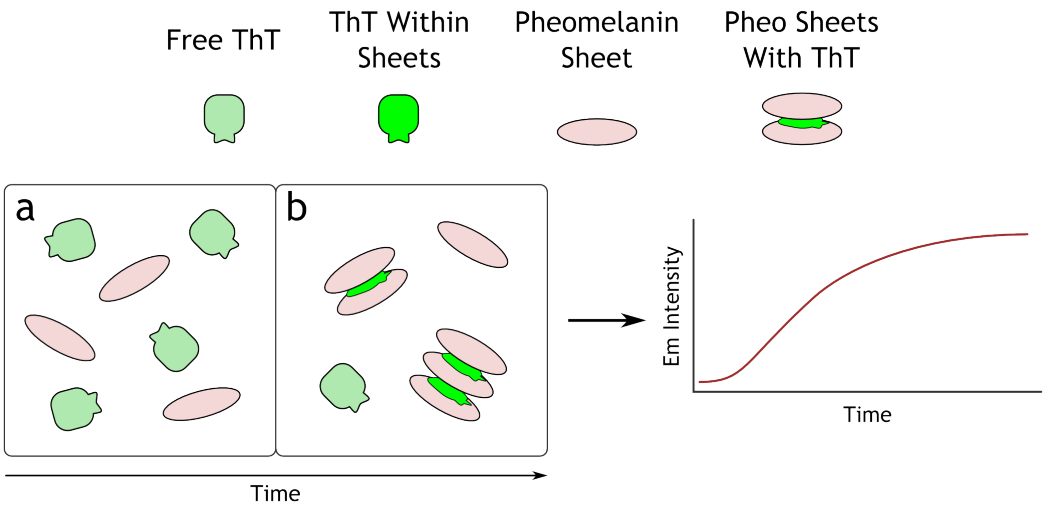

Figure 4.2: Illustration demonstrating the intercalation of ThT within the sheet structures of melanin and the predicted change in emission intensity over time. (a) Initial stages where sheet structures are being formed in the presence of free ThT. (b) At later times, the ThT molecule becomes intercalated within the sheets of pheomelanin.

The use of the extrinsic dye molecule, ThT, could allow for the identification of pheomelanin and eumelanin if the degree of intercalation differs between them. It is expected that pheomelanin would intercalate less ThT due to steric hindrance [105] and therefore have a lower n value than samples of eumelanin.

Most studies on melanin's structure are with eumelanin, ether synthetic or natural (e.g. Sepia melanin). To date, there has been no specific study that investigates sheet structure formation during pheomelanogenesis. This is not helped by pheomelanin being a more complicated system with a lack of convenient commercial sources. [7] Responding to this realisation, the results within this chapter aim to investigate the possible presence of sheet structures within pheomelanin. Following the work of Sutter et al. [91], the fluorescence emission of ThT was monitored during pheomelanin synthesis and time-series trends were fitted to sigmoidal functions, as illustrated in Figure 4.2. In addition to fluorescence emission plots, investigations were extended to include fluorescence lifetime measurements as an additional avenue for investigating the response of ThT within the sheets of pheomelanin and comparison with the dyes response in eumelanin.

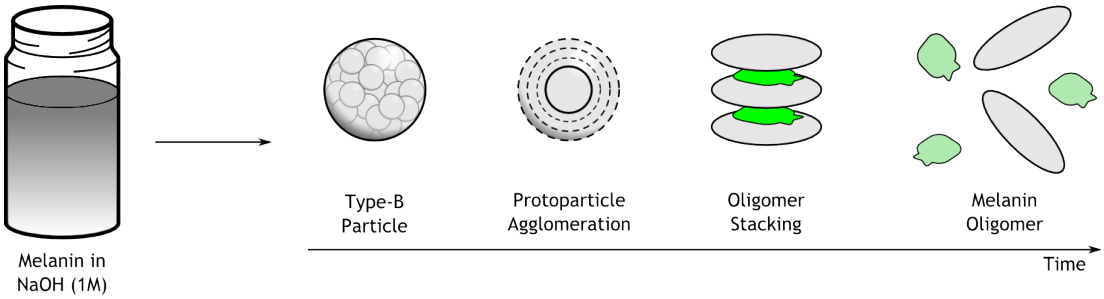

Figure 4.3: Illustration demonstrating how disassembly can separate ThT from within the sheets of melanin.

4.1.2 Disassembly of melanin particles

Utilising the photophysical properties of the fluorescent dye molecule ThT, the sheet formation of pheomelanin was investigated and expanded to include fluorescence lifetime measurements. Samples were processed further in order to disassemble the melanin particles and confirm the release of ThT from within the sheets of melanin.

The method for disassembling the melanin particles was based on the work of Ju et al. [106] where melanin particles were suspended in a solution of sodium hydroxide (NaOH) overnight (Figure 4.3), then neutralised with potassium phosphate (KH_2PO_4). The long suspension time results in the larger melanin particles (type A and B) being reduced to sub-units of oligomer sheets. The breakdown of melanin particles should free the ThT molecule rotor and lower the fluorescence intensity of the locally excited state (at 490 nm) as the restriction placed on the ThT molecule will have been removed.

4.1.3 Excited state complexes

Aromatic molecules comprise carbon rings that have delocalised π-bond, from the overlapping of p-bonds above and below the ring. [107] Exciting the π-electron will promote it to an antibonding orbital (denoted as π^*). [47] Generally, these bonds have band gaps within the visible part of the spectrum and are a reason why aromatic molecules fluoresce. [20, 47] Aromatic molecules can form larger structures when they bond on top of one another, allowing the π-bonds to interact. This π-stacking can lead to the formation of excimers and exciplexes.

While not limited to molecules, an excimer is the formation of an atomic or molecular dimer aggregate that is unstable in the ground state but becomes stable under electronic excitation. [108] An exciplex is a hetro-excimer formed from different molecules. Generally, the emitting complex involves the charge-transfer from an excited species to a non-excited species or vice versa. [20, 47, 108] Both coupled systems demonstrate a broad, structureless, spectral band that is red-shifted from the monomer peaks. [20, 47]

4.2 Methodology

4.2.1 Synthesis of melanin with ThT and disassembly

Chemicals: 3,4-dihydroxy-L-phenylalanine (L-DOPA, $> 98\%$). L-Cysteine (Cyst, $> 97\%$). Tyrosinase from Mushroom (TYR, 2687 u/mg). Melanin from *Sepia Officinalis*. Thioflavin T (ThT). Ammonium Hydroxide solution (max 33% NH_3). Sodium Hydroxide (NaOH, 1M). Potassium Phosphate Monobasic (KH_2PO_4). Distilled water was used to prepare all stock solutions. All chemicals were from Sigma-Aldrich.

Synthesis of melanin with ThT

The protocol was adapted from the work of Sutter et al. [91] where melanin/ThT samples were prepared in a 1:1 ratio of melanin and fluorescent dye. Pheomelanin was synthesised according to the reports of Ito [109] and d'Ishia [7] where aqueous solutions of L-DOPA were mixed with Cyst and the reaction was catalysed by the enzyme TYR. The final concentrations were 1mM for L-DOPA and 1mM for Cysteine and either 500 or 750 units per ml (u/ml) for TYR. The pheomelanin mixture was then added to a 40 μM aqueous dilution of ThT, such that the pheomelanin was diluted to 40 μM. The pH of the samples was within the range of 6.4 to 7.0.

Eumelanin samples were used as a comparison with the observations seen by Sutter et al. [91]. This involved mixing aqueous solutions of L-DOPA and ThT in an environment where the pH had been increased to ~ 10, in order to reduce the synthesis time. Final mixtures of L-DOPA and ThT were 40 μM and 40 μM and the pH was raised to a value of 10 via titration of ammonium hydroxide in distilled water.

The pH was measured with a Horiba Scientific electrochemical pH probe (model D-51). The samples were aspirated with a 1 ml pipette, three times, to ensure adequate mixing. For fluorescence intensity measurements, a 7x2 mm stir bar was added to keep the sample mixed throughout the measurements.

Disassembly protocol

Disassembly of melanin particles followed the protocol detailed in Ju et al. [106]. Melanin samples (Sepia melanin, eu- and pheo -melanin with ThT) were centrifuged at 2000 xg for 10 mins and suspended in distilled water. Centrifugation was carried out twice in order to remove the free ThT dye from the synthetic melanin solutions before disassembly of melanin particles. The melanin pellets were suspended in 1 ml of distilled water and then 3.5 ml of NaOH (1M) was added to the eumelanin and Sepia melanin samples while 1 ml of NaOH was added to the pheomelanin sample. The different amounts of NaOH used reflected the different concentrations of melanin extracted via centrifugation as can be seen in Figure 4.23. The NaOH was purged with N_2 gas for 20 mins before mixing with melanin in order to eliminated dissolved O_2. After mixing the pelleted melanin solutions with NaOH, the mixtures were purged with N_2 gas for a further 20 min, then sealed and left overnight in a dark place at 25^{o}C.

After 12 hours, 1ml of KH_2PO_4 (1M) solution was added to the melanin/NaOH solutions to neutralise the pH and prevent pH-induced oxidation of sub-units under ambient environments. [106] For Sepia melanin the sample was centrifuged at 2500 xg for 10 mins in order to separate the melanin sub-units and the lager structures that had not disassembled. The synthetic melanin samples with ThT where first centrifuged at 2500 xg to separate the lager melanin particles from the disassembled sub-units and freed ThT dye. After removing the pellet of larger melanin particles, the remaining mixture was spun at 5000 xg to separate the disassembled melanin particles from the freed ThT molecules. The pelleted sub-units of melanin were suspended in KH_2PO_4 solution.

4.2.2 Instrumentation and analysis

Absorption measurements

Absorption measurements were carried out on a Perkin-Elmer Lambda 25 spectrophotometer. Measurements were performed in 4 ml clear walled plastic UV grade cuvettes. The wavelength range was set to 200 nm - 1100 nm with a measurement speed of 960 nm/min. The baseline measurement was carried out with empty cuvettes in both the reference and sample chambers. Then for the sample measurement distilled water was used in the reference channel.

Fluorescence intensity measurements

The fluorescence intensity was measured over time using a Horiba Scientific FluoroMax 2 spectroflurimeter. Samples were excited at 450 nm and the fluorescence monochromator scanned between 460 nm and 600 nm. The disassembled Sepia melanin was also excited at 314 nm in order to compare the spectra with those of Ju et al. [106] The fixed-point measurements had the excitation and emission monochromators set to 450 nm and 490 nm, respectfully. Slits were set to 4 nm for both paths and the integration time was set to 1 sec. For spectral measurements, the resolution was set to 1nm and for the fixed wavelength time-series measurements the measurement interval was 1 sec. Measurements were set to run for 2 hours. The instrument has a built-in magnetic stirrer, which was set to speed setting 4. This was fast enough to keep the sample solution mixed while avoiding a strong vortex forming.

Fluorescence lifetime measurements

A DeltaFlex time-correlated single photon counting (TCSPC) spectrometer (HORIBA Jobin Yvon IBH) was used to record fluorescence decays of the melanin samples. The samples were excited with a NanoLED pulsed laser diode that lased at 437 nm and had a repetition rate of 1 MHz with $<$ 200 ps pulse width. [110] The emission monochromator was set to 490 nm with a bandpass of 32 nm. A 450 nm long pass filter was used to help reduce Rayleigh scatter. The time range of the measurement was 100 ns, split between 4000 histogram bins. The emission polariser was set to the magic angle (55^{o}) while the instrument was set to automatically stop measurements when the peak photon count reached 10,000 counts. For the lifetime time-series

measurements, the acquisition was sometimes stopped before the peak reached 10,000 counts. This was done in order to maximise the number of time points measured. The time-series measurements focused on the overall trend of the lifetime components. It was deemed reasonable to balance statistical certainty with maximising time point. The instrumental response was measured with a dilute sample of LUDOX® with neutral density filters in the excitation pathway, should the alpha value exceed 2%.

Fitting sigmoidal function

Fitting to a sigmoidal function and other data processing operations were performed in MATLAB® (R2017b – 9.3.0.713579, MathWorks®). A script was written (code available in Appendix B) to import the time-series data, assign variables, set limits, fit data and plot results. The data was normalised with the `rescale()` function then prepared for fitting with the `prepareCurveData()` function. The `prepareCurveData()` function transforms data for use with the fit function by converting the data into columns and from non-double to double data while removing complex and non-number entries. With the `fittype()` and `fitoptions()` commands the Logistic (Equation 4.1) and Hill (Equation 4.2) functions were inputted and the system told to use the least-squares method. Finally, the `fit()` function was used to fit the Logistic and Hill functions to the processed data and calculate the goodness-of-fit values. Performing deconvolution on the pheo/ThT data with the TYR/ThT response was achieved with the built-in MATLAB function `deconv()`. The function deconvolves a vector 'v' out of a vector 'u' using long division.

4.3 Detecting Sheet Structures During Pheomelanogenesis

One of the challenges of using extrinsic fluorophores with melanin is the fact that the spectral bands of the fluorophore will overlap with the absorption of melanin. Comparing Figure 4.4(a) with Figure 4.4(b) it can be seen that pheomelanin's absorption spectrum also overlaps with ThT's spectral bands. This is important to keep in mind as overlapping spectral bands can lead to the transference of energy from one fluorophore to the other like that seen in Förster Resonance Energy Transfer (FRET) [20] or the reabsorption of the fluorescence photon as seen with inner filtering effects. [17]

Looking closer at the fluorescence emission of the structure probe ThT (Figure 4.4(b)), the absorption peak is at 400 nm with an emission peak at 440 nm. However, the operation wavelengths for ThT, as a sheet sensing probe, uses an excitation wavelength of 450 nm. It is important to exclude the main fluorescence peak from measurements as this would interfere with the spectral change seen at 490 nm when the dye intercalates within sheets.

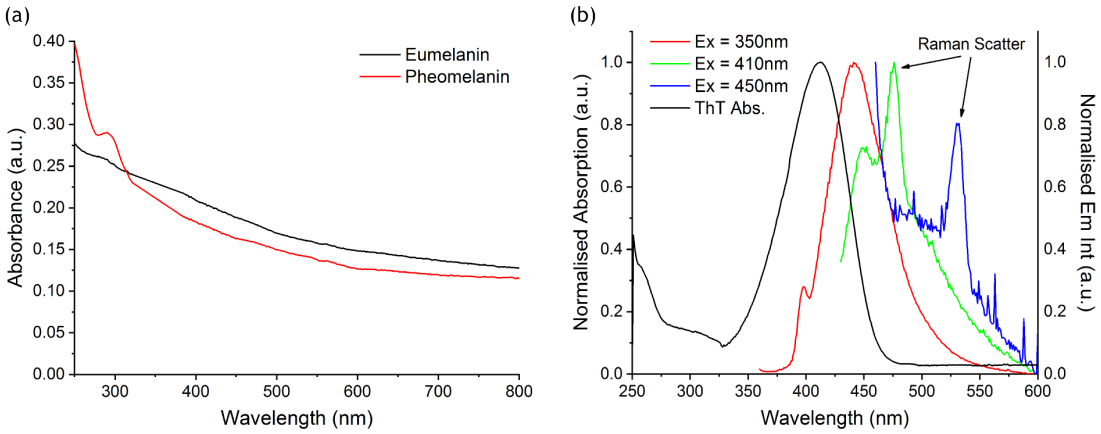

Figure 4.4: (a) Absorption of eumelanin and pheomelanin. (b) Absorption and emission spectrum for ThT, the dye has been excited at different wavelengths and has the water Raman peak indicated.

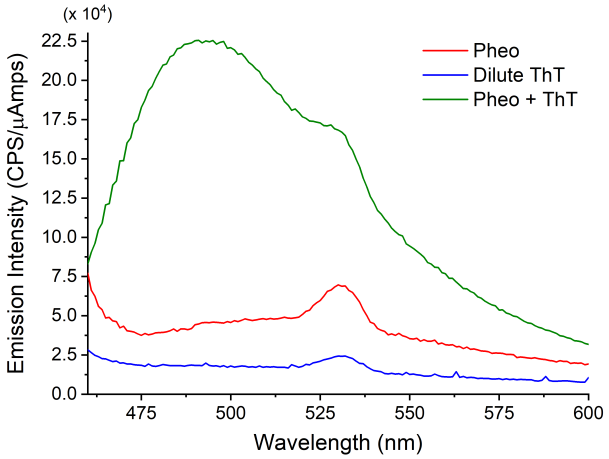

Figure 4.5: Emission spectra (Ex = 450 nm) for pheomelanin (750 u/ml of tyrosinase), dilute ThT and for pheomelanin (750 u/ml of tyrosinase) that had ThT present during the melanogenesis process.

4.3.1 Emission spectra

Figure 4.5 compares the fluorescence emission spectra for a sample of pheomelanin, dilute ThT and a mixture of pheomelanin with ThT, where the ThT was added at the start of pheomelanogenesis. [111] The spectra were measured at 2 hours post mixing and show a prominent emission peak for the mixed pheomelanin with ThT sample which does not appear in the other spectra. This is clear evidence supporting the intercalation of ThT within sheet structures of pheomelanin as the peak at 490 nm matches previous studies in eumelanin [91] and within the sheets of β-amyloid (Aβ). [93, 95, 96] In order to investigate the kinetics of sheet formation, the emission spectra were measured over time.

Figure 4.6(a) shows the change in spectral intensity and the spectral shift that occurs over time for a sample of pheomelanin with ThT. [112] Charting the emission spectrum over time reveals that the fluorescence peak at 490 nm increases with time which agrees with the formation of sheet structures. Focusing on the insert of Figure 4.6(a) it can also be seen that the spectral peak red-shifts with time. This could be related to the increase of pheomelanin particle size; related to energy transfer between the two fluorophores; the formation of an excited complex or the restriction of ThT which results in a greater degree of delocalised electrons. [22, 93, 98]

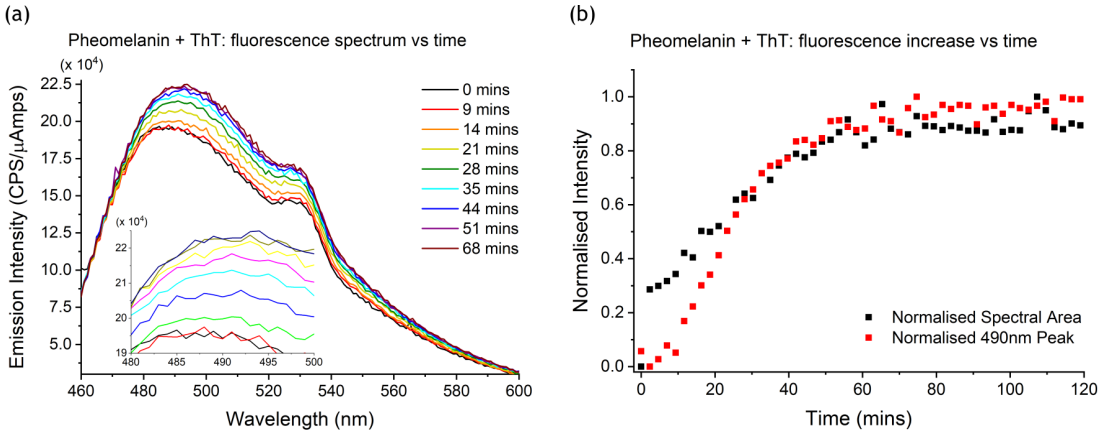

Figure 4.6: (a) The emission spectrum (Ex = 450 nm) was monitored over time for a sample of pheomelanin with ThT. The insert focuses on the red-shift of the 490 nm peak. (b) The emission intensity values for the 490 nm peak and the integrated spectral area over time.

Along with following the peak at 490 nm, the emission spectra were integrated over the wavelength range which determined the area under the spectra. Both are normalised and compared in Figure 4.6(b) and confirm the rise in emission intensity. The trend that follows the peak at 490 nm includes a short delay period, before the intensity rises, while the integrated spectral area trend rises immediately. This is the result of a slight widening of the spectral peak which could also be evidence for larger molecular structures coming together. The spectra collected in Figure 4.6 follow a similar trend seen with eumelanin [91] and offer the chance to compare the sheet formation kinetics of the two pigment molecules. However, given the increased complexity of the pheomelanogenesis process, measurements focused on confirming the effects seen in Figures 4.6 and whether the rise in intensity came from ThT intercalation within sheets of pheomelanin and not just molecular interactions between the dye and the other reactants. Likewise, it is important to confirm the difference between the intrinsic pheomelanin response and the intercalated ThT response.

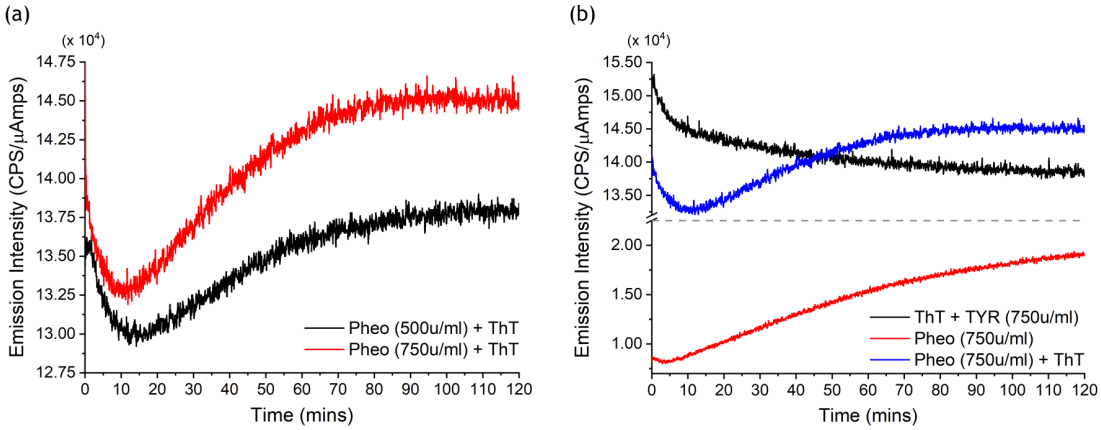

Figure 4.7: (a) Monitoring the emission intensity, over time, for samples of pheomelanin with ThT. The amount of tyrosinase used was altered from 500 u/ml to 750 u/ml. (b) The fixed-point time series for pheomelanin with ThT is compared with the response from intrinsic pheomelanin and tyrosinase with ThT. [111]

4.3.2 Emission fixed point measurements

In order to maximise the number of time-points measured, fixed-point time-series measurements were performed where the excitation and emission monochromators are set to a fixed wavelength and the emission intensity was measured over time. Monitoring the emission peak at 490 nm (Ex = 450 nm) allows for greater time resolution as data points can be taken at 1 sec intervals. Figure 4.7 shows the change in the 490 nm emission intensity for two different samples of pheomelanin, with ThT. One sample was synthesised with 500 u/ml of tyrosinase while the other used 750 u/ml to make pheomelanin. The increase in tyrosinase concentration has increased the overall intensity of the 490 nm signal and slightly decreased the time the signal takes to increase in intensity. This agrees with the behaviour of enzyme reactions as more enzymes units will catalyse more cysteinyldopa reactions, which increases the rate at which sheets can form.

There is strong agreement between Figure 4.7(a) and the 490 nm peak intensity data of Figure 4.6(b). The two trends take around (75 mins) to plateau and the initial rise in intensity occurs after $\sim$ 10 mins. However, charting the intensity every second has revealed an initial decrease in emission intensity that was not reported previously [91] but was observed to a lesser extent with eumelanin [113].

This initial decrease in intensity deviates from the expected behaviour seen in Figure 4.6(b) and required further investigation. Two control measurements were performed with the first being a measurement of the intrinsic pheomelanin response and the second measuring the response of a mixture of ThT and tyrosinase. This would confirm whether the trend observed in Figure 4.7(a) was the result of pheomelanin's intrinsic fluorescence or whether the dye molecule was changed after coming into contact with the enzyme. As with the pheomelanin response in Figure 4.5, the intrinsic melanin emission is several orders of magnitude lower than the melanin with ThT signal. The response of ThT with just tyrosinase is more interesting as the intensity value range is similar to the pheomelanin with ThT sample, but instead of rising in intensity, the emission signal decreases gradually with time. Of particular note is the initial trend which matches the initial decrease of intensity of the pheomelanin with ThT sample, all be it, at a higher starting value. This would imply that this effect is not specific to the formation of melanin and that the rise in emission intensity, after 10 mins is not the result of the enzyme reacting with the ThT fluorophore.

From the evidence of Figure 4.5 - 4.7, the fixed time series data can be interpreted as confirming the formation of sheet structures, within pheomelanin, and exhibits an initial period of quenching which obscures the delay period that is usually seen with such measurements. Since the ThT is diluted from a highly concentrated stock (1 mM), it is possible that the initially high intensity values are contributed to by aggregated ThT molecules which dilute over time. The interaction with ThT quenches this fluorescence, first through collisional quenching then, as the dye molecule electrostatically binds to the pheomelanin precursor structures, through static quenching. At time 'x' (Figure 4.8) the pheomelanin structure start to form sheets, and since the ThT is already linked to the proto-molecules, the ThT becomes intercalated within the newly forming sheets. This restricts the free rotor of ThT and increases the radiative emission from the dye molecule (at 490 nm). Finally, the pheomelanin is formed and all the DOPA has been used up, meaning there are no more sheets being formed, so the ThT emission plateaus.

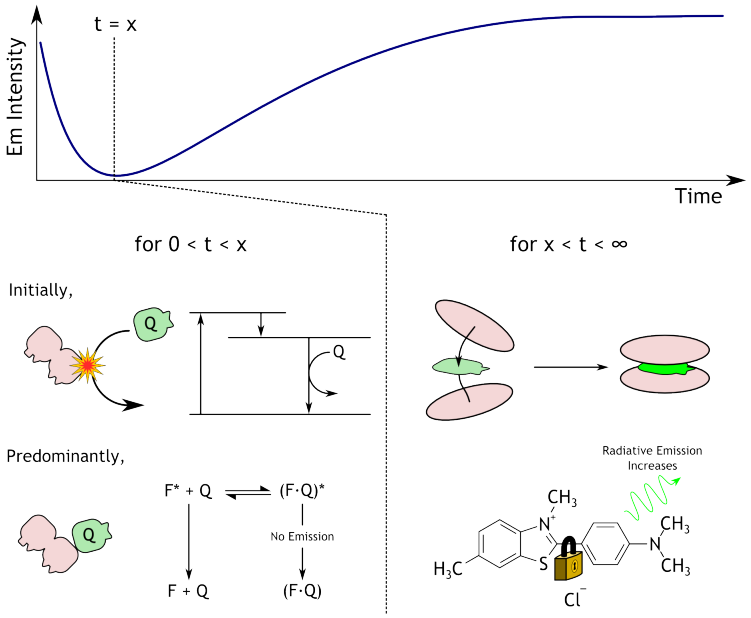

Figure 4.8: Representative graph of the fixed-point emission curve and the interpreted mechanism underpinning the fluorescence. For times less than 'x', the ThT is initially quenching the precursor pheomelanin fluorescence via collisional then static quenching. Once the pheomelanin starts forming, the ThT becomes intercalated in-between the sheets of pheomelanin. This restricts the rotation of the free rotor and increases the radiative emission of ThT.

4.3.3 Sigmoidal fitting of fixed point, time-series, data

Monitoring the fluorescence intensity over time has revealed a rise in intensity that shares a similar shape to a sigmoidal function. Two different sigmoidal functions were fitted to assess whether the trend does follow a sigmoidal function, which performs best and to quantify the kinetics of sheet formation.

Two functions were fitted to the emission data. The first has its roots in determining the change in populations of animals and peoples [99] and is called the logistic function. This function was used by Sutter et al. [91] when quantifying the kinetics of eumelanin sheet formation. The second function used is called the Hill function, formulated by Archibald Hill in 1910 to describe O_2 binding of haemoglobin. [102] The rationale for using the Hill function stems from the uneven nature of the function. The Logistic function has an inverse mirror symmetry about the half maximum value.

Logistic Function Fitting

Sample	I(0)	α	k ($mins^{-1}$)	$t_0(mins)$	χ^2
Pheo + ThT	-0.200	1.13	0.061	31.06	0.99
Sub. Pheo	-0.002	0.83	0.092	28.83	0.93
Div. ThT + TYR	0.012	0.84	0.083	31.65	0.97
Deconvoluted	-0.110	1.04	0.060	32.08	0.99

Hill Function Fitted

Sample	I(0)	α	n	$t_0(mins)$	χ^2
Pheo + ThT	0.03	1.01	2.64	39.86	0.99
Sub. Pheo	0.12	0.88	3.21	33.09	0.93
Div. ThT + TYR	0.11	0.92	2.98	35.71	0.97
Deconvoluted	0.08	0.99	2.54	39.24	0.99

Table 4.1: The table contains the fitted values from fitting the Logistic and Hill functions to the data in figure 4.9.

The Hill function half maximum value is closer to the origin value, so the initial rise of the function occurs sooner and the point where the function plateaus is further from the half maximum value. Referring to the fixed-point data of Figure 4.6(b) and 4.7(a), it can be seen that the half maximum value is not evenly positioned between the initial rise point and the plateau point. Therefore, it is reasonable to attempt fitting to the Hill function.

Both functions fit well to the measured data (Figure 4.9(a) & (b)) with both obtaining χ^2 values of 0.99 (Table 4.1) and good residuals. The Hill function has performed better as the fitted values correlate better with the observable features of the data. The parameters t_0 are meant to be the positions where the function reaches half maximum. From the graph, the half maximum is reached at around 35 mins (given the plateau is closer to 0.9) which both functions fail to match with the Logistic function being around 5 mins under and the Hill function being around 5 mins over. The asymptotes for the Hill function are closer to those of the data as the Logistic function places the lower limit at -0.2, which is not realistic, and the upper limit is over 0.2 above where the data terminates.

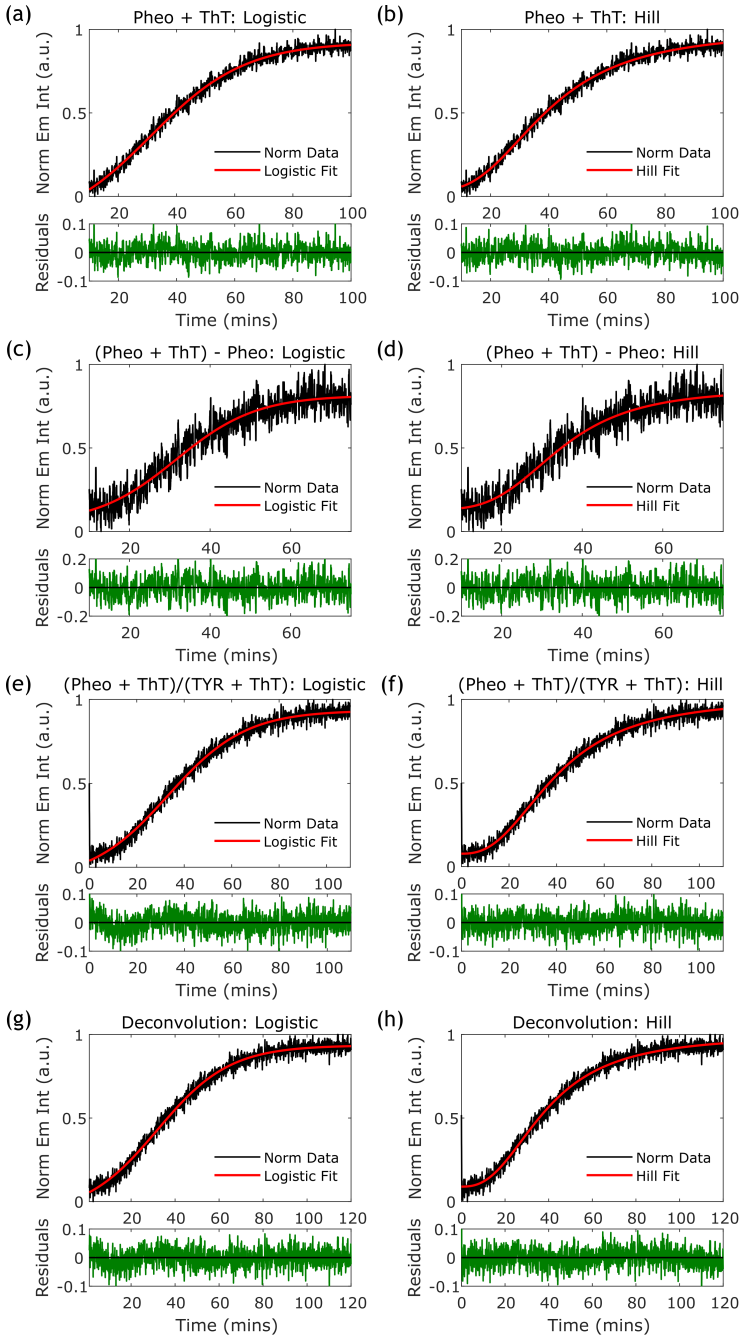

Figure 4.9: Time series data, from Figure 4.7(a), of Pheo with ThT (at 750 u/ml tyrosinase). The sigmoidal Logistic and Hill function fits are shown along with the residuals. (a, b) are for the measured data while (c, d) are for the measured data after subtraction of the intrinsic response of pheomelanin. For (e, f) the responses of a mixture of ThT with tyrosinase and a mixture of pheomelanin with ThT were divided. The mixture of ThT and tyrosinase response was used to deconvolute the response in (g, h) from the pheomelanin with ThT response.

The closer match of the Hill function to the data would suggest that the mechanism behind the ThT intercalation follows the cooperative binding model. This is where the affinity for binding is determined by the prior existence of binding. The Hill coefficient has been linked to the number of binding sites [104] with a value greater than one indicating that there are multiple binding sites. [104] Within the context of these experiments, the Hill coefficient describes the number of ThT molecules that are being intercalated.

Typically, the Hill function is used to describe the binding of a ligand to an enzyme or receptor. Figure 4.9(a) & (b) is illustrative of the intercalation of ThT within sheets and is not strictly analogous to the enzyme/ligand binding system. However, the generation of sheets follows the formation of cysteinyldopa which is through the enzymatic activity of tyrosinase so the intercalation of ThT within sheets will depend on a process that would normally be described by the Hill function. This interpretation agrees with the change in kinetics seen in Figure 4.7(a) as a change in enzyme concentration alters the sigmoidal profile of ThT emission.

From Figure 4.7(b) it is known that the intrinsic pheomelanin sample has its own fluorescence response. While the intensity of this signal is around seven times lower than when ThT is added, it is still a significant fluorescence emission. Understanding that the intrinsic response of pheomelanin could have affected the measurements, the emission from pheomelanin was subtracted from the pheomelanin with ThT data (Figure 4.10(b)). This is similar to subtracting the background signal and Figure 4.9(c) and (d) shows the result of fitting the Logistic and Hill functions to the subtracted data.

The process has caused the time to plateau to decrease and, at later times, the emission intensity decreases. A consequence of the pheomelanin emission continuing to increase while the pheomelanin with ThT response plateaus. While this may indicate that the pheomelanin structures are delaminating, the fact that the sample precipitates particles upon centrifugation suggest that this is just a consequence of the subtraction method and does not speak to an underlying photophysical process. In addition a simple subtraction ignores the likely existence of energy transfer between pheomelanin and ThT which could not be described by a linear addition of fluorescence.

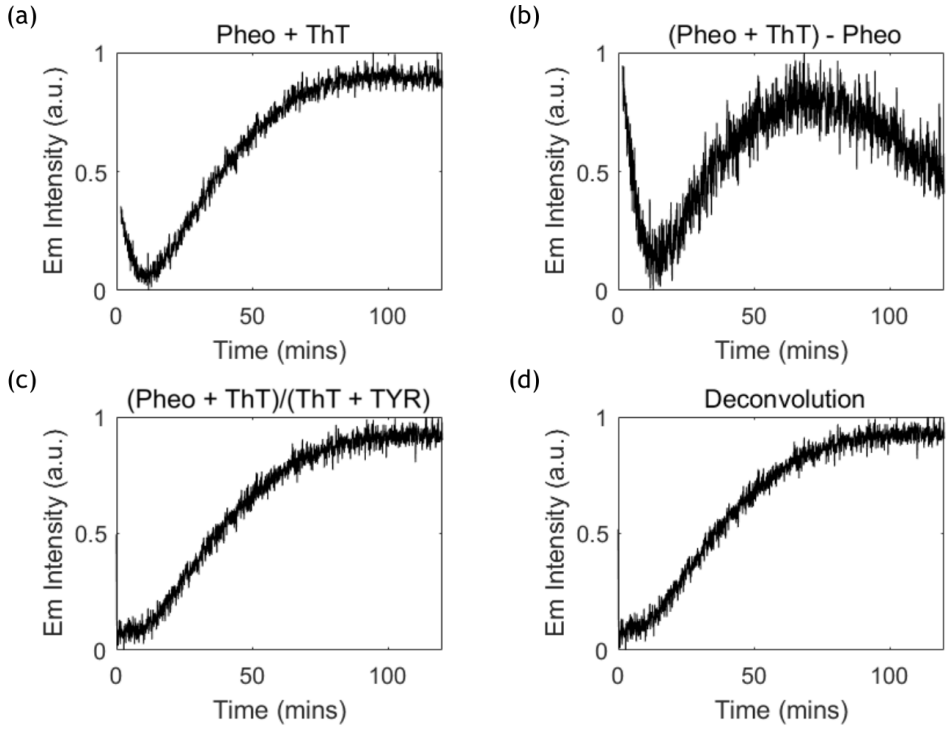

Figure 4.10: (a) Plot showing the measured pheomelanin with ThT trend. (b) The pheomelanin with ThT data after subtracting the intrinsic pheomelanin response, (c) dividing the response of ThT and tyrosinase and (d) deconvolution with the ThT and tyrosinase data. All data was normalised from 0 to 1.

By subtracting the intrinsic response of pheomelanin from the melanin/ThT data, the kinetics have changed. The values fitted via the Logistic and Hill functions show that processing the data in this way speeds up the time the signal takes to reach a plateau (Table 4.1). The time to reach half maximum is less with the logistic function fitting to 28.83 mins ($\sim$ 2 mins shorter than the unprocessed data) while the Hill function has reduced by 7 mins. The rate parameter for the logistical function has increased by $\sim$ 0.02 mins^{-1} while the Hill functions cooperative parameter has increased by $\sim$ 0.6. The goodness of the fit (χ^2) has decreased to 0.93 but the residuals still maintain an even distribution about the zero line.

In subtracting the intrinsic pheomelanin response from the pheomelanin with ThT data, the signal to noise ratio has increased. This can be seen in Figure 4.9(c) and (d) as well as the higher limits of the residuals plot, from 0.1 in Figure 4.9(a) & (b), to 0.2 in Figure 4.9(c) & (d). This would result in a change of the χ^2 value without disrupting the even randomness of the residual plot.

Despite the change in response, subtracting the intrinsic signal has had on the kinetics of the fixed-point measurement data, the emission intensity still conforms to a rising sigmoidal function. This is strong evidence in favour of sheet structure formation as the intrinsic pheomelanin fluorescence cannot solely explain the rise in emission intensity. However, subtracting the pheomelanin response from the pheomelanin/ThT data did not remove the initial decline in fluorescence (Figure 4.10(b)), which is related to the photophysical dynamics of the free dye molecule.

From Figure 4.7(b) it can be seen that the steep decrease in emission intensity, at the start, closely matches the initial response of a solution of tyrosinase with ThT. It is likely that the same mechanism is occurring within each sample so the TYR with ThT signal can be used to remove the initial decrease in intensity from the pheo with ThT data. Unlike the method used for the intrinsic pheomelanin response, the TYR with ThT data cannot be subtracted as this would result in negative intensity values, which has no rational reasoning for. Instead, the TYR with ThT data is treated like the solvent correction of a spectrophotometer.

For a spectrophotometer, the measured signal is divided by the reference signal in order to correct the measured signal from the absorption of the solvent. It is necessary to divide the signals since the measured response is not just a superposition of the analyte and solvent. Considering the possible quenching and energy transfer effects, it is reasonable to correct the pheo with ThT signal by dividing with the TYR with ThT signal.

Dividing the two signals has reduced the presence of the initial intensity decrease and helped recover the lower plateau region, which should be at a constant intensity level as the sheets have not started forming yet. Dividing by the response from a mixture of TYR and ThT has helped recover a more representative start to the kinetics of sheet structure formation.

The loss of the initial signal decrease has altered the I(0) value for the Logistic fit as it is now a positive value. The other three parameters are closer to the response resulting from subtracting the intrinsic pheomelanin signal (Table 4.1). When the Hill function was fitted to the data (Figure 4.9(f)) The value of I(0) closely matches the value from subtracting the pheomelanin response (Figure 4.9(d)) while the other parameters are different from the other fits of Figure 4.9(a-d). By dividing the TYR with ThT data from the pheo with ThT data (4.10(c)), the values of α, n and t_0 now lie in-between the values obtained from Figure 4.9(a-d).

In exploring another way to correct the measured signal, the pheo with ThT signal was deconvoluted with the response of the TYR with ThT Figure 4.9(g) & (h). Like the other correction methods used, deconvolution has retained the sigmoidal rise in intensity and has also removed the initial drop in intensity.

Fitting to the logistic and Hill equations, to the deconvoluted signal, it is clear that the Hill equation has performed better as the residuals show. Despite the good χ^2 values, the Logistic fit performs poorly at times under 20 mins and the starting value (I(0)) is negative. The fitted values obtained bear a close similarity to those of the original fitting, (Figure 4.9(a) & (b)) where there was no correction applied. Performing deconvolution has also not resulted in a decrease in intensity at later times.

Assuming a coupled system, deconvolution shows that the kinetics are not perturbed drastically by the quenching effects of the free dye since the fitted sigmoidal values do not change much from the measured data. The major change is the starting value (I(0)) where the initial decrease in intensity is not present. This implies that at later times the quenching effect of the free dye does not affect the response of intercalated ThT. This would tie in with the quenching mechanics mention earlier and may increase the confidence in the use of deconvolution to correct the measured data.

Sample	Pheo + ThT	Sub. Pheo	Div. ThT + TYR	Deconvolution
t_0 (mins)	33.47	33.17	37.80	36.35

Table 4.2: The time taken to reach half maximum for the time series data in figure 4.10. The values were determined from the graphs themselves by finding the time value at the half maximum point.

Regardless of the method used it is clear from the comparisons of the fitting functions, that the Hill function fits the data better as the residuals are better than the Logistic function fits and the half maximum values are closer to the actual value of t_0 (Table 4.2). Using the Hill function to fit the time-series data has consistently produced a corporative coefficient value above one which suggests that more than one ThT molecule is intercalating within the sheets of pheomelanin. Moving on from fluorescence intensity measurements, the fluorescence decays of melanin samples with ThT were measured in order to investigate the interaction of ThT and melanins in more detail.

4.4 Lifetime Time-Series

4.4.1 Control measurements

Previous measurements of ThT within the sheets of eumelanin did not extend to lifetime measurements [91], but before investigating solutions of pheomelanin, a control measurement was performed. This helped illustrate the change in lifetime values when the ThT molecule becomes restricted and was facilitated by measuring the free dye in water and 99% glycerol. While the increased viscosity of glycerol impacts the photophysics differently than when intercalated within sheets, the decays of Figure 4.11 provide useful information that help with the interpretation of lifetime decays of melanin with ThT.

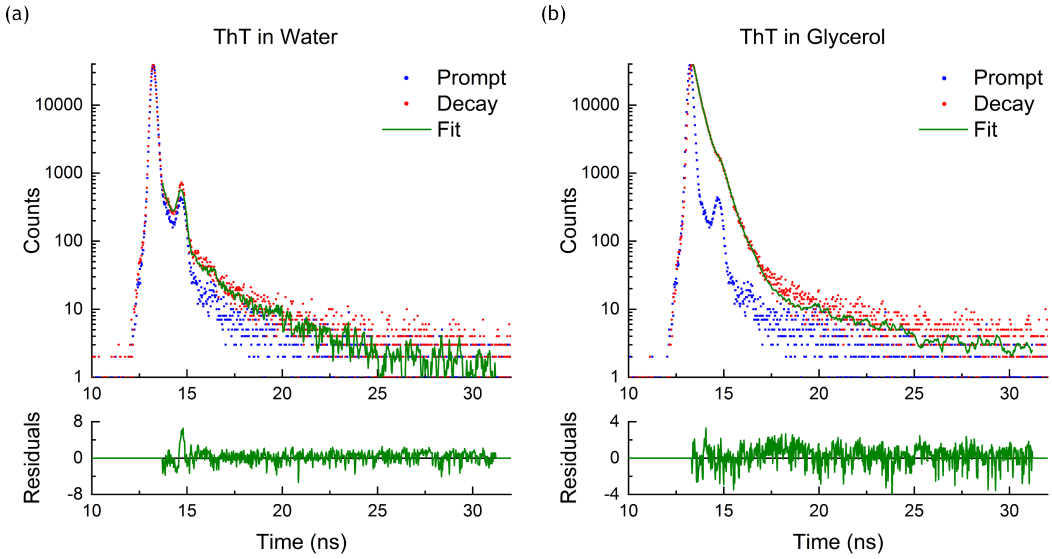

Figure 4.11: Lifetime decays for ThT in (a) water and in (b) glycerol (99%). The residuals are plotted underneath.

Sample	τ_1 (ns)	τ_2 (ns)	B_1 (%)	B_2 (%)	Shift (ns)	A	χ^2
ThT in water	0.037	1.81	99.28	0.72	-0.037	−0.06	1.91
ThT in glycerol	0.216	0.49	54.91	45.09	-0.015	0.25	1.37

Table 4.3: The fitted parameters values for the two-exponential model fitted to the decays of Figure 4.11.

From the profile of the decays in Figure 4.11, it is clear that the glycerol has altered the fluorescence decays. The decays were fitted to a 2-exponential model and resulted in χ^2 values above 1.2. Fitting to more exponentials did reduce the χ^2 values but resulted in two time components approaching equality and with the relative amplitude values being the inverse equivalent of each other. While the fitting algorithm achieved a minimum, the fitted values lose their physical meaning, when this occurs. It is a sign that too many components are being.

The higher χ^2 values from Table 4.3 is likely due to the torsional angle (Figure 4.1) having multiple values, thus generating a distribution of lifetime values. The glycerol is restricting the ThT rotor but there is no angle preference; unlike sheet intercalation where $\theta = 0$ is the dominant configuration. To help improve the fitting the number of data points was increased until 40,000 peak count [48] had been reached. This would help the fit for ThT in water as the second component has such a small contribution to the decay.

Time (mins)	τ_1 (ns)	τ_2 (ns)	B_1 (%)	B_2 (%)	Shift (ns)	A	χ^2
0	0.039	1.43	98.21	1.79	0.149	1.83	1.66
128	0.028	1.74	98.43	1.58	−0.020	1.71	1.71

Table 4.4: The fitted parameters for the two-exponential decay function used to fit the decays of tyrosinase with ThT, at time 0 mins and 128 mins.

The χ^2 values have been improved by increasing the number of photon counts, but the χ^2 values lie above an acceptable 1.2. This may indicate that a different method is needed to adequately describe the decay, like lifetime distribution fitting or using the general relaxation function. However, for the purposes of interpreting the fluorescence decays of melanins with ThT, a multi-exponential model provided an understanding of how the time components changed upon being restricted.

Having gained a better understanding of the fluorescence decay of ThT, in different viscosity solvents, the next control measurement involved replicating the time-series measurements of Figure 4.7(b) by recording the fluorescence lifetime decay of ThT with tyrosinase and intrinsic pheomelanin over time.

Figure 4.12 reveals how little the lifetime decay changes over time, when the ThT was mixed with tyrosinase, in dilute water. Comparing the 2-exponential fit for the first and last decay Table 4.4 shows little significant change. While τ_2 increases from 1.43ns to 1.74ns, the high χ^2 values diminishes the significance of this change. Importantly, each decay exhibits a very short component around 0.03ns and a longer component above 1 ns with the short component dominating the decay with over 98% relative amplitude. While it is difficult to increase the confidence in these fittings, it may be possible that the increase in lifetime of τ_2 (and drop in B_2) is related to the change in emission intensity seen with the tyrosinase with ThT sample of Figure 4.7(b).

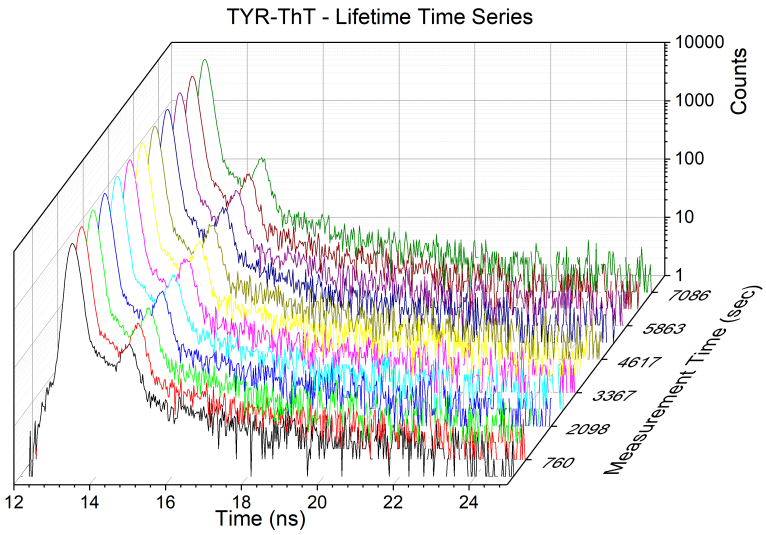

Figure 4.12: Waterfall plot showing the fluorescence decays, over time, for a sample of ThT and tyrosinase.

4.4.2 Pheomelanin lifetime time-series

Looking at the response of intrinsic pheomelanin, over time, reveals a different fluorescence decay to that of the free ThT dye, but is similar to previous melanin lifetime decays seen earlier (Chapter 3). From Figure 4.13 the pheomelanin decay has a dominant short component along with two or three longer components, that increase in prominence over time.

An inherent difficulty of measuring melanin's fluorescence decay is that it takes a relatively long time, as melanins are known to have a low quantum yield value. [19] In measuring the fluorescence lifetimes, over time, a compromise had to be made between achieving high photon counts, that aid fitting, and maximising the number of measurements over time which gives better insights into the kinetics of the lifetime components.

An additional complication to recording lifetime measurements occurs due to the dynamic nature of the system being measured. As the measurement proceeds, different molecular species are being created which contribute their own lifetime components to the final decay profile. Having shorter measurement times would mitigate this effect. However, there won't be enough photon counts to provide reasonable fitting of the multi-exponential function. The best compromise was found to be limiting measurements to around 15 mins ($\sim$ 1000 counts).

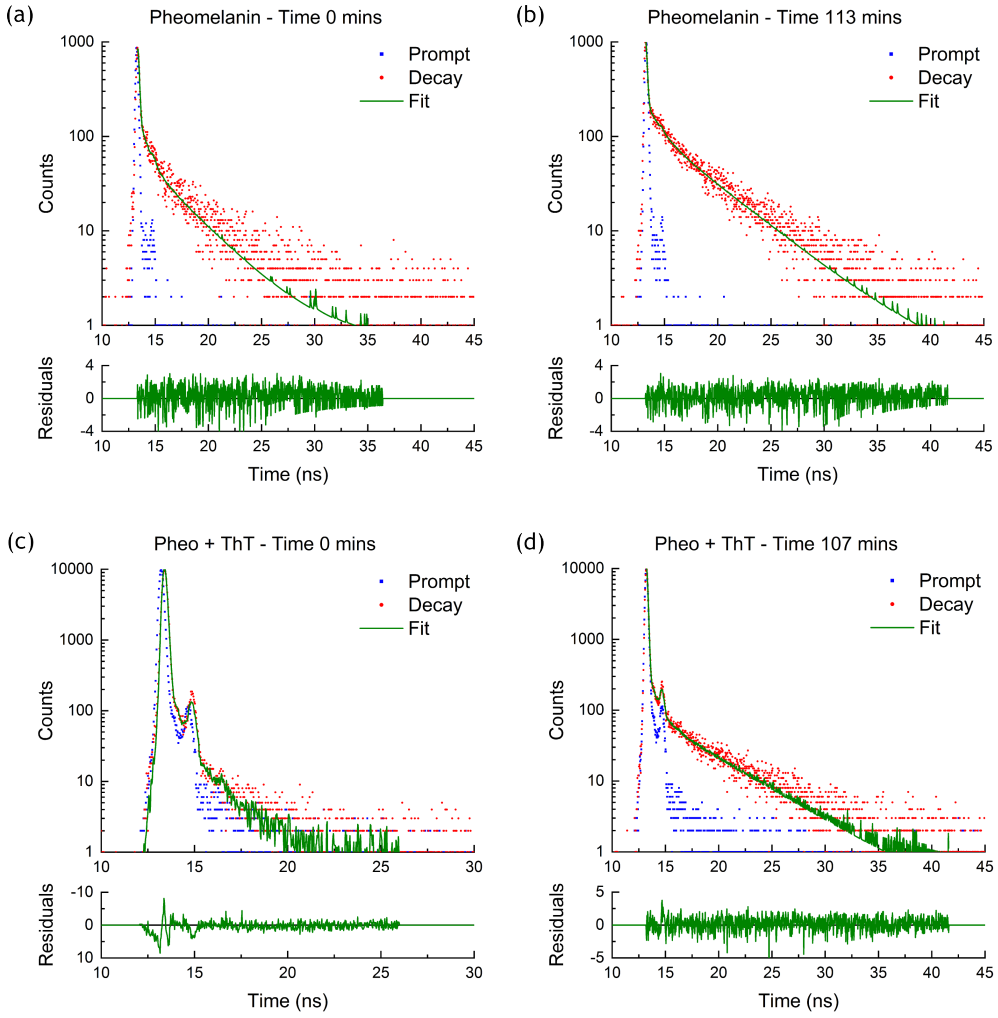

Figure 4.13: The fluorescence decays for pheomelanin at (a) 0 mins and (b) 113 mins. The fluorescence decays for pheomelanin with ThT at (c) 0 mins and (d) 107 mins. The decays are initially fitted to a 2-exponential model (a & c). At later times, the decays need a 3-exponential model to fit the data (b & d).

The decays were fitted to a three exponential function and, for intrinsic pheomelanin, revealed a short component $\langle 55\,ps \rangle$ (Appendix C) that begins as the dominant time component but is replaced by the third time component after 37 mins (Figure 4.14(a)). The third time component begins at 3.8 ns then rises to 4.58 ns after 22 mins, reaching nearly 5 ns by the end of the time-series (Table 4.5). This increase occurs later than the intensity rise seen with the intrinsic pheomelanin fluorescence emission time series data of Figure 4.7(b). As discussed, the number of data points is limited by the need to acquire sufficient photon counts which re-

Pheomelanin

Time (mins)	τ_1 (ns)	τ_2 (ns)	τ_3 (ns)	B_1 (%)	B_2 (%)	B_3 (%)	χ^2
0	0.037	0.70	3.80	52.80	12.40	34.79	1.69
127	0.043	1.11	4.93	34.55	11.65	53.80	1.26

Pheomelanin + ThT

Time (mins)	τ_1 (ns)	τ_2 (ns)	τ_3 (ns)	B_1 (%)	B_2 (%)	B_3 (%)	χ^2
0	0.022	1.50		99.05	0.95		1.65
107	0.022	1.21	5.49	92.12	1.98	5.90	1.23

Table 4.5: Top shows the time component and relative amplitude values fitted to the lifetime decays of Figure 4.13(a) and (b). Bottom shows the values from fitting a two and three exponential decay model to the decay data of Figure 4.13(c) and (d).

sults in much of the early kinetics being grouped into two/three time-series data points, so it is likely that the rise in τ_3 occurs at earlier times. However, the lifetime value of τ_3 at 22 mins is close to the beginning value of 3.8 ns, suggesting that there is an extended delay from when the lifetime measurement can detect the change in the kinetics. Otherwise, the small changes in lifetimes are being suppressed by the distribution of lifetime components during the initial 15 mins of measurement.

The first and second components do not change significantly (Figure 4.14(a)) and suggest that τ_3 is the main component that reflects the progression of pheomelanogenesis. This is reflected in the relative amplitude values as B_3 is the only component to increase with time. B_2 remains consistent throughout the measurement and B_1 mirrors the change in B_3. Since τ_1 does not change significantly and B_1 decreases, with time, it is plausible that τ_1 represents the initial benzothiazole compounds and oligomers that are formed during pheomelanogenesis. From the time-resolved spectroscopic measurements of El-Nahhas et al. [22] and Corani et al. [62], it is known that monomers of benzothiazole can have short lifetime components and that dimer groupings have dominant ($\sim 74\%$) short components (~ 0.31 ps). [62] As the larger structures are formed, the smaller oligomers are consumed, which would result in a decrease of B_1 and an increase in B_3.

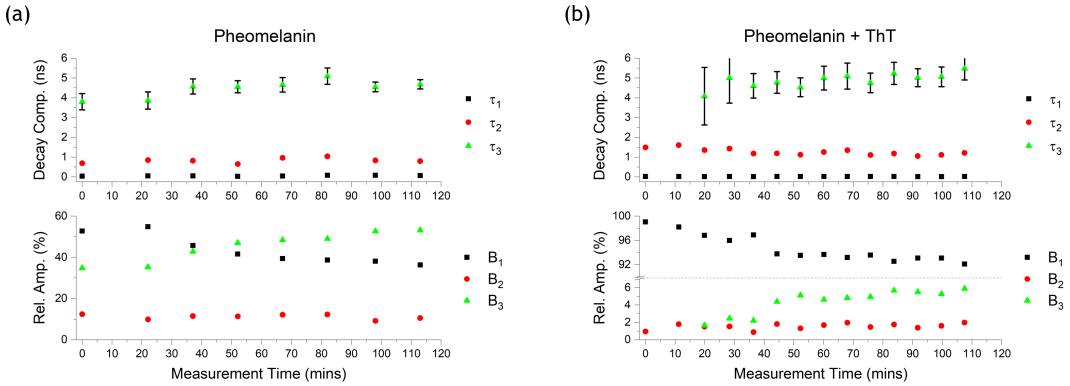

Figure 4.14: Plots of the fitted decay components and corresponding relative amplitude values, over time, for fluorescence decay measurements of (a) pheomelanin and (b) pheomelanin with ThT. Typical error bars (3X SD) are included for τ_3.

Introducing ThT at the start of pheomelanogenesis has altered the fitted parameters with the short component of the free ThT dominating the fluorescence decay components. Fitting, for the first two time points, was with a two-exponential model as three exponentials resulted in unrealistic relative amplitude values. The later decays were fitted to a three-exponential model and share some similarity with the time components of the intrinsic pheomelanin decays.

There is a short component in the tens of picoseconds, a longer component around 1.0 ns – 1.5 ns and a third component around 5ns. The relative amplitudes are similar to the intrinsic data, in that B_2 does not change significantly while B_3 increases with time and B_1 mirrors the rise in B_3. The addition of ThT has increased B_1 to over 90%. This is related to the free ThT dye that hasn't intercalated within the sheets of pheomelanin. The second time component is higher than the intrinsic pheomelanin τ_2 component and is more like the 1.8ns value of the free ThT lifetime decays. Starting at 1.5 ns, the second component from Figure 4.14(b) decreases to around 1.15 ns which would agree with the decrease in lifetime seen with the glycerol measurements of Figure 4.11(b), indicating restriction of the free rotor of ThT but not full intercalation. The third component, τ_3, starts at $\sim$ 4 ns and increases to $\sim$ 5 ns which is, on average, around 0.2 ns higher than the intrinsic pheomelanin values. The standard error bars for τ_3 are shown in Figure 4.14 and highlight the decrease in heterogeneity as the ThT becomes intercalated within the sheets of pheomelanin.

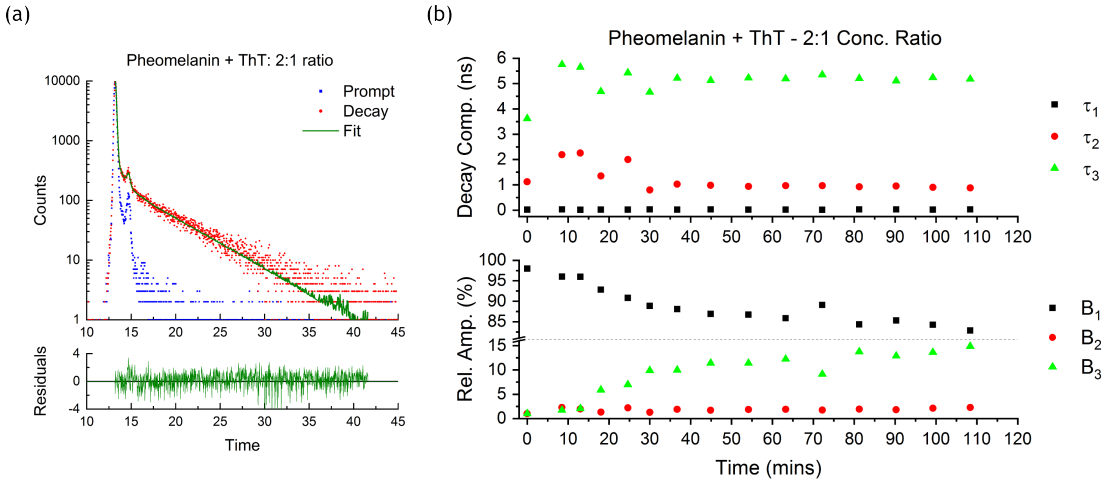

Figure 4.15: The lifetime decay for a sample of pheomelanin with ThT, where the concentration of pheomelanin was doubled. (a) The fluorescence lifetime decay (t = 108 mins) fitted to a three-exponential model, including residuals. (b) The fitted values, over time, for the time components and relative amplitudes.

While convenient, the three-exponential model used to fit the lifetime decays is only an approximation and the fitted values do not represent distinct fluorescent species but rather contributions from multiple photophysical effects and fluorophores. For well defined systems, each lifetime component can be attributed to a distinct species but the melanin with ThT system is not well defined and the structure-spectroscopy relationship of melanins are still not fully understood. [3] As such it is possible that there are more subtle details which multi-exponential fitting cannot reveal. Analysing the decays with the lifetime distribution fitting or using the general relaxation model could help uncover such details. [63, 114]

The dominance of τ_1 in Figure 4.14(b) suggests that there is an abundance of free dye. To explore this possibility the concentration of pheomelanin was doubled, such that the concentration ratio of pheomelanin to ThT was 2:1 (Figure 4.15). The initial values for τ_2 and τ_3 in Figure 4.15(b) are far less consistent but the relative amplitude follows the same trend seen in Figure 4.14(b). Doubling the concentration of pheomelanin (Figure 4.15) creates more sheet structures that the ThT dye can intercalate with and should amplify the changes to the relative amplitude values. Increasing the amount of pheomelanin will increase the intrinsic emission signal. However, the quantum yield of the restricted ThT is greater than melanins (Figure 4.5) so the lifetime values will be driven primarily by the ThT fluorescence.

1:1 ratio of pheomelanin to ThT

Time (mins)	τ_1 (ns)	τ_2 (ns)	τ_3 (ns)	B_1 (%)	B_2 (%)	B_3 (%)	χ^2
107	0.022	1.21	5.49	92.12	1.98	5.90	1.23

2:1 ratio of pheomelanin to ThT

Time (mins)	τ_1 (ns)	τ_2 (ns)	τ_3 (ns)	B_1 (%)	B_2 (%)	B_3 (%)	χ^2
108	0.026	0.88	5.18	82.85	2.28	14.88	1.28

Table 4.6: Values from fitting a three-exponential model to the decays of figure 4.13(d) and 4.15(a). Doubling the concentration of pheomelanin has decreased τ_2 and increased B_3 which indicate even more ThT restriction within the structures of pheomelanin.

Consistent with there being more ThT restriction, the decrease in the value of τ_2 is greater than the 1:1 ratio sample (Table 4.6) as the lifetime value drops from 1.21 ns to 0.88 ns while B_3 has more than doubled in value. An interesting occurrence in Figure 4.15(b) is in the change of τ_2 and τ_3 during the first 25 mins. Unlike the fluorescence decays of Figure 4.14(b), it was possible to fit a three-exponential model. However, it is difficult to say, with confidence, whether time components follow a trend. It is possible to see τ_1 and τ_3 increase in value before decreasing to a plateau value, after 30 mins. The behaviour of τ_2 and τ_3, during this initial time period, is representative of the complex mixture of molecular species present before the majority of sheets are formed. With L-DOPA and Cyst reacting into cysteinyldopa and subsequent oligomers, the interaction of each with ThT could be responsible for this behaviour. While it is not possible to identify exactly what is producing these lifetime components, the rapid change in values does indicate a dynamic system until the sheet formation takes over and the values stabilise.

4.4.3 Eumelanin lifetime time-series

From the fluorescence lifetime time-series data it is possible to identify ThT intercalation within sheet structures of pheomelanin. With this outcome, it is possible to draw comparisons with eumelanin to see if both pigments share similar lifetime kinetics when charting the intercalation of ThT within sheet structures. Figure 4.16 shows the lifetime decays for a sample of eumelanin and a sample of eumelanin with ThT, at the start and end of the melanogenesis process. The decay produced at the end of the time-series measurement (Figure 4.16(d)) is again dominated by the short time component of free ThT and shows a larger time component extending out towards 80 ns.

Fitting multi-exponential functions to the decays produces time component and relative amplitude values which share some similarity with the pheomelanin with ThT decays. The shortest component dominates the decay with over 85% contribution and B_3 gradually increasing to over 10% (Table 4.7). Different to the pheomelanin with ThT decays is the slight increase of τ_2 from 0.46 ns to 0.90 ns (0.84% to 4.31%). Also different is the almost linear increase of τ_3 which may reflect a slower formation of sheets since there is no enzyme present.

Eumelanin

Time (mins)	τ_1 (ns)	τ_2 (ns)	τ_3 (ns)	B_1 (%)	B_2 (%)	B_3 (%)	χ^2
0	0.024	0.63	4.10	75.37	7.59	17.04	1.13
115	0.336	1.54	6.33	44.37	42.10	14.53	1.03

Eumelanin + ThT

Time (mins)	τ_1 (ns)	τ_2 (ns)	τ_3 (ns)	B_1 (%)	B_2 (%)	B_3 (%)	χ^2
0	0.019		1.51	99.49		0.51	1.40
110	0.021	0.90	5.91	84.99	4.31	10.70	1.15

Table 4.7: The parameter values from fitting two/three-exponential functions to the fluorescence decay plots of eumelanin and eumelanin with ThT, at the start and end of the eumelanogenesis process.

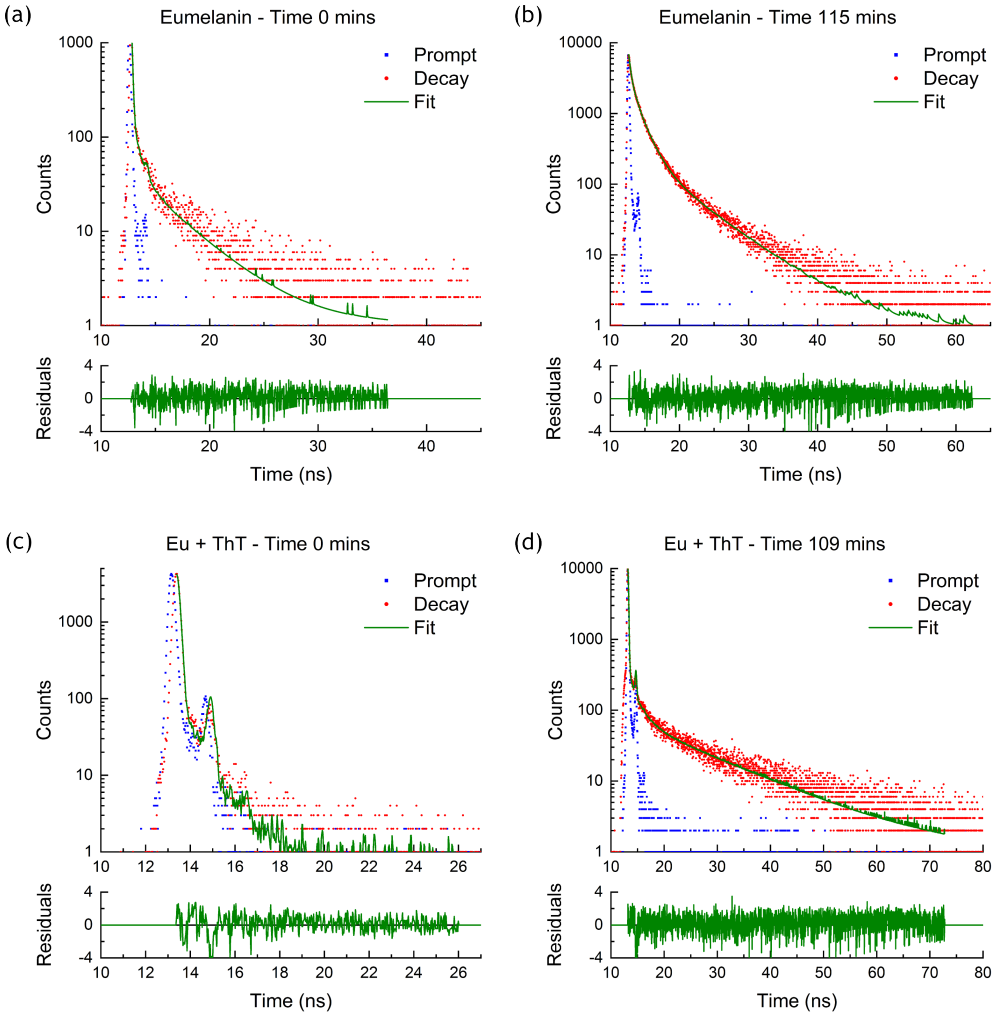

Figure 4.16: Fluorescence decays for a sample of eumelanin at time (a) 0 mins and (b) 115 mins. Underneath are the fluorescence decays for a sample of eumelanin with ThT at time (c) 0 mins and (d) 109 mins into the pheomelanogenesis process.

Comparing τ_3 between the intrinsic eumelanin trend (Figure 4.17(a)) and eumelanin with ThT trend (Figure 4.17(b)) emphasises the photophysical change the ThT goes through. Intrinsic eumelanin has a long time component which begins at 4.10 ns and increases to 6.33 ns (Table 4.7). When ThT is added, τ_3 begins with a value similar to the free ThT time component of Figure 4.11(a). Over time, the value of τ_3 increases to 5.91 ns. While this final value is similar to the intrinsic eumelanin value, the change to the kinetics and the greater quantum yield of intercalated ThT (Figure 4.5) indicate that τ_3 is related to the intercalation of ThT within the sheets of melanins.

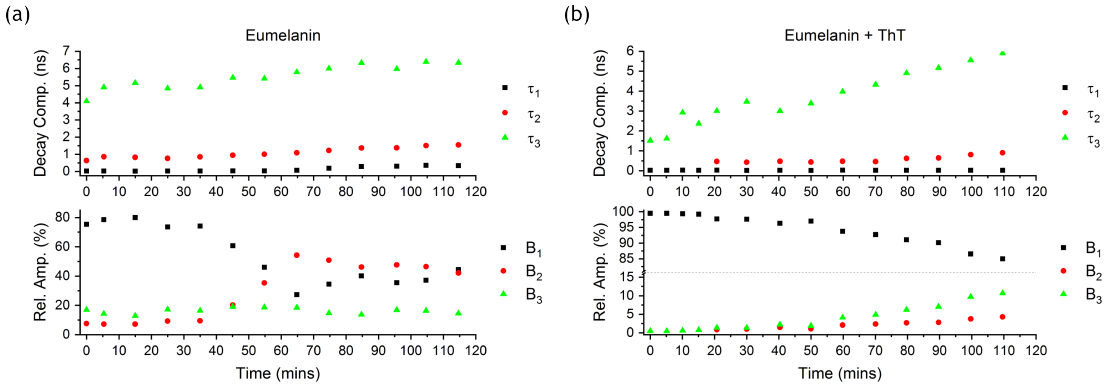

Figure 4.17: Plot of fitted time components and relative amplitudes values for (a) eumelanin and (b) eumelanin with ThT, over time.

4.4.4 Understanding the complex interaction of melanin and ThT

One of the difficulties in interpreting the values from reconvolution analysis is in understanding how the photophysics of ThT and melanins interact with each other. While it is reasonable to assign τ_3 to the intercalation of ThT, within the sheets of melanin, the issue is that ThT is reported to have a maximum lifetime value of 3 ns. [97] Looking at the intrinsic melanin data it would be reasonable to conclude that τ_3 is solely from melanin and not ThT. However, the trend seen in Figure 4.17(b) links the free dye component of 1.5 ns with the longer time values achieved at later measurement times.

If it is assumed that ThT cannot achieve a lifetime value above 3 ns and that the lifetime kinetics of intrinsic melanin cannot solely explain the fitted values, then there must exist a mechanism which explains the trends observed in Figures 4.13 - 4.17. Given the overlapping spectral bands of melanin and ThT, and the excited state charge transfer process present in both molecules, it is proposed that the intercalated ThT forms a coupled excited state with the sheets of melanin. This exciplex, or excited complex, model would explain how the lifetime of intercalated ThT exceeds 3 ns. The formation of an excited complex would also explain the red-shift seen in Figure 4.6(a) as this red-shift is not observed during Aβ fibril formation. [95]

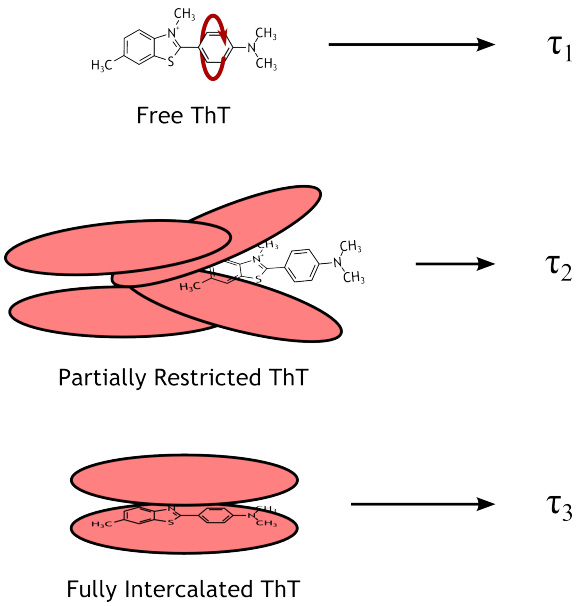

Figure 4.18: Physical interpretation for each lifetime components observed. The shortest component being attributed to the fast relaxation of free ThT. The longest component stems from fully intercalated ThT molecules with excited state coupling to pheomelanin structures which increases the lifetime values. Partially restricted ThT molecules are assigned the second lifetime component.

Figure 4.18 summarises the photophysical rational for each time component with τ_3 beening attributed to fully intercalated ThT, within the sheets of melanin, and τ_1 stemming from the remaining free ThT that is in the solution. The second time component is attributed to ThT that is only partially restricted within the sheets of melanin. The values for τ_2 are under 1.8 ns, expected for free ThT, and are more like the lifetime values for ThT in glycerol. Additionally, it is possible that the stacking of oligomer sheets is not ordered. The work of Micillo et al. [115] shows how the eumelanin components of DHI form π-stacked structures while DHICA form 'bundles'. This could explain how the τ_2 shares a greater similarity to the values of ThT in glycerol. It is also possible that inclusion of ThT impacts the sheet's formation since the sheets would be spaced further apart. However, the exact perturbations to melanin's sheet structures are outwith the scope of these measurements and present an interesting avenue for further investigations.

4.5 Disassembly Of Melanin Particles

The evidence for sheet structure formation in pheomelanin has been demonstrated via monitoring the fluorescence of the structure probe thioflavin T. It has been shown that the photophysical interaction of ThT and pheomelanin is complex as there are quenching effects and possible exciplex formation processes occurring. A further consideration include the different structural forms of pheomelanin. Assuming the hierarchical build-up model of melanin formation, proposed by Büngeler et al. [27], then it is possible that the ThT is becoming intercalated with the layers of larger structures as opposed to in between individual sheets. In order to examine this possibility, reacted samples of pheomelanin and ThT where disassembled with NaOH and the sub-units measured via spectroscopy.

4.5.1 Sepia test

The original work on melanin disassembly was carried out by Ju et al. [106] as they investigate the Janus effect in melanin. Their work focused on Sepia melanin, so before disassembling melanins with ThT, a test sample of Sepia melanin was disassembled to practice the protocol and provide a point of comparison for later measurements with synthetic melanins.

Figure 4.19(a) shows the absorption spectrum for Sepia melanin before and after disassembly. The two dilutions of Sepia melanin were prepared as to match the OD value of the disassembled spectra, at the two excitation wavelengths used for the fluorescence studies. Disassembling Sepia melanin has altered the spectrum significantly as the disassembled sample has less absorption in the visible and near infrared. The featureless form of the spectra has remained, but the distribution of absorbers has shifted towards the UV. This would coincide with a change to smaller sub-units of melanin and is evidence that the protocol has successfully disassembled Sepia melanin.

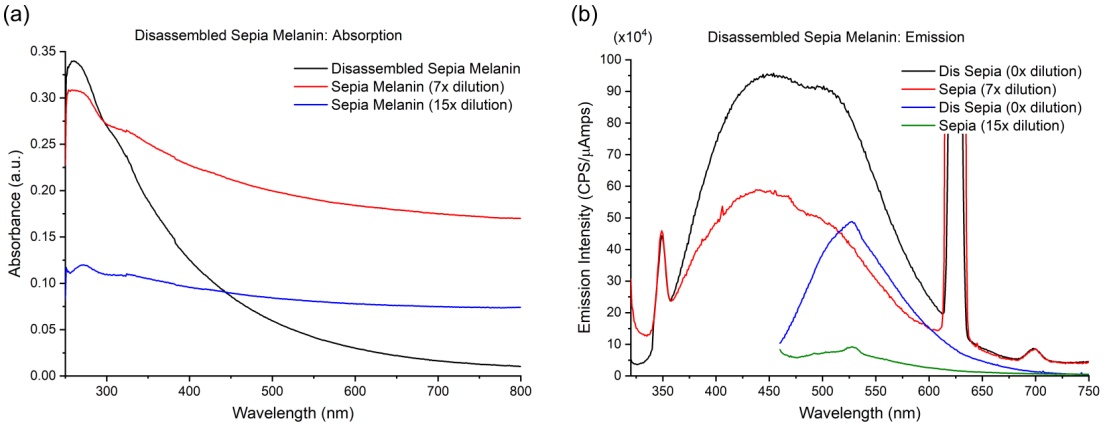

Figure 4.19: (a) Absorption spectrum of Sepia melanin before and after being processed via the disassembly protocol. The Sepia melanin was measured at two different dilutions as to match the disassembled absorption value at the wavelengths the fluorescence measurements would be excited at. (b) Emission spectra for sepia melanin before disassembly when excited at 350 nm (red) and 450 nm (green). The dilutions are the same as in the absorption plot. Included are the spectra for disassembled Sepia melanin which show a significant increase in emission intensity, which follows the work of Ju et al. [106].

The work of Ju et al. [106] excited the samples at 350 nm, which has been done for the samples in Figure 4.19(b). Included in Figure 4.19(b) are the fluorescence spectra when excited at 450 nm as this was the excitation wavelength used to monitor the ThT dye molecules and would be necessary for comparison with the synthetic melanin samples.

In their paper, Ju et al. illustrated that upon disassembly, the emission intensity increases and is indicative of smaller units that don't possess the same non-radiative pathways as the larger particles. For both excitation wavelengths, the emission intensity increases upon disassembly. Since the Sepia melanin was diluted to match the absorption value at the excitation wavelengths, the change in emission intensity must be due to the increased fluorescence of the smaller melanin sub-units and not a consequence of concentration variations. The increase in fluorescence intensity agrees with the results of Ju et al. and confirms that this sample of Sepia melanin was successfully disassembled.

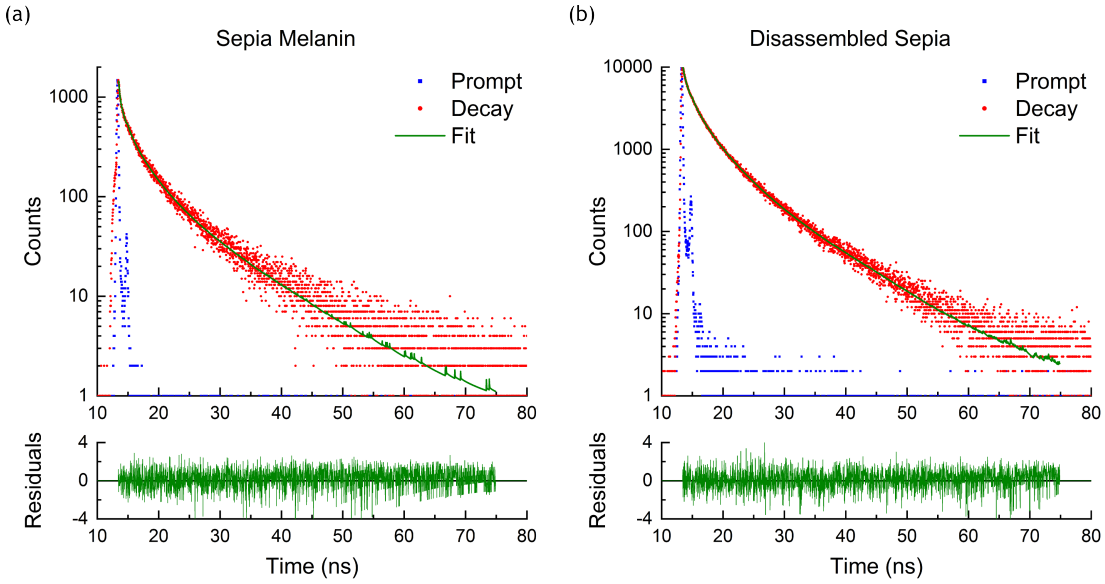

Figure 4.20: Decays for Sepia melanin (a) before and (c) after the disassembly process, excited at 437 nm and emission at 490 nm. The decays were fitted to a five-exponential model and the residuals are included underneath.

The absorption and emission spectra agree with the work by Ju et al. However, they do not extend their investigation towards fluorescence lifetime measurements. As a result, Figure 4.20 is our only point of comparison when comparing the lifetime decays of disassembled samples of melanins with ThT. As seen in chapter 3 the fluorescence lifetime decay of melanin is complex, requiring multiple exponentials to achieve a good fit. Fitting to the decays was done with a five-exponential model, which performed better than the four-exponential function used in Figure 3.18.

While needing an extra exponential to achieve a good fit, the time component values are similar to those seen in Figure 3.18. There is a short component in the tens of picoseconds range, a component around 0.5 ns, another one around 3 ns - 4 ns and a long component close to 10 ns (Table 4.8). The Sepia melanin has an extra component around 1.5 ns. Disassembling the Sepia melanin has done little to change the time component values which implies that the fluorescent species producing these lifetimes have not been structurally altered and that the formation of larger structures are not closely linked to the fluorescence lifetimes and are simply assemblies of distinct photophysical entities. What has changed are the relative amplitudes with the shortest and longest components decreasing in percentage upon disassembly while the other

Parameter	Sepia Before	Disassembled Sepia
τ_1 (ns)	0.02	0.04
τ_2 (ns)	0.55	0.59
τ_3 (ns)	1.36	1.70
τ_4 (ns)	3.41	3.97
τ_5 (ns)	10.34	9.49
B_1 (%)	10.66	4.39
B_2 (%)	6.84	9.57
B_3 (%)	8.66	18.85
B_4 (%)	34.32	40.70
B_5 (%)	39.53	26.49
Shift (ns)	0.11	0.04
A	0.57	0.25
χ^2	1.18	1.14

Table 4.8: The parameter values from fitting a five-exponential model to the decays of Figure 4.20.

components increase in percentage. As disassembling produces smaller melanin structures, the change in relative amplitudes would suggest that the shortest and longest time components are linked to the larger structures of melanin, while the middle time components are more closely linked to the smaller structures of melanin.

A change to the proportion of short lifetime component can be explained by the break-up of larger particles. The work of Corani et al. [62] shows how monomer unit lifetimes, of DHICA, change from predominantly nanosecond components to sub-nanosecond components upon formation of larger oligomer units. [62] This they attribute to the increase in pathways that allow for intra- and interunit proton transfer. Their earlier publication [116] demonstrated the opposite effect with DHI as the lifetime values increased with oligomerisation. The measurements with DHI and DHICA only extended to dimeric or tetrameric models but the proton transfer processes underpinning the change in lifetime values could be scaled to the larger structures of melanin featured in Figure 4.19 and 4.20.

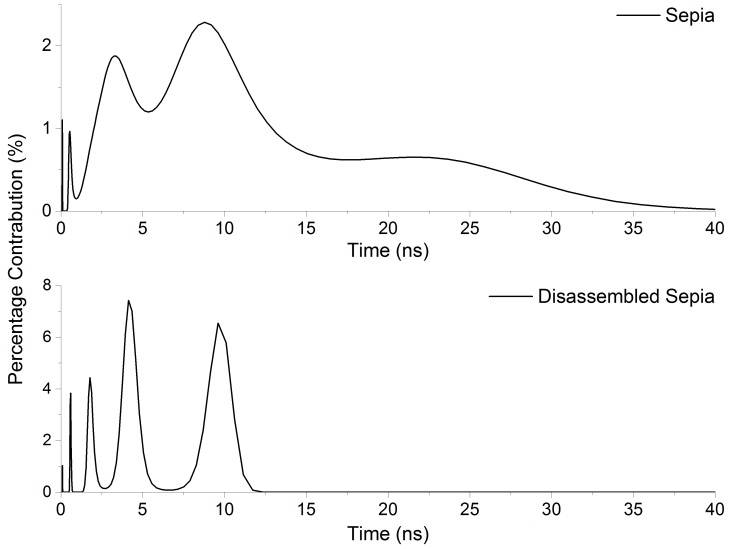

Figure 4.21: Plots showing the distribution of lifetimes that MEM extrapolated from the decays of Sepia and the disassembled Sepia melanin.

The increase in the amplitude of time component B_2, B_3 and B_4 can be explained by the breakdown of larger melanin structures which reduces the pathways that alter the lifetime values. Essentially, disassembly increases the number of emitters that are closer to the monomer form and with that comes the increase in the relative amplitude of the lifetime components that are closer to the monomer's lifetime values.

Using multi-exponential functions to fit Sepia melanin fluorescence decays has highlighted some interesting features when the Sepia particles are disassembled. However, as discussed in Chapter 3 the lifetime decays of melanin may favour fitting to a distribution of lifetimes and given the change in amplitudes seen in Table 4.8 invites the question as to how the lifetime distributions change after disassembling the melanin particles.

	τ (ns)	$d\tau$ (ns)	Flux (%)	dFlux	Width (ns)	dWidth (ns)
Sepia	0.10	0.02	5.19	1.53	0.01	0.02
	0.58	0.24	8.61	5.84	0.11	0.32
	3.11	0.80	40.91	14.51	1.10	0.82
	9.64	2.58	38.40	15.94	3.01	3.27
	24.25	10.47	6.82	9.70	4.26	10.25
Disassembled Sepia	0.10	0.02	2.25	1.28	0.004	0.02
	0.59	0.07	10.33	4.94	0.03	0.08
	1.83	0.36	21.44	8.05	0.20	0.57
	4.20	0.51	40.87	8.81	0.50	0.95
	9.58	0.84	24.73	6.60	0.76	1.62

Table 4.9: The values relating to the main peaks obtained from analysing the lifetime data using MEM.

Figure 4.21 shows the distribution of lifetimes from analysing the decays of Figure 4.20 with maximum entropy method (MEM). Table 4.9 corresponds to the peak values along with their percentage contribution to the total distribution and the FWHM value. The main difference between the distributions of Figure 4.21 is the narrowing of the peaks when the Sepia melanin is disassembled. Before disassembly, the lifetime distributions consist of five peaks (three quite broad) that extend from the picoseconds to around 40 ns. After disassembling the Sepia melanin, the peaks become narrower and there is a change in the peak position. The broad peak centred around 24 ns has disappeared while more peaks have appeared at lower lifetime values. The narrowing of the lifetime distribution peaks would imply that the variety of fluorescent species is less, which can be explained by the breakdown of larger Sepia melanin particles into smaller sub-units that have less structural variety and less long-range coupling interaction.

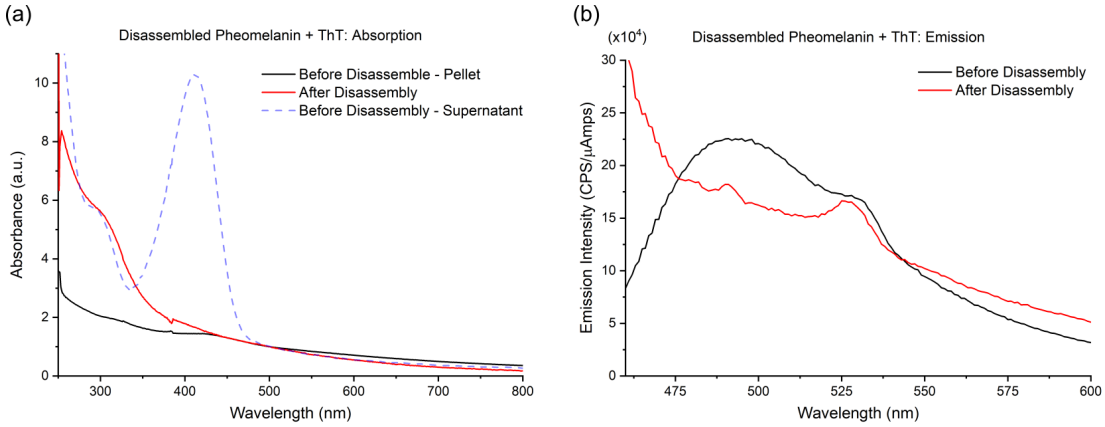

Figure 4.22: (a) Absorption spectra for pheomelanin with ThT, before and after the disassembly process. Included is the absorption spectrum from the supernatant after centrifugation of the sample before the disassemble protocol was started. The absorption spectra were normalised to the OD value at 500 nm to allow for better comparison of the spectral profile. (b) The emission spectra for pheomelanin before and after disassembly. [112]

4.5.2 Disassembly of ThT intercalated pheomelanin structures

Having determined the successful disassembly of Sepia melanin and how the lifetime decay changes, measurements moved on to pheomelanin samples with ThT in order to probe deeper into the interaction of ThT and the forming pheomelanin structures. [112]

Before disassembling the pheomelanin with ThT sample, the free ThT was removed via centrifugation. Figure 4.22(a) shows the absorption of the supernatant before disassembly and the absorption peak of ThT is visible near 400 nm confirming the presence of free ThT and its separation from the pheomelanin pellet. Upon disassembling the pelleted pheomelanin, the absorption spectra show a greater degree of UV absorbers which agrees with what was seen for Sepia melanin. The absorption spectra of Figure 4.22(a) have been normalised to the OD value at 500 nm in order to emphasise this change.

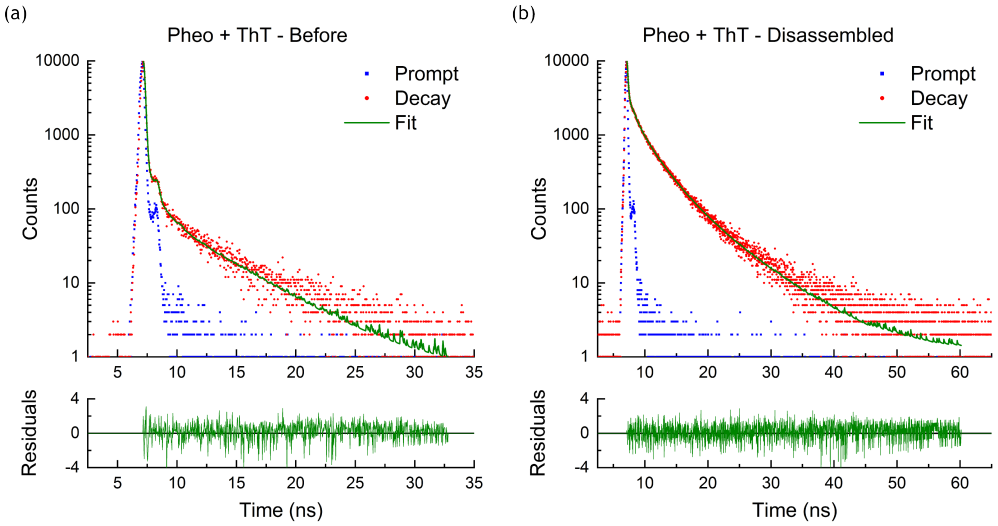

Figure 4.23: Lifetime decays for (a) pheomelanin with ThT before disassembly and (b) after disassembly. A three-exponential model has been fitted to (a) while the disassembled decay of (b) needed a four-exponential model to fit the decay. The residuals are included underneath.

The fluorescence emission spectra are shown in Figure 4.22(b) with the characteristic 490 nm peak of intercalated ThT noticeably absent from the disassembled spectrum. This is clear evidence that the ThT is no longer being restricted within the sheets of pheomelanin. While the 490 nm peak is not present, in the disassembled spectra, the presence of Rayleigh scatter does appear to be more significant as the absorption continues to rise when approaching the excitation wavelength. There also exists a slight peak near 480 nm which may be the result of partially restricted ThT dye molecules that were freed from the sheets of pheomelanin, but are still electrostatically attached to the disassembled structures of pheomelanin.

The time-resolved fluorescence decay for pheomelanin with ThT before disassembly (Figure 4.23) is similar to the decays seen in Section 4.4.2. The values obtained from fitting a three-exponential model to the decay (Table 4.10) are also in keeping with the values obtained in Section 4.4.2. Disassembling the pheomelanin with ThT sample has produced a fluorescence decay which mirrors the disassembled Sepia melanin sample of Figure 4.20. Reconvolution analysis required a four-exponential model, producing an extra component at 6.75 ns. This is consistent with that seen for Sepia melanin.

Parameter	Pheo Before	Disassembled Pheo
τ_1 (ns)	0.05	0.11
τ_2 (ns)	0.99	1.01
τ_3 (ns)	4.64	2.87
τ_4 (ns)		6.75
B_1 (%)	88.10	28.15
B_2 (%)	4.15	13.99
B_3 (%)	7.75	37.51
B_4 (%)		20.36
Shift (ns)	0.04	−0.03
A	0.60	1.16
χ^2	1.15	1.04

Table 4.10: The values obtained by fitting a three/four-exponential model to the fluorescence decays of pheomelanin with ThT before and after disassembly.

Disassembling melanins in the manner described by Ju et al. does not break down all the melanin particles to their individual oligomers. [106] This implies that multiple layers or larger structures are needed to restrict ThT such that the torsional angle is zero degrees and the 490 nm peak can appear. As mentioned in the previous chapter, Büngeler et al. [27] have proposed the three-step, four-level hierarchical build-up mechanism for melanin's structure. After forming oligomeric sheet structures, these sheets then π-stack to form protoparticle which then go on to form onion-like type-A particles. Given the disassembly results, it may be that the ThT becomes restricted after multiple oligomeric sheets are stacked or become intercalated within the type-A particle as the protoparticle come together to form the larger structure.

4.6 Conclusion

Utilising the same methodology as Sutter et al. [91] the sheet sensing fluorescent probe thioflavin T has been used to detect the formation of sheets during pheomelanogenesis. Mixing the fluorescent dye in with a solution of reacting pheomelanin has produced a distinctive peak at 490 nm (Figure 4.5) which conforms to the peak seen when the ThT molecule is intercalated within sheet structures. Monitoring the fluorescence spectrum over time shows an increase in fluorescence intensity that conforms to both the logistic and Hill sigmoidal functions. This behaviour is consistent with that seen for eumelanin [91] and the fibril formation of β-Amyloid [95] and remained regardless of how the signal was corrected for the intrinsic fluorescence from pheomelanin and the quenching effects of free ThT.

Time-resolved fluorescence decay measurements revealed a complex decay profile that required a multi-exponential model to fit the data. Analysis of the fluorescence decays indicates that the time component of 4-5 ns stems from the intercalated ThT, which lead to the conclusion that the radiative rate of intercalated ThT had been altered by the surrounding pheomelanin sheets. This finding illustrates the complexity of the melanin/dye interaction and presents opportunities for further study.

The second time component is attributed to partially restricted ThT that may be attached near the surface of the pheomelanin sheet particles, as illustrated in Figure 4.18. The shortest time component has lifetime values in the tens of picoseconds and is consistent with the decay of free ThT in water. Both fluorescence spectral measurements and time-resolved lifetime measurement demonstrate the existence of sheet structure formation during pheomelanogenesis.

Disassembling pheomelanin particles with ThT successfully released the dye molecules from within the sheets and further demonstrates that the rise in ThT emission stemmed from its intercalation within the sheet structures of pheomelanin. Since the disassembly process does not break down the melanin particles to their individual oligomers [106], and yet the characteristic 490 nm peak from intercalated ThT disappears, the implication is that multiple sheets are needed to restrict the ThT molecule. This may indicate that the ThT is being restricted by the protoparticle [27] structures as they come together to form the type-A particles.

The mixed system of ThT and melanins is photophysically complex and despite the convincing evidence reported here, there is more that could be done to understand the sheet structure formation of pheomelanin better. The primary focus should be on replicating these results with different structure dyes like Nile Red, Coumarin and Prodan to name a few. ThT's sheet sensing capabilities stem from a conformational change of its molecular structure so it would be important to use an extrinsic dye that operates via a different mechanism like solvent polarity. Extending measurements to include time-resolved emission spectra (TRES) would also facilitate deeper understanding of the photophysical interaction between extrinsic fluorophores and melanins. Relating to cancer sensing, it has been shown that there is a loss of structure when melanoma develops. [117–119] Taking this as a melanoma biomarker, ThT could be used to measure the change in structural order by measuring the fluorescence lifetime, of ThT, and comparing the fitted values of τ_3 with normal tissue.

Chapter 5

Toxicity Protocol Development

5.1 Introduction

The photophysics of melanins has been investigated with the aim of uncovering a significant spectral difference that would allow for a simpler, cost-effective, method for detecting melanoma. Initially, studies looked at the intrinsic response of the melanin biomacromolecules in order to identify spectroscopic differences. An extrinsic fluorophore was used to better understand and compare, sheet formation during melanogenesis. Indeed evidence points to the use of ThT fluorescence decay being a potential indicator of melanoma via the loss of sheet order. [117–119]

Over the past decade the use of metalic nanomaterials has expanded into multiple fields, including medical imaging. [120, 121] Their optical/plasmonic properties make them attractive for development of dual acting biosensors that can detect cancers and increase the local dose of radiotherapy. [122–125] Gold nanorods (GNR), with their plasmonic resonances in the red part of the visual spectrum, would in many ways be ideal for melanoma sensing as they can operate away from the highly UV absorbing melanins. The development of a nanoparticle biosensor [122, 125] hinges upon the nanoparticles low toxicity. [126] Hindered by the lack of a clear consensus, on how and why nanoparticles are toxic, [121, 126, 127] it is necessary to establish the degree of the nanorods toxic effects before the development of the biosensor could begin.

Both colourimetric and clonogenic toxicity assays were conducted with three types of GNR. Flow-cytometry and uptake studies were also performed in order to gain deeper insight into the toxicity of the nanorods. Larger GNR (bGNR) with the ligands 6-Mercaptohexanoic acid (MHA) and Poly(sodium 4-styrenesulfonate) (PSS) and smaller GNR (sGNR) with the MHA ligand were considered. Clonogenic results indicate that the sGNR-MHA perform better than the larger GNR. However, questions surrounding uptake, protein aggregation and cell damage suggest a more complicated bio-nanoparticle interface which could hinder the effectiveness of future GNR biosensors.

5.1.1 Nanoparticles

Nanotechnology revolves around the study and development of nanomaterials or nanoparticles. A nanoparticle is defined as a solid particle within the size range 1 nm - 100 nm and can be comprised of a wide variety of materials including carbon, metals, metal oxides, semiconductors and organic matter. [128–132]

Noble metal nanoparticles like gold and silver are some of the oldest nanomaterials used by humans with the Lycurgus Cup dating back to the late Roman period. [133] While these nanomaterials are still used for staining glass, they have also gained relevance within the biomedical field, due in large part to their plasmonic properties. [129] Their optical properties fall within the visible range of the spectrum and can be tuned by altering the size and shape of the particle. [134] These spectral/plasmonic properties have led researchers to develop noble metal nanoparticles for a range of biomedical applications, which is aided by relatively simple synthesis and ligand alteration chemistry. [120]

Applications for nanomaterials are varied and numerous. Within cosmetics, nanomaterials have been used to improve the effectiveness of sunscreens while certain nanomaterials are used to enhance the pigments of lipsticks. In toothpaste, silicon nanoparticles are added and act as abrasives to help remove plaque. Meanwhile, the electrical properties of nanomaterials are utilised in modern LED displays, and their small size makes them ideal as plate separators in mobile phone batteries. With their small size and numbers, nanomaterials offer a large surface area which makes them useful as catalysts, with the automotive industry using platinum nanoparticles to reduce the amount of rare metal used in the catalytic converter. [131]

The addition of nanomaterials has improved the mechanical properties of concrete, steel and ceramics. The addition of titanium dioxide nanoparticles to glass confers a sterilising and catalysing properties which help reduce volatile organic molecules. Mixing nanoparticles with paints has implemented hydrophobic properties which prove useful in preventing saltwater corrosion of metal pipes. While noble metal nanoparticles have uses within the biomedical fields of drug delivery, biosensors, radiosensitisation, photothermal therapy and immunotherapy, [124, 131, 132, 135–137] their uses extend beyond healthcare; examples include the treatment and cleaning of municipal/industrial wastewater, soil contamination, oil spills and decontamination of air. [131]

5.1.2 Gold nanorod biosensor

A proposed strategy for detecting melanoma, with GNR, hinges upon the surface energy transfer (SET) process. An important difference between SET and the more commonly known Förster Resonance Energy Transfer (FRET) is the effective range at which the energy transfer process occurs. According to Förster theory, the rate of FRET energy transfer has a $1/r^6$ dependence on the separation distance (r) while SET has a $1/r^4$ dependence. [20, 138] Since SET is dependent on the distance between the nanoparticle surface and fluorophore, it means the energy transfer process will only occur within 10s of nanometres of the nanoparticles surface. [138]

With SET as the fundamental mechanism, there has been the development of a cancer-specific biosensor which utilises the plasmonic properties and thiol-based conjugation techniques to attach complimentary oligonucleotides (cON) to the surface of gold nanorods. [125] The sequence used for the cON is complimentary to the messenger Ribonucleic Acid (mRNA) of the cancer cell. The mRNA is responsible for transferring the genetic information of the Deoxyribonucleic acid (DNA), that encodes proteins, out of the nucleus to the ribosomes where proteins are produced. [34] Since it is possible to identify which DNA sequences are responsible for a particular cancer it is conceivable to synthesise a complementary oligonucleotide sequence which will combine with the mRNA that is produced from the mutated DNA sequence.

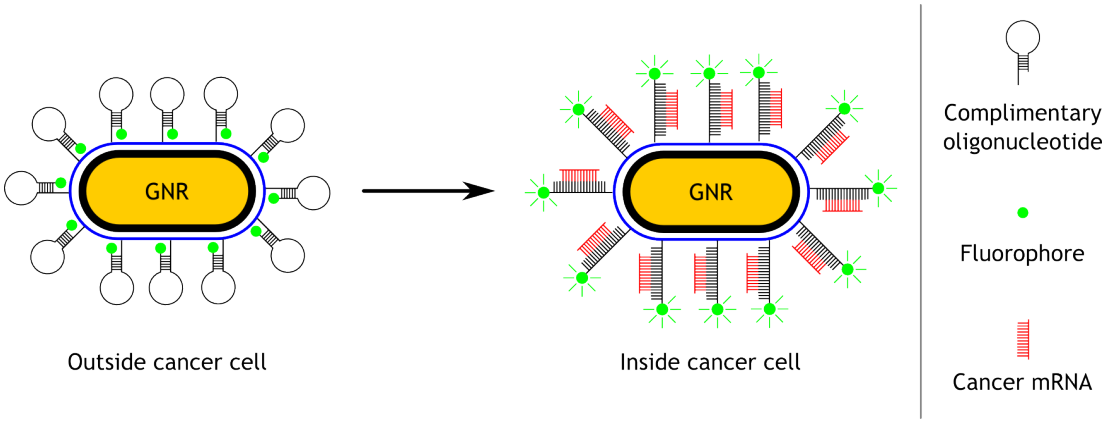

Figure 5.1: Gold nanorod-based biosensor for cancer sensing. [125] Hairpin oligonucleotides are conjugated to the surface of the nanorod. On the other end of the oligonucleotide, a fluorescent molecule is attached. In this configuration, the fluorophore's fluorescence is quenched by the nanoparticle's surface plasmon. Inside the cancer cell, the target mRNA interacts with the oligonucleotide and opens the hairpin structure. This structural change separates the fluorophore from the nanorod, allowing the fluorescence to be detected.

The cON, as shown in Figure 5.1, is in a hairpin configuration and the gold nanorod is attached to one end of the cON sequence, while the opposite end is attached to a fluorescent molecule, while maintaining a complimentary structure in a hairpin structure. Whist in this configuration, the dye molecule is in close proximity to the nanoparticle for energy transference. With the fluorescence of the dye being quenched by the nanoparticle, the biosensor is in an 'off' state. Upon entering the cancer cell, the biosensor will encounter the specific target mRNA oligonucleotide. This results in the hairpin oligonucleotide unfolding and separating the dye molecule from the nanorod. The length of the oligonucleotide is such that the dye molecule is no longer quenched by the nanoparticle and fluorescence is observed. The SET mechanism facilitates the biosensors operation and results in an 'on' and 'off' state. Outside the cancer cell, the biosensor is off, and no light is observed. Inside the cancer cell, the biosensor is on and a fluorescence signal is observed.

An advantage of this scheme is that it can be adapted to detect other types of cancer, and indeed other disease, since all that is required is changing the hairpin oligonucleotide sequence such that it is complementary to the target mRNA sequence. For example, it is known that $\sim$ 60% of melanoma cancers are the result of a mutation in the BRAF gene. [34] With the BRAF gene mutation as the target, a complementary oligonucleotide sequence could be synthesised and conjugated to the nanorods making a biosensor specific to melanoma that resulted from the BRAF mutation.

Due to the high atomic number of noble metal nanoparticles, both gold and silver can act as effective radiosensitisers. [124] A radiosensitiser is a compound or particle that increase the local dose of radiation which could allow for lower X-Ray energies to be used (keV as opposed to MeV) while still providing a therapeutic local dose to the tumour. [139] Combining the optical and atomic properties of noble metal nanoparticles, it is feasible that a gold nanorod-based biosensor could be synthesised which utilises a melanoma-specific BRAF complimentary mRNA sequence which provides the location of a tumour and then uses the same nanorods as radiosensitisers to treat the tumour with radiotherapy.

5.1.3 Nanoparticle optical properties

When a small metal particle is illuminated by an electromagnetic wave, the oscillating electric field exerts a force on the conduction electrons of the particle. This force displaces the electron cloud relative to the rest of the particle. [134] With an induced charge separation, there exists a coulombic restoring force that sets off oscillations of the electron cloud.

The oscillations of the electron cloud is referred to as dipole surface plasmon resonance (SPR), where the entire electron cloud moves together under the influence of the electric field (Figure 5.2). With larger particles, it is possible to have quadrupole resonance where half the electron cloud moves with the electric field and the other half moves against the electric field. [134] The oscillations of the electron cloud are related to electron density, effective electron mass, size and shape of charge distribution. [140]

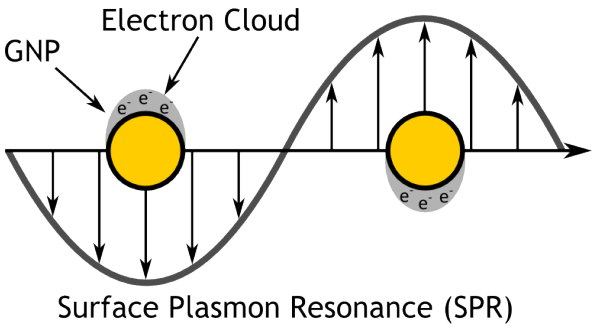

Figure 5.2: Oscillations of gold nanoparticle's electron cloud resulting from the interaction with the electric field component of an electromagnetic wave.

The absorption of a material is the attenuation of light, of intensity I_0, over a path length x. This can be written as a differential, shown in Equation 5.1:

$$\frac{dI(x)}{dx} = -NC_{ext}I(x) \tag{5.1}$$

Where N is the number of particles and C_{ext} is the extinction cross-section of a single particle. To obtain the absorption, Equation 5.1 is integrated:

$$A = log_{10}\frac{I_0}{I(x)} = \frac{NC_{ext}x}{2.303} \tag{5.2}$$

For spherical particles with a wavelength dependent dielectric [140] of the form $\varepsilon'(\lambda) + i\varepsilon''(\lambda)$ in a medium of dielectric function (ε_m), the extinction cross section is given by:

$$C_{ext} = \frac{24\pi^2 R^3 \varepsilon_m^{\frac{3}{2}}}{\lambda} \frac{\varepsilon''}{(\varepsilon' + 2\varepsilon_m)^2 + \varepsilon''^2} \tag{5.3}$$

The real and imaginary parts of the particles complex dielectric function, $\varepsilon'(\lambda)$ and, $\varepsilon''(\lambda)$ are dependent on the plasmon frequency (ω_p), from the surface plasmon resonance.

$$\lambda_p = \frac{2\pi c}{\omega_p} = \sqrt{\frac{4\pi^2 c^2 m^* \varepsilon_0}{Ne^2}} \tag{5.4}$$

The speed of light is c and m^* is the effective electron mass. From Equation 5.4 it is now clear what wavelengths the particles will absorb most strongly at. It should also be clear that the position of the absorption peak will depend on the electron density, effective mass of the electron and the geometry of the particle. [134, 140]

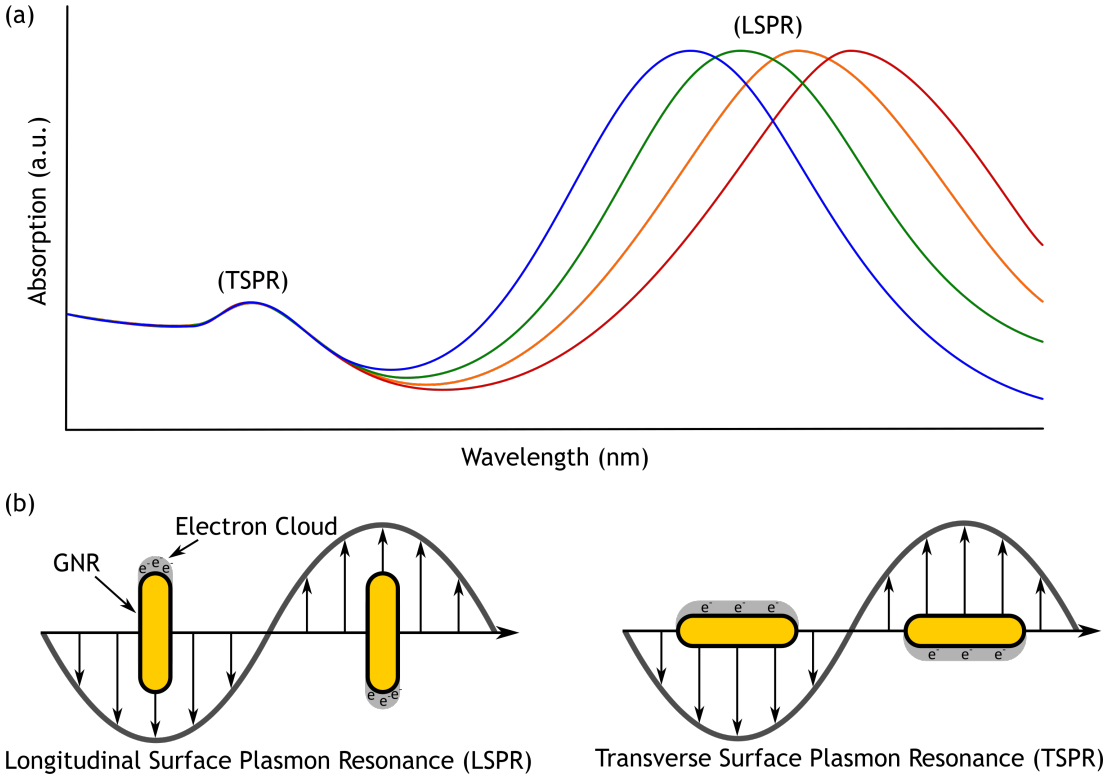

Figure 5.3: (a) The anisotropic shape of the nanorod results in two plasmonic resonance modes, the longitudinal surface plasmon resonance (LSPR) mode and the transverse surface plasmon resonance (TSPR) mode. Changing the aspect ratio of the nanorod increases the LSPR peak position. (b) Oscillations of gold nanorod's electron cloud resulting from the interaction with the electric field component of an electromagnetic wave.

Of the shapes available, the gold nanorod (GNR) has a high potential for biomedical imaging applications. [141–145] This is down to the relationship between the geometry and the surface plasmon absorption peak. Representative absorption spectra for a collection of different GNR are shown in Figure 5.3. The first peak is from the transverse surface plasmon resonance (TSPR) or the induced electron cloud oscillations parallel to the minor axis. The second peak is from the longitudinal surface plasmon resonance (LSPR) or the induced electron cloud oscillations parallel to the major axis. Figure 5.3 provides a visual description of the difference between LSPR and TSPR.

A change in the aspect ratio (the major axis length over the minor axis length) causes a significant change of the LSPR peak. This occurs because the volume occupied by the conduction electrons increases. [146] This makes the longitudinal axis much more polarisable than the transverse axis. From Figure 5.3 it can be seen that the transverse surface plasmon peak does not shift much. As a result, most applications tune the spectroscopic wavelengths to the LSPR peak. The advantage of using GNR over spheres is that the LSPR peaks are in the red part of the visible spectrum, with some nanorods extending out towards the NIR. [147] This is beneficial for medical imaging applications as this allows for the separation of the biosensors optical response from the mostly UV/visible response of tissue and melanins.

5.1.4 Nanoparticle synthesis

Multiple methods have been developed to synthesise metallic nanoparticles including bottom up approaches where the metal is deposited onto shaped substrates, which are dissolved to leave the metal nanoparticles. [120] Other techniques utilise electrochemical deposition or laser ablation, while some grow nanoparticles within inverse micelles. [140] Gold nanorods generally use the surfactant hexadecyltrimethylammonium bromide (CTAB) to direct the growth of gold onto the ends of the particle, [140] with wet-chemical techniques proving popular. [148]

GNR made with the wet-chemical, seed-mediated technique, involves the reduction of Au^{+3} ions to Au^{+1}. The technique starts with making a seed solution by reducing chloroauric acid with sodium borohydride, in the presence of the surfactant CTAB. The seeds are added to a growth solution of chloroauric acid, CTAB, silver nitrate and ascorbic acid. In the presence of CTAB, the ascorbic acid reduces Au^{+3} ions to Au^{+1} via Reaction 5.5. Then the reduction of Au^{+1} takes place through electron transfer at the surface of the seed particle (Reaction 5.6). [140]

$$AuCl_4^- + 2e^- \leftrightarrow AuCl_2^- + 2Cl^- \tag{5.5}$$

$$AuCl_2^- - CTAB_{mic} + Au_m \leftrightarrow Au_{m+1} - CTAB_{mic} + CTAB_{mic} + 2Cl^- \tag{5.6}$$

The Au seeds are encapsulated in CTAB, and the reduced Au ions are attached to CTAB micelles. The formation of the nanorods come from the collisions of the CTAB micelles and the seeds. Calculations of the potential distribution and potential gradient demonstrate that there is a faster rate of collisions at the tip of the nanorod which promotes anisotropic growth. [140]

The silver goes through reduction of Ag^{+1} to Ag^{0} at the Au surface via underpotential deposition. [149] This is where the surface of the Au lowers the potential needed to reduce Ag^{+1}. A greater positive shift in potential for silver deposition has been observed on the side facets. [150] This means that deposition of silver is quicker at the sides and slower at the ends. Therefore, nanorod formation is a result of quick silver deposition, followed by strong CTAB binding, to the sides of the seeds. This restricts Au growth to the ends allowing the formation of gold nanorods. Eventually, enough silver deposits at the ends to halt the growth process. By altering the Ag concentration, the length of the nanorods can be changed (Figure 5.9).

5.1.5 Nanoparticle toxicity

The optical properties, radiotherapeutic and oligonucleotide conjugation properties make gold nanorods an attractive foundation for a cancer biosensor. The first step in development involves measuring the toxic effect of gold nanorods. Although gold nanorods are frequently cited as being non-toxic the following will demonstrate this is actually not the case. It is well known that the shaping and stabilising ligand CTAB has a cytotoxic effect on cells. [121, 151, 152] While CTAB is necessary for the synthesis and optical tuning of the nanorods it needs to be replaced with a stabilising ligand that will not confer a toxic effect. Examples include sodium citrate, polystyrene sulfonate (PSS), polyethylene glycol (PEG), sodium polyacrylate acid (Na-PAA) and polyallylamine hydrochloride (PAH). [121, 151]

It is important to measure the toxicity in order to demonstrate both that the ligand exchange occurred and that the new coating does not confer a cytotoxic effect. This would also provide a point of comparison for later toxicity studies when the biosensor was functionalised with the oligonucleotide. Whilst the literature on nanoparticle toxicity is large, with some journals specialising [121] a consensus of the toxicity of gold nanoparticles and what mechanisms attribute to these toxic effects has not been concluded. [121, 126] The principle reasons for this uncertainty are two-fold; the first is the inherent complexity of the question and the second is due to the vastly varying protocols researchers are using in their studies.

Nanoparticle properties which affect toxicity include size, shape, surface chemistry and material. These features of the nanoparticle can then interact with the cell environment like medium proteins, the cell membrane and other organic material of the cell. Additionally, there will be differences between how different cell types respond to the nanoparticles, be they immune cell, cancer cells, skin, liver, heart cells. Another major part of the toxicity question surrounds the number of particles that are taken up by the cell. Nanoparticle uptake will be affected by the type of cell and how the nanoparticle interacts with the cell membrane. [121]

Given the number of parameters, it is clear that further investigation is required to understand the nanoparticle/biological interface better. While variation is at the heart of research, upon review of the available literature on nanoparticle toxicity, it has become apparent that standardisation is required in the field in order for results to be compared; both in the methodologies used and in the formation of a nanoparticle toxicity database. [121, 126, 127, 153] Additionally, these standards would help mitigate experimental issues commonly found in the literature like the apparent dependence of toxicity on particle size which was found to be due to the different sedimentation behaviour of the nanoparticles. [154]

These methodologies would need validating against a standard, which also does not exist, as certain measurements may not be adequate or need careful consideration of the results. An example of this would be the use of colourimetric assays, like MTT and alamar blue. These use a molecule that changes its optical properties when the cell metabolises it. By measuring the absorption, or fluorescence, of the cell solution and charting the change in wavelength, it is possible to quantify the toxic effects of the target substance. However, since the nanomaterials have their own intrinsic optical properties, which lie within the same wavelength range as the metabolite, they introduce significant errors and complicate the analysis of the results. [155]

Further complications involve distinguishing between cytotoxic effects and damaging effects. While a cytotoxic particle will induce necrosis or apoptosis of the cell, another particle may induce cell damage. This could involve the formation of ROS which affects how the cell functions but might not kill the cell. The damaged cell could still undergo mitosis, passing whatever mutations on. [126]

In order to measure the long-term effects of nanoparticles (on cells) it is necessary to monitor the degree of cell proliferation. Most colourimetric assays only distinguish between alive and dead cells. For these reasons, it was necessary to conduct clonogenic assays on the nanoparticles as well as colourimetric assays. [156] The clonogenic assay plates the treated cells onto Petri dishes, and lets cell colonies grow over a two-week period, at which point the dishes are washed and stained. The number, size, shape and intensity of colour all provide information on how the cells have responded to the nanoparticles. [156]

5.2 Methodology

5.2.1 Nanoparticle synthesis & ligand exchange

Nanorod synthesis

Chemicals Gold (III) chloride trihydrate ($HAuCl_4$. $3H_2O$) ($\geq$ 49.0% Au basis). Hexadecyltrimethylammonium bromide (CTAB) ($\geq$ 99%). Sodium borohydride ($NaBH_4$) ($\geq$ 98%). Silver nitrate ($AgNO_3$) ($\geq$ 99%). Ascorbic acid (A.A.). Hydrochloric acid (HCl, 0.5 M). All chemicals were acquired from Sigma-Aldrich at their high possible purities and distilled water was used thoughout.

Large metallic gold nanorods (bGNR) were synthesised using an adapted protocol developed by the Murphy group (Figure 5.4). [149] The synthesis of gold nanorods is a two-step procedure starting with the synthesis of CTAB stabilised gold nanospheres ($\sim$ 2 nm). These particles act as the seeding particle for the nanorod growth step. In the growth solution, the CTAB preferentially binds to the edge surfaces, restricting gold deposition to the ends of the particle and thus forming nanorod shaped gold particles.

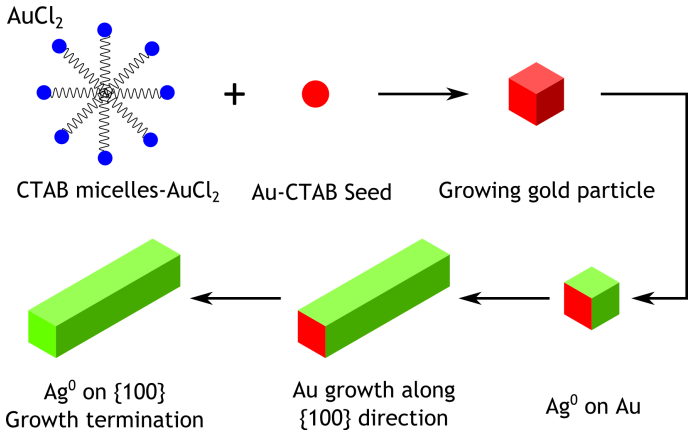

Figure 5.4: Stages of gold nanorod synthesis. Beginning with the synthesis of gold seed particles, the nanorod is formed by the selective deposition of gold onto the ends of the nanoparticle. The deposition of silver gradually caps the ends of the nanorod which prevents the continued growth of the nanorod.

Specifically, the seeds were synthesised by mixing a solution of CTAB (0.2 M, 7.5 ml) with $HAuCl_4$ (1 mM, 2.5 ml), then the strong reducing agent $NaBH_4$ (10 mM, 0.6 ml) was added. The $NaBH_4$ solution was prepared with 5^{o}C water, and the solution was kept in the fridge until needed. During the addition of $NaBH_4$, the seed solution was mixed with a stir bar (10 mm x 5 mm) at a rapid speed. The rapid stirring was necessary to ensure the $NaBH_4$ quickly distributed throughout the mixture and reduce all of the gold salt. After addition of the $NaBH_4$ solution, the seed mixture was left at room temperature, in a dark cupboard for 3 hours to allow the seed particles to form.

The growth solution comprised of CTAB (0.2 M, 250 ml) and $HAuCl_4$ (1 mM, 250 ml) mixed together to make a 500 ml batch of nanorods. To this mixture of CTAB and gold salt, $\sim$ 15 ml of $AgNO_3$ (4 mM) was added. Altering the silver concentration changes the rate at which the silver deposits onto the nanorod, which results in different aspect ratios of the final nanorod. Given the slower growth of the nanorods the weaker reducing agent, ascorbic acid (77.8 mM, 3.5 ml) was used to reduce the $Au^{3+}$to Au^{1+}. The reduction of the gold salt was indicated by the change of colour from $HAuCl_4$ reddish-orange to a colourless solution. Once the growth solution had turned clear, 400 μl of the seed solution was added. There was no mixing performed after the addition of the seeds. Instead, the nanorod solution was left to react overnight, at room temperature, in the dark. The solution was kept away from direct sunlight as the gold is photosensitive.

Smaller gold nanorods (sGNR) were synthesised using the approach by Moustafa et al. [157] where there are no seed particles. Rather, the strong reducing agent ($NaBH_4$) was added to the growth solution directly. This reduced some of the gold immediately, which formed seeding particles within the growth solution. The protocol used the same volumes and concentrations as the larger nanorod growth solution except the $NaBH_4$ (750 μL, 10 mM)was added directly to the growth solution and the solution was made acidic with 9 ml (0.5 M) of HCl such that the pH was within 1 – 1.15.

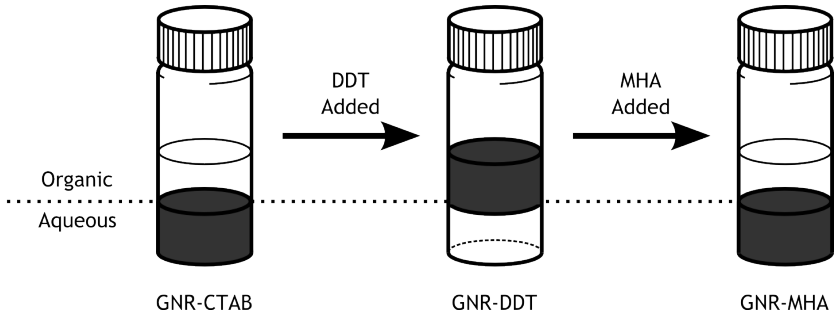

Figure 5.5: Stages of round trip phase transfer protocol where GNR capped with CTAB are first exchanged with DDT, then MHA.

Ligand exchange

Chemicals 6-Mercaptohexanoic acid (MHA) (90%). Sodium citrate (NaCit) ($\geq$ 99%). Poly (sodium 4-styrenesulfonate) (PSS) (70,000 MW). 1-dodecanethiol (DDT) ($\geq$ 98%). Toluene (99.8%). Methanol ($\geq$ 99.8%). Acetone ($\geq$ 99.9%). 2-propanol ($\geq$ 99.5%). Tris-Borate-EDTA buffer (5x concentrate).

The MHA ligand exchange followed the protocol by Wijaya and Hamad-Schifferli, [158] where the CTAB gold nanorods (GNR-CTAB) were first changed to nanorods capped with 1-dodecanethiol, termed GNR-DDT. The DDT ligand turns the nanorods hydrophobic as there is a phase shift to the organic phase. The GNR-DDT are extracted and undergo exchange with MHA (GNR-MHA) which returns the nanorods to the aqueous phase. The round trip [158] phase transfer ligand exchange protocol (Figure 5.5) has the advantage of superior separation of the exchanged nanorods since the organic and aqueous solutions naturally separate themselves.

Beginning with a GNR-CTAB colloidal solution (between 25 nM to 50 nM) of volume V_{GNR}, an equal volume of DDT was added, then $4V_{GNR}$ of acetone was added and sonicated for several seconds. The DDT has a greater affinity for the metallic surface and replaces the CTAB. The organic GNR-DDT solution separated itself from the aqueous CTAB solution and was syphoned off the top. The syphoned GNR-DDT solution then had an equal volume of acetone added along with 5x the nanorod volume of methanol added. The solution was left overnight to allow the GNR-DDT to precipitate for collection.

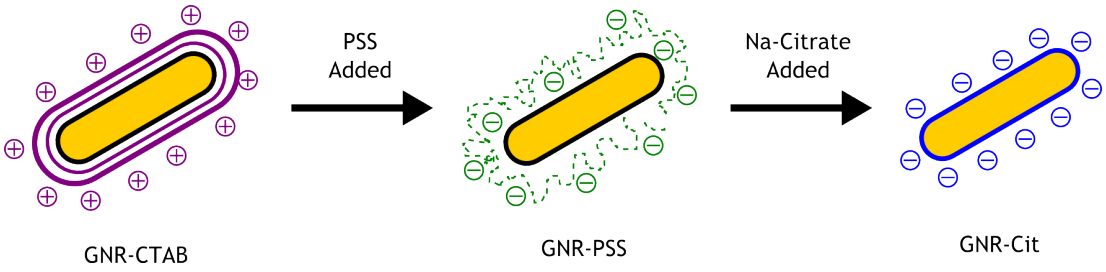

Figure 5.6: Concept behind the exchange of CTAB with PSS then with Na-citrate.

The next day, a solution of toluene (9 ml) was heated (90°C – 95°C) for 10 mins to ensure a consistent temperature was maintained. The toluene was vigorously mixed with a stir bar (10 mm x 5 mm). To the toluene, 20 μl of MHA was added. The GNR-DDT were extracted and added to 1 ml of toluene and sonicated to disperse them. They were then added to the heated toluene/MHA solution for 15 minutes or until the mixture returned to a colourless solution, with small precipitates of nanorods visible. The GNR-MHA precipitates were collected and washed once with toluene and then with 2-propanol. The washed GNR-MHA particles were centrifuged at 4722 xg for 6 mins. The nanorod pellet was then suspended in Tris-Borate-EDTA buffer, ready for characterisation.

The other exchange protocol (Figure 5.6), replaced the CTAB with NaCit via the intermediate step where CTAB was replaced with PSS. The protocol, adapted from Mehtala et al. [159] involves six steps but is essentially a case of centrifuging the nanorods and suspending the pelleted nanoparticles in PSS first, then NaCit second.

In detail, the synthesised GNR-CTAB were centrifuged at 12,000 xg for 30 mins and dispersed in distilled water. This was done for four times. The nanorods were then suspended in a 0.15 wt% of PSS. After an hour, the GNR-PSS were centrifuged at 12,000 xg, for 15 mins. After repeating the PSS suspension, the GNR-PSS were suspended in a 5 mM solution of NaCit. The NaCit nanorod solutions were left for 12 hours before being centrifuged. Steps 5 and 6 involved the centrifugation of the NaCit nanorod solutions and suspension in NaCit. The different viscosity of NaCit meant the centrifugation speed was lowered to 7,500 xg and they were spun for 30 mins. After the final centrifugation, the NaCit capped nanorods (GNR-Cit) were suspended in 5 mM NaCit and stored. Solutions were serviceable for a couple of weeks.

5.2.2 Nanoparticle characterisation

Absorption spectra

The most common method for characterising metallic nanoparticles is via spectrophotometry. Since the optical characteristics are closely linked to the size and shape of the nanoparticle, a simple UV/Vis measurement can provide enough information on the physical dimensions of the nanoparticles as well as reveal which wavelengths the particles respond to the most.

Measuring the excitation spectra was done with a Perkin Elmer Lambda 25 spectrophotometer. Two 6Q grade quartz microcuvettes were used, and distilled water was used for the reference channel. The instrument was set-up to measure from 190 nm to 1100 nm at a scan speed of 960 nm/min. The slits on the instrument are fixed at 1 nm, and the wavelength the instrument switches from the halogen bulb to the deuterium bulb was 325 nm.

From the work of Orendorff and Murphy, [149] it is possible to use the absorption spectra to calculate the nanoparticle concentration. Specifically, the excitation coefficient is calculated from the wavelength of the plasmonic peak via Equation 5.7. [149] Where 'x' is the peak position of the longitudinal surface plasmon peak, and 'y' is the extinction coefficient. The concentration of nanorods can then be determined using the Beer-Lambert law Equation 1.13, Chapter 1).

$$y = 0.0123x - 5.0192 \tag{5.7}$$

Since $AgNO_3$ was the compound that mainly controls the dimensions of the nanorod, it was important to know what concentrations produced which longitudinal surface plasmon resonance peak wavelengths. Silver may be used to tune the optical properties of the nanorods, but CTAB concentrations also affect the outcome. For this reason, a concentration sweep was conducted where the only concentration changed was for the $AgNO_3$ compound. Plotting the peak position of the longitudinal plasmon peak versus the silver concentration produced a calibration curve that could be used to determine how much silver was needed to achieve a particular plasmonic peak.

Scanning electron microscopy

For scanning electron microscope (SEM) images, an FEI Quanta 250 environmental field-emission SEM was used. The nanorod solutions were dried out on a square metallic plate that was placed inside the microscope. Since it was possible to place a drop of GNR solution onto each corner of the metallic plate, four samples could be measured in one session. The GNR had LSPR peaks at 698 nm, 735 nm, 754 nm and 811 nm. The nanorods were prepared as described above and their absorbance measured. The samples were diluted until the particle concentration was around 0.3 nM. To prepare the GNR for measurement, a 10 μl pipette was used to place a droplet of solution onto the corners of the metallic plate. The samples were placed under an incandescent bulb (60 W) desk lamp in order to speed up the evaporation process. Since gold is often used for sputter coating non-conductive materials, before imaging [160], there was no need for coatings or additional sample preparation. The SEM was capable of achieving a maximum of 250,000 x magnification, at a voltage of 10 kV. With this set-up, it was possible to acquire images of the GNR with around 40 - 70 measureable particles.

To measure the particles, the Java-based image processing program, Fiji was used. [161, 162] Along with post-processing tools, the package includes a measuring tool. The measuring tool allows the user to set the scale used by the software, to measure the particles. This was done by drawing a line over the scale bar (included with the SEM imaging) and inputting the value this length corresponds to: in this case 300 nm. With this done, the measurement tool was now calibrated to output the correct dimensional information.

Measuring as many rods as were observable, the dimensional information was compiled into histograms, on the software package Origin® (OriginLab®). Then using the non-linear fit feature, a Gaussian curve was fitted to the histograms. The mean of the Gaussians was taken to be the measured length of the nanorods.

5.2.3 Cell line & toxicity studies

UVW cell line

For the colourimetric and clonogenic toxicity assays, the human glioblastoma cell line (UVW) was used. [163] While not a melanoma cell line, the UVW glioma cells are a cancer cell line and a particularly robust line. Motivations for their use stemmed primarily from the experience of the project's collaborators who have years of experience working with this particular cell line. As a result, the refined protocols for conducting Alamar Blue and clonogenic toxicity assays were well established. [156, 164, 165] This meant that the toxicity studies could start immediately without the need to set-up new systems and protocols for working with a different cell line.

The UVW glioma cells also allow for clonogenic assays since the cells can form colonies when plated onto dishes. The cells can be bio-reacted into spheroid formations that better mimic the response of *in vivo* environments. This was an attractive property as this could have formed a useful transition step towards studying the nanorods *in vivo*. [166]

The UVW glioma cells were cultured in 75 cm^2 flasks that contained minimum essential medium (MEM) with 10% (v/v) foetal bovine serum, penicillin/streptomycin (100 units/ml), fungizone (2 μg/ml) and glutamine (200 mM). All medium solutions were from Life Technologies. Cells were incubated at 37^{o}C in an atmosphere of 5% CO_2.

Colourimetric

The colourimetric assay revolves around the change in spectroscopic wavelength of a fluorescent metabolite. A metabolite is a compound that the cell can process into compounds it needs to survive. As the living cell processes the fluorescent metabolite, the molecule undergoes a structural change which shifts its optical properties. By measuring the absorption, or fluorescence, of the cultured cells, it is possible to measure whether the nanorods have had a toxic effect.

The colourimetric assay used was the Alamar Blue assay. [164] The active ingredient was resazurin (7-hydroxy-10-oxidophenxazin-10-ium-3-one) and undergoes a change in redox state when metabolised by the cell. Resazurin is a blue, non-fluorescent dye, that is reduced to the highly fluorescent resorufin. The spectroscopic measurement of resazurin can be conducted via recording the absorption at either 570 nm or 600 nm, depending on which redox state the researcher wishes to focus on. Focusing on the fluorescence, the excitation wavelength is set between 530 nm - 560 nm and emission is recorded at 590 nm. [164]

Preparation of the cells for treating with the nanorod solution involved washing the cultured cells (in 75 cm^2 flasks) with PBS then treating with trypsin. Trypsin is an enzyme that is used to cleave the proteins that adhere the cells to the surface of the culture flask. This allows the cells to be suspended in fresh medium for the cell counting procedure. The fresh medium neutralised the trypsin but can result in cells clinging onto each other. To separate the cells, from each other, a 21 gauge needle and 5 ml syringe was used and only needed a few aspirations to achieve a single cell suspension.

Counting the number of cells within a known volume allows for the cell concentration to be determined. Cell counting was done with a hemocytometer, a glass slide with a thin well (3 mm x 3 mm x 0.1 mm) at its centre. A coverslip, on top, creates a chamber ($\sim$ 900 μl) that the cells can be pipetted into. The hemocytometer has a grid pattern etched onto it, and when viewed under a microscope, the user is able to use the grid to count the number of cells within a predetermined volume. Since the volume of the grid chamber is known, the cell concentration can be calculated.

Knowing the cell concentration, 1 ml tubes (Eppendorf) were prepared with a 3000 cell/ml (300 μl) solution. Not including the two control tubes, a specific amount of nanorod solution was added in order to achieve a concentration range from 1 pM to 10 nM. The cell/nanorod solutions were pipetted into the wells of a 96-well plate (Corning). Each well held 100 μl of solution and each concentration, plus the two controls, were done in triplicate. With the wells filed, the well plate lid was replaced, labelled, and the plate was incubated for 24 hours.

The next day, the medium from the well plate was removed and 100 μl of resazurin (0.02 wt%) (Sigma-Aldrich) and cell medium was added to each well. A stock resazurin solution was prepared at a 0.2 wt% concentration with sterile water then diluted by a factor of 10 with cell medium. The cells were then incubated for 2 hours which gave the surviving cells time to metabolise the resazurin compound. The 96-well plate was then fed into a Spectra Max Gemini XS plate reader (Molecular Devices Corporation) and the well solution's optical properties were measured. The instrument was set to record the fluorescence at 590 nm with excitation at 560 nm. Since each concentration was measured in triplicate, the fluorescence values were averaged then normalised to the control sample's value.

Clonogenic

The basis of the clonogenic toxicity assay was that after treating the cells with the nanorods, they are plated onto dishes and the cells formed colonies over a 2 week period. Once the cell colonies have formed, the dishes are washed and stained with a Giemsa solution. The staining makes the colonies visible so that they can be counted or imaged. The surviving fraction is then calculated and is corrected based on the efficiency of the plating step.

Treating the cells with the nanorod solution followed a different procedure. The stock cell flask was trypsinised and naturalised in fresh medium. In order to achieve a single cell suspension a 21 gauge needle and 5 ml syringe was used to aspirate the solution. The cell concentration was determined with a hemocytometer.

The cells were cultured in 25 cm^2 flasks with 5 ml of medium and approximately 80,000 cells. One 25 cm^2 flask was prepared for each concentration being tested, along with two control flasks. The flasks were incubated for two days (or until 50% - 60% confluent), at which point, they were washed with PBS, and 1 ml of fresh medium was added. Nanorods were added to the flasks to from a concentration range from 1 pM to 1 nM. The flasks were incubated for 24 hours then washed with PBS to clean the cells and remove any excess nanorods.

For each flask, the cells were trypsinised and neutralised in 5 ml of fresh medium. Single cell suspensions were achieved as described earlier and the cell concentrations were determined with a hemocytometer. The cell suspensions were diluted to achieve a 40 cell/ml (15 ml volume) solution and were evenly distributed into 60 mm x 15 mm Petri dishes, in triplicate. The lids were labelled, and the dishes were incubated for 14 days.

After a fortnight, the medium was removed, and the dishes were washed with PBS. The cells were fixed by filling the dishes with methanol. After 15 mins, the cell colonies were stained with a 5% v/v Giemsa solution (VWR International Ltd). The staining solution was left to work for 30 mins before the excess was removed. To clean the dishes and remove the last of the excess staining solution, the dishes were submerged into tap water. It was important not to use running water as this could wash away the cell colonies. After two submersions in fresh tap water, the dishes were left to dry at room temperature. The drying process could be hastened by putting the dishes in an incubator set to 37^{o}C.

5.2.4 ColonyArea for assessing clonogenic dishes

Once the dishes were stained, common practice involves counting the number of colonies and determining the plating efficiencies, that being the ratio of counted colonies over the number of initially plated cells. [165] Then the normalised (to the control) values usually defines the surviving fraction that quantifies the toxicity.

However, the number of cell colonies is only one parameter that can reveal information about how toxic the nanorods are. The size and density can also be used to determine the toxic effect. For instance, the nanorods may not kill the cell immediately but instead damaged the cell. During the time the cells are left to form colonies, the damaged cell may produce daughter cells and start forming a colony until the damaged cells can no longer survive. This results in the same number of colonies, but their size is much less than those of the control dishes. In order to capture this additional information, the ImageJ plug-in, ColonyArea, was used to process images of the stained dishes. [167]

The distribution of ImageJ used was the open-source platform Fiji, [161] and the ColonyArea plug-in [167] was simply copied into the plugin folder within the Fiji program files. [162] Its operation involves several steps but can be grouped into three processes: crop and arrange images, perform threshold detection, and measure the area percentage and the intensity weighted area percentage (referred to as, intensity percentage). The reader is directed to the work of Guzman et al. [167] for a complete review of the plug-in's operation.

The initial operations of the plug-in involves creating a mask that was overlaid onto the image of the clonogenic dishes. This mask ensures that the software knows which part of the image contains the stained cells. The plug-in has been optimised for well plates and not 60 mm x 15 mm Petri dishes. However, there was a custom setting that can be used to alter the mask to the user's specifications. This meant it was possible to take individual images of the clonogenic dishes and then generate a combined image (Figure 5.7) that ColonyArea could process.

The stained dishes were individually imaged with a 13-megapixel camera (Honor X5), and the JPEG images were cropped and arranged (Inkscape) in a similar fashion to the wells of a well plate (Figure 5.7). Cropping was with a circle shape so that only the stained colonies were left; this simplified the set-up of the ColonyArea mask since the spacing between each dish was zero. With the processed image in ImageJ, the contrast and brightness were increased as this helped improve the threshold calculation and reduced the chance that the background was included as part of the colonies.

The output from ColonyArea was the area percentage and the intensity percentage. The area percentage was the percentage of the dishes total area that was covered with cells. The intensity percentage was the intensity weighted area percentage. This means that the area percentage was altered depending on the intensity of the staining, which was dependent on the number of cells in the colony. As a result, the intensity percentage not only accounts for the number of colonies but the number of cells within each colony, thus giving information about the damaging effects of nanorods as well as the toxic effects. Once ColonyArea had been run and the intensity percentages obtained, the values were averaged for each triplicate and normalised to the control value.

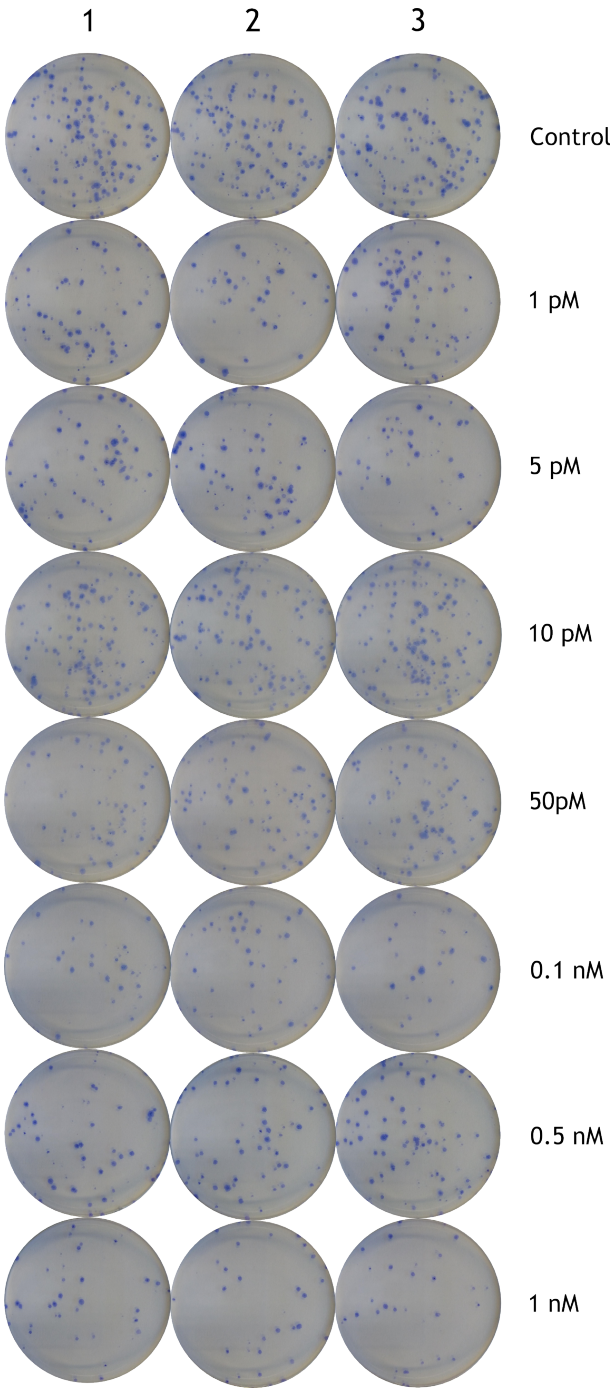

Figure 5.7: Processed images arranged into an array which the ColonyArea plug-in could process. Columns are for each dish as part of the triplicate and the rows are for each concentration of GNR used, including the control which had 0 nM of GNR.

5.2.5 Uptake measurement via ICP-MS & bright field microscopy

Toxicity assays, such as the Alamar Blue and clonogenic assays, provide information on what dose produces a toxic effect. However, there is no guarantee that every nanoparticle gets inside the cell which is important because only the nanoparticles inside the cell can affect toxicity. In order to quantify how many nanorods were taken up by the cell, the treated cells were spun and digested in aqua regia. This broke down the nanorods so that the amount of atomic gold, inside the cells, could be measured via inductively coupled plasma – mass spectrometry (ICP-MS). With the measured mass of gold, the dimensions of the nanorod, and the number of cells treated, it was possible to calculate the number of nanorods per cell.

Cells were treated with bGNR-MHA as describe for the clonogenic assay. After incubating for 24 hours, the treated cells were trypsinised and neutralised in 10 ml of fresh medium. The cells were centrifuged at 1200 xg for 5 mins and then suspended in 1 ml of media. The cell concentration was determined by haemocytometers, as described previously. This allows for the determination of how many cells were present in each sample, which was needed for the uptake calculation. The cells were spun again at 1200 xg for 5 mins then suspended in 0.5 ml of aqua regia. The digesting samples were heated to 60 ^{o}C overnight then diluted with distilled water to an aqua regia concentration of 2%. An Agilent 7700X ICP-MS (Agilent Technologies) was used with a micromist nebuliser and an octopole collision cell.

Calibration was done using solutions prepared from a Qmx ICP gold standard (Qmx Laboratories). The standards were digested in 2% aqua regia and covered a concentration range from 0 μg/L to 1000 μg/L. Measurement of the gold concentration within the digested cell samples used the 197Au isotope while the internal standard used the 175Lu isotope. Operating conditions used were 1,550 W RF forward power, 0.85 L/min plasma carrier gas flow, 4.6 ml/min helium gas flow in the collision cell and 0.2 L/min makeup gas flow. The nebuliser pump operated at 0.1 revolutions per second while the sample depth was 8 mm. The integration time was 0.1 s while the sample period was 0.31 s.

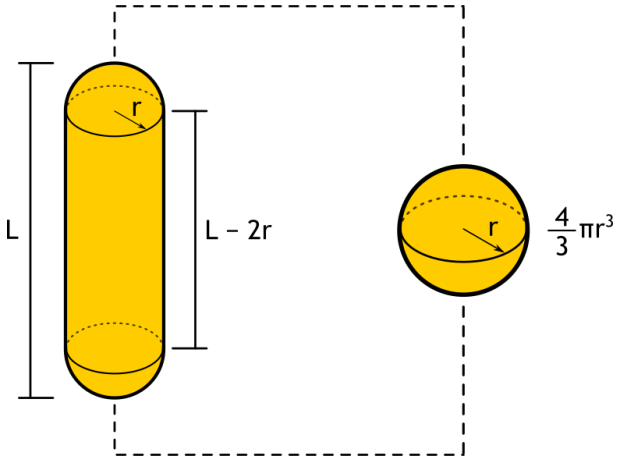

Figure 5.8: Capsule-shape of GNR use to determine the volume of the nanoparticle. Can be formed by a cylinder capped with half spheres.

Calculation of the GNR volume used Equation 5.8 which is equal to the volume of a capsule. [168] The capsule geometry consists of a cylinder that is capped by half spheres (Figure 5.8). The mass of one nanorod was calculated by multiplying the volume by the density of gold (19300 kg/m^3). The number of GNR was determined by dividing the measured mass (from ICP-MS) by the calculated mass of one GNR. The number of GNR could then be divided by the calculated number of cells (determined from the hemocytometer measurements) to arrive at the number of GNR per cell.

$$V = L\pi r^2 - \frac{2}{3}\pi r^3 \tag{5.8}$$

Along with ICP-MS measurements, the treated cells were fixed onto slides in order to observe the samples with bright field microscopy. After the treated cells were trypsinised and neutralised, 50 μl of cell suspension was pipetted onto glass coverslips and incubated for 15 mins. Once the cells had adhered onto the coverslips, the coverslips were washed with PBS, and then 100 μl of 10% formalin (Sigma-Aldrich) was placed onto the coverslips to fix the cells to the glass. After 30 mins the formalin was removed, and the coverslips were washed twice with PBS then twice with distilled water.

Once dry, the coverslips were placed onto glass slides (cell side down) and sealed in place with clear nail varnish. The nail varnish was applied along the edge of the coverslip to fix and seal the coverslip onto the glass slide. To view the prepared slides, a Zeiss Axioskop 2 F45S MOT microscope was used. The microscope uses a 100 W halogen bulb for illumination, during bright field operation. A Nikon D3300 DSLR camera (24.2 Megapixels) was connected to the microscope and used to record bright field images.

5.2.6 Cell-cycle percentages via fluorescence assisted cell sorting

The percentage of treated cells in each stage of the cell cycle was determined via fluorescence assisted cell sorting (FACS). The treated cells (bGNR-MHA) were neutralised and centrifuged at 1200 xg for 5 mins, then suspended in PBS. Following the second round of centrifugation, the pelleted cells were fixed by suspending the cells in ethanol and storing the samples at 4 ^{o}C for 2 hours. After two hours, the fixed cells were centrifuged at 2000 xg for 5 mins and resuspended in PBS. The cell solutions were then transferred to FACS tubes and 50 μg/ml of Ribonuclease A, from bovine pancreas (Sigma-Aldrich), was added to digest the RNA. This ensured that only the DNA would be stained. After 30 mins the DNA was stained by the addition of propidium iodide (50 μg/ml) (Thermo Fischer Scientific Inc.). The fluorescence, forward and side scatter were measured using a FACSCanto flow cytometer (Becton Dickinson Systems). A total of 10,000 events per sample were recorded and the cell populations where gated to exclude debris. The FACSDiva (Becton Dickinson Systems) software was used to determine the percentages of cells in the G1, S and M stages of the cell cycle.

The size of the cell correlates with the forward scatter measurement while the internal complexity is determined by measuring the side scatter. The quantity of DNA is related to the fluorescence intensity of the propidium iodide dye. In order to ascertain which part of the cell cycle each cell was in, the histogram of cell count versus propidium iodide fluorescence intensity was used. Limits were placed on the histogram in order to define the different stages of the cell-cycle. The software then used these limits to calculate the cell-cycle percentages. In order to improve the accuracy of the measurement, the plot of forward scatter verses side scatter was used to exclude doublet measurements (measurement of two cells at the same time). [169]

5.3 Nanorod Synthesis & Characterisation

The formation of metallic nanorods results in two characteristic plasmonic peaks when the absorption spectrum was measured. Figure 5.9 shows the absorption spectrum for different batches of nanorods, where the concentration of $AgNO_3$ was altered. In keeping with the literature on gold nanorods, the spectra show similar peaks, with the transverse peak being at 517 nm and the longitudinal peak being within the range of 670 nm to 890 nm. The difference in wavelength is the result of the longitudinal mode having a higher electron density of its oscillating electron cloud.

As the concentration of $AgNO_3$ is lowered, the ratio of the absorption between the two peaks (A_{LSPR}/A_{TSPR}) decreases until nanorod formation was no longer possible and spheres, with one plasmon peak, were synthesised. The ratio of absorption can be used as a gauge of nanorod purity since the presence of spherical particles will increase the transfers plasmon peak.

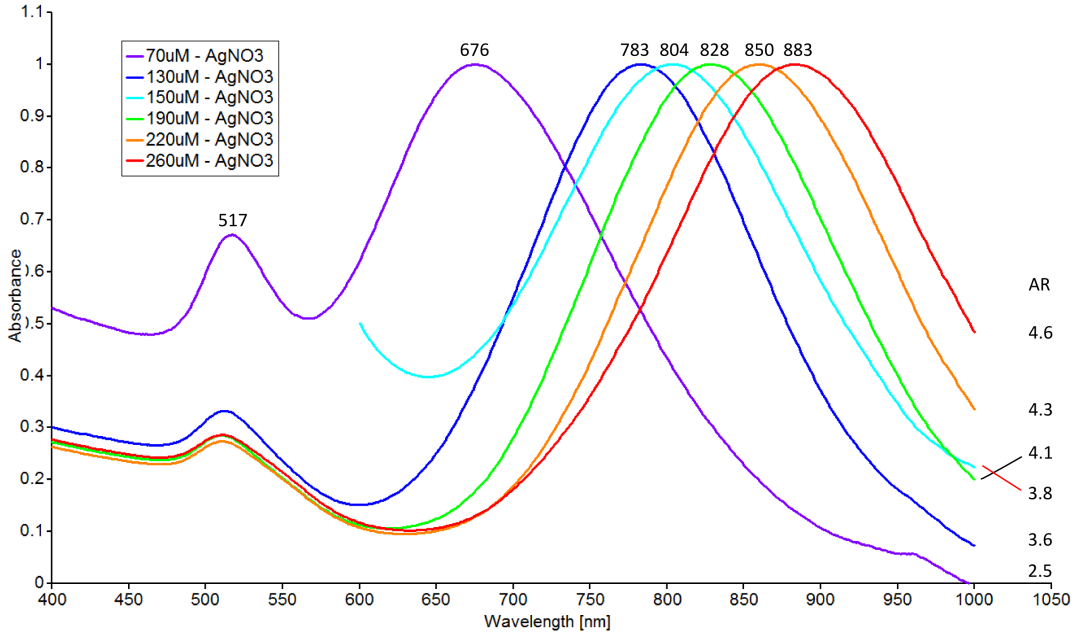

Figure 5.9: Absorption spectra of gold nanorods where the concentration of $AgNO_3$ has been changed. Along with labelling the peak values, the aspect ratio has also been included.

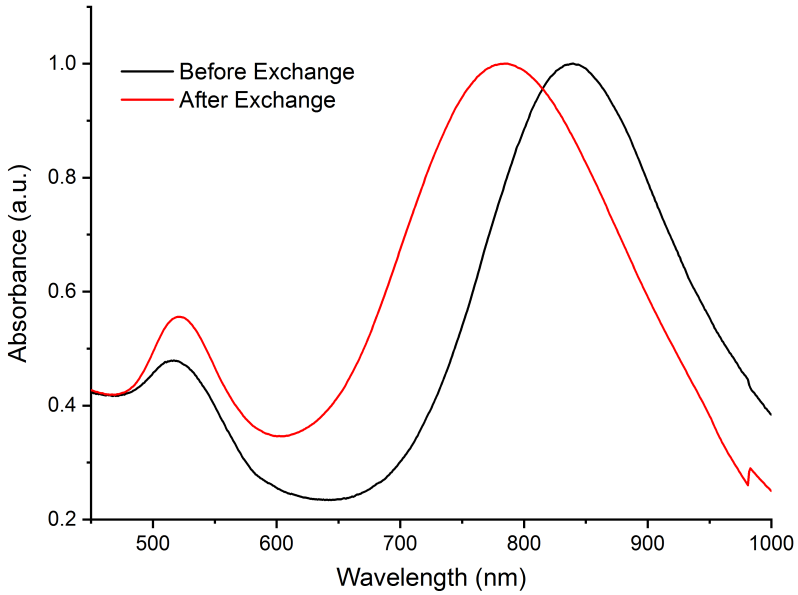

Figure 5.10: Absorption spectrum of GNR before and after ligand exchange.

Peak ratio values above two were considered viable nanorod samples and batches under this value were disposed of and a new batch was synthesised. The lower size limit of the nanorods occurred with a LSPR peak around 670 nm. Although, as Figure 5.9 shows the peak ratio for nanorods with 70 μM of $AgNO_3$ was only $\sim$ 1.42. This would suggest a high percentage of spherical nanoparticles present.

Nanorod batches with high sphere populations can have the two particle types separated according to the protocol by Park et al. [170] This was not necessary for the nanorods used in the toxicity tests as the sphere population was $\leq$ 10% of the nanorod population. It is also possible to lower the sphere population by synthesising at concentrations where the system is most efficient at nanorod formation (LSPR peak $\sim$ 800 nm).

Tuning the nanorods plasmonic properties depends on the concentrations of the synthesis chemicals but they are altered by the ligand exchange procedure. Figure 5.10 shows the absorption spectrum for a batch of gold nanorods just after synthesis along with the same nanorods after the CTAB was exchanged with MHA. The plasmonic properties will change with different ligands since this alters the dielectric constant of the local nanorod environment. [134] However, other processes like heating and centrifugation can also affect the shape of the nanorod. Particularly, during the MHA ligand exchange since the particles need to be heated to 90^{o}C -

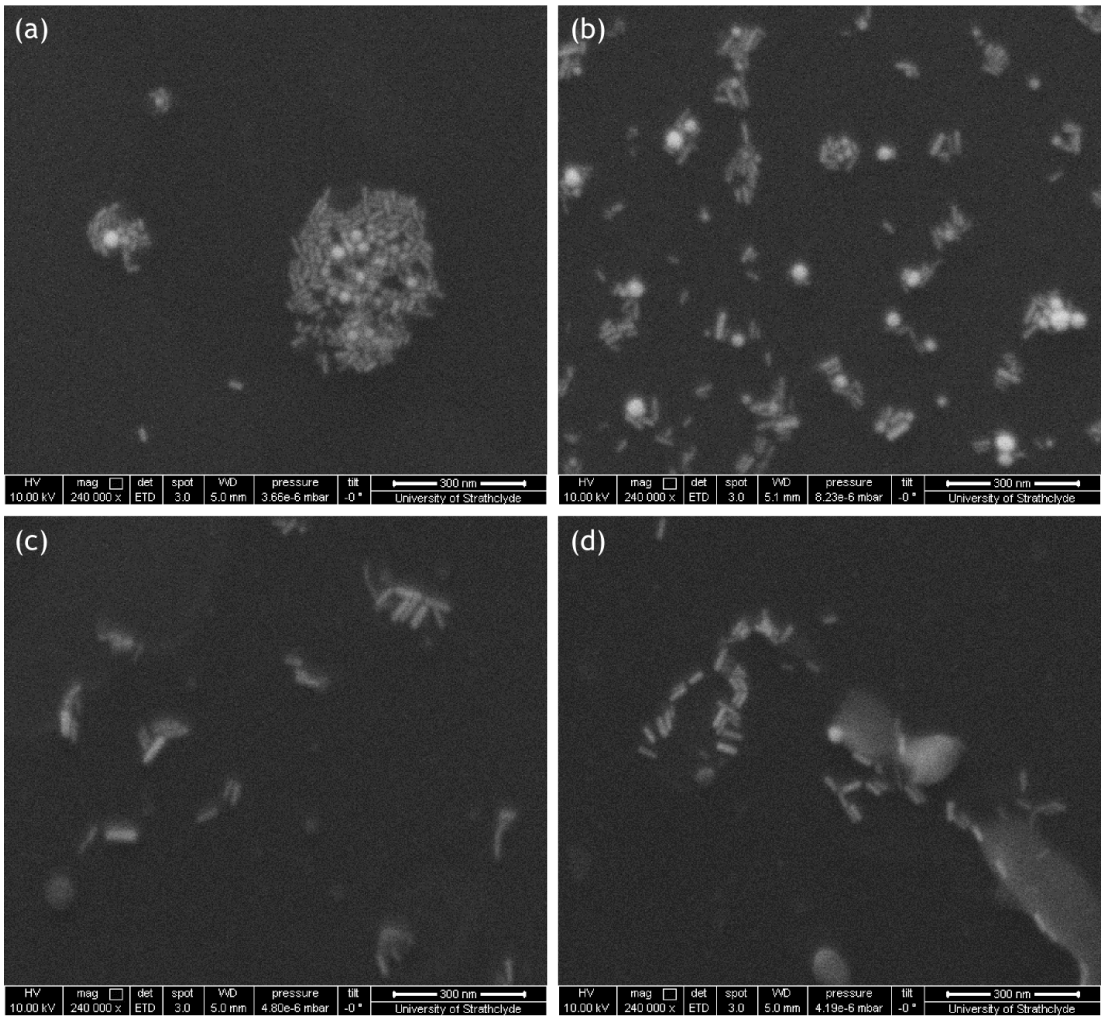

Figure 5.11: 240,000x magnification SEM image for GNR of different aspect ratios. The LSPR peak of the nanorods were (a) 698 nm, (b) 735 nm, (c) 754 nm (d) and 811 nm.

95°C and undergo several rounds of centrifugation. Comparing the absorption spectrum before and after the ligand exchange, Figure 5.10, the LSPR peak has blue shifted by 56 nm, and the full-width half maximum (FWHM) has increased by 10 nm.

The LSPR peak will naturally blueshift over time as the nanorods undergoes a process called Ostwald ripening. This is when metallic ions come off the nanorods and alter the aspect ratio of the nanorods, over time. [171] For nanorod particles, this ripening occurs mostly at the corners, which rounds out the ends of the nanoparticles and causes a blueshift in the LSPR peak.

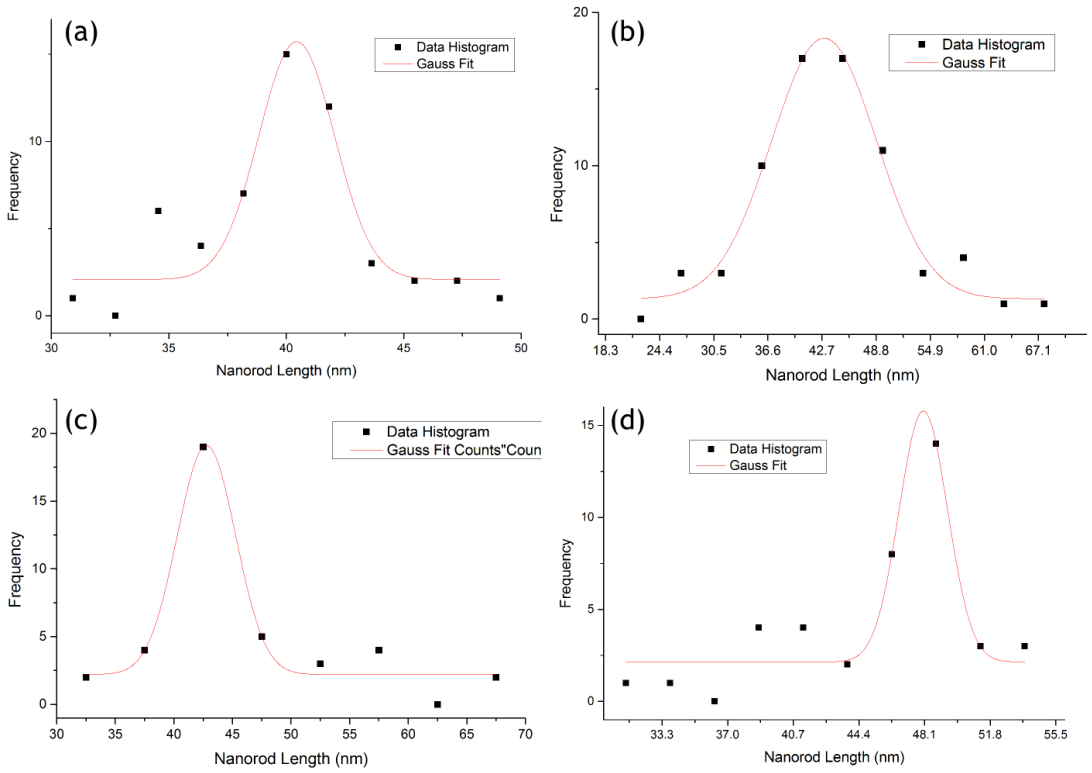

Figure 5.12: Histograms of particle length with Gaussian functions fitted. The mode was used as the measured length while the FWHM indicates how homogeneous the size distributions were. LSPR peaks were (a) 698 nm, (b) 735 nm, (c) 754 nm and (d) 811 nm.

This natural process normally takes days or weeks to happen but given the temperature changes, centrifugation processes and the chemicals used the alteration in nanorod shape occurs much sooner than the natural mechanism. Should the plasmonic resonance wavelength need to match the optical properties of a fluorophore, then it is necessary to synthesis nanorods with slightly larger aspect ratios so that the ligand exchange process does not result in a mismatch of the optical properties.

In addition to dimensional alterations via chemical processing, the distribution in particle size also affects the plasmonic properties. From Figure 5.12 the nanorod solutions contain nanorods with a range of different lengths. Each population of nanorod, with a specific length, will have a plasmonic peak that is slightly different from its neighbouring nanoparticles.

	Sample (a)	Sample (b)	Sample (c)	Sample (d)
LSPR Peak (nm)	698	735	754	811
Calculated Length (nm)	40.2	42.1	43.4	47.2
No. Particles	53	70	39	40
$\bar{x}$ from Gauss Fit (nm)	40.4	42.9	42.8	48.0
$\bar{x}$ error ($\pm$ nm)	0.25	0.41	0.58	0.35

Table 5.1: Table comparing calculated size from Equation 5.7 and measured size from fitting Gaussian functions to the histograms of Figure 5.11(b).

Given an even distribution of particle sizes, the absorption spectrum would cease to have defined peaks. However, as Figure 5.12 shows, the distribution can be fitted to a Gaussian function. With the FWHM indicating how homogenious the nanorod aspect ratios were.

Fitting a Gaussian function to the histograms of Figure 5.12 and taking the mode provided a value for the measured length of the nanorod. These values are compared to values calculated from the LSPR peak of the absorption spectrum in Table 5.1. [149]

The values, of nanorod length, and the mode of the fitted Gaussians are consistent with the calculated lengths from the LSPR peak values and confirm that the synthesised nanorods are similar to those of the literature. This validates the method of calculating nanoparticle properties (extinction coefficient and nanoparticle dimensions) from the absorption spectrum. The data from the characterisation studies of the nanorods agrees with the literature and validate that the nanorod synthesis protocols are sufficient for the toxicity studies.

5.4 Toxicity Assays & Uptake

5.4.1 Colourimetric

Figure 5.13 shows the change in normalised fluorescence value as the concentration of bGNR was increased. The CTAB ligand was more toxic than the MHA ligand as the bGNR-MHA response begins to decrease after 1 nM rather than 0.005 nM. This agrees with the literature which shows CTAB as being cytotoxic. [121, 151] By 2.5 nM, both particles show significant cytotoxic effects. The normalised fluorescence values do not reach zero which may imply that regardless of concentration, some cells survive. However, it is more likely to be the result of particle sedimentation. [154]

Conventional toxicity results follow a sigmoidal trend, and while the profiles of Figure 5.13 follow a similar shape, they are more angular than expectations and would be demonstrated by particles which had sedimented. The broader range of concentrations, represented by only 11 points, does result in a low resolution of data points. While it would be possible to 'fill in the gaps' by including more intermediate concentration, the aim of the Alamar Blue assay was to provide a rough indicator as to where the toxic region lay. This then informed the concentration values used for the clonogenic assay.

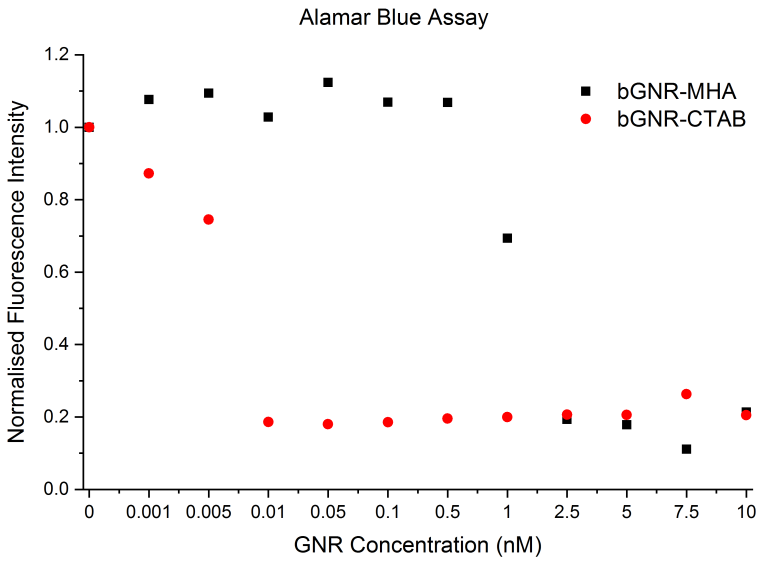

Figure 5.13: Normalised fluorescence of metabolised resazurin after cells were treated with different concentrations of gold nanorods.

The rapid change in the normalised fluorescence values could also be related to the sedimentation of the nanorods. [154] Within the small volume of the 96-well plate wells, the nanorods may agglomerate together, and instead of interacting with the cell membranes, they form a layer that covers the cells and deprives the cells of the nutrients needed to survive. This 'blanket effect' would occur at a concentration value where the nanorods can cover the area of the well and exaggerate the toxic effects of the nanorods.

The blanket effect would explain how the normalised fluorescence values do not significantly change for the bGNR-MHA, until 0.5 nM. This is not unreasonable since $\sim 10^{11}$ particles would be needed to cover the well (well diameter = 6.94 mm and the particles average dimensions are (10 x 40) nm). The change in ligand help the nanorods remain as a colloidal suspension until the concentration is high enough that the nanorods precipitate and blanket the cells, causing the immediate change in normalised fluorescence values.

The difference between the bGNR-CTAB and bGNR-MHA profiles suggest that the profiles of Figure 5.13 are not solely the result of nanorod blanketing. At 0.01 nM of GNR, there would not be enough nanorods to cover the whole area of the well. For bGNR-CTAB, the toxic effects appear to be genuine. While at larger GNR concentrations, the effect of blanketing becomes more prominent.

While the GNR solutions where washed multiple times before treating the cells, there will be a small residual of synthesis compounds left (most notably CTAB). Also, the ligands can become free from their parent particle. This not only introduces free ligands, that can impact the health of the cells, but also reduces the stability of the nanorod and increases the chance the nanorods will aggregate together. The amount of free ligand will be small but given the small volume used in this type of assay (100 μl) the influence of these free compounds should be noted.

Despite the sources of interference, that can alter the true effect of the nanorod toxicity, the reduction of cytotoxicity, by changing the ligand from CTAB to MHA, has been shown. However, the Alamar Blue assay only gives a rough indicator about nanoparticle toxicity. Moving to the clonogenic assay provides a better indicator of how toxic the nanorods are.

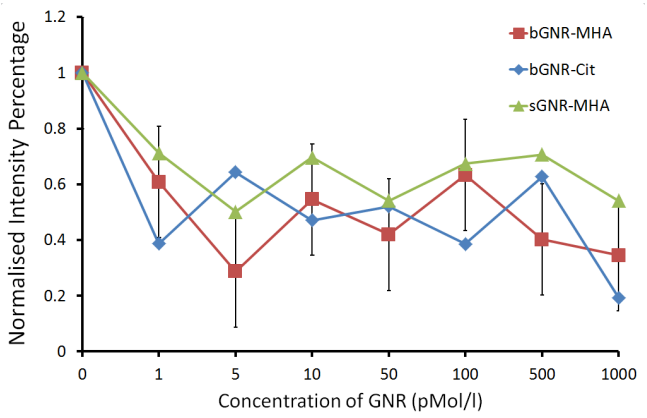

Figure 5.14: Line and scatter plot for the normalised intensity percentages acquired from measurement of clonogenic dishes with ColonyArea. The error bars are shown for bGNR-MHA only for the sake of clarity. The errors were the SD of the averaged values.

For the clonogenic assays, the nanorods with CTAB were not tested as the evidence for their cytotoxic effects is quite conclusive. [121, 151] Based on the colourimetric results of Figure 5.13, a concentration range of 1 pM to 1 nM was chosen. While, the Alamar Blue studies show bGNR-MHA only starting to exhibit cytotoxic effects after 0.5 nM the concerns outlined above make it worth measuring a concentration range from 1 pM to 1 nM.

5.4.2 Clonogenic

Running the similar concentrations through the clonogenic assay has produced different results from the colourimetric assay. The profiles of Figure 5.14 do not fit the sigmoidal trend of a toxicity dose curve. Based on the data acquired, each nanorod had a significant toxic effect on the cells but, apart from the initial decrease, there is no dependence on concentration. The work of Li et al. [172] show that smaller nanorods perform better than larger ones, in vivo. However, the errors (SD $\sim$ 0.2) associated with each point, of Figure 5.14, indicate little difference between the toxic effects of the nanorods. The experimental errors and the lack of a sigmoidal response suggests that other factors are at play, which alter the clonogenic results.

Consideration of which factors may influence the clonogenic assay includes ripening, leeching of surfactant ligands from nanorods, protein binding and sedimentation of nanorods. [126, 151, 154] The number of metal ions that will enter the surrounding medium will be small due to the bulk of the ripening process having taken place during the ligand exchange.

The nanorods used for treating were centrifuged and washed with distilled water several times so that the residual surfactant concentration was as low as possible. This should keep the amount of free ligand in the medium to a minimum. Should the amount of GNR bound to proteins be high then the amount of free GNR would be reduced and effect how many GNR were able to enter the cell. In this case, increasing the GNR concentration results in more protein binding rather than increased toxicity.

The lack of a clear toxicity profile may be the result of the nanoparticles not entering the cell or in such low numbers as to have a minimal impact. This could explain the plateau of the intensity percentage data. After 1 pM the cells do not take up any more nanorod, and the toxicity effect becomes capped. In order to investigate the uptake of the nanorods, inductively coupled plasma mass spectrometry (ICP-MS) was used, and flow cytometry was used to investigate how the nanorods affected the cell cycle, which relates to the colony growing capabilities of the cells.

5.4.3 Uptake & cell cycle

The ICP-MS results allow for the quantification of how many GNR there were per cell and are plotted in figure 5.15. The two highest concentrations from Figure 5.15(a) have a significantly higher number of nanorods per cell and are inconsistent with the trend formed by the other concentrations. For clarity, the lower concentrations are plotted separately, without the 500 pM and 1000 pM data points (Figure 5.15(b)). Typically, the cells have a large enough mass, in relation to the nanoparticles, that low centrifugation (1200 xg) is enough to separate the cells from the excess nanorods. However, when the GNR concentration was $\geq$ 500 pM, the protein bound nanoparticle aggregates could have become large enough that some of them pelleted along with the cells.

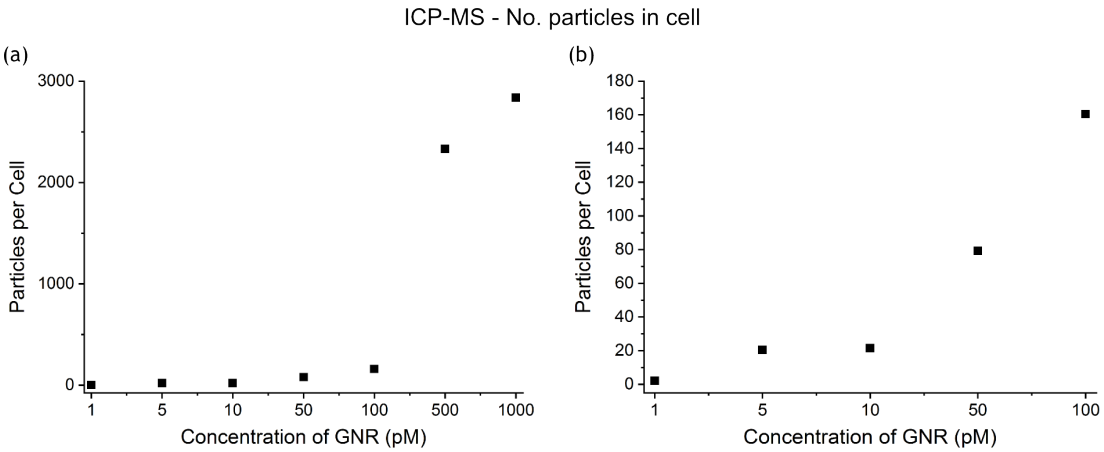

Figure 5.15: Plots of particles per cell versus the concentration of nanorods the cells were treated with. (a) Includes every concentration that was used while (b) only shows the first five concentrations.

Focusing on the first five concentration (1 pM to 100 pM) the calculated number of GNR per cell increase in a non-linear fashion. The trend observed in Figure 5.15(b) is consistent with the work of Hauck et al. [173] and help verify that nanorods were inside the cells. The values in Table 5.2 show the measured mass of gold, from ICP-MS, along with the number of GNR and cells that were in the sample. This representation of the uptake assumes that there was an even distribution of nanorods per cell.

Looking at the treated cells under bright field microscopy (Figure 5.16) shows the faint outline of the cells (images have had the brightness and contrast increased to make the cells clearer to the reader) and the black spots are taken to be aggragated groupings of GNR. Increasing the GNR concentration has increased the number of dark regions observed, but only a subset of cells have these larger groupings of nanorods.

A more detailed transmission electron microscopy measurement [152,173] would be needed to quantify the number of nanorods within the cells. However, it is clear from the bright field images that the uptake of nanorods is not consistent throughout the cell population. Also, from Figure 5.16(c) there are aggregates of GNR outside the cell indicating that either the separation of cells from the excess nanorods were not sufficient or during the preparation of the slides, some cells ruptured and released their nanorods. The extracellular GNR visible in Figure 5.16(c) also suggests that the ICP-MS values for concentrations above 100 pM are not representative of the true uptake value.

Initial particle conc. (pM)	ICP-MS measured Au mass (kg/m^3)	No. particles	Cell cenc. (cell/ml)	Particles per cell
1	$3.33x10^{-13}$	$1.03x10^{6}$	$2.45x10^{5}$	4.2
5	$2.12x10^{-12}$	$6.55x10^{6}$	$1.60x10^{5}$	40.9
10	$2.84x10^{-12}$	$8.79x10^{6}$	$2.05x10^{5}$	42.9
50	$1.92x10^{-11}$	$5.94x10^{7}$	$3.75x10^{5}$	158.3
100	$2.23x10^{-11}$	$6.89x10^{7}$	$2.12x10^{5}$	320.7
500	$7.54x10^{-11}$	$2.33x10^{8}$	$5.00x10^{4}$	4662.8
1000	$1.10x10^{-10}$	$3.40x10^{8}$	$6.00x10^{4}$	5671.2

Table 5.2: From the ICP-MS data, the number of nanoparticles per cell for different concentration of nanorods that the cells were treated with.

The uneven uptake of the nanorods, within the cells, would explain the profile of the clonogenic assay in Figure 5.14. Upon treating the cultured cells with the nanorod solution, only a fraction of the cells takes up a cytotoxic quantity of nanorods. Leaving the majority of cells unaffected, or with much fewer nanorods inside. As a result, the clonogenic results indicate an initial drop in viability but plateau around the 60% - 80% since most of the nanorod were taken up by a small subset of the cell population.

The presence of aggregates in Figure 5.16 and the fact the nanorods remained in a colloidal suspension in distilled water, suggests that protein binding was the cause for the nanorod aggregation. This could explain the uneven uptake of the nanorods since it would take some time for proteins to bind to the nanorods. Initially, the nanorods are taken up by the cells which result in the large quantity seen within the cells of Figure 5.16. After some time, the nanorods bind onto the proteins and form aggregates too large to be taken up by the cells.

Looking at the flow cytometer results (Figure 5.17), the effect of the nanorods on the cell cycle population can be seen. Focusing on the data for G1, the values show an initial decrease followed by an increase at higher concentrations. The values for G0 follow the inverse of G1 while the S and G2 phases do not change significantly. Given that the S phase is related to the replication of DNA, it is fair to say the nanorods do not make it into the nucleus. This is consistent with other studies which show that nanorods do not pass the boundary between the nucleus and cytoplasm. [173, 174] The G2 phase is related to the growth of the cell as it

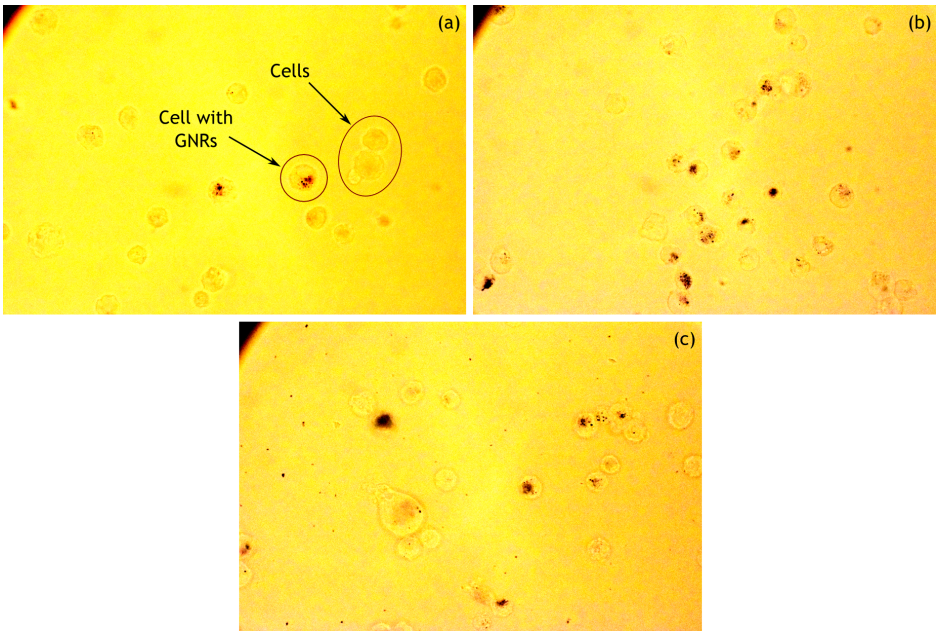

Figure 5.16: Bright field microscope images of treated cells showing aggregation. (a) 5 pM, (b) 50 pM and (c) 500 pM. A grouping of cells has been identified in part (a) along with a cell that has taken up a large grouping of nanorods.

prepares for the mitosis phase. Again, the percentage of cells that are in this phase does not seem to change significantly, implying that the gold does not hinder the cell, once the DNA has been replicated.

While the percentage of cells that are in the S and G2 phase does not change, there is a change in the population as the cells in the G1 phase become arrested by the nanorods and enter the G0 phase. While in this phase, the cells do not grow and therefore cannot undergo mitosis. [175] The number of cells in the G1 phase increases again at higher concentrations and the population of G0 cells decreases. This is attributed to the fact that not all cells have taken up the nanorods and at higher concentrations, the cells that have taken up large amounts of nanorods die. These are washed out during the preparation for measurement, so the cells that are left are generally in good health. This effect can be observed in the microscope images (Figure 5.16) as only a small group of cells show the aggregated nanorods inside them.

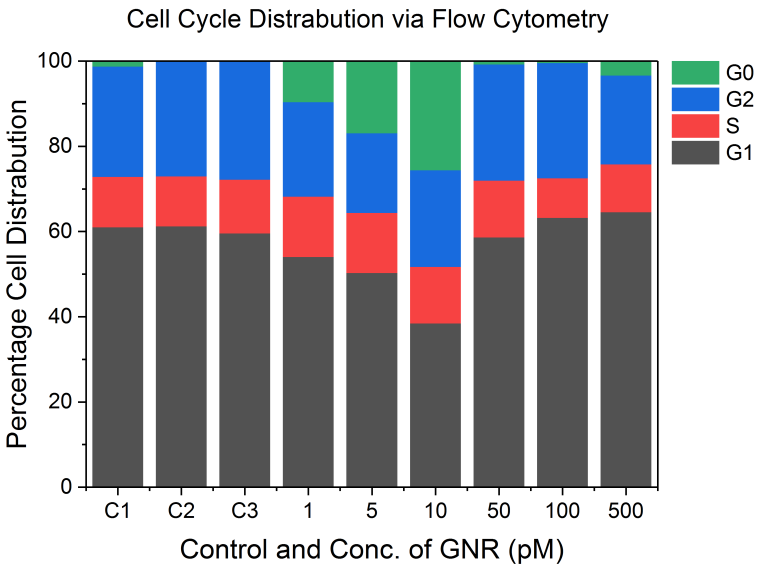

Figure 5.17: Plot of percentage distribution of cell cycle phases for cells treated with different concentrations of bGNR-MHA.

At lower concentrations, the nanorods result in an increasing number of cells in the arrested state, G0. Reaching a maximum of 25% at 10 pM of GNR. Since these cells are unable to grow, they would hinder the formation of colonies. Comparing the stained dishes of the control cells and the cells treated with 10 pM, shown in Figure 5.18, it is clear that the number of colonies remains high, but the diameter of the colonies is reduced. The percentage change in both the number of colonies and area percentage are listed in Table 5.3 and emphasise how it is the longevity of the colonies that have been effected by the GNR. This may also be a sign that the cells have been damaged by the nanorods, which negatively affect the number of cell divisions.

Sample	Colony count	Area percentage (%)	Colony count change (±%)	Area percentage change (±%)
Control	159	9.62	-13.8	-56.5
10 pM	137	4.18		

Table 5.3: Table showing the manually counted number of colonies visible in the dishes of Figure 5.18 and the area percentage values calculated form the ColonyArea plug-in. The percentage change from the control dish to the 10 pM dish is also included.

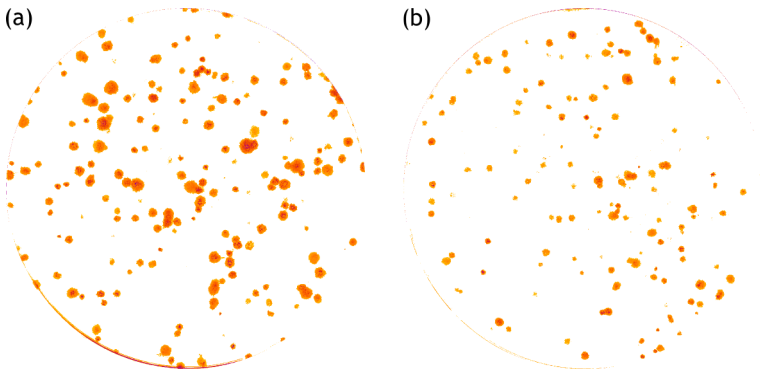

Figure 5.18: Stained clonogenic dishes (after processing with ColonyArea) which show the change in colony size when nanorods are introduced. (a) control dish, (b) dish treated with 10 pM of GNR.

While the clonogenic data failed to produce a clear dose range for the nanorods tested, the testing of both uptake and cell cycle distribution has made clear what mechanisms were at play in producing these results and has allowed for a clearer understanding of the challenges when investigating the nanoparticle-biological interface. Future investigations should aim to repeat these studies using a concentration range plotted in nanoparticles per cell. Nanoparticles per cell is a more useful unit as it is independent of the assay being used. The Alamar Blue assay uses 900 cells per well, while the clonogenic assay uses 25 cm^2 flasks with 80,000 cells, during the treatment processes. Using the same particle concentration (pM) will result in different ratios of particles per cell and may result in misleading results. Based on the work of Unciti-Broceta et al. [176] a new concentration range is proposed (Table 5.4) which aims to cover a wide range of nanoparticle concentration while still being physiologically relevant.

80,000 cells per 25 cm^2 flask (5 ml)	
Cell:GNR ratio	No. Particles ($x10^5$)
1:1	0.8
1:10	8
1:50	40
1:200	160
1:500	400
1:1333	1070
1:3000	2400
1:5000	4000

Table 5.4: Proposed cell to GNR ratio and number of GNR when treating 80,000 cells as part of the clonogenic assay protocol.

5.5 Conclusion

Gold nanorods of two different sizes were synthesised with different capping ligands and toxicity, uptake and flow-cytometry measurements were performed in order to test the suitability of these particles for development of a melanoma biosensor. The plasmonic properties of GNR, leading to visible/NIR spectral properties, make the nanorod an ideal candidate for biomedical sensing. Their ability to increase the local dose of keV radiation also lends GNR towards radiosensitising applications. Discouraged by the ambiguity of the current literature surrounding nanoparticle toxicity, measurements were conducted to assess the performance of GNR within an in vitro environment.

Treating cultured dishes of the human glioblastoma cell (UVW), with different concentrations of GNR produce toxicity curves that did not follow the standard sigmoidal curve. Suspecting additional factors were at play, uptake and cell cycle studies were also performed. ICP-MS measurements of the gold contained within the cells show an increase in intracellular nanorod quantity with an increase of nanorod concentration used to treat the cells. However, bright field images of the treated cells showed that only a fraction of the cells contained larger nanorod quantities. This selective uptake of nanorods was attributed to the gradual binding of GNR to the proteins, in the media. Initially, nanorods are taken up by the cells, while the initial protein binding takes place. Later, the degree of protein binding results in sizable nanorod aggregates which are too large to enter the cell. This leaves many cells free of nanorods and able to grow colonies, during the clonogenic assay.

Using FACS flow cytometry to measure the percentage distribution of cells in the four stages of the cell cycle, revealed a change from the G1 stage to the G0 stage, with increasing GNR concentration. The S and G2 stages remained unaffected by the introduction of nanorods. The flow cytometry results corroborate the uptake studies as a higher concentration of GNR do not follow the traditional toxicity trend. Above 10 pM the flow cytometry results are the same as the control, indicating no toxic effect.

This would be the case if the nanorods were aggregating (via protein binding) to the point that they are no longer able to enter the cells. The change from the G1 to the G0 stage may also indicate that the nanorods damaged the cells which result in smaller colonies forming during the clonogenic assay.

Despite the potential of metallic nanoparticles within biomedical applications, these results highlight many of the issues which arises when investigating their use. The issues surrounding protein binding, aggregation, uptake and toxicity would need to be addressed before the development of a melanoma biosensor could commence. These are only a few concerns as the immune response, retention and bio-distribution are still not fully understood.

Chapter 6

Conclusions

Melanin is a complex biomacromolecule whose structure/spectroscopic relationship is still unclear. Photoluminescence in of itself is a multiparameter problem which can only be measured in part with multiple instruments required to gain a fuller understanding. Along with absorption and fluorescence emission intensity measurements, the time-domain technique of time-correlated single photon counting was used to measure the intrinsic spectroscopic response of the two main melanin pigments, the black/brown eumelanin and the red/yellow pheomelanin.

Measurements of melanin's absorption spectrum revealed 4-5 isosbestic points which occurred at similar wavelengths for both pigments. Looking at the fluorescence spectra across a range of excitation wavelengths does indicate regions of higher intensity which may result from distinct fluorescence species. Analysing the excitation-emission matrix data with a multivariant parallel factor algorithm consistently converged with 2-3 factors which indicate that despite the broadness of melanin's fluorescence, it could be described by a few distinct emission peaks. From the analysis of melanin's lifetime decay, a similar interpretation can be drawn as 4-5 exponentials were needed to fit the decay and even when extended to lifetime distribution fitting, the distribution of lifetimes contained 4-5 peaks.

The spectroscopic results provide evidence to the interpretation that melanin's photophysics stems from a discrete (≤ 5) number of fluorescent species. The localised spectral peaks and discrete lifetime components are then broadened via photophysical interactions like quenching, energy transference, solvent relaxation and formation of larger structures.

In order to gain insight into the structural forms of melanin, the extrinsic fluorescence structure dye molecule Thioflavin T was used to investigate potential sheet structure formation during the synthesis of pheomelanin. As the less studied form of melanin there is less evidence for the existence of sheet structures within the pheomelanin structure. The results demonstrate a similar rise in the structure dye's emission intensity that was previously observed for eumelanin [91] which is strong evidence in favour of sheet structures being formed during the formation of pheomelanin.

Extending the measurements to look at the fluorescence lifetimes revealed a complex interaction between the pheomelanin structures and fluorescence dye molecules. The shortest component is interpreted to be from free dye while the second shortest component is linked to partially intercalated dye. The longest component shared a similarity to the long time component of melanin which has been attributed to coupling of the intercalated thioflavin T's photophysics with that of pheomelanin's.

The capability to measure the presence of sheet structures, with thioflavin T, opens the possibility to develop a melanoma sensing technique based of time-resolved fluorescence spectrofluoromety. Using the loss of melanin structural order [117–119] as a biomarker, a system could be developed to measure the change in ThT lifetime decay components between malignant and healthy tissue.

Comparison of the spectroscopy of the two pigments also aimed to uncover fundamental differences which would help facilitate the development of a simpler, cost-effective, spectroscopic device that could detect melanoma as it is known that melanoma cells have a higher ratio of pheomelanin to eumelanin than normal skin cells. [9, 10]

While each method met the criteria for being simple and cost-effective, they failed to provide a clear or repeatable difference that could be used for melanoma sensing. Analysing the excitation-emission matrix data with parallel factor analyse did reveal underlying spectra that initially showed a distinct difference between the two melanin. However, when expanded to analyse melanin samples with different concentrations of L-cysteine, the parallel factor analysis results did not show a significant change from eumelanin to pheomelanin.

Multi-exponential fitting of melanin's fluorescence lifetime decays demonstrated differences between eumelanin and pheomelanin. However, the complex nature of melanin's fluorescence decay suggests that lifetime distribution fitting is a better model for analysing the lifetime decays of melanin.

Looking at the normal Stokes shifted fluorescence of melanin upon excitation with near-infrared light did produce a fluorescence peak which gave a lifetime decay that fitted to a two-exponential model. This is evidence for the two-photon excitation of melanin following a step-wise path. However, the low quantum yield, high thermal background and interference from reflections made measuring and analysing the data challenging.

Continuing the theme of melanoma sensing, the toxicity of gold nanorods were investigated as their optical and radiosensitisation properties make them attractive for biosensor development. Unlike an intrinsic spectroscopic technique, the toxicity of the nanorods is important to establish since the dosage will affect the future development of the biosensor. Clonogenic assay results and cell cycle data indicate that the nanorods induce damaging effect when they enter the cell. This long term toxic effect requires further investigation in order to establish what properties of the nanorod are responsible and what can be done to reduce this effect. Overall toxicity proved challenging to determine as the nanoparticles were prone to protein aggregation which could be improved by running the assays with a more refined concentration range where the ratio of nanoparticles to cells is considered.

The fundamental question surrounding both the photophysics of melanin and the detection of melanoma is rooted in understanding the exact form of melanin's structure. With this information, the photophysics of melanin could be understood, and melanoma detection strategies could be developed based on this fundamental understanding. In order to answer this question, it is necessary to capture more of the fluorescence landscape, during the process of melanogenesis. The emergence of new technologies such as single photon avalanche diodes could potentially allow for the measurement of time-resolved emission spectra during the melanogenesis process. These measurements could be repeated for different excitation wavelengths which would include further spectroscopic information like that seen in the excitation-emission matrix data.

The successful use of thioflavin T in detecting sheet structure formation during pheomelanogenesis prompts the continued use of extrinsic fluorophores for melanin research as there has been limited use so far. With recent advances in fluorescent probe designs and the advent of super-resolution techniques, there are new opportunities available in investigating the capabilities of these new techniques for uncovering more details about the protomolecular structure of melanins.

Appendix A

PARAFAC & Data Clean-up Code

The following code prepares the EEM data for inclusion within the PARAFAC array $\underline{X}$.

```
%%%%%%%                    Import Data                    %%%%%%%

warning('off','MATLAB:interp1:NaNstrip');     % Turns off warning about NaN
    entries being ignored during interpolation.

% The 'uigetfile' function opens up Windows explorer so you can select the
    file for importing (like a standard 'open' icon).
[filename1, filepath1] = uigetfile('*.*','Select Absorption File');
filenameAbsorption = strcat(filepath1, filename1);
DataAbs = importdata(filenameAbsorption);

[filename2, filepath2] = uigetfile('*.*','Select Solvent EEM File');
filenameSolvent = strcat(filepath2, filename2);
DataSolvent = importdata(filenameSolvent);

[filename3, filepath3] = uigetfile('*.*','Select Sample EEM File');
filenameEEM = strcat(filepath3, filename3);
DataEEM = importdata(filenameEEM);


%%%%%%%          SET SAMPLE DATA TO BE ANYSISED.        %%%%%%%

SampleName = 'data1';     % Reference name of processed data.
```

```
% Numbered in this way to make constructing PARAFAC matrix easier.

TargetEEM = DataEEM;     % Change of name to help me identify solvent and
    sample EEM.
TargetAbs = DataAbs(:,2);

% Set limits of excitation and emission and the width of values to be 'cut'.
     Use (nm) values.
CropExLow = 260;
CropExhigh = 600;
CropEmlow = 290;
CropEmhigh = 750;
Slit = 9;     % Equivalent to bandpass value.


%%%%%%% DEFINE INTENSITY VALUES AND WAVELENGTH VALUES %%%%%%%

% idetify size of EEM data and find wavelength info.
x1 = find(TargetEEM(:,1) == CropEmlow);
x2 = find(TargetEEM(:,1) == CropEmhigh);
y1 = find(TargetEEM(1,:) == CropExLow);
y2 = find(TargetEEM(1,:) == CropExhigh);
x = TargetEEM(x1:x2,1); % define Em wavelengths (nm).
y = TargetEEM(1,y1:y2); % define Ex wavelengths (nm).
[xsize, colx] = size(x); % how many Em wavelengths.
[rowy, ysize] = size(y); % how many Ex wavelengths.
EEMsol = DataSolvent(x1:x2,y1:y2); % Just the intensity values for the
    solvent EMM.
EEMsample = TargetEEM(x1:x2,y1:y2); % Just the intensity values for the
    Sample EMM.


%%%%%%%      SET AXIS LIMITS AND VIEWING ANGLE      %%%%%%%%
Exlow = min(y);
Exhigh = max(y);
Emlow = min(x);
Emhigh = max(x);
```

```
55
56 Intlow = 0;
57 Inthigh = 100000;
58
59 % figure viewing angle.
60 az = 140; % 140 or -45
61 el = 30; % 30 or 45
62
63 %%%%%%%       PLOT DATA TO CHECK IT IS CORRECT       %%%%%%%
64 % Absorption spectrum.
65 plot(DataAbs(:,1), DataAbs(:,2));
66 title('Absorption Spectrum: 0mM Cyst');
67 xlabel('Wavelengths (nm)');
68 xlim([Exlow Emhigh]);
69 ylabel('Absorption (a.u.)');
70
71 % Solvent EEM data
72 surf(x,y,EEMsol');
73 caxis([Intlow Inthigh]);
74 axis([Emlow Emhigh Exlow Exhigh Intlow Inthigh]);
75 title('Solvent EEM');
76 xlabel('Em Wavelengths (nm)');
77 ylabel('Ex Wavelengths (nm)');
78 zlabel('Intensity (cps/\muAmp)');
79 view(az, el);
80
81 % Sample EEM data
82 surf(x,y,EEMsample');
83 caxis([Intlow Inthigh]);
84 axis([Emlow Emhigh Exlow Exhigh Intlow Inthigh]);
85 view(az, el);
86 title('Raw Sample EEM');
87 xlabel('Em Wavelengths (nm)');
88 ylabel('Ex Wavelengths (nm)');
89 zlabel('Intensity (cps/\muAmp)');
90
91
```

```
%%%% PICK OUT ABSORPTION VALUES MATCHING EEM WAVELENGTH  %%%%

% This is needed so that the IFE (inner filtering effect) matrix has the
    same dimentions as the EEM matrix.

% wavelengths of absorption data.
AbsWavelengths = DataAbs(:,1);

% find wavelength rows that correspond to EEM wavelengths (every 1/5th
    wavelength in this case).
LogicEx = AbsWavelengths == y;    % Creates a logic matrix with a 1 value
    where the Abs. wavelengths match the EEM wavelengths.
TempEx(:,1) = zeros(ysize,1);     % Define variable to prevent MATLAB
    warning.
TempEm(:,1) = zeros(xsize,1);     % Define variable to prevent MATLAB
    warning.

% Interates through every column of the logic matrix to find the row value
    that contains the 1 value.
for i = 1:ysize
    TempEx(i,1) = find(LogicEx(:,i) == 1);
    AexRows = TempEx;     % Vector containing Abs row values that match the
    EEM wavelengths used.
end

% Same as before but for the EEM emission wavelengths.
LogicEm = AbsWavelengths == x';
for i = 1:xsize
    TempEm(i,:) = find(LogicEm(:,i) == 1);
    AemRows = TempEm;
end


%%%%%%%    IFE CORRECTION & BACKGROUND SUBTRACTION    %%%%%%%

% construct IFE correction matrix.
AOPL = 0.5; % (absorption optical path length).
```

```
AlphaEm = (TargetAbs.*log(10))/AOPL;
AlphaEx = AlphaEm';
kfull = exp(AlphaEx.*AOPL + AlphaEm.*AOPL);
k = kfull(AemRows,AexRows); % IFE correction matrix.

Ik = EEMsample .* k; % sample EEM corrected for IFE.

Ic = Ik - EEMsol; % The corrected EEM.

% Plot IFE matrix as colour contour.
contourf(x,y,k');
colorbar;
title('IFE Correction EEM');
xlabel('Em wavelengths (nm)');
ylabel('Ex Wavelengths (nm)');

% Plot corrected EEM data.
surf(x,y,Ic');
caxis([Intlow Inthigh]);
view(az, el);
title('Corrected Sample EEM');
xlabel('Em Wavelengths (nm)');
ylabel('Ex Wavelengths (nm)');
zlabel('Intensity (cps/\muAmp)');
axis([Emlow Emhigh Exlow Exhigh Intlow Inthigh]);


%%%%%%%                SACTTER REMOVAL                %%%%%%%

Vmask = zeros(xsize,ysize); % prealocate matrix size to stop MATLAB
    complaining about it.

% First order Rayleigh
for i = 1:ysize
    j = find((x < (y(1,i) + (Slit + 5))) & (x > (y(1,i) - Slit)));
    Vmask(j,i) = NaN;
end
```

```
158
159 % First order Raman
160 for i = 1:ysize
161     yRam = 1e7*(((1e7./y(1,i))-3400).^-1);
162     j = ((x < (yRam + Slit)) & (x > (yRam - Slit)));
163     Vmask(j,i) = NaN;
164 end
165
166 SSlit = 2*Slit;
167 % Second order Rayleigh
168 for i = 1:ysize
169     j = find((x < (2*y(1,i) + SSlit)) & (x > (2*y(1,i) - SSlit)));
170     Vmask(j,i) = NaN;
171 end
172
173 % Second order Raman
174 for i = 1:ysize
175     yRam = 1e7*(((1e7./y(1,i))-3400).^-1);
176     j = find((x < (2*yRam + SSlit)) & (x > (2*yRam - SSlit)));
177     Vmask(j,i) = NaN;
178 end
179
180 % Plot 'Mask' that is used to "cut" scatter lines out of EEM data.
181 surf(x,y,Vmask'+1);
182 axis([Emlow Emhigh Exlow Exhigh 0.5 1.5]);
183 view(az, el);
184 title('Scatter Mask');
185 ylabel('Ex Wavelengths (nm)');
186 xlabel('Em Wavelengths (nm)');
187
188 % Plot of corrected EEM data with scatter lines removed.
189 Vcut = (Vmask+1).*Ic; % raise Vmask by one (since original z values equal 0)
      and then multiply by the corrected matrix.
190 surf(x,y,Vcut');
191 caxis([Intlow Inthigh]);
192 axis([Emlow Emhigh Exlow Exhigh Intlow Inthigh]);
193 view(az, el);
```

```
194 title('Scatter Removed');
195 xlabel('Em Wavelengths (nm)');
196 ylabel('Ex Wavelengths (nm)');
197 zlabel('Intensity (cps/\muAmp)');
198
199 %%%%%%%                  INTERPOLATION                  %%%%%%%
200
201 Vint = Vcut;     % prealocate matrix size to stop MATLAB complianing about
        it.
202 Vint(1,:) = 0;     % set edges to zero. Prevents spikes apearing.
203 Vint(xsize,:) = 0;
204 Vint(:,1) = 0;     % set edges to zero. Prevents spikes apearing.
205
206 for i = 1:ysize % should solvent cause some negativity in the data, this
        sets it to NaN.
207     j = find(Vint(:,i) < 0);
208     Vint(j,i) = NaN;
209 end
210
211 % Interpolation of missing data.
212 for i = 1:ysize
213     w = isnan(Vint(:,i));     % Generates logic array with 1 values where
        NaN appear and 0 elsewhere.
214     ww = find(w==1);     % Find row values of logic array where 1 appears.
215     xcut = x(ww);     % Construct xcut from EEM emission wavelength values (
        x) with row values matching ww.
216     mm = interp1(x,Vint(:,i),xcut,'pchip','extrap');
217     vv = ww';
218     Vint(vv,i) = mm;     % Interpolated EEM data.
219 end
220
221 % Plot corrected EEM data that has had the scatter lines removed and
        replaced with interpolated values.
222 surf(x,y,Vint');
223 caxis([Intlow Inthigh]);
224 axis([Emlow Emhigh Exlow Exhigh Intlow Inthigh]);
225 view(az, el);
```

```
title('Dopa-melanin','FontSize',16);
xlabel('Em Wavelength (nm)','FontSize',14);
ylabel('Ex Wavelength (nm)','FontSize',14);
zlabel('Intensity (cps/\muAmp)','FontSize',14);

%%%%%%%               Export Vint Data                %%%%%%%
clearvars -except DataAbs DataSolvent DataEEM SampleName Vint x y     %
    Clears variables that are not needed for PARAFAC.
save(SampleName);     % Saves all variables from the current workspace in a
    MATLAB formatted binary file (MAT-file) using the string variable '
    SampleName' as the file name. If filename exists, save overwrites the
    file.
%%%%%%%                        END                        %%%%%%%
```

Using the code above, it is possible to generate processed EEM data for each sample to be analysised with the PARAFAC algorithm. The code below takes each processed EEM data array and generates one array $\underline{X}$ that contains all the EEM data in the following format:

X = [A, B, C].

Where A is the sample name for each EEM dataset. B and C are the intensity values of the EEM. The array $\underline{X}$ is then passed to the PARAFAC algorith for analysis.

```
clearvars -except onemM pointeightmM zeromM

%{
EEM files need to be saves with the file name 'dataN'
where 'N' is an interger.
e.g. 'data1.mat', 'data2.mat', data3.mat', etc.
this way the script can use a for loop to construct the
matrix 'X' for whatever number of EEMs you want processed.
%}

%%%%%%%       Set number of EEMs to be processed       %%%%%%%

n = 12; % total number of EEM file to be processed.
m = n - 1;
F = 3; % number of factors to be used.

```

```
%%%%%%%              Construct variable X              %%%%%%%

for i = 1:m
    load(strcat('data', num2str(i),'.mat')); % load processed data.
    X(i,:,:) = Vint; % set processed matrix as ith matrix.
    clearvars -except X n F zeromM pointeightmM onemM; % clears  data.
end

load(strcat('data', num2str(n),'.mat')); % loads last EEM data.
X(n,:,:) = Vint; % sets last EEM data as the final matrix.
clearvars -except X x y F zeromM pointeightmM onemM; % clears all variables
    apart from X and the Ex/Em wavelength values.

%%%%%%%        Perform parallel factor analysis        %%%%%%%

FactNo = F; % defines the number of factors to use in the parafac analysis.
[Factors] = parafac(X,FactNo,[],[0 2 2]); % performing the parallel factor
    analysis.
[A,B,C] = fac2let(Factors); % converts the factors into individual
    components that can be plotted.

%%%%%%%        Plot results of parafac operation       %%%%%%%

subplot(2,2,1), plot(A, '-o', 'LineWidth',2);
legend('Species 1','Species 2','Species 3','Location','best');
title('Relative Concentration');
%axis([1 10 1E5 6E5]);
xlabel('Axis Label');
xticks([1:12]);
xticklabels({'0','0.01','0.1','0.2','0.4','0.6','0.8','1.0','1.5','3.0','
    Sepia','Dopa'});
ylabel('Relative Contrabution');
subplot(2,2,2), plot(x,B,'LineWidth',2);
legend('Species 1','Species 2','Species 3');
title('Emission');
%axis([290 750 0 0.35]);
xlabel('Wavelength (nm)');
```

```
ylabel('Intensity (a.u.)');
subplot(2,2,3), plot(y,C,'LineWidth',2);
legend('Species 1','Species 2','Species 3');
title('Excitation');
%axis([250 600 0 0.5]);
xlabel('Wavelength (nm)');
ylabel('Intensity (a.u.)');
%}
%%%%%%%                        END                        %%%%%%%
```

Appendix B

Sigmoidal Fitting to Melanin ThT Data

Code used to prepare the fixed emission time series data for fitting and then fitting both the Logistic and Hill sigmoidal functions to the data.

```
% FITTING SIGMOIDAL FUNCTIONS TO THE EMISSION TIME SERIES DATA OF
    PHEOMELANIN WITH THT.

%%%%%%%%%%%% Load Data & Assign Variables %%%%%%%%%%%%

% Load data from .dat file.
DataLoad = strcat('C:\Users\Davy\Google Drive\01-PhDYear#1\01-DATA\02-
    FluorologData\02-Melanin\19-ThT_Pheomelanin\', 'Sig_Fit_Data.dat');
Data = importdata(DataLoad);

% Code to assign columns of .dat file to variables.
Time = Data(:,2);
Pheo = Data(:,3); % Intrinsic pheomelanin.
Pheo_ThT_750 = Data(:,6); % Pheomelanin with 750u/ml tyrosinase and ThT.
ThT_Tyro = Data(:,8); % Tyrosinase with ThT.

% Simple plot to check the right data has been loaded.
plot(Time, Pheo, Time, Pheo_ThT_750, Time, ThT_Tyro)
axis([0 120 0 160000]);
```

```
title('Measured Data');
xlabel('Time (mins)');
ylabel('Emission Intensity (a.u.)');
legend('Pheo','Pheo+ThT (750u/ml)','ThT+Tyro','location','best');

%%%%%%%%%%%%%% Correcting For Intrinsic Responses %%%%%%%%%%%%%%

% Process Data, 'Apply corrections'.
Pheo_ThT_sub_intrinsic = Pheo_ThT_750 - Pheo;    % Intrinsic pheomelanin
    response subtracted from the Pheo+ThT response.
Pheo_ThT_Divide_ThT_Tyro = Pheo_ThT_750./ThT_Tyro;     % ThT+Tyro response
    divided from the pheo+ThT response.
[q, Pheo_ThT_deconv_ThT_Tyro] = deconv(Pheo_ThT_750, ThT_Tyro);     %
    Deconvolution of the Phto+ThT data with the ThT+Tyro data.

% Set limits
a0 = Time(1:7200,1);
A0 = Time(100:7200,1);
Pheo_ThT_750(1:100,1) = NaN;     % Initial values above plateau, which
    interferes with normalisation.
Pheo_ThT_sub_intrinsic(1:100,1) = NaN;     % Set initial values as 'Not-a-
    Number' to solve normalisation issue.
a1 = rescale(Pheo_ThT_750(1:7200,1));
a2 = rescale(Pheo_ThT_sub_intrinsic(1:7200,1));
a3 = rescale(Pheo_ThT_Divide_ThT_Tyro(1:7200,1));
a4 = rescale(Pheo_ThT_deconv_ThT_Tyro(1:7200,1));

% Plot to check processed data is corrected.
subplot(2,2,1);
plot(a0, a1,'k');
axis([0 120 0 1]);
title('\rm Pheo + ThT');
xlabel('Time (mins)');
ylabel('Em Intensity (a.u.)');
%legend('Pheo+ThT','location','best');
subplot(2,2,2);
plot(a0, a2, 'k');
```

```
axis([0 120 0 1]);
title('\rm (Pheo + ThT) - Pheo');
xlabel('Time (mins)');
ylabel('Em Intensity (a.u.)');
%legend('(Pheo+ThT) - Pheo','location','best');
subplot(2,2,3);
plot(a0, a3, 'k');
axis([0 120 0 1]);
title('\rm (Pheo + ThT)/(ThT + Tyro)');
xlabel('Time (mins)');
ylabel('Em Intensity (a.u.)');
%legend('(Pheo+ThT)/(ThT+Tyro)','location','best');
subplot(2,2,4);
plot(a0, a4, 'k');
axis([0 120 0 1]);
title('\rm Deconvolution');
xlabel('Time (mins)');
ylabel('Em Intensity (a.u.)');
%legend('Deconvolution','location','best');


%%%%%%%%%%%%%%%% Fitting Sigmodial To Data %%%%%%%%%%%%%%%%

% Prepares data for fitting and assigns variables for 'fit' function.
[xData1, yData1] = prepareCurveData(Time(550:6000,1), a1(550:6000,1));
[xData2, yData2] = prepareCurveData(Time(575:4500,1), a2(575:4500,1));
[xData3, yData3] = prepareCurveData(Time(1:6600,1), a3(1:6600,1));
[xData4, yData4] = prepareCurveData(Time(1:7200,1), a4(1:7200,1));


% Set up fittype (function for fit, in- and dependend variables) and options
    (Fitting method and initial values).

% For fitting the Logistic function.
ftL = fittype( '(a/(1 + exp(-b*(x - t)))) + c', 'independent', 'x', '
   dependent', 'y' );
optsL = fitoptions( 'Method', 'NonlinearLeastSquares' );
```

```
optsL.Display = 'Off';
optsL.StartPoint = [0.9 0.01 0 35];

% For fitting the Hill function.
ftH = fittype('c+(a-c)*((x^b)/((t^b)+(x^b)))', 'independent', 'x', '
    dependent', 'y');
optsH = fitoptions('Method', 'NonlinearLeastSquares');
optsH.Display = 'Off';
optsH.StartPoint = [0 1 3 35];

% Fit model to data.
% 'fitresults' contains fitted data and parameters. 'gof' contains goodness-
    of-fit statistics.
[fitresultL1, gofL1] = fit(xData1, yData1, ftL, optsL);
[fitresultL2, gofL2] = fit(xData2, yData2, ftL, optsL);
[fitresultL3, gofL3] = fit(xData3, yData3, ftL, optsL);
[fitresultL4, gofL4] = fit(xData4, yData4, ftL, optsL);

[fitresultH1, gofH1] = fit(xData1, yData1, ftH, optsH);
[fitresultH2, gofH2] = fit(xData2, yData2, ftH, optsH);
[fitresultH3, gofH3] = fit(xData3, yData3, ftH, optsH);
[fitresultH4, gofH4] = fit(xData4, yData4, ftH, optsH);

%%%%%%%%%%%%%%%%%%%%%%%%%%%%%%%%%%%%%%%%%%%%%%%%%%%%%%%%%%%%%%%%%%%%%%%
% Plot Results

% Pheo + ThT: Logistic.
subplot( 3, 1, [1,2] );
h = plot( fitresultL1, 'r', xData1, yData1, 'k');
axis([1 120 0 1]);
legend( h, 'Norm Data', 'Logistic Fit', 'Location', 'SouthEast');
legend boxoff
title('\rm Pheo: Logistic')
% Label axes
xlabel('');
ylabel('Norm Em Int (a.u.)');
grid off
```

```
120
121 subplot( 3, 1, 3 );
122 h = plot( fitresultL1, 'r', xData1, yData1, 'k', 'residuals' );
123 axis([1 120 -0.2 0.2]);
124 legend('hide');
125 % Label axes
126 xlabel('Time (mins)');
127 ylabel('Residuals');
128 grid off
129
130
131 % Pheo + ThT: Hill
132 subplot( 3, 1, [1,2] );
133 h = plot( fitresultH1, 'r', xData1, yData1, 'k');
134 axis([0 120 0 1])
135 legend( h, 'Norm Data', 'Hill Fit', 'Location', 'SouthEast');
136 legend boxoff
137 title('\rm Pheo: Hill')
138 % Label axes
139 xlabel('');
140 ylabel('Norm Em Int (a.u.)');
141 grid off
142
143 subplot( 3, 1, 3 );
144 h = plot( fitresultH1, 'r', xData1, yData1, 'k', 'residuals' );
145 axis([0 120 -0.1 0.1])
146 legend('hide');
147 % Label axes
148 xlabel('Time (mins)');
149 ylabel('Residuals');
150 grid off
```

Appendix C

Tables of Fitted Lifetime Values

Tables containing the fitted decay values for fluorescence lifetime decays of melanin with ThT, over time. Relavent to sections 4.4.2 and 4.4.3.

Pheomelanin with ThT

Time (mins)	τ_1 (ns)	τ_2 (ns)	τ_3 (ns)	B_1 (%)	B_2 (%)	B_3 (%)	χ^2
0	0.022	1.50		99.05	0.95		1.65
11	0.027	1.61		98.21	1.79		1.76
20	0.020	1.36	4.09	96.83	1.51	1.66	1.31
28	0.022	1.43	5.00	96.00	1.54	2.46	1.28
36	0.013	1.18	4.61	96.90	0.89	2.21	1.16
44	0.024	1.19	4.78	93.79	1.81	4.40	1.11
52	0.027	1.12	4.53	93.55	1.32	5.12	1.13
60	0.022	1.26	5.00	93.68	1.69	4.63	1.16
68	0.023	1.35	5.10	93.20	1.97	4.83	1.28
76	0.021	1.11	4.75	93.59	1.46	4.95	1.26
84	0.023	1.18	5.23	92.56	1.76	5.68	1.27
92	0.020	1.05	5.01	93.10	1.38	5.52	1.17
100	0.019	1.11	5.06	93.10	1.61	5.28	1.22
107	0.022	1.21	5.49	92.12	1.98	5.90	1.23

Pheomelanin

Time (mins)	τ_1 (ns)	τ_2 (ns)	τ_3 (ns)	B_1 (%)	B_2 (%)	B_3 (%)	χ^2
0	0.037	0.70	3.80	52.80	12.40	34.79	1.69
22	0.050	0.85	3.86	54.85	9.86	35.29	1.62
37	0.051	0.82	4.58	45.75	11.45	42.78	1.48
52	0.035	0.66	4.56	41.63	11.36	47.01	1.33
67	0.043	0.96	4.66	39.42	12.16	48.42	1.44
82	0.083	1.04	5.10	38.67	12.30	49.03	1.37
98	0.087	0.83	4.55	38.11	9.18	52.71	1.45
113	0.066	0.80	4.68	36.31	10.50	53.19	1.27
127	0.043	1.11	4.93	34.55	11.65	53.80	1.26

Eumelanin with ThT

Time (mins)	τ_1 (ns)	τ_2 (ns)	τ_3 (ns)	B_1 (%)	B_2 (%)	B_3 (%)	χ^2
0	0.019		1.51	99.49		0.51	1.40
5	0.023		1.61	99.51		0.49	1.36
10	0.027		2.93	99.37		0.63	1.30
15	0.022		2.37	99.22		0.78	1.46
21	0.025	0.46	3.01	97.75	0.84	1.40	1.58
30	0.016	0.43	3.47	97.63	1.01	1.37	1.58
40	0.021	0.48	3.00	96.31	1.50	2.19	1.59
50	0.014	0.44	3.39	97.01	1.11	1.89	1.51
60	0.026	0.47	3.98	93.77	2.10	4.13	1.38
70	0.022	0.46	4.33	92.73	2.37	4.90	1.20
80	0.022	0.62	4.91	91.10	2.66	6.24	1.18
90	0.019	0.64	5.17	90.16	2.79	7.05	1.17
100	0.024	0.81	5.55	86.52	3.73	9.74	1.16
110	0.021	0.90	5.91	84.99	4.31	10.70	1.15

Eumelanin

Time (mins)	τ_1 (ns)	τ_2 (ns)	τ_3 (ns)	B_1 (%)	B_2 (%)	B_3 (%)	χ^2
0	0.024	0.63	4.10	75.37	7.59	17.04	1.13
5	0.017	0.85	4.91	78.57	7.10	14.34	1.19
15	0.015	0.82	5.15	79.98	7.13	12.89	1.15
25	0.025	0.76	4.84	73.52	9.22	17.25	1.19
35	0.022	0.85	4.91	74.15	9.42	16.42	1.20
45	0.032	0.94	5.46	60.70	20.21	19.09	1.09
55	0.033	1.00	5.41	45.99	35.32	18.69	1.06
65	0.065	1.08	5.79	27.32	54.24	18.44	1.04
75	0.187	1.23	6.00	34.41	50.80	14.79	1.09
85	0.288	1.36	6.32	40.14	46.15	13.71	1.09
96	0.302	1.37	5.97	35.49	47.61	16.90	1.16
105	0.352	1.51	6.39	37.15	46.46	16.39	1.07
115	0.336	1.54	6.33	44.37	42.10	14.53	1.03

Bibliography

[1] K. Dybvig, L. L. Voelker, T. Merghoub, D. Polsky, and A. N. Houghton, "Molecular Biology of Melanoma," in *Mol. Basis Cancer*, 3rd ed., D. Meloni, Ed. Philadelphia: Elsevier Science, 1996, vol. 168, pp. 25–57.

[2] C. Wasmeier, A. N. Hume, G. Bolasco, and M. C. Seabra, "Melanosomes at a glance," *J. Cell Sci.*, vol. 121, no. 24, pp. 3995–3999, 2008.

[3] M. D'Ischia, K. Wakamatsu, F. Cicoira, E. Di Mauro, J. C. Garcia-Borron, S. Commo, I. Galván, G. Ghanem, K. Kenzo, P. Meredith, A. Pezzella, C. Santato, T. Sarna, J. D. Simon, L. Zecca, F. A. Zucca, A. Napolitano, and S. Ito, "Melanins and melanogenesis: From pigment cells to human health and technological applications," *Pigment Cell Melanoma Res.*, vol. 28, no. 5, pp. 520–544, 2015.

[4] W. D. Bush, J. Garguilo, F. A. Zucca, A. Albertini, L. Zecca, G. S. Edwards, R. J. Nemanich, and J. D. Simon, "The surface oxidation potential of human neuromelanin reveals a spherical architecture with a pheomelanin core and a eumelanin surface," *Proc Natl Acad Sci U S A*, vol. 103, no. 40, pp. 14 785–14 789, 2006.

[5] R. C. Sealy, J. S. Hyde, C. C. Felix, I. A. Menon, and G. Prota, "Eumelanins and Pheomelanins: Characterization by Electron Spin Resonance Spectroscopy," *Science*, vol. 217, no. 8, pp. 545–547, 1982.

[6] T. Sarna, I. A. Menon, and R. C. Sealy, "Photosensitization of melanins: a comparative study," *Photochem. Photobiol.*, vol. 42, no. 5, pp. 529–532, 1985.

[7] M. D'Ischia, K. Wakamatsu, A. Napolitano, S. Briganti, J. C. Garcia-Borron, D. Kovacs, P. Meredith, A. Pezzella, M. Picardo, T. Sarna, J. D. Simon, and S. Ito, "Melanins and

melanogenesis: Methods, standards, protocols," *Pigment Cell Melanoma Res.*, vol. 26, no. 5, pp. 616–633, 2013.

[8] S. Ito, "A Chemist's View of Melanogenesis," *Pigment Cell Res.*, vol. 16, no. 3, pp. 230–236, 2003.

[9] D. Leupold, M. Scholz, G. Stankovic, J. Reda, S. Buder, R. Eichhorn, G. Wessler, M. Stücker, K. Hoffmann, J. Bauer, and C. Garbe, "The stepwise two-photon excited melanin fluorescence is a unique diagnostic tool for the detection of malignant transformation in melanocytes," *Pigment Cell Melanoma Res.*, vol. 24, no. 3, pp. 438–445, 2011.

[10] T. B. Krasieva, C. Stringari, F. Liu, C.-H. Sun, Y. Kong, M. Balu, F. L. Meyskens, E. Gratton, and B. J. Tromberg, "Two-photon excited fluorescence lifetime imaging and spectroscopy of melanins in vitro and in vivo." *J. Biomed. Opt.*, vol. 18, no. 3, p. 31107, 2013.

[11] C. Fink and H. A. Haenssle, "Non-invasive tools for the diagnosis of cutaneous melanoma," *Ski. Res. Technol.*, vol. 23, no. 3, pp. 261–271, 2017.

[12] P. Meredith and T. Sarna, "The physical and chemical properties of eumelanin," *Pigment Cell Res.*, vol. 19, pp. 572–594, 2006.

[13] C. Kittel, *Introduction to Solid State Physics*, 8th ed. New York: John Wiley & Sons Ltd, 2004.

[14] F. Solano, "Melanin and melanin-related polymers as materials with biomedical and biotechnological applications – Cuttlefish ink and mussel foot proteins as inspired biomolecules," *Int. J. Mol. Sci.*, vol. 18, no. 7, 2017.

[15] J. Riesz, "The spectroscopic properties of melanin," Ph.D. dissertation, University of Queensland November, 2007.

[16] B. J. Powell, T. Baruah, N. Bernstein, K. Brake, R. H. McKenzie, P. Meredith, and M. R. Pederson, "A first-principles density-functional calculation of the electronic and

vibrational structure of the key melanin monomers," *J. Chem. Phys.*, vol. 120, no. 18, pp. 8608–8615, 2004.

[17] J. Riesz, J. Gilmore, and P. Meredith, "Quantitative scattering of melanin solutions," *Biophys. J.*, vol. 90, no. 11, pp. 4137–4144, 2005.

[18] ISS. (2019) Lifetime Data of Selected Fluorophores.

[19] S. P. Nighswander-Rempel, J. Riesz, J. Gilmore, and P. Meredith, "A quantum yield map for synthetic eumelanin," *J. Chem. Phys.*, vol. 123, no. 19, p. 194901, nov 2005.

[20] J. R. Lakowicz, *Principles of fluorescence spectroscopy, 3rd Edition, Joseph R. Lakowicz, editor*, 3rd ed. New York: Springer, 2006.

[21] S. E. Forest, W. C. Lam, D. P. Millar, J. B. Nofsinger, and J. D. Simon, "A model for the activated energy transfer within eumelanin aggregates," *J. Phys. Chem. B*, vol. 104, pp. 811–814, 2000.

[22] A. El Nahhas, T. Pascher, L. Leone, L. Panzella, A. Napolitano, and V. Sundström, "Photochemistry of pheomelanin building blocks and model chromophores: Excited-state intra- and intermolecular proton transfer," *J. Phys. Chem. Lett.*, vol. 5, no. 12, pp. 2094–2100, 2014.

[23] A. Corani, "Photochemistry of Eumelanin Precursors Role of Excited State Proton Transfer for UV Photoprotection," Ph.D. dissertation, Lund University, 2015.

[24] J. McGinness, P. Corry, and P. Proctor, "Amorphous Semiconductor Switching in Melanins," *Science*, vol. 183, no. 4127, pp. 853–855, 1974.

[25] T. Sarna, J. S. Hyde, and H. M. Swartz, "Ion-exchange in melanin: An electron spin resonance study with lanthanide probes," *Science*, vol. 192, no. 4244, pp. 1132–1134, 1976.

[26] E. Di Mauro, R. Xu, G. Soliveri, and C. Santato, "Natural melanin pigments and their interfaces with metal ions and oxides: Emerging concepts and technologies," *MRS Commun.*, vol. 7, no. 2, pp. 141–151, 2017.

[27] A. Büngeler, B. Hämisch, and O. I. Strube, "The supramolecular buildup of eumelanin: Structures, mechanisms, controllability," *Int. J. Mol. Sci.*, vol. 18, no. 9, 2017.

[28] A. A. R. Watt, J. P. Bothma, and P. Meredith, "The supramolecular structure of melanin," *Soft Matter*, vol. 5, no. 19, p. 3754, 2009.

[29] C. M. R. Clancy and J. D. Simon, "Ultrastructural organization of eumelanin from Sepia officinalis measured by atomic force microscopy," *Biochemistry*, vol. 40, no. 44, pp. 13 353–13 360, 2001.

[30] E. Kaxiras, A. Tsolakidis, G. Zonios, and S. Meng, "Structural model of eumelanin," *Phys. Rev. Lett.*, vol. 97, no. 21, p. 218102, 2006.

[31] S. Meng and E. Kaxiras, "Theoretical models of eumelanin protomolecules and their optical properties," *Biophys. J.*, vol. 94, no. 6, pp. 2095–2105, 2008.

[32] C. Chen, C. Chuang, J. Cao, V. Ball, D. Ruch, and M. J. Buehler, "Excitonic effects from geometric order and disorder explain broadband optical absorption in eumelanin," *Nat. Commun.*, vol. 5, no. 1, p. 3859, 2014.

[33] Cancer Research UK. (2014) Skin cancer incidence statistics.

[34] R. Hesketh, *Introduction to Cancer Biology*, 1st ed. Glasgow: Cambridge University Press, 2013.

[35] J. G. Elmore, R. L. Barnhill, D. E. Elder, G. M. Longton, M. S. Pepe, L. M. Reisch, P. A. Carney, L. J. Titus, H. D. Nelson, T. Onega, A. N. A. Tosteson, M. A. Weinstock, S. R. Knezevich, and M. W. Piepkorn, "Pathologists' diagnosis of invasive melanoma and melanocytic proliferations: observer accuracy and reproducibility study," *BMJ*, vol. 357, p. j2813, 2017.

[36] P. Corrie, M. Hategan, K. Fife, and C. Parkinson, "Medical Management of Melanoma," *Br. Med. Bull.*, vol. 111, pp. 149–162, 2014.

[37] M. E. Vestergaard, P. Macaskill, P. E. Holt, and S. W. Menzies, "Dermoscopy compared with naked eye examination for the diagnosis of primary melanoma: A meta-analysis of

studies performed in a clinical setting," *Br. J. Dermatol.*, vol. 159, no. 3, pp. 669–676, 2008.

[38] A. Scope, C. Benvenuto-Andrade, A.-L. C. Agero, J. Malvehy, S. Puig, M. Rajadhyaksha, K. J. Busam, D. E. Marra, A. Torres, I. Propperova, R. G. Langley, A. A. Marghoob, G. Pellacani, S. Seidenari, A. C. Halpern, and S. Gonzalez, "In vivo reflectance confocal microscopy imaging of melanocytic skin lesions: Consensus terminology glossary and illustrative images," *Journal of the American Academy of Dermatology*, vol. 57, no. 4, pp. 644–658, oct 2007.

[39] S. Seidenari, F. Arginelli, C. Dunsby, P. M. W. French, K. König, C. Magnoni, C. Talbot, and G. Ponti, "Multiphoton Laser Tomography and Fluorescence Lifetime Imaging of Melanoma: Morphologic Features and Quantitative Data for Sensitive and Specific Non-Invasive Diagnostics," *PLoS ONE*, vol. 8, no. 7, p. e70682, jul 2013.

[40] K. Teuchner, J. Ehlert, W. Freyer, D. Leupold, P. Altmeyer, M. Stücker, and K. Hoffmann, "Fluorescence studies of melanin by stepwise two-photon femtosecond laser excitation," *J. Fluoresc.*, vol. 10, no. 3, pp. 275–281, 2000.

[41] G. Santa Cruz, J. Bertotti, J. Marín, S. González, S. Gossio, D. Alvarez, B. Roth, P. Menéndez, M. Pereira, M. Albero, L. Cubau, P. Orellano, and S. Liberman, "Dynamic infrared imaging of cutaneous melanoma and normal skin in patients treated with BNCT," *Applied Radiation and Isotopes*, vol. 67, no. 7-8, pp. S54–S58, jul 2009.

[42] T. C. O'Haver, "Development of luminescence spectrometry as an analytical tool," *J. Chem. Educ.*, vol. 55, no. 7, p. 423, 1978.

[43] B. Valeur and M. N. Berberan-Santos, "A brief history of fluorescence and phosphorescence before the emergence of quantum theory," *J. Chem. Educ.*, vol. 88, no. 6, pp. 731–738, 2011.

[44] D. T. Burns, "Robert Boyle and the birth of analytical spectroscopy," *Anal. Spectrosc. Libr.*, vol. 6, pp. 3–17, 1995.

[45] N. T. Kalyani, H. Swart, and S. Dhoble, "Luminescence: Basic Principles and Applications," in *Princ. Appl. Org. Light Emit. Diodes*. Kindlington: Woodhead Publishing, 2017, ch. 1, pp. 1–37.

[46] J. Albani, *Principles and applications of fluorescence spectroscopy*. Chennai: Blackwell Pubishing, 2008.

[47] B. Valeur, *Molecular Fluorescence: Principles and Applications*. Weinheim: Wiley-VCH, 2001.

[48] P. Yip, "Nanometrology using Time-Resolved Fluorescence Techniques," Ph.D. dissertation, University of Strathclyde, 2016.

[49] W. Becker, *Advanced Time-Correlated Single Photon Counting Techniques*, ser. Springer Series in Chemical Physics. Berlin, Heidelberg: Springer Berlin Heidelberg, 2005, vol. 81.

[50] D. V. O'Connor and D. Phillips, *Electronics: Time-Correlated Single Photon Counting*. London: Academic Press, 1984.

[51] K. A. Selanger, J. Falnes, and T. Sikkeland, "Fluorescence lifetime studies of rhodamine 6G in methanol," *J. Phys. Chem.*, vol. 81, no. 20, pp. 1960–1963, 1977.

[52] S. Ito and K. Fujita, "Microanalysis of eumelanin and pheomelanin in hair and melanomas by chemical degradation and liquid chromatography," *Anal. Biochem.*, vol. 144, no. 2, pp. 527–536, 1985.

[53] R. Bro, "PARAFAC. Tutorial and applications," *Chemom. Intell. Lab. Syst.*, vol. 38, no. 2, pp. 149–171, 1997.

[54] A. K. Livesey and J. C. Brochon, "Analyzing the Distribution of Decay Constants in Pulse-Fluorimetry Using the Maximum Entropy Method," *Biophys. J.*, vol. 52, no. 5, pp. 693–706, 1987.

[55] J. M. Kainerstorfer, M. Ehler, F. Amyot, M. Hassan, S. G. Demos, V. Chernomordik, C. K. Hitzenberger, A. H. Gandjbakhche, and J. D. Riley, "Principal component model

of multispectral data for near real-time skin chromophore mapping," *J. Biomed. Opt.*, vol. 15, no. 4, p. 046007, 2010.

[56] S. Toyota, I. Fujiwara, M. Hirose, N. Ojima, K. Ogawa-Ochiai, and N. Tsumura, "Principal Component Analysis for the Whole Facial Image With Pigmentation Separation and Application to the Prediction of Facial Images at Various Ages," *J. Imaging Sci. Technol.*, vol. 58, no. 2, p. 20503, 2014.

[57] A. G. Mignani, L. Ciaccheri, B. Gordillo, A. A. Mencaglia, M. L. González-Miret, F. J. Heredia, and B. Culshaw, "Identifying the production region of single-malt Scotch whiskies using optical spectroscopy and pattern recognition techniques," *Sensors Actuators, B Chem.*, vol. 171-172, pp. 458–462, 2012.

[58] R. A. Harshman and M. E. Lundy, "PARAFAC: Parallel factor analysis," *Comput. Stat. Data Anal.*, vol. 18, no. 1, pp. 39–72, 1994.

[59] C. A. Andersson and R. Bro, "The N-way Toolbox for MATLAB," *Chemom. Intell. Lab. Syst.*, vol. 52, no. 1, pp. 1–4, 2000.

[60] K. R. Murphy, C. A. Stedmon, D. Graeber, and R. Bro, "Fluorescence spectroscopy and multi-way techniques. PARAFAC," *Anal. Methods*, vol. 5, no. 23, p. 6557, 2013.

[61] R. Bro and N. B. Gallagher, "PARAFAC for Analysis of Fluorescence EEM Data," 2005, Document by Eigenvector Research Inc.

[62] A. Corani, A. Huijser, T. Gustavsson, D. Markovitsi, P. Å. Malmqvist, A. Pezzella, M. D'Ischia, and V. Sundström, "Superior photoprotective motifs and mechanisms in eumelanins uncovered," *J. Am. Chem. Soc.*, vol. 136, no. 33, pp. 11 626–11 635, 2014.

[63] O. J. Rolinski, D. McLaughlin, D. J. Birch, and V. Vyshemirsky, "Resolving environmental microheterogeneity and dielectric relaxation in fluorescence kinetics of protein," *Methods Appl. Fluoresc.*, vol. 4, no. 2, 2016.

[64] K. Weron and A. Jurlewicz, "Two forms of self-similarity as a fundamental feature of the power-law dielectric response," *J. Phys. A. Math. Gen.*, vol. 26, no. 2, pp. 395–410, 1993.

[65] L. Dissado and R. Hill, "Self-similarity as a fundamental feature of the regression of fluctuations," *Chem. Phys.*, vol. 111, no. 2, pp. 193–207, 1987.

[66] M. N. Berberan-Santos, E. N. Bodunov, and B. Valeur, "Mathematical functions for the analysis of luminescence decays with underlying distributions 1. Kohlrausch decay function (stretched exponential)," *Chem. Phys.*, vol. 315, pp. 171–182, 2005.

[67] M. N. Berberan-Santos, E. N. Bodunov, and B. Valeur, "Mathematical functions for the analysis of luminescence decays with underlying distributions: 2. Becquerel (compressed hyperbola) and related decay functions," *Chem. Phys.*, vol. 317, pp. 57–62, 2005.

[68] H. Mahr, "Two-Photon Absorption Spectroscopy," in *Quantum Electron. A Treatise*, H. Rabin and C. L. Tang, Eds. London: Academic Press, 1975, ch. Chapter 4, pp. 285–361.

[69] K. Teuchner, W. Freyer, D. Leupold, A. Volkmer, D. J. Birch, P. Altmeyer, M. Stücker, and K. Hoffmann, "Femtosecond two-photon excited fluorescence of melanin." *Photochem. Photobiol.*, vol. 70, no. 2, pp. 146–51, 1999.

[70] T. G. Salopek, K. Yamada, S. Ito, and K. Jimbow, "Dysplastic Melanocytic Nevi Contain High Levels of Pheomelanin: Quantitative Comparison of Pheomelanin/Eumelanin Levels Between Normal Skin, Common Nevi, and Dysplastic Nevi," *Pigment Cell Res.*, vol. 4, no. 4, pp. 172–179, 1991.

[71] A. J. Lawaetz and C. A. Stedmon, "Fluorescence Intensity Calibration Using the Raman Scatter Peak of Water," *Appl. Spectrosc.*, vol. 63, no. 8, pp. 936–940, 2008.

[72] J. U. Sutter and D. J. Birch, "Metal ion influence on eumelanin fluorescence and structure," *Methods Appl. Fluoresc.*, vol. 2, no. 2, 2014.

[73] C. D. McGuinness, A. M. Macmillan, K. Sagoo, D. McLoskey, and D. J. S. Birch, "Excitation of fluorescence decay using a 265 nm pulsed light-emitting diode: Evidence for aqueous phenylalanine rotamers," *Appl. Phys. Lett.*, vol. 89, no. 6, p. 063901, 2006.

[74] G. M. Robinson and M. R. Smyth, "Simultaneous Determination of Products and Intermediates of L -Dopa Oxidation Using Capillary Electrophoresis With Diode-array Detection," *Analyst*, vol. 122, no. August, pp. 797–802, 1997.

[75] H. Ozeki, S. Ito, K. Wakamatsu, and A. J. Thody, "Spectrophotometric characterization of eumelanin and pheomelanin in hair," *Pigment Cell Res.*, vol. 9, no. 5, pp. 265–270, 1996.

[76] J. Riesz, J. Gilmore, and P. Meredith, "Quantitative photoluminescence of broad band absorbing melanins: A procedure to correct for inner filter and re-absorption effects," *Spectrochim. Acta - Part A Mol. Biomol. Spectrosc.*, vol. 61, no. 9, pp. 2153–2160, 2005.

[77] A. Corani, A. Pezzella, T. Pascher, T. Gustavsson, D. Markovitsi, A. Huijser, M. D'Ischia, and V. Sundström, "Excited-state proton-transfer processes of DHICA resolved: From sub-picoseconds to nanoseconds," *J. Phys. Chem. Lett.*, vol. 4, no. 9, pp. 1383–1388, 2013.

[78] D. Stoppa, D. Mosconi, L. Pancheri, and L. Gonzo, "Single-Photon Avalanche Diode CMOS Sensor for Time-Resolved Fluorescence Measurements," *IEEE Sensors Journal*, vol. 9, no. 9, pp. 1084–1090, sep 2009.

[79] N. Krstajic, R. Walker, J. Levitt, S. P. Poland, D. Li, S. Ameer-Beg, and R. K. Henderson, "A 256 $\times$ 8 SPAD line sensor for time resolved fluorescence and raman sensing," in *ESSCIRC 2014 - 40th European Solid State Circuits Conference (ESSCIRC)*. IEEE, sep 2014, pp. 143–146.

[80] O. J. Rolinski and V. Vyshemirsky, "Fluorescence kinetics of tryptophan in a heterogeneous environment," *Methods Appl. Fluoresc.*, vol. 2, no. 4, 2014.

[81] O. J. Rolinski, T. Wellbrock, D. J. Birch, and V. Vyshemirsky, "Tyrosine Photophysics during the Early Stages of β-Amyloid Aggregation Leading to Alzheimer's," *J. Phys. Chem. Lett.*, vol. 6, no. 15, pp. 3116–3120, 2015.

[82] M. N. Berberan-Santos, P. Choppinet, A. Fedorov, L. Jullien, and B. Valeur, “Multichromophoric cyclodextrins. 6. Investigation of excitation energy hopping by Monte-Carlo simulations and time-resolved fluorescence anisotropy,” *J. Am. Chem. Soc.*, vol. 121, no. 11, pp. 2526–2533, 1999.

[83] M. L. Tran, B. J. Powell, and P. Meredith, “Chemical and Structural Disorder in Eumelanins: A Possible Explanation for Broadband Absorbance,” *Biophys. J.*, vol. 90, no. 3, pp. 743–752, 2006.

[84] S. Reale, M. Crucianelli, A. Pezzella, M. D’Ischia, and F. De Angelis, “Exploring the frontiers of synthetic eumelanin polymers by high-resolution matrix-assisted laser/desorption ionization mass spectrometry,” *J. Mass Spectrom.*, vol. 47, no. 1, pp. 49–53, 2012.

[85] L. Panzella, A. Pezzella, A. Napolitano, and M. D’Ischia, “The first 5,6-dihydroxyindole tetramer by oxidation of 5,5’,6, 6’-tetrahydroxy-2,4’-biindolyl and an unexpected issue of positional reactivity en route to eumelanin-related polymers,” *Org. Lett.*, vol. 9, no. 7, pp. 1411–1414, 2007.

[86] A. Pezzella, L. Panzella, A. Natangelo, M. Arzillo, A. Napolitano, and M. D’Ischia, “5,6-Dihydroxyindole tetramers with "anomalous" interunit bonding patterns by oxidative coupling of 5,5’,6,6’-tetrahydroxy-2,7’- biindolyl: Emerging complexities on the way toward an improved model of eumelanin buildup,” *J. Org. Chem.*, vol. 72, no. 24, pp. 9225–9230, 2007.

[87] Z. Liu and Y. Bando, “A novel method for preparing copper nanorods and nanowires,” *Adv. Mater.*, vol. 15, no. 4, pp. 303–305, 2003.

[88] D. J. Kim, K.-y. Ju, and J.-k. Lee, “The Synthetic Melanin Nanoparticles Having An Excellent Binding Capacity of Heavy Metal Ions,” *Bull. Korean Chem. Soc*, vol. 33, no. 11, pp. 3788–3792, 2012.

[89] G. W. Zajac, J. M. Gallas, M. Eisner, and S. C. Moss, “The fundamental unit of synthetis melanin: a verification by tunneling microscopy of X-ray scattering results,” *Biochim. Biophys.*, vol. 1199, pp. 271–278, 1994.

[90] O. I. Strube, A. Büngeler, and W. Bremser, "Site-specific in situ synthesis of eumelanin nanoparticles by an enzymatic autodeposition-like process," *Biomacromolecules*, vol. 16, no. 5, pp. 1608–1613, 2015.

[91] J. U. Sutter, T. Bidláková, J. Karolin, and D. J. S. Birch, "Eumelanin kinetics and sheet structure," *Appl. Phys. Lett.*, vol. 100, no. 11, p. 113701, 2012.

[92] A. A. Maskevich, V. I. Stsiapura, V. A. Kuzmitsky, I. M. Kuznetsova, O. I. Povarova, V. N. Uversky, and K. K. Turoverov, "Spectral properties of thioflavin T in solvents with different dielectric properties and in a fibril-incorporated form," *J. Proteome Res.*, vol. 6, no. 4, pp. 1392–1401, 2007.

[93] S. Freire, M. H. De Araujo, W. Al-Soufi, and M. Novo, "Photophysical study of Thioflavin T as fluorescence marker of amyloid fibrils," *Dye. Pigment.*, vol. 110, pp. 97–105, 2014.

[94] N. Benseny-Cases, M. Cócera, and J. Cladera, "Conversion of non-fibrillar β-sheet oligomers into amyloid fibrils in Alzheimer's disease amyloid peptide aggregation," *Biochem. Biophys. Res. Commun.*, vol. 361, no. 4, pp. 916–921, 2007.

[95] O. J. Rolinski, M. Amaro, and D. J. S. Birch, "Early detection of amyloid aggregation using intrinsic fluorescence," *Biosens. Bioelectron.*, vol. 25, no. 10, pp. 2249–2252, 2010.

[96] J. Mohanty, S. Dutta Choudhury, H. Pal, and A. C. Bhasikuttan, "Early detection of insulin fibrillation: A fluorescence lifetime assay to probe the pre-fibrillar regime," *Chem. Commun.*, vol. 48, no. 18, pp. 2403–2405, 2012.

[97] V. I. Stsiapura, A. A. Maskevich, V. A. Kuzmitsky, V. N. Uversky, I. M. Kuznetsova, and K. K. Turoverov, "Thioflavin T as a molecular rotor: Fluorescent properties of thioflavin T in solvents with different viscosity," *J. Phys. Chem. B*, vol. 112, no. 49, pp. 15 893–15 902, 2008.

[98] V. I. Stsiapura, A. A. Maskevich, S. A. Tikhomirov, and O. V. Buganov, "Charge transfer process determines ultrafast excited state deactivation of thioflavin T in low-viscosity solvents," *J. Phys. Chem. A*, vol. 114, no. 32, pp. 8345–8350, 2010.

[99] D. Kucharavy and R. De Guio, "Application of S-shaped curves," *Procedia Eng.*, vol. 9, pp. 559–572, 2011.

[100] I. W. Hamley, "Peptide fibrillization," *Angew. Chemie - Int. Ed.*, vol. 46, no. 43, pp. 8128–8147, 2007.

[101] C. C. Lee, A. Nayak, A. Sethuraman, G. Belfort, and G. J. McRae, "A three-stage kinetic model of amyloid fibrillation," *Biophys. J.*, vol. 92, no. 10, pp. 3448–3458, 2007.

[102] S. Goutelle, M. Maurin, F. Rougier, X. Barbaut, L. Bourguignon, M. Ducher, and P. Maire, "The Hill equation: A review of its capabilities in pharmacological modelling," *Fundam. Clin. Pharmacol.*, vol. 22, no. 6, pp. 633–648, 2008.

[103] J. N. Weiss, "The Hill equation revisited: uses and misuses," *FASEB*, vol. 11, no. 1, pp. 835–841, 1997.

[104] H. Prinz, "Hill coefficients, dose-response curves and allosteric mechanisms," *J. Chem. Biol.*, vol. 3, no. 1, pp. 37–44, 2010.

[105] J. Riesz, T. Sarna, and P. Meredith, "Radiative relaxation in synthetic pheomelanin," *J. Phys. Chem. B*, vol. 110, no. 28, pp. 13 985–13 990, 2006.

[106] K. Y. Ju, J. Kang, J. H. Chang, and J. K. Lee, "Clue to Understanding the Janus Behavior of Eumelanin: Investigating the Relationship between Hierarchical Assembly Structure of Eumelanin and Its Photophysical Properties," *Biomacromolecules*, vol. 17, no. 9, pp. 2860–2872, 2016.

[107] T. Soderberg, "Organic Chemistry with a Biological Emphasis: Volume 1," pp. 67–76, 2016.

[108] T. Föster, "Excimers and Exciplexes," in *The Exciplex*, M. Gordon and W. R. Ware, Eds. London: Academic Press Inc., 1975, ch. Chapter 1, pp. 1–23.

[109] S. Ito, "Optimization of Conditions for Preparing Synthetic Pheomelanin," *Pigment Cell Res.*, vol. 2, pp. 53–56, 1989.

[110] C. D. McGuinness, K. Sagoo, D. McLoskey, and D. J. Birch, "A new sub-nanosecond LED at 280 nm: Application to protein fluorescence," *Meas. Sci. Technol.*, vol. 15, no. 11, 2004.

[111] A. D. Davy and D. J. S. Birch, "Evidence for pheomelanin sheet structure," *Appl. Phys. Lett.*, vol. 113, no. 26, p. 263701, 2018.

[112] A. D. Davy and D. J. S. Birch, "Probing pheomelanin synthesis using thioflavin T fluorescence," in *Proc. SPIE 10893, Reporters, Markers, Dyes, Nanoparticles, and Molecular Probes for Biomedical Applications XI*, 108930L, 2019.

[113] J. U. Sutter, Private communication, 2018.

[114] A. Siemiarczuk, B. D. Wagner, and W. R. Ware, "Comparison of the maximum entropy and exponential series methods for the recovery of distributions of lifetimes from fluorescence lifetime data," *J. Phys. Chem.*, vol. 94, no. 4, pp. 1661–1666, 1990.

[115] R. Micillo, L. Panzella, K. Koike, G. Monfrecola, A. Napolitano, and M. D'Ischia, ""Fifty Shades" of Black and Red or How Carboxyl Groups Fine Tune Eumelanin and Pheomelanin Properties," *Int. J. Mol. Sci.*, vol. 17, no. 5, p. 746, 2016.

[116] A. Corani, A. Huijser, A. Iadonisi, A. Pezzella, V. Sundström, and M. Dschia, "Bottom-Up approach to eumelanin photoprotection: Emission dynamics in parallel sets of water-soluble 5,6-dihydroxyindole-based model systems," *J. Phys. Chem. B*, vol. 116, no. 44, pp. 13 151–13 158, 2012.

[117] R. C. Curran and B. G. McCann, "The ultrastructure of benign pigmented naevi and melanocarcinomas in man." *J. Pathol*, vol. 119, pp. 135–146, 1976.

[118] J. Borovansky, P. Mirejovsky, and P. A. Riley, "Possible Relationship between Abnormal Melanosome Structure and Cytotoxic Phenomena in Malignant-Melanoma." *Neoplasma*, vol. 38, pp. 393–400, 1991.

[119] A. R. Rhodes, Y. Seki, T. B. Fitzpatrick, and R. S. Stern, "Melanosomal Alterations in Dysplastic Melanocytic Nevi - a Quantitative, Ultrastructural Investigation." *Cancer*, vol. 61, pp. 359–369, 1988.

[120] S. Eustis and M. a. El-Sayed, "Why gold nanoparticles are more precious than pretty gold: noble metal surface plasmon resonance and its enhancement of the radiative and nonradiative properties of nanocrystals of different shapes." *Chem. Soc. Rev.*, vol. 35, no. 3, pp. 209–17, mar 2006.

[121] A. M. Alkilany, S. E. Lohse, and C. J. Murphy, "The gold standard: Gold nanoparticle libraries to understand the nano-bio interface," *Acc. Chem. Res.*, vol. 46, no. 3, pp. 650–661, 2013.

[122] Y. Zhang, J. Yu, D. J. S. Birch, and Y. Chen, "Gold nanorods for fluorescence lifetime imaging in biology." *J. Biomed. Opt.*, vol. 15, no. April 2010, p. 020504, 2015.

[123] Y. Cheng, T. Stakenborg, P. Van Dorpe, L. Lagae, M. Wang, H. Chen, and G. Borghs, "Fluorescence Near Gold Nanoparticles for DNA Sensing," *Anal. Chem.*, vol. 83, no. 4, pp. 1307–1314, feb 2011.

[124] K. T. Butterworth, S. J. McMahon, F. J. Currell, and K. M. Prise, "Physical basis and biological mechanisms of gold nanoparticle radiosensitization," *Nanoscale*, vol. 4, no. 16, p. 4830, 2012.

[125] Y. Zhang, G. Wei, J. Yu, D. J. S. Birch, and Y. Chen, "Surface plasmon enhanced energy transfer between gold nanorods and fluorophores: application to endocytosis study and RNA detection," *Faraday Discuss.*, vol. 178, pp. 383–394, 2015.

[126] I. Fratoddi, I. Venditti, C. Cametti, and M. V. Russo, "How toxic are gold nanoparticles? The state-of-the-art," *Nano Res.*, vol. 8, no. 6, pp. 1771–1799, 2015.

[127] N. Khlebtsov and L. Dykman, "Biodistribution and toxicity of engineered gold nanoparticles: a review of in vitro and in vivo studies." *Chem. Soc. Rev.*, vol. 40, no. 3, pp. 1647–1671, 2011.

[128] H. Chen, L. Shao, Q. Li, and J. Wang, "Gold nanorods and their plasmonic properties," *Chem. Soc. Rev.*, vol. 42, no. 7, pp. 2679–2724, 2013.

[129] X. Huang and M. a. El-Sayed, "Gold nanoparticles: Optical properties and implementations in cancer diagnosis and photothermal therapy," *J. Adv. Res.*, vol. 1, no. 1, pp. 13–28, 2010.

[130] C. S. P. Nikam A.P., Mukesh P., R., "Nanoparticles – an overview," *Int. J. Res. Dev.Pharm. L. Sci.*, vol. 3, no. 5, pp. 1121–1127, 2014.

[131] A. M. Ealias and M. P. Saravanakumar, "A review on the classification, characterisation, synthesis of nanoparticles and their application," *IOP Conf. Ser. Mater. Sci. Eng.*, vol. 263, no. 3, 2017.

[132] I. I. Khan, K. Saeed, and I. I. Khan, "Nanoparticles: Properties, applications and toxicities," *Arab. J. Chem.*, 2017.

[133] U. Leonhardt, "Optical metamaterials: Invisibility cup," *Nat. Photonics*, vol. 1, no. 4, pp. 207–208, 2007.

[134] K. L. Kelly, E. Coronado, L. L. Zhao, and G. C. Schatz, "The Optical Properties of Metal Nanoparticles: The Influence of Size, Shape, and Dielectric Environment," *J. Phys. Chem. B*, vol. 107, pp. 668–677, 2003.

[135] D. B. Chithrani, S. Jelveh, F. Jalali, M. van Prooijen, C. Allen, R. G. Bristow, R. P. Hill, and D. A. Jaffray, "Gold Nanoparticles as Radiation Sensitizers in Cancer Therapy," *Radiat. Res.*, vol. 173, no. 6, pp. 719–728, 2010.

[136] J. P. M. Almeida, E. R. Figueroa, and R. A. Drezek, "Gold nanoparticle mediated cancer immunotherapy," *Nanomedicine Nanotechnology, Biol. Med.*, vol. 10, no. 3, pp. 503–514, 2014.

[137] E. C. Dreaden, A. M. Alkilany, X. Huang, C. J. Murphy, and M. a. El-Sayed, "The golden age: gold nanoparticles for biomedicine," *Chem. Soc. Rev.*, vol. 41, no. 7, pp. 2740–2779, 2012.

[138] T. Sen and A. Patra, "Recent Advances in Energy Transfer Processes in Gold-Nanoparticle-," *J. Phys. Chem. C*, vol. 116, no. 1, pp. 17 307–17 317, 2012.

[139] S. J. McMahon, W. B. Hyland, M. F. Muir, J. A. Coulter, S. Jain, K. T. Butterworth, G. Schettino, G. R. Dickson, A. R. Hounsell, J. M. O'Sullivan, K. M. Prise, D. G. Hirst, and F. J. Currell, "Biological consequences of nanoscale energy deposition near irradiated heavy atom nanoparticles." *Sci. Rep.*, vol. 1, no. 18, pp. 1–9, 2011.

[140] J. Perez juste, I. Pastorizasantos, L. Lizmarzan, P. Mulvaney, J. Pérez-Juste, I. Pastoriza-Santos, L. M. Liz-Marzán, and P. Mulvaney, "Gold nanorods: Synthesis, characterization and applications," *Coord. Chem. Rev.*, vol. 249, no. 17-18 SPEC. ISS., pp. 1870–1901, sep 2005.

[141] N. J. Durr, T. Larson, D. K. Smith, B. a. Korgel, K. Sokolov, and A. Ben-Yakar, "Two-photon luminescence imaging of cancer cells using molecularly targeted gold nanorods," *Nano Lett.*, vol. 7, no. 4, pp. 941–945, 2007.

[142] X. Huang, I. H. El-sayed, W. Qian, and M. A. El-sayed, "Cancer Cell Imaging and Photothermal Therapy in the Near-Infrared Region by Using Gold Nanorods," *Jacs*, vol. 128, no. 3, pp. 2115–2120, 2006.

[143] A. Jayagopal, K. C. Halfpenny, J. W. Perez, and D. W. Wright, "Hairpin DNA-functionalized gold colloids for the imaging of mRNA in live cells," *J. Am. Chem. Soc.*, vol. 132, no. 28, pp. 9789–9796, 2010.

[144] C.-Z. Li, K. B. Male, S. Hrapovic, and J. H. T. Luong, "Fluorescence properties of gold nanorods and their application for DNA biosensing." *Chem. Commun.*, pp. 3924–3926, 2005.

[145] M. A. MacKey, M. R. K. Ali, L. A. Austin, R. D. Near, and M. A. El-Sayed, "The most effective gold nanorod size for plasmonic photothermal therapy: Theory and in vitro experiments," *J. Phys. Chem. B*, vol. 118, no. 5, pp. 1319–1326, 2014.

[146] S. Jayabal, A. Pandikumar, H. N. Lim, R. Ramaraj, T. Sun, and N. M. Huang, "A gold nanorod-based localized surface plasmon resonance platform for the detection of environmentally toxic metal ions," *Analyst*, vol. 140, no. 8, pp. 2540–2555, 2015.

[147] L. Vigderman and E. R. Zubarev, "High-yield synthesis of gold nanorods with longitudinal SPR peak greater than 1200 nm using hydroquinone as a reducing agent," *Chem. Mater.*, vol. 25, no. 8, pp. 1450–1457, 2013.

[148] T. K. Sau and C. J. Murphy, "Seeded high yield synthesis of short Au nanorods in aqueous solution," *Langmuir*, vol. 20, no. 11, pp. 6414–6420, 2004.

[149] C. J. Orendorff and C. J. Murphy, "Quantitation of Metal Content in the Silver-Assisted Growth of Gold Nanorods," *J. Phys. Chem. B*, vol. 110, pp. 3990–3994, 2006.

[150] J. Liu, C. Detrembleur, M. C. De Pauw-Gillet, S. Mornet, C. Jérôme, and E. Duguet, "Gold nanorods coated with mesoporous silica shell as drug delivery system for remote near infrared light-activated release and potential phototherapy," *Small*, vol. 11, no. 19, pp. 2323–2332, 2015.

[151] D. S. Wang, S. C. Wei, S. C. Liao, and C. W. Lin, "Gold nanorods as probes in two-photon fluorescence correlation spectroscopy: Emerging applications and potential artifacts," *Microsc. Res. Tech.*, vol. 76, pp. 882–889, 2013.

[152] A. M. Alkilany, P. K. Nagaria, C. R. Hexel, T. J. Shaw, C. J. Murphy, and M. D. Wyatt, "Cellular uptake and cytotoxicity of gold nanorods: Molecular origin of cytotoxicity and surface effects," *Small*, vol. 5, pp. 701–708, 2009.

[153] C. F. Jones and D. W. Grainger, "In vitro assessments of nanomaterial toxicity," *Adv. Drug Deliv. Rev.*, vol. 61, no. 6, pp. 438–456, 2009.

[154] E. C. Cho, Q. Zhang, and Y. Xia, "The effect of sedimentation and diffusion on cellular uptake of gold nanoparticles." *Nat. Nanotechnol.*, vol. 6, no. 6, pp. 385–391, 2011.

[155] K. J. Ong, T. J. MacCormack, R. J. Clark, J. D. Ede, V. A. Ortega, L. C. Felix, M. K. M. Dang, G. Ma, H. Fenniri, J. G. C. Veinot, and G. G. Goss, "Widespread nanoparticle-assay interference: Implications for nanotoxicity testing," *PLoS One*, vol. 9, no. 3, 2014.

[156] N. a. P. Franken, H. M. Rodermond, J. Stap, J. Haveman, and C. van Bree, "Clonogenic assay of cells in vitro." *Nat. Protoc.*, vol. 1, no. 5, pp. 2315–9, 2006.

[157] M. R. K. Ali, B. Snyder, and M. a. El-Sayed, "Synthesis and optical properties of small Au nanorods using a seedless growth technique," *Langmuir*, vol. 28, no. 25, pp. 9807–9815, 2012.

[158] A. Wijaya and K. Hamad-Schifferli, "Ligand customization and DNA functionalization of gold nanorods via round-trip phase transfer ligand exchange," *Langmuir*, vol. 24, no. 18, pp. 9966–9969, 2008.

[159] C.-s. G. Nanorods, J. G. Mehtala, D. Y. Zemlyanov, J. P. Max, N. Kadasala, S. Zhao, and A. Wei, "Citrate-stabilized gold nanorods," *Langmuir*, vol. 30, no. 46, pp. 13 727–13 730, 2014.

[160] L. microsystems. EM Sample Preparation Coating Technology.

[161] J. Schindelin, C. T. Rueden, M. C. Hiner, and K. W. Eliceiri, "The ImageJ ecosystem: An open platform for biomedical image analysis," *Mol. Reprod. Dev.*, vol. in press, 2015.

[162] J. Schindelin, I. Arganda-Carreras, E. Frise, V. Kaynig, M. Longair, T. Pietzsch, S. Preibisch, C. Rueden, S. Saalfeld, B. Schmid, J.-Y. Tinevez, D. J. White, V. Hartenstein, K. Eliceiri, P. Tomancak, and A. Cardona, "Fiji: an open-source platform for biological-image analysis." *Nat. Methods*, vol. 9, no. 7, pp. 676–82, 2012.

[163] M. Boyd, R. J. Mairs, W. N. Keith, S. C. Ross, P. Welsh, G. Akabani, J. Owens, G. Vaidyanathan, R. Carruthers, J. Dorrens, and M. R. Zalutsky, "An efficient targeted radiotherapy/gene therapy strategy utilising human telomerase promoters and radioastatine and harnessing radiation-mediated bystander effects," *J. Gene Med.*, vol. 6, no. 8, pp. 937–947, 2004.

[164] S. N. Rampersad, "Multiple Applications of Alamar Blue as an Indicator of Metabolic Function and Cellular Health in Cell Viability Bioassays," *Sensors*, vol. 12, no. 12, pp. 12 347–12 360, 2012.

[165] X. Yang, "Clonogenic Assay to Test Cancer Therapies," *Bio-protocol*, vol. 2, no. 10, pp. 1–3, 2012.

[166] M. Boyd, S. H. Cunningham, M. M. Brown, R. J. Mairs, and T. E. Wheldon, "Noradrenaline transporter gene transfer for radiation cell kill by131I metaiodobenzylguanidine," *Gene Ther.*, vol. 6, no. 6, pp. 1147–1152, 1999.

[167] C. Guzmán, M. Bagga, A. Kaur, J. Westermarck, D. Abankwa, C. Guzmn, M. Bagga, A. Kaur, J. Westermarck, and D. Abankwa, "ColonyArea: An ImageJ plugin to automatically quantify colony formation in clonogenic assays," *PLoS One*, vol. 9, no. 3, pp. 14–17, 2014.

[168] B. Goris, S. Bals, W. Van den Broek, E. Carbó-Argibay, S. Gómez-Graña, L. M. Liz-Marzán, and G. Van Tendeloo, "Atomic-scale determination of surface facets in gold nanorods," *Nat. Mater.*, vol. 11, no. 11, pp. 930–935, 2012.

[169] D. Davies and P. Allen, *DNA Analysis by Flow Cytometry*. Totowa, NJ: Humana Press, 2007, pp. 165–179.

[170] K. Park, H. Koerner, and R. A. Vaia, "Depletion-induced shape and size selection of gold nanoparticles," *Nano Lett.*, vol. 10, no. 4, pp. 1433–1439, 2010.

[171] S. T. Gentry, S. F. Kendra, and M. W. Bezpalko, "Ostwald ripening in metallic nanoparticles: Stochastic kinetics," *J. Phys. Chem. C*, vol. 115, no. 26, pp. 12 736–12 741, 2011.

[172] Z. Li, S. Tang, B.-k. Wang, Y. Li, H. Huang, H. Wang, P. Li, C. Li, P. K. Chu, and X. Yu, "Metabolizable Small Gold Nanorods: Size-dependent Cytotoxicity, Cell Uptake and In Vivo Biodistribution," *ACS Biomater. Sci. Eng*, vol. 2, no. 5, pp. 789–797, 2016.

[173] T. S. Hauck, A. A. Ghazani, and W. C. Chan, "Assessing the effect of surface chemistry on gold nanorod uptake, toxicity, and gene expression in mammalian cells," *Small*, vol. 4, no. 1, pp. 153–159, 2008.

[174] T. B. Huff, M. N. Hansen, Y. Zhao, J.-X. Cheng, and A. Wei, "Controlling the Cellular Uptake of Gold Nanorods," *Langmuir*, vol. 23, no. 4, pp. 1596–1599, 2007.

[175] M. Tomura, A. Sakaue-Sawano, Y. Mori, M. Takase-Utsugi, A. Hata, K. Ohtawa, O. Kanagawa, and A. Miyawaki, "Contrasting Quiescent G0Phase with Mitotic Cell Cycling in the Mouse Immune System," *PLoS One*, vol. 8, no. 9, pp. 1–10, 2013.

[176] J. D. Unciti-Broceta, V. Cano-Cortés, P. Altea-Manzano, S. Pernagallo, J. J. Díaz-Mochón, and R. M. Sánchez-Martín, "Number of Nanoparticles per Cell through a Spectrophotometric Method - A key parameter to Assess Nanoparticle-based Cellular Assays," *Sci. Rep.*, vol. 5, p. 10091, 2015.